Antimicrobial surface engineering : combining topography and functionalisation with initiated chemical vapour deposition and cold atmospheric plasma polymerisation

Amelia Jane Whiteley

THÈSE

Pour obtenir le grade de

DOCTEUR DE L'UNIVERSITÉ GRENOBLE ALPES

École doctorale : I-MEP2 - Ingénierie - Matériaux, Mécanique, Environnement, Energétique, Procédés, Production
Spécialité : MAT - Matériaux
Unité de recherche : CEA Grenoble - LETI

Ingénierie de surfaces antimicrobiennes : combinaison de topographie et de fonctionnalisation par dépôt chimique en phase vapeur par polymérisation amorcée in situ et plasma atmosphérique froid

Antimicrobial surface engineering: combining topography and functionalisation with initiated chemical vapour deposition and cold atmospheric plasma polymerisation

Présentée par :

Amelia Jane WHITELEY

Direction de thèse :

Vincent JOUSSEAUME DIRECTEUR DE RECHERCHE, CEA - Centre de Grenoble	Directeur de thèse
Guillaume NONGLATON INGENIEUR CHERCHEUR, CEA	Co-encadrant de thèse

Rapporteurs :

Vincent HUMBLOT
DIRECTEUR DE RECHERCHE, CNRS délégation Centre Est
Mireille RICHARD-PLOUET
DIRECTRICE DE RECHERCHE, CNRS délégation Bretagne et Pays de la Loire

Thèse soutenue publiquement le **5 juillet 2024**, devant le jury composé de :

Vincent HUMBLOT, DIRECTEUR DE RECHERCHE, CNRS délégation Centre Est	Président
Vincent JOUSSEAUME, DIRECTEUR DE RECHERCHE, CEA centre de Grenoble	Directeur de thèse
Mireille RICHARD-PLOUET, DIRECTRICE DE RECHERCHE, CNRS délégation Bretagne et Pays de la Loire	Rapporteure
Christelle YEROMONAHOS, MAITRESSE DE CONFERENCES, Ecole Centrale de Lyon	Examinatrice
Marianne WEIDENHAUPT, MAITRESSE DE CONFERENCES HDR, Grenoble INP	Examinatrice

Invités :

Guillaume NONGLATON
INGENIEUR DOCTEUR, CEA Leti

To Pop-pop and Granny,

Acknowledgements

As I write these last words, it only feels right to express my gratitude in the language in which I would naturally exchange with each and every person who has helped me through this adventure. C'est ainsi que je vais transitionner vers le français pour la majorité de ces remerciements.

Tout d'abord je souhaiterais remercier les deux personnes qui ont encadré mon travail de thèse, qui m'ont fait confiance et qui m'ont aidé et encouragé à le mener à terme : mon directeur de thèse Vincent Jousseaume et mon encadrant Guillaume Nonglaton. Merci à vous deux pour votre bienveillance et votre gentillesse. Merci aussi pour votre rigueur scientifique qui m'a toujours poussée à faire mieux. Je vous remercie pour votre disponibilité et d'avoir toujours eu le temps de répondre à mes questions quand je venais vous voir au bureau. Merci à Vincent de m'avoir fait découvrir l'iCVD et merci à Guillaume de l'avoir découvert avec moi. Je suis très reconnaissante d'avoir pu travailler à vos côtés pendant 3 ans et j'ai beaucoup appris professionnellement et personnellement. Merci.

Je voudrais ensuite exprimer ma gratitude envers les membres de mon jury de thèse qui ont accepté d'évaluer mon travail. Merci à Vincent Humblot, directeur de recherche CNRS et Mireille Richard-Plouet, directrice de recherche CNRS, d'avoir lu et commenté mon manuscrit avec précision, en tant que rapporteurs. Vincent, que j'ai eu le plaisir de croiser plusieurs fois au cours de ma thèse, je te remercie aussi d'avoir accepté de présider mon jury. Je remercie ensuite Christelle Yeromonahos, maîtresse de conférences à l'INL et Marianne Weidenhaupt, maîtresse de conférences à Grenoble INP pour votre contribution en tant qu'examinatrices. Je vous remercie tous pour vos remarques constructives, nos échanges enrichissants et votre bienveillance.

Je remercie ensuite l'équipe chimie de surface : Caroline Fontelaye, Hippolyte Durand, Malika Amdouad, Axelle Aubert, Eve Le-dauphin. Merci pour votre accueil à bras ouverts dans l'équipe. Les pauses cafés et même nos réunions du lundi matin me manquent ! Caro, on pourrait te nommer reine de la salle blanche et maman des pépettes, merci pour ta douceur et pour toutes nos discussions scientifiques mais aussi celles à propos de tout et de rien. Hippo, merci pour ta bienveillance, ton aide précieuse quand il s'agissait de faire des caracs ou de la microbio. Merci aussi pour les heures passées à rédiger notre review ! Malika, merci pour ta gentillesse, ton énergie et ton sourire. J'espère que tu continues de danser. Axelle, merci beaucoup d'être arrivée parmi nous au cours de ma thèse, pile au moment où j'avais besoin d'une copine. On aura vécu des aventures ensemble en peu de temps, des pistes de ski à la plage, sans compter les heures passées en salle blanche à discuter en attendant la fin de nos process. Eve, nous ne nous sommes pas croisées longtemps, mais en ce peu de temps tu m'as beaucoup fait rire et m'a montré une détermination dont je suis admiratrice. Vous êtes tous de très belles personnes et je suis très chanceuse d'avoir pu partager tous ces moments avec vous.

Je dois ensuite exprimer ma profonde gratitude envers les techniciens de Trescal : Claude Gaillard, Rémi Lajoinie, Giuseppe Vela et Marco Lecci. Merci pour tout le temps que vous avez passé sur l'iCVD ainsi que pour la réactivité avec laquelle vous intervenez toujours. Claude et Rémi, ma thèse n'aurait jamais été la même sans vous et je n'aurais certainement jamais eu les résultats que je souhaitais. Merci infiniment de vous être battus avec moi pour dompter la bête et d'avoir toujours pris le temps de m'expliquer les différentes procédures de maintenance. J'ai beaucoup appris à vos côtés. Rémi, merci d'avoir toujours réussi à me faire rire, même quand j'avais plutôt envie de pleurer (on se rappellera la plaque en morceaux, ou plutôt en miettes :O, dans l'équipement…). Claude, merci d'avoir su me rassurer et merci pour toutes nos discussions à propos de maintenance, du cea et de la vie. Et surtout, merci mille fois pour votre optimisme !!

Je souhaiterais aussi remercier Chara Zavvou avec qui j'ai partagé mes galères d'équipement. Merci pour ton savoir et tes conseils à propos de l'iCVD, merci pour ton énergie folle et tous nos fous rires en salle. Tu es une très belle personne.

Je voudrais ensuite remercier toutes les personnes qui m'ont aidé avec des caractérisations de matériaux à la PFNC. Merci à Christophe Licitra qui m'a longuement aidé avec l'ellipsométrie et m'a fait découvrir la beauté du mapping. Névine Rochat, je te remercie pour ton aide précieuse à déchiffrer mes spectres FTIR, même si tu ne les aimais pas beaucoup avec tout leur Si-O. Denis Mariolle et Thomas Jalabert, merci pour toutes les images AFM. Denis, merci aussi pour ta gentillesse et toutes nos discussions ! Frédéric Fillot, merci pour les analyses XRR. Eugénie Martinez, je te remercie pour toutes les analyses XPS. Claire Guyot, merci aussi à toi pour ton aide précieuse avec Casa (accompagnée des meilleures madeleines de la planète c'est encore mieux <3). Merci aussi à Jérôme Rêche et Zouhir Mehrez pour les surfaces structurées.

Pierre, Thibaut et Stéphan, merci pour tout ce que vous m'avez appris en microbiologie. Même si vous n'avez pas réussi à me transmettre votre passion pour les microbes, je vous suis reconnaissante d'avoir essayé. Xavier, merci pour ton aide avec le microscope. Paul et Clément, merci pour vos programmes python, qui vous ont pris 3 minutes alors qu'il m'aurait fallu 3 mois !

Olivier, Marion et Catherine, merci pour votre aide avec mes lots foireux et les images MEB. Merci aussi de compléter l'équipe chimie au quotidien pour former la team café :).

Merci à Séverine Vignoux, Amélie Revaux et Christophe Serbutoviez. Trois chefs de labo en trois ans, je n'y aurais jamais cru. Merci à chacun d'entre vous.

Yoann Roupioz et Muriel Matheron, merci d'avoir accepté de faire partie de mon CSI et d'avoir suivi mes travaux tout au long de ma thèse. Je vous remercie pour vos nombreux conseils ainsi que pour votre gentillesse.

Je voudrais ensuite remercier Mélanie, Anastasiia et Marta pour nos discussions dans notre carré, généralement le soir quand il ne restait plus que nous dans l'open space.

J'ai aussi une pensée pour Dorothée en écrivant ces derniers mots, ma première voisine de bureau, qui m'a si bien accueillie.

Merci ensuite à toutes les personnes qui ont fait de ces trois années une très belle expérience personnelle, avec qui j'ai partagé de très nombreux repas à H1 ou H3, des cafés, des bières, des discussions et des sourires. Merci à Charles, Gauthier, Marie-Hélène (et Maya), Ilaria, Laurabelle, Lénaïc, Mehrsa, Pierre, Bastien, Rémy, Elodie, Sacha, Adélèye, Mathis, Laura, Anouchka, Emilie, Antoine, Maxime, Juliette, Paul, Léna, Marie, Mathilde, Katell, Mohammed, Zakaria, Mahfod, François, Manu, Joris, Marie, Aurélie, Dom, Fred, Léna, Jb.

Merci à tous mes amis, mes kikoos et mes coquillages, qui m'ont soutenue à travers les bons moments et aussi les moments les plus difficiles. J'ai une très grande chance de vous avoir dans ma vie.

I would also like to thank my family. Mum and Dad, thank you for always pushing me to do my best, even when that meant moving to the other side of France. Dad, you're going to have to find another curry house now sorry. Mum, thanks for turning the kitchen into a factory for my defense, it was hugely appreciated. Patrick, Ben et Anaïs, merci d'être qui vous êtes, je sais que je ne serais jamais seule avec vous à mes côtés.

Enfin merci à la personne sans qui je n'aurais jamais eu le courage de terminer cette aventure. Bertrand, merci pout tout ton amour et tout ton soutien. Je t'aime.

Table of contents

List of abbreviations

AFM	Atomic Force Microscopy
AR	Aspect Ratio
BET	Brunauer-Emmett-Teller
BSA	Bovine Serum Albumin
C	Carbon
CA	Cellulose Acetate
CFU	Colony Forming Units
CVD	Chemical Vapour Deposition
D3	Hexamethylcyclotrisiloxane
D4	Octamethylcyclotetrasiloxane
DBD-CAP	Dielectric Barrier Discharge Cold Atmospheric Plasma
DMTSO	Decamethyltetrasiloxane
EGDA	Ethylene glycol acrylate
EGDMA	Ethylene glycol dimethacrylate
EPS	Extracellular Polymeric Substance
FDTS	1H,1H,2H,2H-perfluorodecyltrichlorosilane
FESEM	Field Emission Scanning Electron Microscopy
FTIR	Fourier Transform InfraRed
fwhm	Full width half maximum
GMA	Glycidyl Methacrylate
HBr	Hydrogen Bromide
HEMA	Hydroxyethyl methacrylate
HFCVD	Hot Filament Chemical Vapour Deposition
HMDSO	Hexamethyldisiloxane
HWCVD	Hot Wire Chemical Vapour Deposition
iCVD	Initiated Chemical Vapour Deposition
IR	InfraRed
LbL	Layer-by-Layer
LDH	Layered double hydroxide
McF	McFarland
MPC	2-methacryloryloxyethyl phosphorylcholine
MSE	Mean Square Error
N	Nitrogen
NIL	Nano Imprint Lithography
O	Oxygen
PA	Polyamide
PDMS	polydimethylsiloxane
PE	Polyethylene
PECVD	Plasma Enhanced Chemical Vapour Deposition
PEDOT	Polyethylenedioxythiophene
PEG	Polyethylene glycol
PEGDA	Polyethylene glycol acrylate
PEI	polyethylenimine
PFBSF	Perfluorobutanesulfonyl fluoride
PFOSF	Perfluorooctane sulfonyl fluoride
PGMA	Poly(glycidyl methacrylate)
PI	Propidium iodide
PLA	Polylactic acid
PMDA	Pyromellitic dianhydride

POEGMA	Poly(ethylene glycol methacrylate)
POX	Poly(oxazolines)
PP-PiCVD	Atmospheric Pressure Plasma-initiated CVD
PSF	Polysulfone
PSPMA	Poly(3-sulfopropyl-methacrylate) potassium salt
PSS	Poly(styrene sulfonate
PTFE	Polytetrafluoroethylene
PVA	Poly(vinyl alcohol)
PVDF	Polyvinylidene fluoride
PVP	Polyvinylpyrrolidone
QACs	Quaternary Ammonium Compounds
RMS	Root Mean Square
ROS	Reactive oxygen species
sccm	Standard cubic centimetres per minute
SEM	Scanning Electron Microscopy
SF_6	Sulphur hexafluoride
Si	Silicon
SiO_2	Silicon dioxide
SS-ATRP	Sub-Surface initiated Atomic Transfer Radical Polymerisation
TBPO	Tert-butyl peroxide
TEL	Tokyo Electron Limited
TFC	Thin film composite
TiO_2	Titanium dioxide
TMCTS	Tetramethylcyclotetrasiloxane
TMDSO	Tetramethyldisiloxane
TMDSO	1,1,3,3-tetramethyldisiloxane
TSA	Tryptic Soy Agar
UV	Ultraviolet
V3D3	1,3,5-trimethyl-1,3,5-trivinylcyclotrisiloxane
V4D4	1,3,5,7-tetramethyl1,3,5,7-tetravinylcyclotetrasiloxane
VDP	Vapour Deposition Polymerisation
VP	Vinyl pyrrolidone
WCA	Water Contact Angle
XPS	X-ray Photoelectron Spectroscopy
XRR	X-Ray Reflectivity

General introduction

General introduction

Bacterial biofilm is formed when bacteria come into contact with the surface of any device found in a liquid non-sterile media. Bacteria form biofilm as a means of protection as they are much less vulnerable to biocides, to antibiotics and to the human immune system, as they are when they are found in planktonic form. The formation of biofilm affects a wide range of fields from the marine industry to medical implants. In domains such as the marine industry, where ship hulls, water buoys and turbines are often colonised by biofilm, it can lead to device failure and high costs. When bacterial biofilm grows on medical devices, healthcare-acquired infections can develop, increasing the risks of morbidity and mortality for patients and inducing a financial impact on the healthcare system. These nosocomial infections are often associated with catheters or other medical devices such as ventilators.

While most solutions targeting biofilm rely on killing bacteria, many of them are now showing their limits. For example, while antibiotics have proven to be very effective in the past, the recent and alarming rise of antibioresistance highlights the risks this method has induced. Metallic nanoparticles have also shown effective bactericidal activity through the creation of reactive oxygen species (ROS) which can damage the bacterial membrane. However, the arising concerns over the cytotoxicity of these species limits their use.

Rather than killing bacteria, targeting the initial bacterial adhesion is a strategy that is emerging in the literature. Turning towards living species, it has become apparent that tuning surface properties such as chemistry and topography can influence the adhesion of bacteria. There exist many different methods of engineering such surfaces, imparting them with a specific topography and chemistry. However, the precise impact of surface properties on bacterial adhesion and biofilm formation remains unclear. In this work, the influence of surface roughness, topography and hydrophobic or hydrophilic chemistry will be studied by coating structured surfaces. Working with polymer thin films allows the formation of robust, conformal and versatile coatings which can be deposited on both planar and structured surfaces. There are many techniques to deposit polymer thin films, however initiated chemical vapour deposition (iCVD) is the only vacuum-based method based on free radical polymerisation. This allows a strong control over the chemical composition of the resulting polymer. Furthermore, this method has been proven to produce conformal thin films even on structures with high aspect ratios. Dielectric barrier discharge cold atmospheric plasma (DBD-CAP) offers an alternative route to depositing functional coatings. Although allowing less control over the polymerisation step, this technique has other advantages such as its quick adaptability to many different precursors. The first monomer which was chosen is organosilicon V3D3 which can lead to a hydrophobic coating without the use of fluorine. PVP was also deposited by iCVD as it is known for its superhydrophilicity and biocompatibility. A systematic study of the adhesion and viability of bacteria was then carried out by varying chemistry, roughness and topography to identify the most impacting parameters.

In the **first chapter** of this thesis, the state of the art on antibiofouling strategies combining chemistry and topography will be presented. Largely inspired by a literature review written and published in *ACS Applied Bio Materials* during this thesis, in collaboration with Hippolyte Durand, Pascal Mailley and Guillaume Nonglaton and entitled “Combining Topography and Chemistry to Produce Antibiofouling Surfaces: A Review”, this chapter focuses on hydrophobic and hydrophilic chemistry for their antiadhesive activity. Techniques used to deposit polymer thin films will then be presented, giving their advantages and drawbacks and justifying the choice of DBD-CAP and iCVD.

In the **second chapter** of this manuscript, the deposition processes will be presented for each polymer after giving the specificities of each method. The co-injection of two monomers using iCVD

will also be discussed. The surface characterisation techniques used to analyse the various coatings will also be presented.

The **third chapter** will focus on the film obtained from the V3D3 monomer. Two polymers were studied: conventional polymer poly(V3D3), deposited by iCVD, and plasma polymer pp(V3D3) obtained through DBD-CAP. Analysis of some of the properties of these thin films shows that, while these polymers share many similarities, the deposition method has a significant impact on the chemical composition and structure of the final coating.

In the **fourth chapter**, superhydrophilic PVP thin films deposited by iCVD were studied. While these coatings exhibited superhydrophilicity, they were also soluble in water, making them unadapted for antibiofouling surfaces. In the second part of this chapter, copolymers poly(VP-co-V3D3) were studied where V3D3 acts as a crosslinking agent to stabilise the hydrophilic film. Varying the injected fractions of each monomer led to different copolymers and their chemical analysis allowed to determine the fractions of each monomer present in the final copolymer. By applying the Fineman-Ross equation, the reactivity ratios and the type of copolymer could be determined.

In the **fifth chapter** of this manuscript, the fabrication and functionalisation of hierarchical structures will be presented. These structures, fabricated in the CEA Leti's 200 and 300 mm microsystems platform, are a combination of microstructures obtained by nanoimprint lithography (NIL) and nano scale roughness brought by different plasma etching. These substrates were then combined with the polymers discussed in the previous chapters. Analysis of the surface chemistry, roughness and wettability was carried out for these structured surfaces, with and without further polymer coating.

Finally, in the **sixth and last chapter**, microbiology assays will be presented. After presenting the protocols carried out for these experiments, the adhesion and viability of *E. coli* and *S. epidermidis* on the different surfaces developed throughout this project will be discussed.

Chapter 1: Antibiofouling surfaces

1. Biofilm and its consequences

1.1. The discovery and definition of biofilm

Biofilms were first observed at the end of the 17th century by microbiology pioneer, Van Leeuwenhoek[1,2]. These matrices are formed by the spontaneous deposition of molecules, macromolecules and microorganisms onto any surface in a non-sterile aqueous medium[3], and are irreversibly attached to a surface[1]. They can be found on a variety of surfaces, from living tissues to ship hulls and can cause problems from nosocomial infections[4] to performance loss[3].

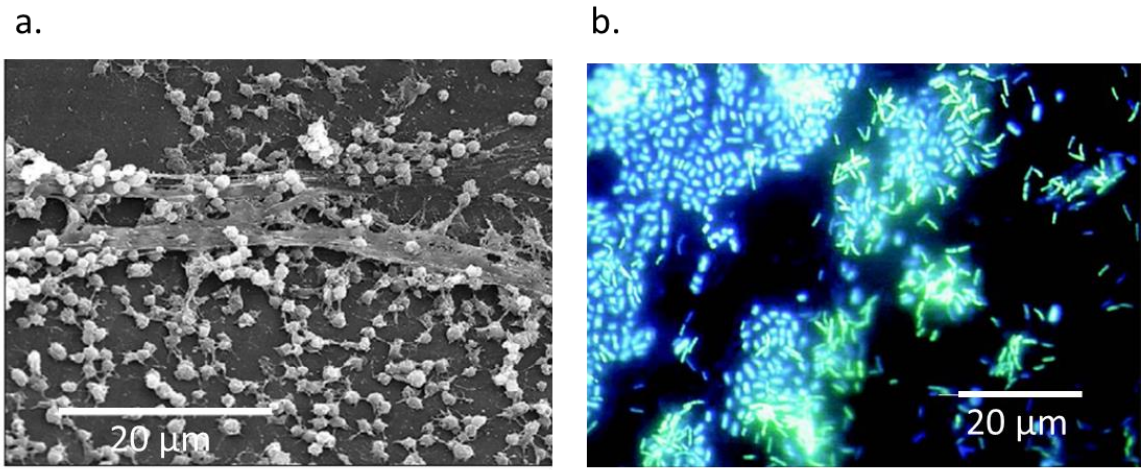

Figure 1: a. Staphylococcal biofilm on a medical device. b. Polymicrobic biofilm grown on a stainless-steel surface in a laboratory potable water biofilm reactor for 14 days, then stained with 4,6-diamidino-2-phenylindole (DAPI) and examined by epifluorescence microscopy. Adapted from Donlan[1].

Both Gram-positive and Gram-negative bacteria can create biofilm. The difference between these types of bacteria, determined by Gram coloration, is the structure of their membranes. Indeed, while both contain an inner cytoplasmic membrane, Gram-positive bacteria have a much thicker membrane, predominantly constituted of peptidoglycans. Gram-negative bacteria on the other hand have a smaller layer of peptidoglycans but also have an exterior membrane[5]. Biofilms are constituted of bacterial cells imbedded in extracellular polymeric substance (EPS) which are mostly constituted of polysaccharides. However, depending on the bacteria involved in the biofilm formation, the nature of these polysaccharides can vary. For example, Gram-negative bacteria generally produce neutral or polyanionic EPS whereas some Gram-positive bacteria such as staphylococci tend to produce cationic EPS[1]. Furthermore, other properties such as wettability, structure and solubility may vary depending on the type of EPS[1].

Bacterial biofilms can be constituted of one (Figure 1a) or more (Figure 1b) species of bacteria and in both cases are heterogeneous with microcolonies encapsulated in EPS and separated by water channels which allow the transfer of nutrients and oxygen but also antimicrobial agents[1]. Once the biofilm is mature, it provides an ideal environment for bacteria as the proximity between the cells favours gene exchange and quorum sensing. Furthermore, biofilms assure strong protection to the cells as bacteria in biofilms are more resistant to antibacterial agents[6] as well as host immune systems when developed in the human body[1].

In some environments a bacterial biofilm can lead to more complex biofilms containing other components such as marine diatoms, blood components, or even clay or corrosion particles[1]. This is often the case in sea water for example where bigger organisms such as shellfish or algae can create marine biofilms.

1.2.Consequences of biofilm

Biofilm can be a problem in many different fields ranging from big industries to the human body. As well as leading to device failure and contamination, biofilm formation generates many costs, both for removing it, and because it decreases device's functionalities.

Marine

In the marine industry, biofouling is well known on ships[7], but it can also occur on marine farming installations, turbines, water buoys, floating pontoons and other devices emerged in water[8]. Areas with high aeration such as ship propellers show the highest amount of marine biofouling. The presence of species such as shellfish and algae can lead to non-negligible friction which impacts fuel consumption and, consequently costs and greenhouse gas emissions[9].

Industrial

Artificial structures found in a great number of different industries can also suffer from biofouling. For example, it has been pointed out that biofilms constituted of bacteria, fungi and algae[10], can develop in water cooling systems of nuclear power plants, accelerating aging and leading to higher risks[11]. Membranes, which can be used, among others, in water treatment or desalination, can also be obstructed by bacterial and fungi biofilm, leading to pore obstruction and consequently flow rate decrease[12], as well as water contamination.

Food

In the food industry, thermal treatments, on dairy products for example, encourage bacterial biofilm formation[13] which can lead to food contamination.

Medical

In the medical field, bacterial biofilm can form on medical equipment, prosthetic and dental implants, catheters, biosensors and other devices[9]. This can lead to device failure, rejection of implants and major infections. As well as increasing mortality rates, biofilm in the medical field can increase the length of hospital stays and induce many costs. Bacterial biofilm is thought to be responsible for nearly half of nosocomial infections, and more precisely, clinical implants such as urethral catheters, tracheal tubes or vascular catheters could lead to infections for 1 out of 10 patients[9]. Ventilator-associated pneumonia can also be bought on by biofilm formation in the respiratory device. Biofilm can also form on more permanent implants such as pacemakers, orthopaedic implants, bone plates, dental implants or biosensors. This generally leads to their replacement[9]. When formed on biosensors, biofilm can cause inaccuracy and eventually impede the sensing capabilities of the device.

These examples show the importance of tackling biofilm, as it affects numerous different fields, causing health issues but also generating many costs due to maintenance operations or device failure.

1.3. Biofilm formation

Biofilm formation happens in several steps, as represented in Figure 2. The first is reversible adhesion where microorganisms come into contact with the surface of interest. This can sometimes be favoured by a conditioning layer of macromolecules such as proteins on the surface. However, gentle washing will still eliminate the bacteria from the surface at this stage. Next, the attached bacteria excrete extracellular polymeric substances to secure their adhesion which then becomes irreversible. From this stage, removing the biofilm cannot be done without harsher methods. Once the microbial adhesion is irreversible upon the substrate, microcolonies can form which further develop into a mature biofilm. From this protective matrix, bacteria can then disperse and colonize other nearby surfaces[14].

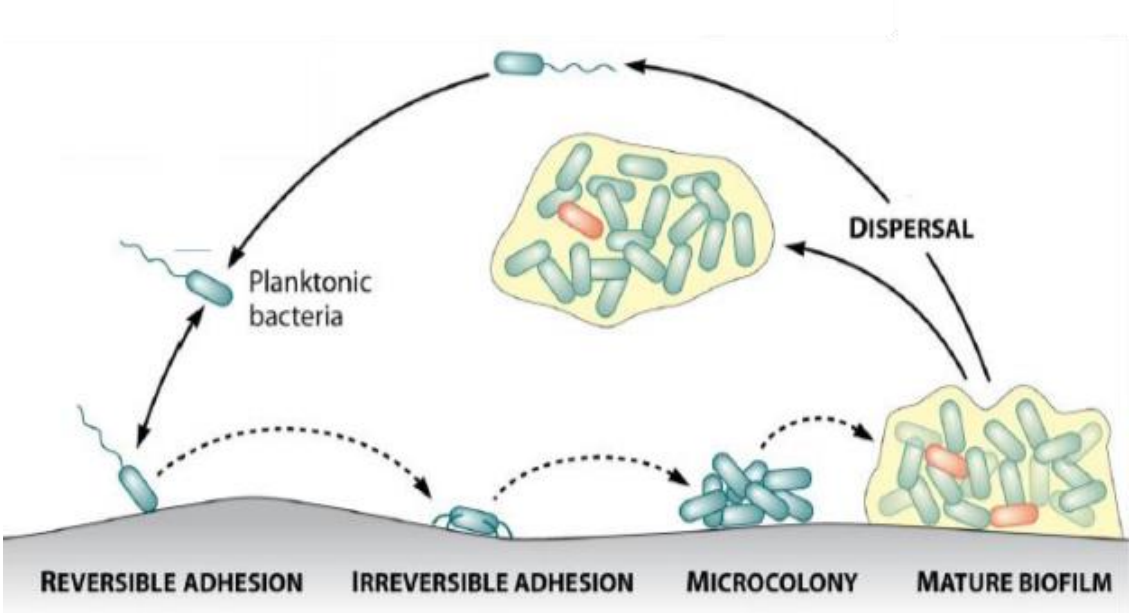

Figure 2: Schematic representation of biofilm formation. Adapted with permission from Lebeaux et al.[15] *Copyright © 1997 American Society for Microbiology.*

Evaluating biofilm formation in a clinical setting is complicated. However, in vitro studies and animal experimentation have shown that it often occurs within hours. After its initial attachment onto a surface, *Pseudomonas aeruginosa* can begin expressing genes involved in biofilm formation within 15 min[16] and form a mature biofilm within 8 h[17].

These numerous steps in biofilm formation mean there are also various ways of fighting it. While many focus on bactericidal strategies to eliminate the already mature biofilm; others focus on preventing biofilm formation at the start[15]. These different strategies used for fighting biofilm will be presented in the following section.

2. Eliminating biofilm

2.1. Curative biocidal methods and their limitations

For decades, the fight against biofilm relied on curative methods such as biocides and antibiotics. Indeed, antibiotics are globally used to fight bacterial infections and can have various modes of action on the bacterial cells (Figure 3). However, after administering antibiotics to livestock as well as humans, antibioresistance has rocketed, becoming an urgent health threat according to the World Health Organization (WHO)[18]. In fact, the European Commission predicts 10 million deaths each year from antibioresistance by 2050 if antibiotics' use is not globally reduced[19]. Moreover, while antibiotics are generally efficient on planktonic bacteria despite the rise of resistant strains, on bacterial biofilm they can be up to 1000 times less efficient[6,9].

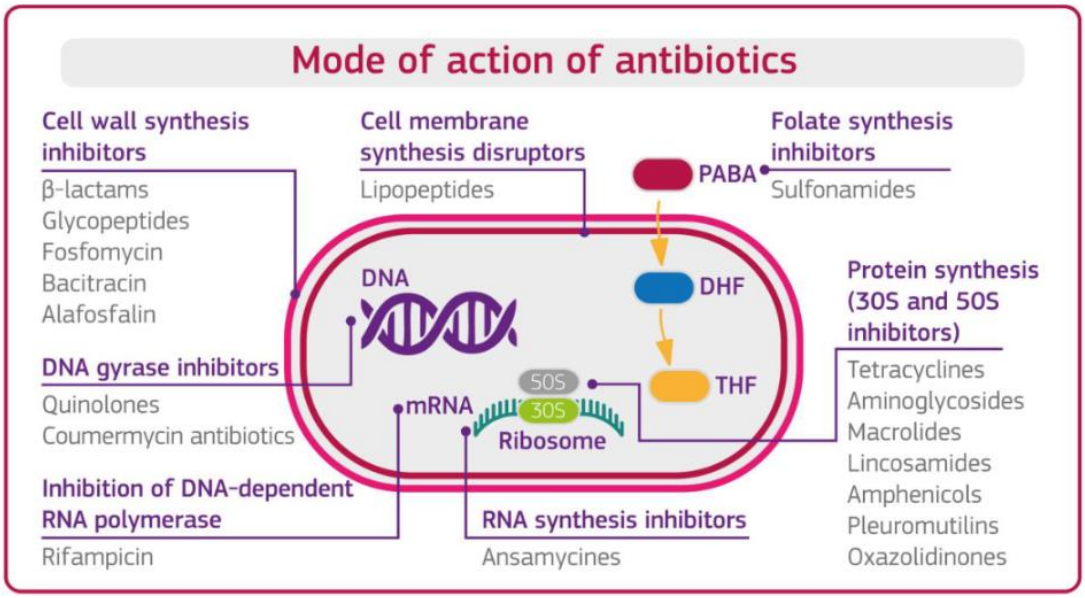

Figure 3: Mechanisms of action of antibiotics. Reprinted from Sanseverino et al.[20]

As for biocides such as sodium hypochlorite or iodine, used in hospitals to eradicate bacteria, some studies are showing there may also be emergence of biocide-resistance[21].

Metals, such as silver and copper, and nanoparticles have also been used for their biocidal properties as they release reactive oxygen species (ROS) which can have various effects on the cell membranes (Figure 4). For example, these ROS can lead to electrostatic interactions with the membrane, between electronegative polysaccharides and metal cations for instance, causing membrane permeation. Accumulation of metal ions can also lead to unbalancing the metabolic functions, damaging deoxyribonucleic acid (DNA) and protein, as well as inhibiting the transduction signal[22]. However, these components are also raising concern due to their presumed toxicity[23]. Their use is therefore prohibited for some applications such as the space industry[24].

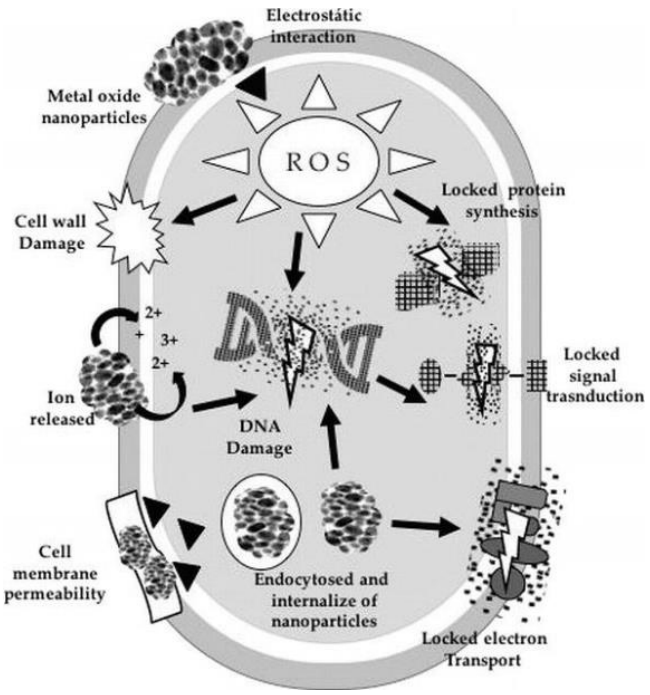

Figure 4: Bactericidal mechanisms of action of metal oxide nanoparticles. Reprinted from Vega-Jimenez et al. [22]

2.2.Preventive methods to inhibit biofilm formation

As traditional antibacterial strategies show their limits, new approaches are being developed. Rather than trying to remove established biofilm, the focus has shifted towards preventing its growth by limiting bacterial adhesion. Three main strategies have emerged for inhibiting biofilm formation and can be achieved with different surface functionalisation[3].

Release-killing mechanism

First, the release-killing mechanism relies on the use of biocidal agents that are encapsulated on the surface and released, killing bacteria that are found at proximity. The release can be spontaneous or controlled in the case of a bioresponsive surface. In this case, a change in temperature[25,26], pH[25], mechanical stimulation[27] or application of an electric field[28], will lead to a change in configuration of the material which will then release the active molecules. However, this method often relies on the release of biocidal agents such as antibiotics or nanoparticles which again raises the issue of antibioresistance and toxicity. Furthermore, while this strategy can be efficient in the short-term, only a limited number of biocidal agents can be stored in the material which becomes inactive after a given time[4].

Contact killing surfaces

Secondly, contact-killing surfaces refer to materials that inactivate cells upon contact. While immobilizing antibiotics or nanoparticles can be efficient in this case, with the interest of turning to more environmentally friendly and non-cytotoxic solutions, other strategies are being developed. For instance, charged surfaces such as quaternary ammonium compounds (QACs) have been used for their bactericidal activity which is due to the presence of cations[29,30]. Antimicrobial peptides (AMPs), which penetrate the bacterial membrane, inducing cell lysis are also widely studied[6,31–33], as well as some natural essential oils such as rosemary or lemongrass which can be incorporated into polymers[34]. Furthermore, strategies consisting of modifying the material's topography to induce mechanical stress

on the bacteria are also being developed[35,36]. However, one issue with contact-killing is that dead cells on a surface can become a conditioning layer for surrounding planktonic bacteria.

Preventing bacterial adhesion

Last but not least, preventing biofilm formation has also been carried out by developing surfaces that inhibit the first step in biofilm formation which is bacterial adhesion (Figure 2). This can be achieved by tuning the stiffness of the surface[37,38], or by functionalising the surface with specific enzymes[39], but controlling the wettability is the most common approach. This can be done by coating materials with hydrophobic or hydrophilic chemistry as it will be seen in the following section.

2.3.Hydrophobic and hydrophilic surfaces to prevent bacterial adhesion

2.3.1. Surface wetting mechanisms

Describing surface wettability is a way of depicting interactions between a liquid and a surface. Indeed, as a droplet is deposited onto a surface, it spreads until an equilibrium is found between gravity forces, internal forces (cohesion) and capillarity forces. More precisely, these terms are linked to the contact angle θ in air on the given surface by Young's equation:

$$\gamma_{SG} = \gamma_{SL} + \gamma_{LG}\, cos\theta$$

with γ_{SG}, γ_{SL} and γ_{LG} the surface tension coefficients of solid-gas, solid-liquid and liquid-gas, respectively[40].

Following this model, a hydrophobic surface is a surface that repels water, and on the contrary, when a surface has a strong affinity with water, it is said hydrophilic. As represented in Figure 5, when the water contact angle (WCA) is over 90°, the surface is hydrophobic, when it is under 90°, the surface is hydrophilic[41]. Furthermore, a surface can also be said superhydrophobic, when the WCA is over 150°. This means that there is hardly any contact between the liquid and the surface. On the other hand, a surface can be superhydrophilic when its WCA is under 10°. This occurs with perfect wetting and the liquid spreading completely onto the surface[42].

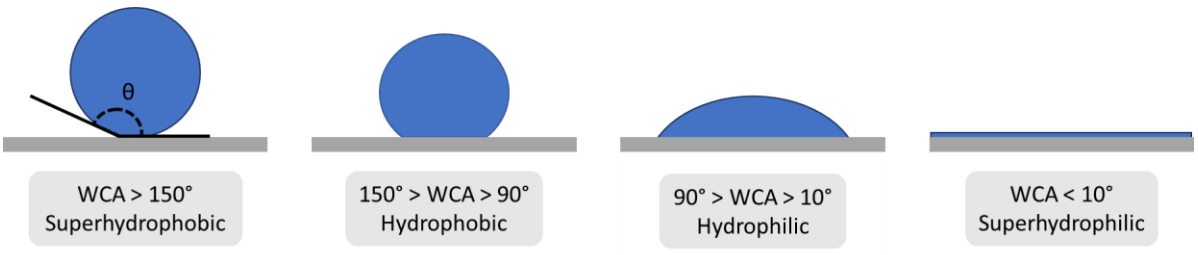

Figure 5: Water Contact Angles (WCAs) and the corresponding wettability.

While Young's model is adapted for smooth and homogeneous surfaces[40], it has been shown that modifying the surface's roughness and/or topography can also affect its affinity with water.

Wenzel was the first to take interest in the change of wettability with the surface roughness and his theory describes the change in wettability with roughness as an extension of the solid-liquid

interface in comparison to a projected smooth surface due to a higher actual surface area[43]. This model leads to the following equation:

$$cos\ \theta' = r\ cos\theta$$

where θ' is the apparent contact angle, r is the ratio of the real rough surface area to the projected perfectly smooth surface area and θ is the contact angle in the ideal smooth surface[44].

This theory thus leads to the conclusion that a hydrophobic surface (WCA > 90°) with a high surface roughness can lead to a superhydrophobic surface. On the other hand, a rough hydrophilic surface (WCA < 90°) can become superhydrophilic. This model is valuable when the water droplet penetrates into the various micro and nano asperities of the rough surface[44].

However, while this model is generally applicable to hydrophilic surfaces, when the WCA is over 90°, the entrapment of air bubbles in between the various asperities, can lead to discontinuities in the liquid/solid interface[40]. This was studied by Cassie and Baxter who gave the Cassie-Baxter equation which gives the apparent contact angle θ' of a water droplet on a heterogeneous surface composed of a solid substrate and air:

$$cos\theta' = f cos\theta - (1 - f)$$

with f the area fraction of the solid, (1-f) the area fraction of air on the composite surface, and θ the contact angle in the ideal smooth surface[44].

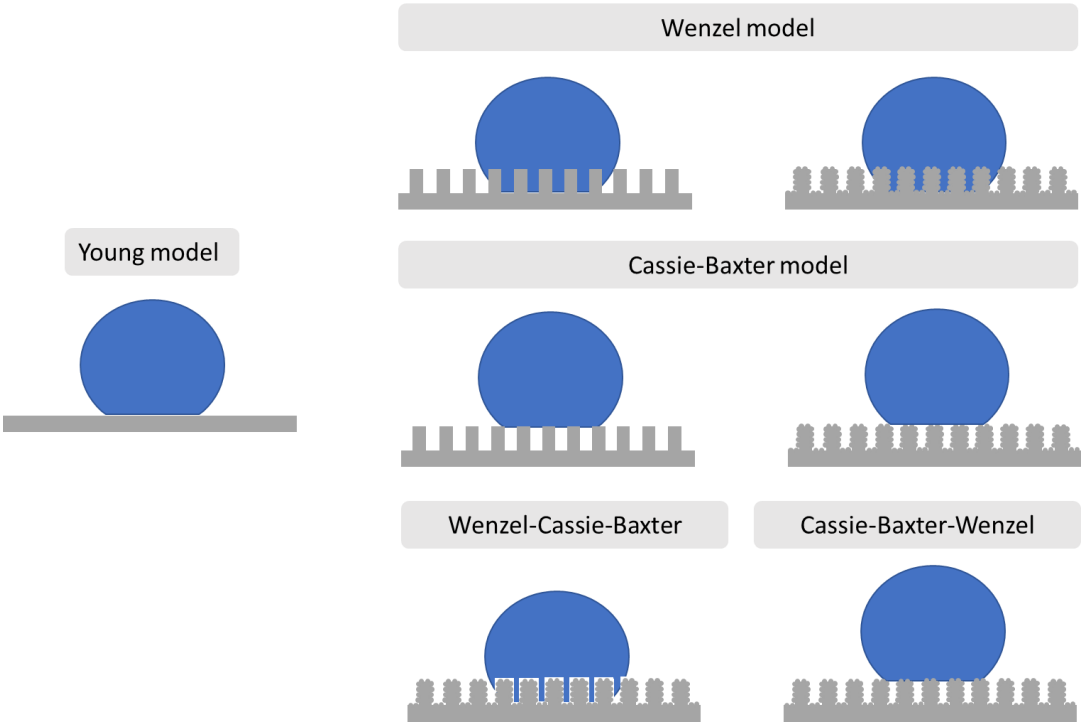

Figure 6: Surface wetting mechanisms on a planar substrate, substrates with microstructuration and substrates with micro and nanostructuration. The representation of the water droplet's spreading is not characteristic of the surface wettability in these schemes.

Figure 6 shows various scenarios for surface wetting, on both an ideal smooth and homogeneous surface where Young's model can be used, and structured surfaces. The Wenzel model can be adapted when the water droplet penetrates any microstructures or nanoscale asperities. The Cassie-Baxter model, which is generally applicable when WCA > 90°, can also be considered for surfaces with micro and/or nanosized texture. Finally, in some cases, the multiscale topography can lead to more complex situations. For example, if a water droplet penetrates microstructures but air bubbles trapped in the nano asperities impede further spreading, the surface can be described with Wenzel-Cassie-Baxter. On the other hand, Cassie-Baxter-Wenzel can describe a surface on which a water droplet infiltrates nanotexture but not microstructures[44].

The description of these wetting mechanisms highlights the possibility of tuning surface wettability by adjusting the topography of a given surface. This has been observed in nature where many species including plants, insects, corals, fish, and larger animals such as sharks or pilot whales, have developed strategies based on topography to avoid fouling[9,34].

2.3.2. Antiadhesive surfaces found in nature

The natural surface most known for its repellency properties is the lotus leaf which has given its name to the "Lotus effect" used to designate self-cleaning surfaces[45]. The study of this surface has led to the realisation that its superhydrophobicity is the result of a combination of waxy chemical composition containing nonacosanediols and hierarchical tubular structures[45,46] (Figure 7) leading to the Cassie-Baxter effect.

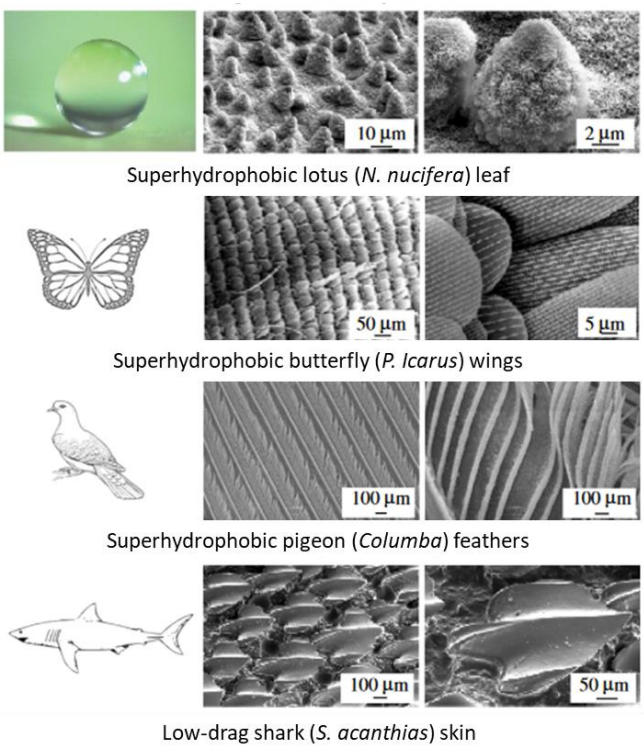

Figure 7: Examples of antibiofouling preventive strategies found in nature. Lotus leaves, butterfly wings and pigeon feathers have superhydrophobic properties and sharkskin produces low drag which contributes to its antibiofouling activity. Adapted with permission from Bixler and Bhushan[9] Copyright © 1996 The Royal Society (UK).

Cicada wings also lead to the Cassie-Baxter effect by combining a waxy surface[47] with aligned nanopillars roughly 70 nm in diameter and spaced from one another by around 90 nm[48]. Many other species have evolved to develop hydrophobic or superhydrophobic surfaces which impede the adhesion of smaller organisms and inhibit the formation of biofilm based on the same strategy of combining their chemical composition with micro or nano topography. This is the case for plants such as jewelweed[49], Indian Cress[50], or the lady mantle[51] which all have hydrophobic surfaces. Superhydrophobicity can be found for water ferns[52], broccoli[51], butterfly wings[48], and bird feathers[53] such as doves, pigeons[54] or ducks. As well as having a non negligeable effect on the surface wettability, it has also been shown that in some cases, microstructures can participate in antibiofouling activity by creating hydrodynamic fluxes in agitated conditions. This is the case for shark skin[55] for instance when the animal is in movement.

Some superhydrophilic surfaces can also be found in nature. Here again, this is a result of combinations of chemical composition and structuration, although analysis is still ongoing to determine the hydrophilic components for many species[56]. For example, some mosses have developed a highly porous structure to favour water intake[57]. Other plants such as *Ruellia devosiana* have complex hierarchical structures that help reach superhydrophilicity. Indeed the leaves of this plant have five different level of microstructuration: hair papillae (HA), papillae cells (PC), multicellular hair-trichomes (MT), tabular channel forming cells (CH) and spherical glands (GL) (Figure 8)[56].

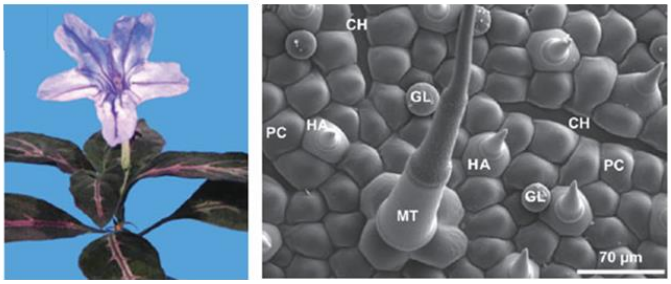

Figure 8: Photo of Ruellia devosiana *and SEM images of the surface of its superhydrophilic leaf which has five different level of microstructuration: hair papillae (HA), papillae cells (PC), multicellular hair-trichomes (MT), tabular channel forming cells (CH) and spherical glands (GL). Adapted with permission from Zhang* et al.[56] *Copyright © 2012 Taylor and Francis.*

These observations show that through evolution some species have developed surfaces with highly controlled hydrophobicity or hydrophilicity by combining their chemical properties and the nano and/or micro structuration at their surface. While the species with superhydrophobic surfaces are known for their self-cleaning and antibiofouling properties, superhydrophilic surfaces have been developed in natural environments for survival, by enhancing the ability of the specie to absorb water and nutrients. However, the combined knowledge that highly wettable surfaces can inhibit bacterial adhesion and that both chemistry and topography can play a part in reaching superhydrophilicity confirms the potential of this combined approach for developing superhydrophilic antibiofouling surfaces as well as superhydrophobic antibiofouling ones.

2.3.3. Engineered surfaces based on the combination of chemistry and topography

The following sections will give some examples found in the literature of engineered surfaces combining chemistry and topography and leading to hydrophobic and hydrophilic materials for antibiofouling applications. These examples were taken from a literature review entitled "Combining Topography and Chemistry to Produce Antibiofouling Surfaces: A Review" which was written during this thesis in collaboration with Hippolyte Durand, Pascal Mailley and Guillaume Nonglaton, and published in *ACS Applied Bio Materials*[3].

These combined strategies can have various effects which can either prevent the adhesion of microorganisms or have a bactericidal action. These mechanisms are summarized in Figure 9. For hydrophobic surfaces, the combination of chemistry and topography aims in reaching the Cassie-Baxter state, creating an air barrier at the liquid/solid interface which inhibits bacterial adhesion. The effects of combining hydrophilic chemistry with topography, however, are more diverse. First, the addition of micro or nanostructures to a hydrophilic surface can lead to the Wenzel effect, creating superhydrophilic surfaces which exhibit a dense hydration layer, impeding bacterial adhesion. Furthermore, the structures can have an antiadhesive effect by creating turbulent flows. Many hydrophilic compounds also have a bactericidal effect, killing the cells on contact. This is the case for example with quaternary ammonium compounds (QACs)[58] whose charge can damage the bacterial membranes or antimicrobial peptides[59]. Finally, in some cases, the use of microstructures can lead to mechanical stress on the cells, damaging the membranes and thus killing the bacteria.

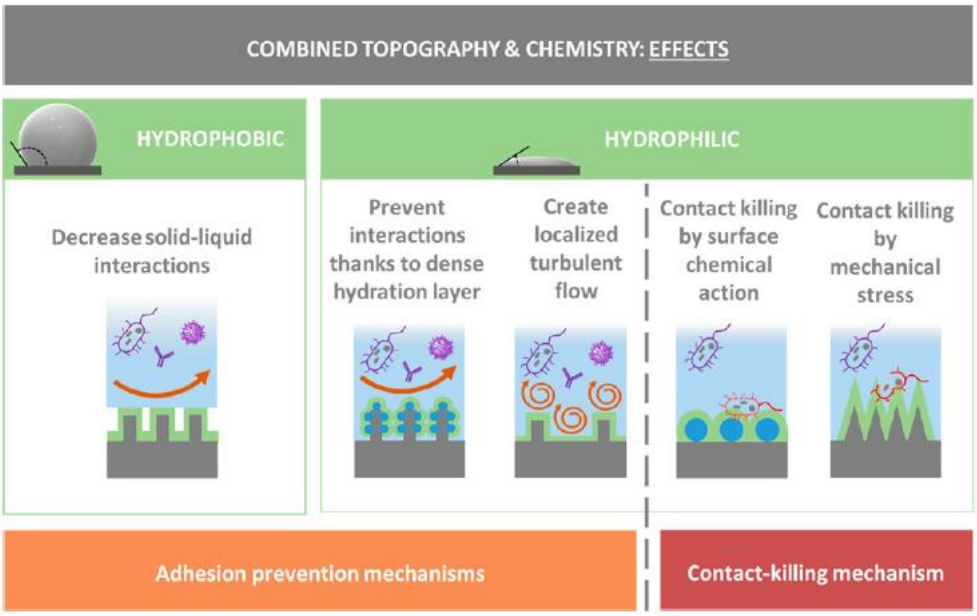

Figure 9: Schematic representation of the diverse effects of combined topography and chemistry for antibiofouling surfaces. Adapted with permission from Durand, Whiteley et al.*[3] Copyright © 2022 American Chemical Society.*

2.3.3.1. Hydrophobic surfaces obtained by combining chemistry and topography

Such approaches can be achieved on various types of substrates, such as metals, glass and silicon or even polymer substrates[3]. Indeed, depending on the field of activity, different substrate materials may be used. For instance, metals can be found in the marine industry, healthcare and the food industry. Polymers can be found for water treatment, as well as in the marine industry and in the medical field.

The examples of combined hydrophobic chemistry with specific topography are grouped by field of application to highlight the variability of the domains these surfaces can be used in. The first group of studies focused on developing combined surfaces for various industries, then research targeting the marine industry will be presented, and finally the publications aiming to develop materials for the medical field will be summarized.

Various industries

The publications in this section aim to develop functional surfaces which can be used in various industries such as food, pharmaceuticals, the marine industry and other fields. These studies focused on modifying metal substrates. To structure these substrates, either the metal itself can be modified, or an extra material can be added.

The former method can easily be achieved for metal substrates by immersion in alkaline or acid solutions. Indeed, as well as modifying the surface chemistry as an oxide or hydroxide layer is formed, hierarchical micro or nanostructures can be created. For example, bovine serum albumin (BSA) has been reduced on aluminium sheets, as the latter were structured through acid etching and coated with 1H,1H,2H,2H-perfluorodecyltrichlorosilane (FDTS)[60]. These modified surfaces, which had a WCA of 163°, also showed a promising 80 % reduction of bacterial adhesion when tested against *Pseudomonas aeruginosa, Staphylococcus epidermidis*, and *Staphylococcus aureus.*

A similar study on an aluminium alloy was carried out resulting in the limitation of *Escherichia coli* growth. In this case, an extra microimprinting step was added, leading to square micropillars which were further modified by boiling water to lead to flake-like nanostructures. These nanostructures were superhydrophilic with a WCA close to 0° and showed antibacterial activity against *E. coli*. However, after chemical vapour deposition (CVD) of 1H, 1H, 2H, 2H-perfluorooctyltriethoxysilane (FOTES), these substrates became superhydrophobic and repelled the adhesion of the bacterial cells (Figure 10) [61,62].

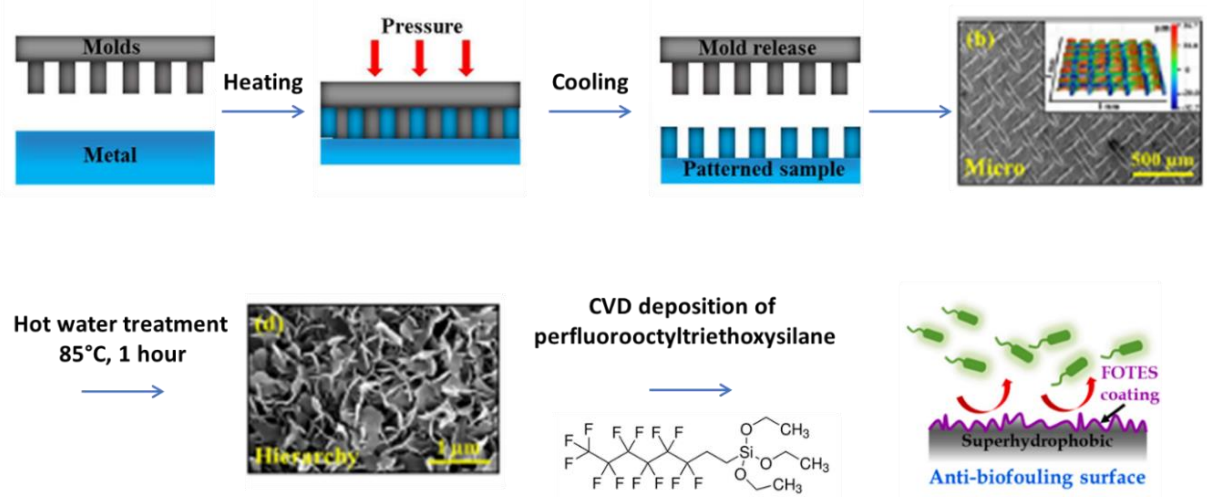

Figure 10: Microimprinted aluminium pillars with flake-like nanostructures obtained by hot water treatment. The structures surface was then coated with a fluorosilane by chemical vapour deposition (CVD). Adapted with permission from Mandal et al.[61] Copyright © 2022 Elsevier and Mandal et al.[62] *Copyright ©2013 IOP Publishing, Ltd.*

Metal substrates can also be structured by laser etching[63,64]. For example, gecko mimicking structures have been created on stainless steel by laser imprint patterning. These structured surfaces,

which were superhydrophilic (WCA ≈ 0°), became superhydrophobic (WCA ≈ 157°) when adding a coating composed of polydopamine and octadecylamine, and showed a growth reduction of 90 % for *E. coli* and of 99 % for *S. aureus*[65].

Other superhydrophobic surfaces were obtained by combining vertical and horizontal microlines, created by ultraviolet (UV) laser etching, with a coating of polytetrafluoroethylene (PTFE) nanoparticles which were sprayed on. These surfaces, composed of both micro and nanotopography, as well as hydrophobic fluorine-based chemistry led to contact angles over 150° for many different liquids, thus revealing superamphiphobic properties[66].

As mentioned previously, additional material can also be used to create specific exogenous topography[3]. For instance, electrodeposition onto metallic substrates can be used to create a coating which can exhibit nanostructures. This was carried out with a phosphate containing electrolyte on copper and led to the formation of copper-phosphate ion complexes which had a microflower-like structure. Adding a dodecylamine coating to these structured surfaces enabled superhydrophobicity[67]. Similar structures[68] coated with Teflon® showed good antiadhesive properties against *E. coli* and *S. aureus*[69].

Other flower-like structures were obtained on polished E40 steel by electrodeposition of tungsten trioxide (WO3) and exhibited superhydrophilicity (WCA ≈ 5°). This petal mimicking topography was then coated with PTFE by sputtering. This led to superhydrophobic surfaces (WCA ≈ 159°) due to the Cassie-Baxter effect with the formation of nano and microbubbles (Figure 11). These surfaces showed good antibiofouling activity, as well as being anti-icing and antipollution[70].

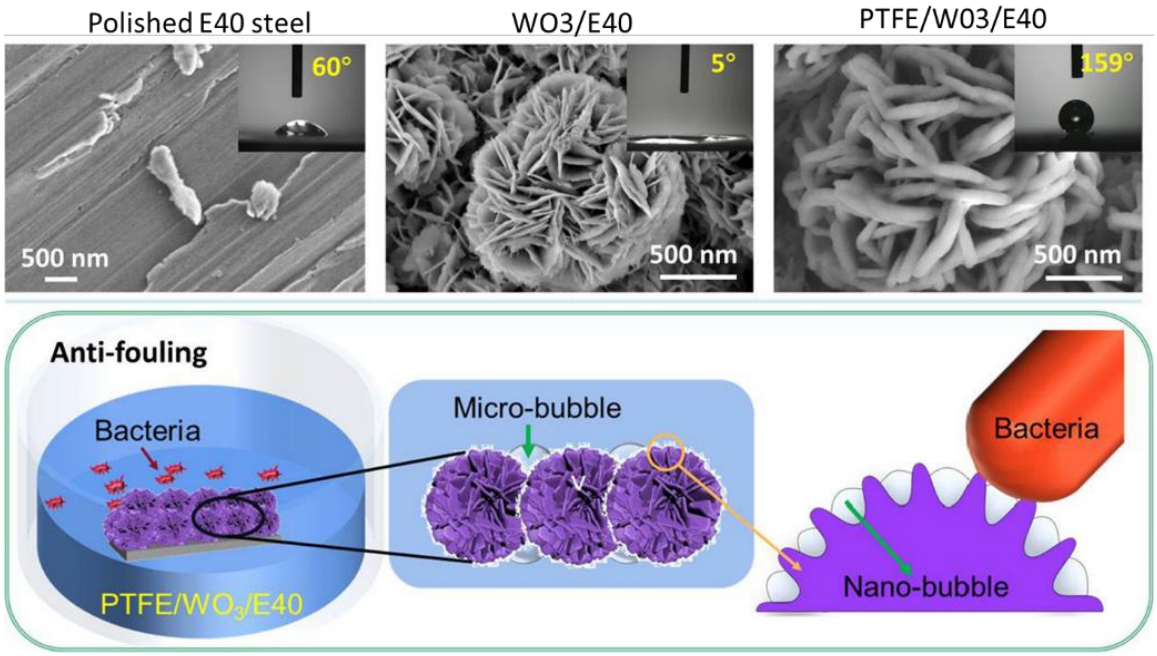

Figure 11: Flower-like nanosheets produced with $Na_2WO_4{\cdot}2H_2O$ electrolyte on polished steel, covered with a PTFE sputtered layer. Adapted with permission from Chang et al.[70] *Copyright © 2022 Elsevier.*

Marine

Metal substrates are also often used in the marine industry which is the focus of the teams developing the following combined surfaces.

For example, silver electrodeposition has been carried out on titanium to create dendritic micro/nanostructures. By coating the latter with dodecanethiol and adding dimethyl silicone oil, slippery liquid-infused porous surfaces (SLIPS) were created[71] (Figure 12). Each modification step leads to a change in the wettability of the material. Indeed, the titanium substrate has a WCA of around 76°. When functionalised with Ag dendrites, the WCA is close to 0°. Superhydrophobicity is reached after adding the dodecanethiol coating giving a WCA of around 158°. These water repellent surfaces show good affinity to oil which allows the infusion with silicon oil creating smooth surfaces on which water droplets can easily roll off[71]. These types of surfaces have proven to be very efficient at inhibiting biofilm formation[71–74]. Here for instance, it was shown that adhesion of diatom *Navicula minima* and green algae *Chlorella vulgaris* was reduced by 4 log over 14 days[71].

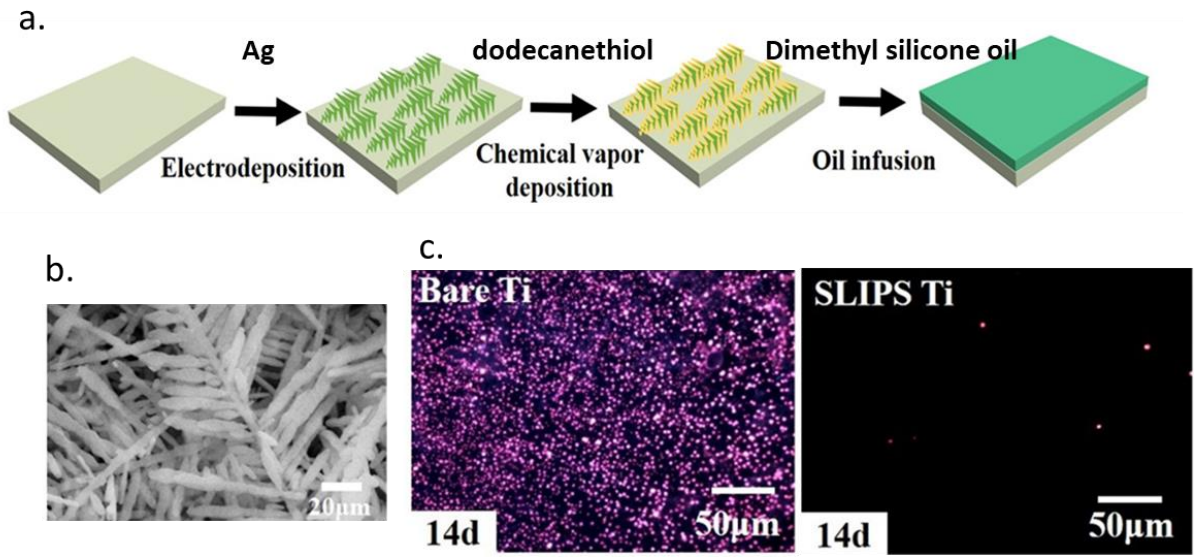

Figure 12: Super hydrophobic oil-infused silver dendritic nanostructures on titanium. a. Fabrication process, b. SEM image of the dodecanethiol modified Ag dendrites, c. Fluorescence microscope images of the biofouling state of Chlorella vulgaris *on bare Ti and SLIPS-Ti after immersion for 14 days in suspension of algae. Adapted with permission from Ouyang* et al.[71] *Copyright © 2019 Elsevier.*

Silicon oil has also been infused into microwrinkles created by thermal treating Teflon® coated polyethylene. The resulting surfaces showed good antiadhesive performance against *Pseudomonas spp.*, but also avoided marine biofouling for up to 7 weeks[73].

Another strategy for creating SLIPS was carried out using a block copolymer of polystyrene (PS) and polylactic acid (PLA) on polydimethylsiloxane (PDMS). The PLA was then decomposed by hydrolytic treatment, leading to a surface exhibiting both microwrinkles and nanopores which were infused with silicon oil[72]. This last study highlighted the importance of combining strategies to reach the optimum antibiofouling surface. It also showed that the space between the microwrinkles influences adhesion of green algae as fewer attachment points can be found when the spacing is larger[72].

Electrodeposition is not the only method for adding exogenous material to metal substrates to form specific topography. Indeed, this can also be achieved by hydrotalcite preparation which leads to layered double hydroxide (LDH) films. It has been shown that lithium-aluminium LDH films coated

with 4-amino-2-((hydrazine methylene)amino)-4-oxobutanoic acid (AOA) and 1H,1H,2H,2H-perfluorooctyltriethoxysilane (PFOTES) give surfaces which are hydrophobic, antibiofouling and anticorrosion[75]. Indeed, these complex surfaces can repel up to 96 % of *E. coli*, *Bacillus subtilis* and sulphite-reducing bacteria.

Other superhydrophobic and antibiofouling surfaces were created by using alumina or zinc nanorods embedded in PDMS on steel. These combined surfaces, reaching a WCA of around 150°, showed good resistance towards *Micrococcus sp*., *Pseudomonas putida*, or fungi *Aspergillus niger*. Field assays also highlighted the efficiency of such surfaces against marine fouling[76,77].

While not all studies systematically evaluated the effect of topography, chemistry and the combination of both, Wang *et al.*[78] focused on the effect of both structuration and coating, as well as identifying the impact of the initial substrate. Indeed, in their work, they developed diamond hemisphere structures by hot filament chemical vapour deposition (HFCVD). By repeating the structuration process, they created micro and nano features leading to a two-level topography. These structures reached a WCA of around 120° on glass slides and around 150° on Ti and Si substrates. These structures were then coated with hydrophobic FDTS leading to surfaces with WCAs reaching 170° for the modified Ti and Si, and around 160° for the glass slides. The superhydrophobic surfaces obtained by combining structuration and FDTS coating showed the best results against *E. coli* and *P. aeruginosa* adhesion[78].

Medical

In the medical industry, few materials such as titanium, stainless-steel, ceramics or silicone, chosen for their biocompatibility and robustness, are used. Despite the use of sterilisation before implanting a device, biofilm formation is very problematic on medical implants and studies are being carried out to limit the phenomenon. The following focus on combining hydrophobic coatings with topography.

In a first example, electrodeposition was used to deposit conductive and hydrophobic polymer polyethylenedioxythiophene (PEDOT) derivatives onto stainless steel. The chosen monomers contained either a fluorocarbon (EDOT-F_4) or a hydrocarbon (EDOT-H_8) chain giving the capacity to create nanofibers by adjusting the deposition charge. This study highlighted the importance of combining hydrophobic chemistry with topography to develop superhydrophobic surfaces and reduce bacterial adhesion and biofilm formation. Indeed, when depositing PEDOT-F_4 with a deposition charge of 1mC/cm², the WCA was around 105°. However, increasing the deposition charge to 10 mC/cm², which gave vertically aligned nanofibers spaced by about 147 nm, led to a WCA over 160°. These superhydrophobic surfaces, created by combining both chemistry and topography led to the highest reduction of *P. aeruginosa* and *Listeria monocytogenes* adhesion[79].

Lee *et al*. carried out nanostructuration of glass by femtosecond laser patterning, followed by coating with a fluorinated self-assembled monolayer and infusion of perfluorocarbon-based lubricant, leading to the formation of superhydrophobic surfaces called lubricant-infused directly engraved nano/microstructured surfaces (LIDENS). Before functionalisation with the fluoro-compound, the structured surfaces were superhydrophilic (WCA < 5°). After coating, the WCA was increased to over 160°. These surfaces showed good anti-adsorption against fibrinogen and albumin[80].

Other strategies focused on creating surfaces exhibiting both micro and nanostructures. Jiang *et al.*, for example, inspired by the lotus-leaf structure, used reactive ion etching to create microstructures on the substrate itself, before using zinc oxide crystal seeds to initiate the growth of zinc oxide nanoneedles on top (Figure 13). By dip coating these structured surfaces into a solution of

fluoroalkyl silane, these surfaces became superhydrophobic (WCA ≈ 174°) due to the Cassie-Baxter effect and showed 99 % repellency against *E. coli*. Furthermore, in this case, the nanoneedles also had a bactericidal effect[81].

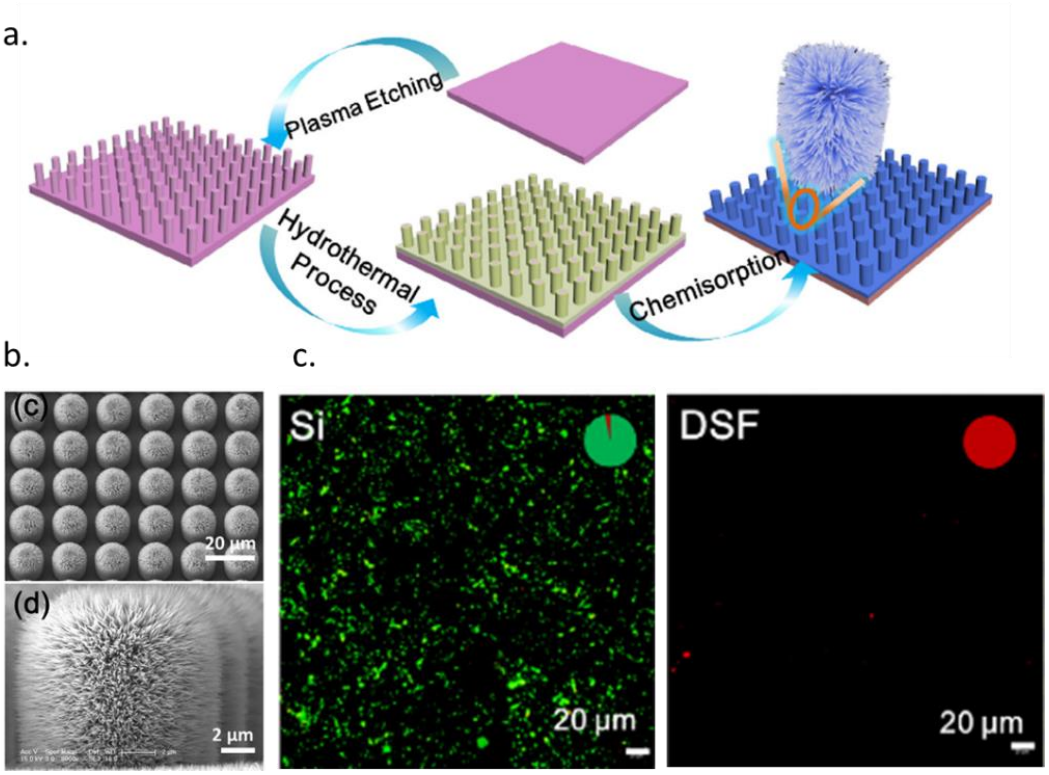

Figure 13: Microcylinders produced by etching of silicon wafer and covered with zinc oxide nanoneedles coated with a fluoroalkyl silane. a. Fabrication process, b. Scanning Electron Microscopy (SEM) images of the dual-scale topography, c. Confocal laser scanning microscopy images of E. coli *on silicon and dual-scale fluorinated (DSF) surfaces. The green bacteria are living, while the bacteria appearing in red are non-viable. Adapted with permission from Jiang* et al.[81] *Copyright © 2020 Elsevier.*

A famous type of biomimicking microstructure is the sharkskin pattern which has been replicated in many different works[55,82–84]. The combination of this bioinspired structure with a specific chemistry has also been carried out on various occasions. For instance, in a study by Dolid *et al*., it was spray-coated with a mixture of dopamine and peptides, leading to a hydrophobic surface (WCA ≈ 118°) which reduced *E. coli* adhesion by 85 % and *S. epidermidis* adhesion by 72 %[82].

Plasma and vapour deposition have also been carried out to deposit hydrophobic coatings onto structured surfaces. For example, fluorine-based octafluorocylobutane (C_4F_8) was deposited by plasma onto polymethylmethacrylate (PMMA) sheets which had previously been textured by oxygen plasma treatment. Perfluorooctyltrichlorosilane (pFOTS) was also deposited onto the same patterned substrates by vapour deposition. These superhydrophobic surfaces (WCA ≈ 158°) obtained by combining chemistry and topography seemed to show good antiadhesive performance against cyanobacteria *Synechococcus sp*. even after 72 hours[85].

Such surface modifications have also been carried out on medical devices such as intraocular lenses used after cataract surgery. Indeed, one team carried out oxygen plasma treatment on the lenses to give them nanotopography. PDMS brushes were then coated onto the surface by CVD, leading to a liquid-like surface created by the non-grafted ends of the polymer brushes. While

conserving the optical and mechanical properties of the initial lens, the modified one additionally shows good bacterial repellency as well as cell viability. This makes this improved lens a good candidate for avoiding posterior capsule opacification which often occurs after cataract surgery[86].

As it has been seen throughout this section, many studies have been carried out combining hydrophobic chemistry and topography to develop superhydrophobic surfaces with antibiofouling properties. Still, these examples highlight the fact that, while the combined strategy remains the same for all these studies, there does not yet appear to be an ideal combination. While the hydrophobic chemistry used is generally a fluorine containing compound, some fluorine free solutions have also been studied which is encouraging because of the arising restrictions of the former due to toxicity concerns[87]. As for the choice of structuration, for the moment, there are still many different possibilities due to the recent emergence of this topic[33]. However, the aim remains reaching the Cassie-Baxter effect by trapping air bubbles.

In the next subsection, combined strategies based on hydrophilic chemistry and topography will be studied with the aim of creating superhydrophilic surfaces through the Wenzel effect (Figure 6). This should allow the formation of a water barrier at the interface between the substrate and the surrounding media which can inhibit bacterial adhesion.

2.3.3.2. Hydrophilic surfaces obtained by combining chemistry and topography

Hydrophilicity has been less extensively studied for antibiofouling applications although this strategy shows as much promise as hydrophobicity for antiadhesive surfaces. Similarly to the previous subsection on hydrophobic surfaces, the following works are grouped depending on the application targeted by the research group.

Marine industry

As mentioned previously, the marine industry suffers from biofilm formation, inducing efficiency reductions and increasing costs. Therefore, there are many studies focusing on combining topography and hydrophilic chemistry to reduce biofilm in a marine environment.

Unlike when developing superhydrophobic surfaces, metals are not a common substrate when aiming to reach hydrophilic and bacteria-repellent devices. Still, some studies can be recognized for doing so. For example, potentiostatic anodization of titanium led to the formation of titanium dioxide (TiO_2) nanotubes with 2 different pore sizes: 20 nm (TN20) and 80 nm (TN80). These substrates were then coated with polyethylene glycol silane (PEG-silane) to confer the structured surface with superhydrophilicity[88] (Figure 14a, b). Measuring the WCA confirmed the combination of hydrophilic chemistry and nanotubes led to the Wenzel effect with an enhanced wettability. However, these measurements (Figure 14c) also show the importance of controlling the size of the structures. Indeed, before PEG-silane functionalisation, the TN80 structures are much more hydrophilic than the TN20. It is thought that this is due to the water penetrating the bigger structures of TN80. However, with the PEG-silane, the lowest hydrophilicity is obtained on the TN20 nanotubes. Furthermore, the most hydrophilic surface is in this case not the most efficient against *S. aureus* adhesion (Figure 14d, e)[88] due to adhesion and frictions forces.

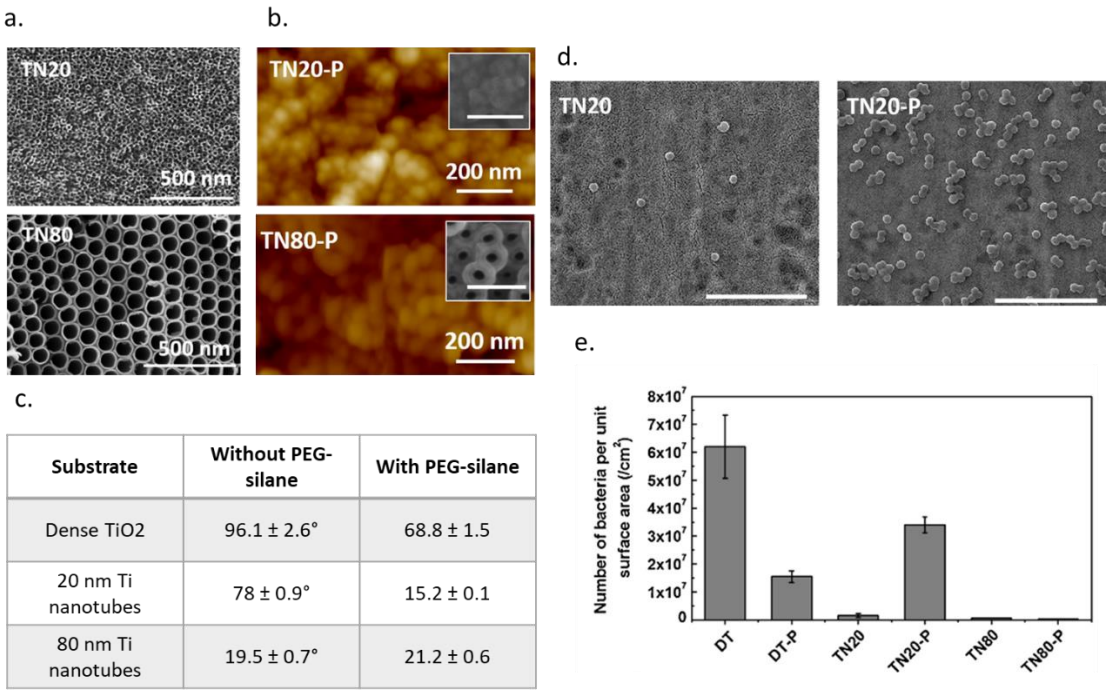

c.

Substrate	Without PEG-silane	With PEG-silane
Dense TiO2	96.1 ± 2.6°	68.8 ± 1.5
20 nm Ti nanotubes	78 ± 0.9°	15.2 ± 0.1
80 nm Ti nanotubes	19.5 ± 0.7°	21.2 ± 0.6

Figure 14: PEG-silane on TiO_2 nanotubes. a. Field Emission Scanning Electron Microscopy (FESEM) of TiO_2 nanotubes with a pore size of 20 nm (TN20) or 80 nm (TN80), b. Atomic force microscopy (AFM) images of PEG-silane functionalised TN20 (TN20-P) and TN80 (TN80-P), c. WCA of the different nanotubes with and without PEG-silane, d. FESEM images of S. aureus *adsorbed onto TN20 and TN20-P, e. The bacterial density of* S. aureus *attached on various TiO_2 surfaces. Adapted with permission from An* et al.[88] *Copyright © 2017 Elsevier.*

Another type of hydrophilic antibiofouling surface is self-cleaning mucus-like hierarchical ciliary bionic antifouling surfaces (SMCAS)[89]. These substrates, created by electrostatic flocking technology and spraying, result in a combination of polyamide (PA) microfibers, carbon nanotubes and poly(vinyl alcohol) (PVA) hydrogel particles. These surfaces showed good antiadhesive activity against marine bacteria *Marinobacter lipolyticus* SM19(T) due to high water retention leading to a camouflage effect[89].

Hydrophilic peptides have also been used to functionalize structured surfaces in some studies. For example, nisin was deposited onto ion etched glass with quadrangle structures (10 x 5 µm²). In this study, the depth of the microstructures was varied (3, 5 and 7 µm) to evaluate its impact on the antibiofouling properties. It was shown that the deeper the grooves, the higher was *Bacillus sp*. adhesion, due to the bacteria getting trapped between the microstructures. However, when coating these structures with hydrophilic nisin, the fouling was reduced[90].

Simultaneous modification of chemistry and topography of glass has also been carried out by depositing zwitterion poly(sulfobetaine methacrylate) (PSBMA) by sub-surface initiated atomic transfer radical polymerisation (SSI-ATRP). Indeed, this technique leads to the creation of wrinkles for which size can be tuned with the reaction time[91,92]. These superhydrophilic surfaces (WCA < 10°) showed encouraging antibiofouling activity against macromolecules[91], bacteria[91], diatoms[92] and red algae[92]. This study shows that different foulants react differently on the same surface. Indeed, protein showed the least adhesion on 2 µm thick PSBMA whereas bacteria and diatoms absorbed the least on a 10 µm thick zwitterionic coating[91].

Polymer substrates such as PDMS have also been modified to gain wettability and hopefully limit bacterial adhesion. For example, plasma treating PDMS can lead to the formation of wrinkles on the substrate, increasing the WCA from around 90° to over 100°. These structured surfaces can then be functionalized by silanisation and surface-initiated ATRP to add polymer brushes of poly(ethylene glycol methacrylate) (POEGMA) or poly(3-sulfopropyl-methacrylate) potassium salt (PSPMA). These wrinkled and functionalised PDMS surfaces had a WCA of 46° and 12° for POEGMA and PSPMA respectively. It was shown that both wrinkles and polymer brushes alone reduced the adhesion of *Ulva* zoospores and microalgae *Chlorella*. However, the combination of topography and chemistry gave the best results for antifouling[93].

Other teams have modified PDMS to replicate topography that can be found in nature. For instance, Brzozowska *et al*.[94] moulded PDMS to give it a structure resembling that of marine decapod crab *Myomenippe hardwickii.* The resulting topography had various scales of structuration ranging between 5 µm and 250 µm as it can be seen in Figure 15. The structured PDMS was then functionalized with either zwitterionic sulfobetaine polymer brushes or by Layer-by-layer (LbL) deposition of poly(isobutylene-alt-maleic anhydride) and polyethylenimine (PEI) (Figure 15a.). These modified surfaces were tested against cyprids *Amphibalanus amphitrite* and diatoms *Amphora coffeaeformis.* For both species, the surface which exhibited the highest antifouling activity was the zwitterion-coated structured PDMS[94].

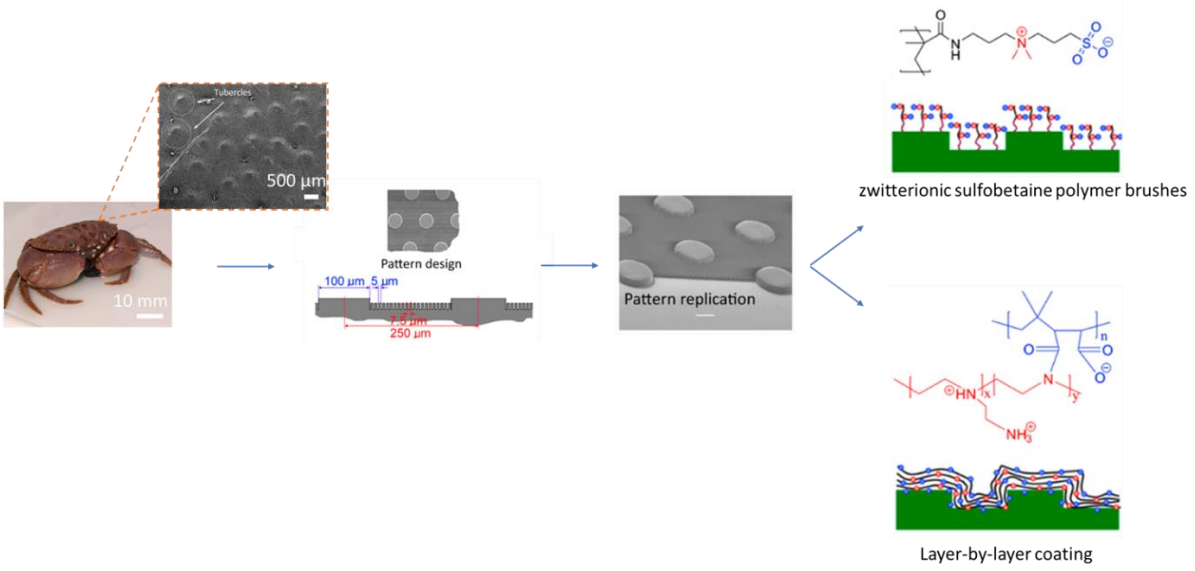

Figure 15: Replicating the structure of M. Hardwickii *and coating it with polymer brushes or by LbL deposition. Adapted with permission from Brzozowska* et al.[94] *Copyright © 2014 American Chemical Society.*

A similar study was also conducted to mimic the surface of algae *Laminaria japonica.* Here, PDMS was moulded to give it the bioinspired topography, and LbL deposition of sodium alginate and poly(guanidine-hexamethylenediamine-poly-ethyleneimine) (poly(GHPEI)). This chemistry led to a WCA around 44° on smooth PDMS and 35° on the moulded PDMS. Here again, the surfaces created by combining topography and chemistry gave the best antiadhesive results against diatoms and *E. coli* bacteria[95].

Water filtration

Furthermore, polymer substrates are the material of choice for water filtration applications. In this field, biofouling can lead to a non-negligeable performance reduction as the pores of the filtration membranes get clogged. Therefore, combining topography and chemistry is also being used to address biofilm on water filtration membranes. Here, hydrophilic surfaces are being sought in order to enhance water separation[3].

A first type of polymer often seen for water treatment applications is polyamide (PA). This substrate has been modified by various research teams in order to limit biofilm formation. In a first example, it was structured by thermal embossing which enabled the creation of nanolines and grooves. The modified PA membrane was then functionalized with poly(ethylene glycol) diglycidyl ether (PEGDE). It was shown that these modified surfaces lead to less flux reduction (8 % instead of 20 %) than the pristine PA membranes, demonstrating their effectiveness[96].

Choi *et al.* also studied modification of membranes for water filtration. They began by modifying thin film composite (TFC) membranes (WCA ≈ 72°) with cylindrical TiO_2 pillars[97], then further developed the structuration to give the substrate a pattern resembling sharkskin (TFC_{sk})[55,84,98]. Hydrophilic tannic acid was then added to these structures (TA-TFC_{sk}) from the liquid phase to achieve a hydrophilic surface (WCA ≈ 42°) and an antiadhesive effect[98] (Figure 16). These structures showed antiadhesive activity when tested with *P. aeruginosa*, especially in dynamic conditions as the sharkskin-inspired topography created an isolated vortex. Furthermore, the hydrophilic coating actually enhanced the permeance of the membrane, thus improving its functionality[55].

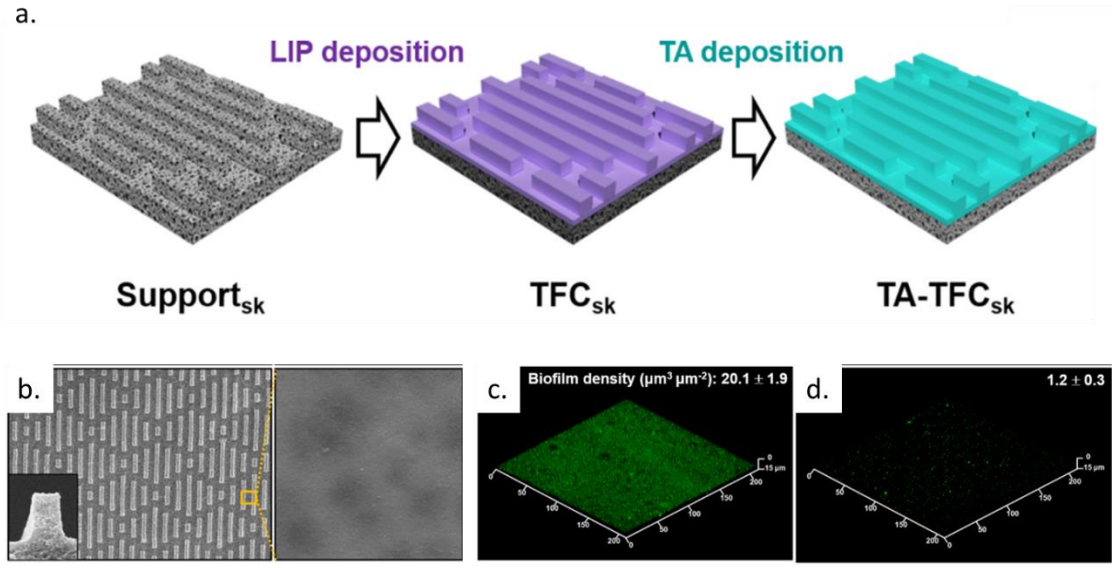

Figure 16: Tannic acid coated sharkskin-inspired microstructures. a. Fabrication process, b. Surface and cross-sectional SEM images of TA-TFC_{sk}, Confocal laser scanning microscopy images of the c. TFC_{flat} and d. TA-TFCsk membranes after static biofouling tests with P. aeruginosa. *Adapted with permission from Choi* et al. [98] *Copyright © 2021 Elsevier.*

Polysulfone (PSF) membranes are also often used for water filtration applications and have been chemically and topographically modified to improve their functionality. For instance, polyethersulfone membranes have been coated with a mixture of cellulose nanofibrils and PVA to impart the substrate with both charged chemistry and a nanoscale roughness. Quartz crystal microbalance with dissipation monitoring (QCM-D) was used to study protein adhesion with model BSA and showed very little adhesion which is attributed to the hydrophilicity (WCA ≈ 49°) of the

surface. Furthermore, *E. coli* biofouling seemed very limited on these functionalized surfaces. This was attributed to the charged chemistry and the aldehyde and carboxyl groups which led to bactericidal as well as repulsive properties. Furthermore, it was thought that low specific surface area from the nanoroughness also impacted the bacterial adhesion[99].

PSF membranes were also modified using a combination of tannic acid, PEI and (3-amino-1-propanesulfonic acid) which is known as taurine. These molecules were co-deposited onto the surface before interfacial polymerisation with trimesoyl-chloride which led to the formation of Turing striped structures. In this case, the zwitterionic taurine gave a strong hydration layer and the WCA decreased to under 40° when increasing the taurine content, which limited foulant adsorption. In parallel, the Turing stripes enhanced the water flux through higher specific surface area[100].

Polyvinylidene fluoride (PVDF) membranes were also modified to limit biofouling. In a first study, these substrates were coated with hydrophilic copolymer poly(vinylpyrrolidone-co-ethylene glycol diacrylate) (poly(VP-co-EGDA))[101]. The technique used was iCVD which allows conformal coating of the substrate and in this case enables conservation of the material's pores. WCA measurements revealed an increase in hydrophilicity with a higher proportion of VP, reaching superhydrophilicity (WCA < 10°) for some copolymers. In vitro assays showed encouraging results against *E. coli* and BSA adsorption[101].

Finally, PVDF membranes have also been functionalized with amine-terminated silicon dioxide (SiO_2) nanoparticles after being microstructured by imprinting. The functionalized nanoparticles added nanoscale topography to the microscale pattern of the membrane, as well as bringing hydrophilicity to the surface. These superhydrophilic surfaces (WCA < 10°) were tested against bacterial suspensions of *Bacillus thuringiensis* and *E. coli*. The membrane's permeance was higher for the modified membranes than the pristine ones (WCA ≈ 50°), due to both higher wettability and turbulent flows created by the microstructures[102].

Medical devices

Many medical devices are polymer-based due to the many advantages these materials offer. However, for medical devices, and implants in particular, inhibiting biofilm formation is crucial as its development can induce nosocomial infections. Thus, many studies have also been carried out with this application in mind.

For instance, a flexible cellulose acetate (CA) nanoneedle array was created by drop-casting the cellulose solution onto a PDMS mould. This led to an increase in WCA from 70° for the planar CA to 100° with nanoneedles (300 nm high, 50 nm diameter at the tip of the needles, 200 nm diameter at the bottom of the needles and 500 nm from tip to tip (Figure 17b)). 2-methacryloryloxyethyl phosphorylcholine (MPC) was then added by spin-coating to achieve superhydrophilicity. The resulting WCA was indeed under 10°. To test the efficiency of this modified material, LIVE/DEAD staining and fluorescence microscopy was carried out with *E. coli* (Figure 17c) and *B. subtilis*. This showed a reduction in bacterial adsorption, attributed to the chemical functions of MPC, and a bactericidal effect as the microneedles pierce the cell's membrane[103]. Similar results were achieved with poly(ethylene glycol dimethacrylate) (PEGDMA) nanoneedles[104].

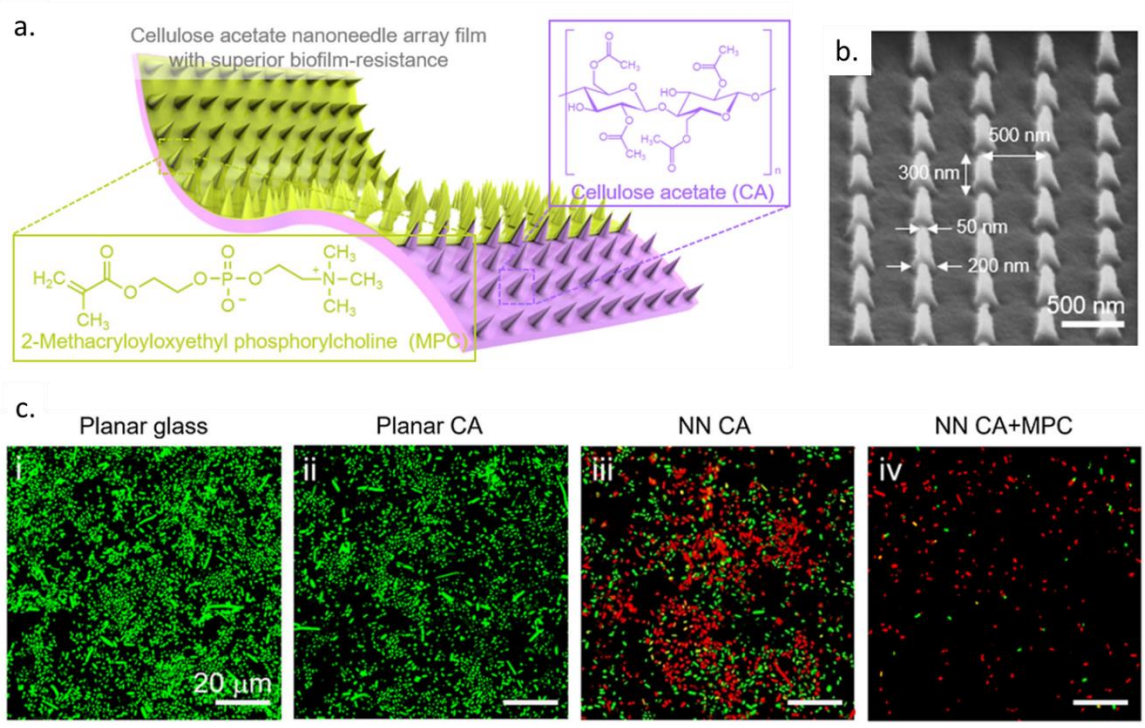

Figure 17: a. Cellulose acetate nanoneedle array functionalized with MPC, b. SEM image of the CA nanoneedle array, c. Confocal microscopy images of E. coli *grown on the planar glass, planar CA, CA nanoneedle, and MPC-coated CA nanoneedle surfaces for 18 h. Adapted with permission from Park* et al. *[103] Copyright © 2002 Springer Nature BV.*

Intraocular lenses used for cataract surgery have also been modified in the aim of reducing bacterial biofilm and thus the risk of nosocomial infections. Here, a nanopillar array was established by stamping a polymer mixture. Once the latter was structured, it was coated by iCVD with copolymer poly(4-vinylbenzyl chloride-co-2-(dimethylamino)-ethyl methacrylate). In this study, the micropillars capture the bacteria whose membrane is then destabilized by mechanical deformation as well as the presence of quaternary ammonium compounds in the coating. While these substrates are antibacterial, cell viability was also highlighted for human corneal epithelial cells for up to 7 days[105].

Some combined surfaces show antibiofouling activity against only a certain type of bacteria. For instance, charged surfaces will not have the same effect on Gram-positive and Gram-negative bacteria. This was underlined in a study focusing on creating a microstructured surface by femto-second laser patterning on borosilicate glass, before adding polyvinylamine (PVAm) and polylactic acid (PAA) by Layer-by-layer (LbL) deposition. Indeed, in this case, *E. coli* adhesion was enhanced in comparison to that of *S. aureus*[106]. Higher efficiency against *S. aureus,* in comparison to *E. coli*, was also noted with poly(acrylic acid-co-(poly(ethylene glycol)diacrylate)) films plasma-treated to give them microsized wrinkles[107].

These examples based on hydrophilic chemistry show a large variety of both chemical compounds and topography. Indeed, here, the choice for hydrophilic chemicals is wider and the use of polymer brushes, zwitterions or quaternary ammonium compounds can be found among others. These can have a bactericidal effect as well as leading to highly hydrophilic surfaces by reaching the Wenzel effect when combined with micro and/or nanostructures.

2.3.4. Conclusions and limitations of these studies

These examples show that, when applying the bioinspired strategy of combining chemistry and topography to induce antibiofouling activity on given substrates, many different combinations can be studied. Generally, created in two steps: modulation of the topography before chemical functionalisation, in some cases the fabrication of these biomimicking surfaces can be simultaneous. This is summarised in the figure below.

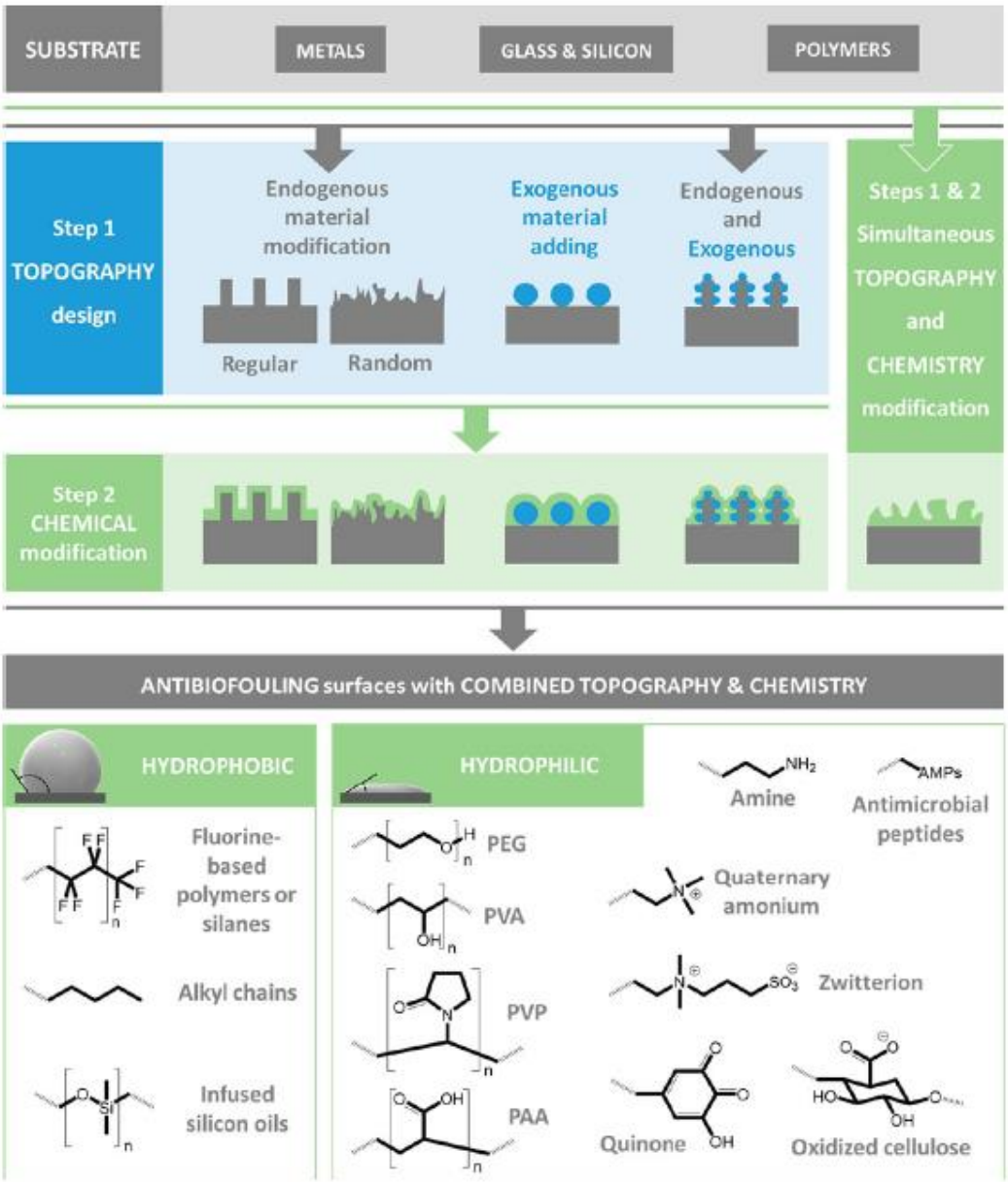

Figure 18: Combining topography and chemistry to obtain antibiofouling surfaces on different substrates (metals, glass and silicon, polymers). The first step consists in designing regular or random topography. In the second step a specific chemistry is added. It is also possible to obtain topography simultaneously with the surface chemistry modification process. Detail of the potential chemical modifications is also given. Adapted with permission from Durand, Whiteley et al.[3] *Copyright © 2022 American Chemical Society.*

Concerning the surfaces using hydrophobic chemistry, the majority of the chemical compounds used were fluorine based. The combination with micro or nanostructures generally aims to create a Cassie-Baxter effect, leading to superhydrophobicity by trapping air bubbles at the solid/liquid interface. However, due to the relatively recent timeline of this field of research (the biocidal effect of surface structuration was first analysed around 2010[33]), no real synergies between different works seem to emerge yet in what concerns the chosen topography, which can be regular or random and of various sizes.

As for the hydrophilic surfaces, the variety of studied chemical compounds is wider and their effects are not solely on the wettability of the surface. Indeed, as well as creating a strong hydration barrier at the surface of the substrate, some compounds also have a strong bactericidal effect. Here, the combination with topography can lead to an enhancement of the wettability which can be explained by the Wenzel effect. Furthermore, some structures can cause hydrodynamic effects in agitated conditions, leading to antiadhesive activity, or mechanical stress on the bactericidal membranes, leading to their death. Here again, many different structures and chemicals were used, making it difficult to highlight which combinations are the most promising for the moment, especially as there is no uniformised microbiology assay to evaluate the efficiency of these surfaces.

While in the given examples from the literature, both polymers and other chemical compounds, such as self-assembled monolayers were used, in this thesis, it was chosen to study polymers as they offer many advantages. Indeed, Maan *et al.* emphasize in their literature review that numerous polymer coatings are non-toxic and biocompatible as well as being robust, versatile, low cost and easy to process at large-scale[108]. Furthermore, for hydrophobic coatings, it is possible to use fluorine-free polymers. This is important because the toxicity and accumulation of fluorine containing compounds is raising concern[109]. As for hydrophilic coatings, using polymers can allow better control over the thickness of the coating and thus create a denser hydration layer at the interface between the substrate and any liquid. Different methods for polymer thin film deposition will be presented in the following section and their advantages and inconveniences will be discussed.

3. Different methods for creating polymer thin film coatings

Thin films are coatings with a thickness comprised between an atomic layer and a few microns. For creating organic polymer thin films, various methods can be used based on wet or dry processes[110].

3.1. Liquid-based methods

3.1.1. Dip-coating

Dip-coating is a very simple method to deposit polymer thin films. This technique consists in immersing the substrate into a solution containing the polymer of interest diluted in a solvent. As the substrate is removed, the solvent dries, leaving a coating of polymer as seen in Figure 19. In order to achieve a repeatable deposition, it is important to control the solution's concentration, movement in and out of the solution, as well as the time of immersion and the time and temperature of drying. The dipping process can be repeated in order to increase the polymer's thickness upon the surface[111,112].

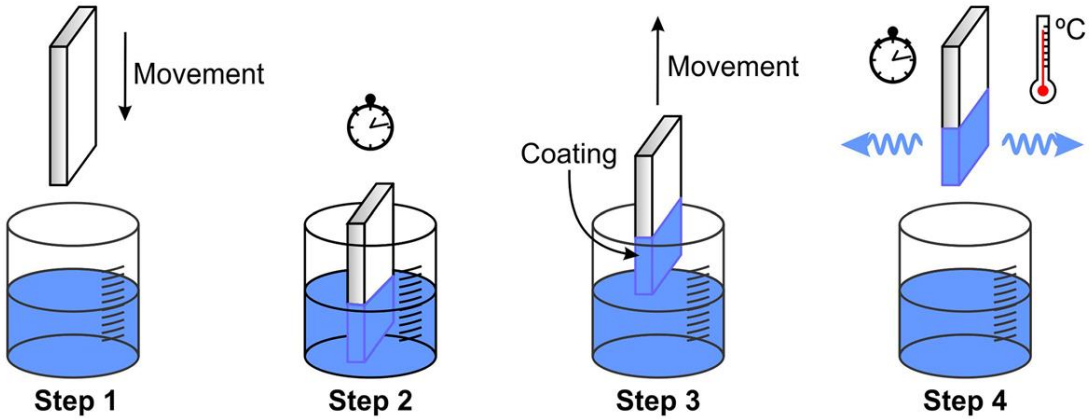

Figure 19: Dip coating process. Reprinted with permission from Frederichi et al. [111] *Copyright © 1994 Springer Nature BV.*

As the polymer must be diluted in a solvent for this process, it cannot be applied to all polymers. For example, many fluorine-containing or crosslinked polymers are insoluble in solvents[113,114]. Moreover, the substrate also has to be chosen in adequation with this solvent-using method. Finally, while dip coating on a planar substrate, can lead to homogeneous films, this method is not adequate for structured surfaces[112].

3.1.2. Spin coating

Like dip coating, spin coating requires the dilution of a polymer in a solvent. This method then consists of dropping the solution in the middle of the substrate which is placed on a spin-coater. Once the solution is deposited, the spin coater is activated and begins spinning at fast velocity. Centrifugal force then plays an important role by spreading the polymer coating over the substrate to create a thin film. After evaporation of the solvent, a homogeneous polymer thin film can be obtained[112,115].

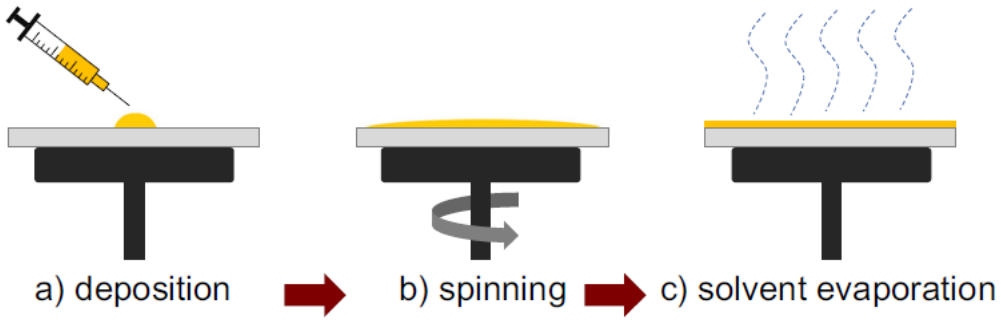

Figure 20: Spin coating process. Reprinted with permission from Obregón and Rodríguez[116] Copyright © 2021 Springer Nature.

The thickness of the thin film can be controlled by adjusting the viscosity of the polymer solution, the acceleration and the rotational speed of the spin coater as well as the time it spins. Similarly to dip coating, this method works well for planar substrates with soluble polymers, but when functionalising 3D structures it is not adapted to create conformal coatings[112].

Many of the works presented in section 2.3.3 rely on coating the combined surfaces by dip coating or spin coating. Therefore, further examples will not be given here.

3.1.3. Electrochemical polymerisation

Electrochemical polymerisation or electropolymerisation refers to the deposition of a polymer coating onto a metal substrate which is the working electrode. Unlike the two former methods, for electropolymerisation, it is the monomer that is diluted in a solvent. This solution is the electrolyte in which the working, counter and reference electrodes are placed. The electrodeposition can then take place by applying a constant current (galvanostatic) or potential (potentiostatic) to the electrochemical cell[117]. Potentiodynamic conditions (cyclic voltammetry) are also possible. This leads to the oxidation of the monomer consequently initiating the polymerisation.

The example of electropolymerisation of poly(ethylenedioxythiophene) (PEDOT) doped with poly(styrene sulfonate) (PSS) is given below (Figure 21a). Here, the monomer is first oxidized and forms a radical. Two of these radical cations then link together forming a dimer. Dimers join with one another by deprotonation. After n repetitions of this two-step anodic process, the polymer is formed[118]. The deposition time enables to tune the thickness of the coating on the substrate (Figure 21b)[119].

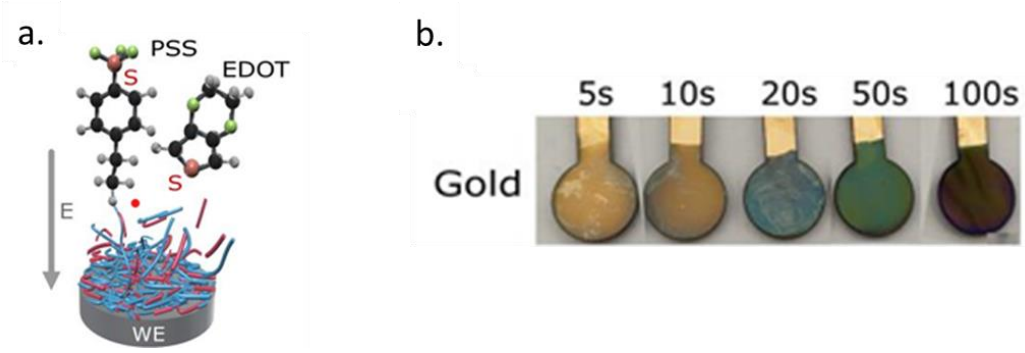

Figure 21: a. Schematic representation of the electropolymerisation of PEDOT/PSS. b. PEDOT/PSS thickness growth of gold substrate with an increasing deposition time. Adapted from Mousavi et al.*[119].*

While this technique can improve the adherence of the polymer with the substrate, the latter must be metallic, restricting the use of this method. The morphology and stability of the obtained thin films can vary depending on the method used: galvanostatic, potentiostatic or potentiodynamic[117,120]. Furthermore, the monomer has to be an organic redox specie such as thiophene, ethylenedioxythiophene (EDOT), pyrrole or aniline[121].

As seen in section 2.3.2, hydrophobic PEDOT has been electrodeposited on stainless steel to create antibiofouling surfaces[79]. Furthermore, a hydrogel of polyaniline-polythionine was synthesized by electropolymerisation. This electrochemical immunosensor also demonstrated good antifouling properties due to the strong hydrophilicity bought by crosslinking agent phytic acid[122].

While liquid-based coatings offer often rapid and versatile functionalization, these methods are not adapted for conformally coating structured substrates. This can be achieved by using Chemical vapour deposition (CVD) which can lead to very thin films with no defects and good adherence to the substrate.

3.2.Chemical Vapour Deposition (CVD)

First used for depositing inorganic coatings, CVD has also been developed for polymers[123] and refers to, in this case, a technique in which the polymerisation reaction occurs directly on a substrate from a monomer or a mixture of monomers in vapour form. In most cases, this technique requires a vacuum to vaporise the monomers. We'll see in the next few paragraphs that there are several types of CVD techniques. These vacuum-based techniques offer many advantages over thin film depositions from liquids. First, they do not require the use of solvents, which are often toxic and corrosive, to solubilize the precursor. This also allows to deposit insoluble polymers. Removing the use of solvents for thin film deposition also means there is no evaporation step which could lead to the presence of organic contaminants[123], sometimes critical in applications such as medical devices. Furthermore, they allow a much more precise deposition with control over the thickness of the coating. This makes CVD techniques the method of choice for coating structures with functional polymers.

3.2.1. The Gorham process for depositing parylene thin films

The first polymer to be deposited in a thin film was poly(p-xylylene) or parylene. This technique was invented by Szwarc in 1947[124] and optimized by Gorham in 1966[125]. It consists in heating di-p-xylene to induce its sublimation and its pyrolysis which occurs at 600°C. The resulting reactive p-xylene monomers are then introduced into a deposition chamber where the polymerisation occurs spontaneously onto the substrate which is kept at room temperature[125] (Figure 22).

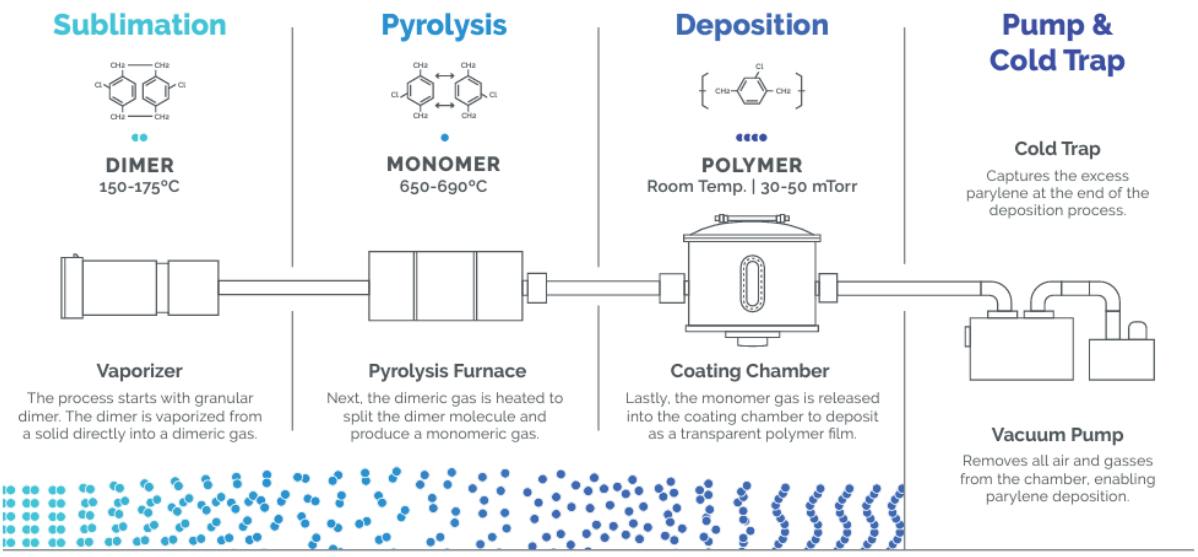

Figure 22: Process mechanism for parylene deposition. Reprinted with permission from VSI Parylene[126].

Parylene coatings can be deposited on a diversity of substrates and their properties depend on the type of parylene deposited[127]. Often used for their biocompatibility[126,127], parylenes are still deposited using the Gorham process today. Its major disadvantage is that this process is only applicable to parylene. This explains the development of other CVD methods to deposit polymers.

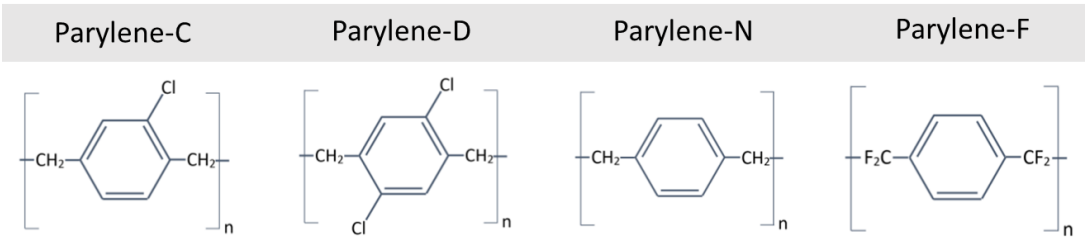

Figure 23: Different types of parylene. Adapted from Kuppusami and Oskouei[127].

Concerning antibiofouling surfaces, parylene-F has demonstrated dual antibacterial-antiadhesive activity against both Gram-positive and Gram-negative bacteria[128]. A further study also showed that while parylene-C also demonstrated anti-adhesive activity, this was not the case for parylene-D[129].

3.2.2. Vapour Deposition Polymerisation (VDP)

Vapour Deposition Polymerisation (VDP) allows, as its name indicates, the creation of polymer thin films directly on a substrate. It requires the vaporisation of two monomers in the reaction chamber which is under vacuum (Figure 24a). These monomers react with one another following a step-growth polymerisation mechanism when condensing on the substrate's surface[130]. This allows the formation of a uniform thin film.

VDP has allowed the formation of polymers such as polyimides[130,131], polyamides[132], polyamic acids[133] or polyazomethines[134]. Formation of polyimides is detailed in Figure 24b. The mechanism requires the injection of aromatic pyromellitic dianhydride (PMDA) and aromatic diamine oxydianiline (ODA) into the vacuum chamber. These molecules then condensate on the surface of the substrate where they react by polyaddition to form polyamic acid. Water removal then leads to the formation of polyimide.

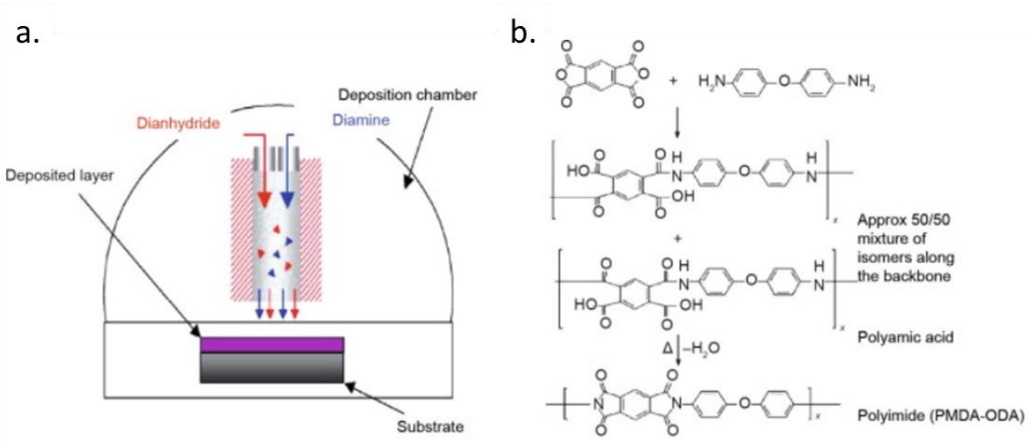

Figure 24: a. Schematic representation of VDP of polyimide. Both monomers are injected in vapour form in stoichiometric conditions. b. Step-growth polymerisation of polyimide. Reprinted from Zhao and Gleason[135].

The polymerisation being a step-growth mechanism, the monomers have to be injected in stoichiometric conditions which is not easily controlled[130]. Furthermore, this technique requires high temperature annealing. These are the main inconveniences of this polymerisation technique.

Few works using VDP were found for the development of antibacterial or antifouling surfaces. However, one study used this technique to deposit polyimides from 3,5-diamino benzoic acid and anhydrous PMDA. Here, the antibacterial activity from the benzoic acid led to coatings which showed bactericidal activity against many types of bacteria[136].

3.2.3. Plasma Enhanced Chemical Vapour Deposition (PECVD)

Plasma enhanced CVD (PECVD) is a technique which is often used to coat devices for various applications: microelectronics, photovoltaics and medical devices. This technique leads to plasma polymers which are unconventional organic polymer thin films. Strictly speaking, the latter cannot be referred to as polymers as such, because they do not consist of repeating monomer units but rather present a crosslinked structure resembling the precursor's chemistry[137,138].

During plasma polymerisation, a monomer is introduced into a plasma reactor under vapour form at a set flowrate. Inside the reaction chamber, the radiofrequency power ignites the precursor and carrier gas into a plasma state, forming many radicals and other reactive species such as cations, anions and free electrons (Figure 25). These unstable molecules will then react on the given substrate which is placed on the bottom electrode. This process leads to a crosslinked thin film. Depending on the monomer, its flowrate, the radiofrequency power and the time of deposition, the thin film obtained after deposition can have different characteristics.

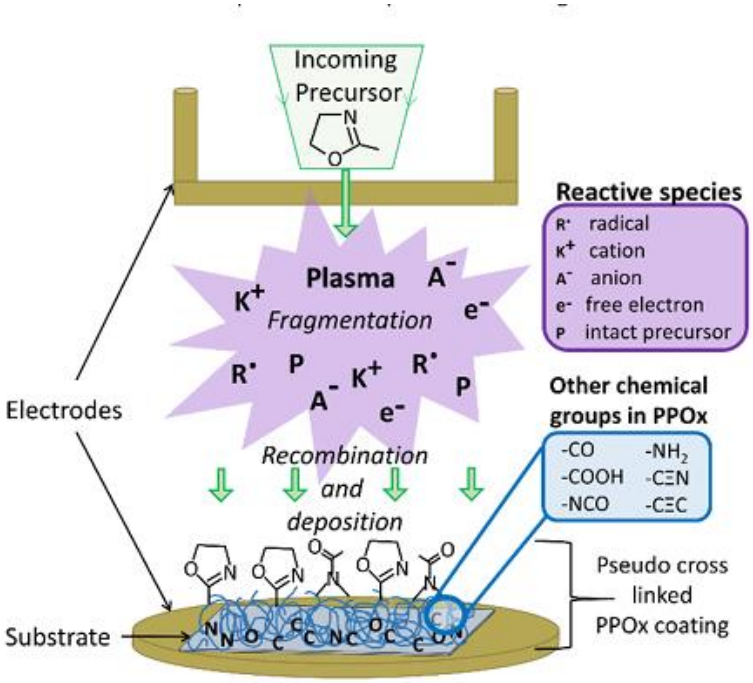

Figure 25: Schematic representation of the PECVD process. This example is illustrated with an oxazoline as a precursor. Reprinted with permission from Macgregor-Ramiasa et al.*[139] Copyright 2013 Royal Society of Chemistry.*

This technique is highly versatile as many different monomers can be deposited by PECVD. It is not substrate-dependent, it is simple and does not require the use of solvents[139]. Furthermore, the plasma polymers obtained using this technique are generally chemically inert, mechanically strong and thermally stable[137]. Adjusting the deposition parameters of PECVD can allow control over the crystallisation and morphology of the resulting film[140]. However, this technique does not allow the full conservation of the monomer's structure and offers limited control over the fragmentation and recombination of the precursor's various functional groups. Variations of this technique have also emerged such as pulsed-PECVD where the plasma is not continuously ignited. This should favour the conservation of the functional groups of the precursor and limit dangling bonds which can be oxidized[137].

PECVD has been used to deposit organosilicon coatings such as hexamethylcyclotrisiloxane (D3)[137], tetramethylsilane (4MS)[141], hexamethyldisiloxane (HMDSO) and tetramethyldisiloxane (TMDSO)[142]. There are also many examples of antibiofouling or antibacterial surfaces obtained with the use of PECVD which can be found in the literature. Polyoxazoline (POX) coatings for instance have been deposited by PECVD for this purpose. However, it has been highlighted that there is sometimes a compromise to make between stability of the coating and antibiofouling activity[143]. Octadiene plasma polymers have also been used to encapsulate D-amino acids (DAA). The controlled release of the DAA showed efficiency against *Enterococcus Faecalis* biofilms[144,145]. Furthermore, non-synthetic molecules such as terpinen-4-ol (found in tea tree oil)[146,147], geranium essential oil[148] and oregano secondary metabolites[149] have been used to create plasma polymers that can fight against bacterial colonisation.

3.2.4. Dielectric Barrier Discharge Cold Atmospheric Plasma (DBD-CAP)

Dielectric barrier discharge cold atmospheric plasma (DBD-CAP) was first invented by Siemens in 1857[150]. Initially used for creating ozone, it now has various applications such as pollution control, excitation of CO_2 lasers, surface modification and plasma chemical deposition[151].

In this technique, the precursor is injected as an aerosol pushed by a carrier gas which is generally, nitrogen, helium or argon[152]. In this case, the plasma is not created directly between the electrodes as at least one of them is covered by a dielectric. The atmospheric conditions also make it a cheaper and easier method than PECVD. In this method, the monomer is activated by the plasma, creating charged and ionic molecule fragments which then react on the substrate's surface forming a thin film[152].

Figure 26 represents a plasma torch used for thin film deposition and based on DBD-CAP. Indeed, this mechanism, used in Molecular Plasma Group's (MPG, Luxembourg) Plasmaspot®, consists of 2 circular electrodes, one inside the other and separated by a dielectric. The precursor is injected by a nebulizer in aerosol form and goes through the inner electrode pushed by a carrier gas (nitrogen). An inert gas (nitrogen, argon or helium) is injected in between both electrodes and as a current is applied to the electrodes, a plasma of this gas is ignited. At the extremity of the electrode, the precursor is activated by the afterglow of the plasma and the reactive species that are created (radicals, anions, cations, electrons, ozone) form a crosslinked thin film at the surface of the substrate[153]. This technique therefore gives a similar coating to PECVD, without having to vaporise the precursor and work under vacuum.

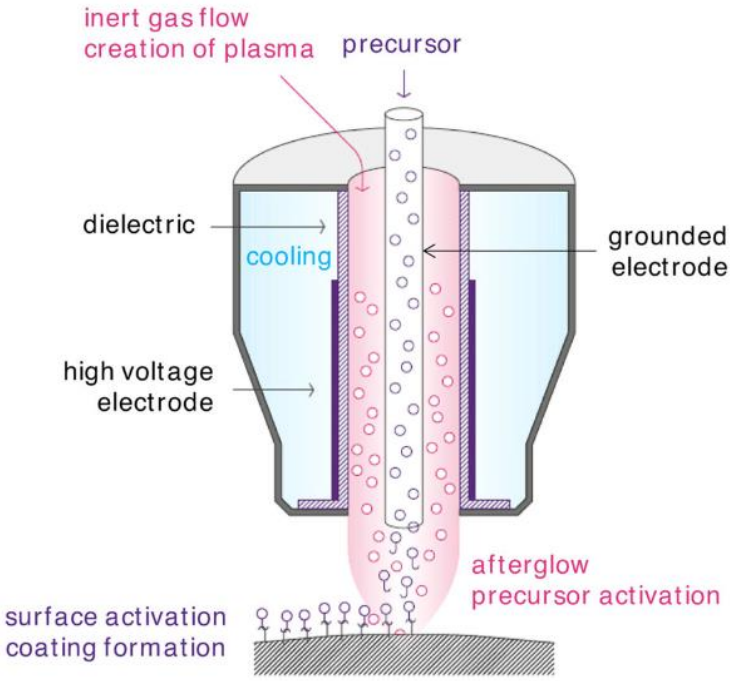

Figure 26: Schematic representation of a DBD-CAP plasma torch. Reprinted with permission from Borek-Donten et al.[153] *Copyright © 2022 John Wiley & Sons - Books.*

DBD-CAP can be used with many precursors, which can be pure or diluted in solvents. Furthermore, the cold plasma allows this method to deposit thin films on a wide range of substrates, from stainless steel to textiles[150].

DBD plasma deposition has been used previously for coating di(ethylene glycol) vinyl ether (DVE) with the aim of creating antibiofouling surfaces[154]. It was underlined that the plasma parameters have a significant effect on the chemistry of the poly(ethylene oxide)-like obtained films which in turn influences the adsorption of model foulant fibrinogen. Superhydrophobic surfaces have also been obtained by using DBD-CAP to functionalize surfaces with C_xF_y based films[155]. This publication highlighted the impact of the discharge gas (argon or helium in this case) on the chemical composition and consequently, the hydrophobicity of the film. Other hydrophobic surfaces have been created using this deposition technique by using organosilicon precursors such as HMDSO[152], decamethyltetrasiloxane (DMTSO), 1,3,5,7-tetramethyl1,3,5,7-tetravinylcyclotetrasiloxane (V4D4), octamethylcyclotetrasiloxane (D4)[156] or 1,3,5-trimethyl-1,3,5-trivinylcyclotrisiloxane (V3D3)[157,158].

A DBD plasma jet such as the one represented in Figure 26, has also been used to deposited fluorinated precursors such as trimethoxy(3,3,3-trifluoropropyl) silane. The fluorine present in the final coatings led to a reduction in *P. aeruginosa* and *S. aureus* adhesion[159]. Antibacterial surfaces functionalized with antimicrobial peptides such as nisin have also been developed by using DBD-CAP to deposit a plasma polymer thin film onto which nisin can be immobilized[160,161].

3.2.5. Hot Wire Chemical Vapour Deposition (HWCVD)

Hot Wire CVD (HWCVD), also called Hot Filament CVD or pyrolytic CVD[162] is a technique in which the monomer is injected into the reactor in vapour phase and is pyrolyzed as it goes through a heated filament. This leads to the creation of reactive species issued from the precursor which then,

similarly as to in PECVD, react at the surface of the cooled substrate, creating an organic thin film. This process is illustrated in Figure 27. Furthermore, HWCVD allows for better control of the monomer activation which does not suffer from UV and ion bombardment as it does in PECVD[162]. Moreover, it has been shown that the temperature of the filament in HWCVD can have a significant effect on the resulting thin film[163].

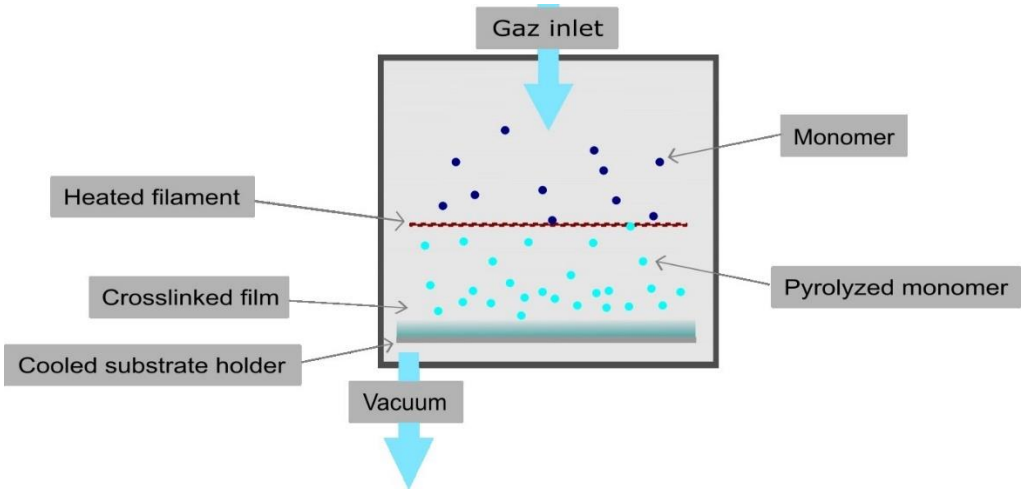

Figure 27: Schematic representation of HWCVD.

This deposition method has been used with organosilicon molecules such as D3, D4[162,164] or methyltriethoxysilane (MTES)[165]. HWCVD has also been used to synthesize hydrophobic fluorocarbon–organosilicon copolymers from V3D3 and perfluorooctane sulfonyl fluoride (PFOSF)[163]. PFOSF can be used as an antibiofouling coating due to its superhydrophobicity[78]. Furthermore, V3D3, which is also a hydrophobic polymer, has previously been used to coat neural implants due to its biocompatibility[166–169].

Moreover, HWCVD paved the way for novel deposition technique initiated Chemical Vapour Deposition (iCVD) which will be presented next.

3.2.6. Initiated Chemical Vapour Deposition (iCVD)

Initiated Chemical Vapour Deposition (iCVD) is a technique that was developed by Karen Gleason's group at MIT in the early 2000s, with a first iCVD-deposited vinyl polymer in 2004[123,170]. This method, based on radical polymerisation, shows similarities with HWCVD as it also necessitates the use of a heated filament. However, in this case, the latter does not act on the monomer itself but activates a radical initiator.

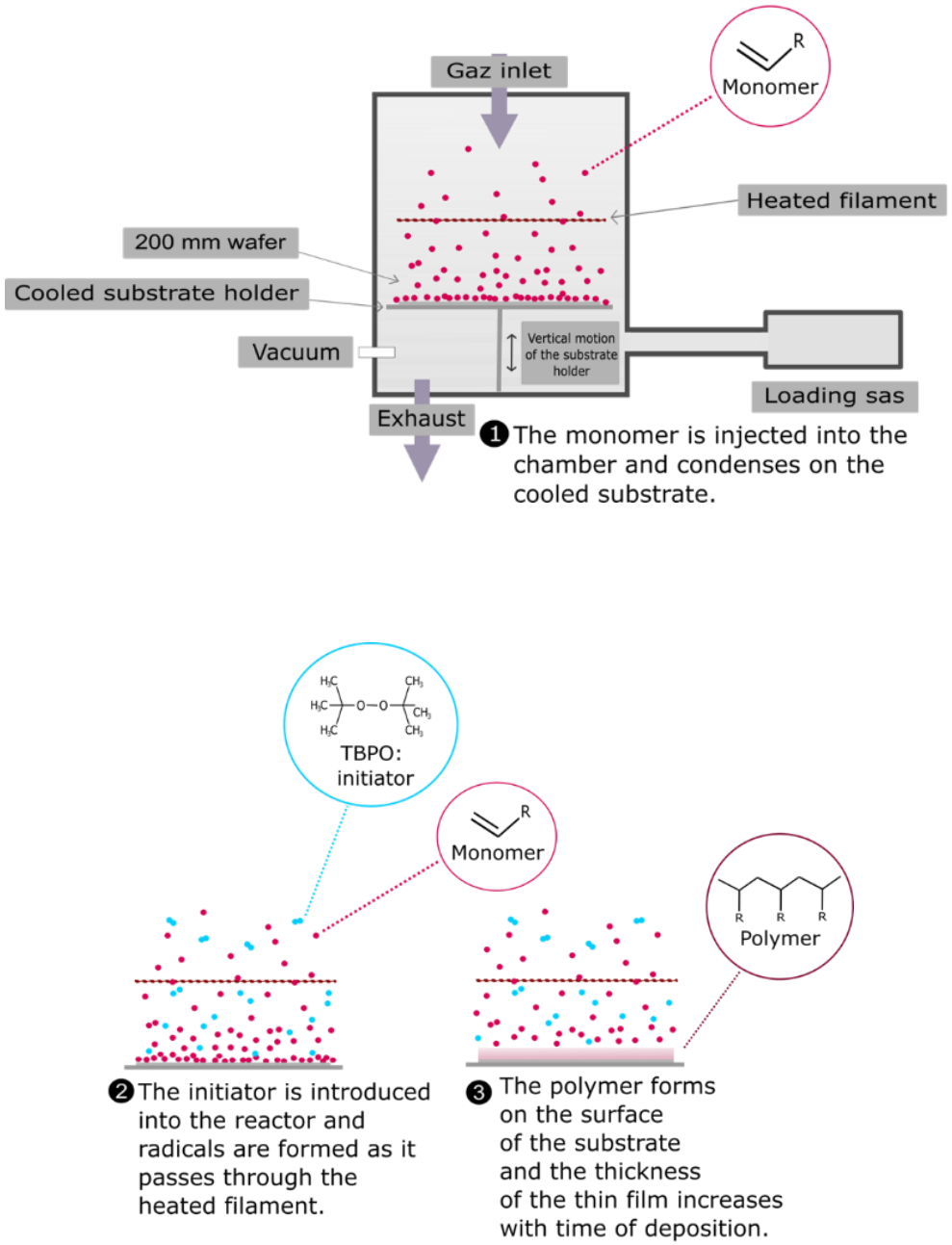

Figure 28: Schematic representation of the initiated Chemical Vapour Deposition (iCVD) process.

Indeed, in this method, as represented in Figure 28, the monomer is injected into the vacuum chamber in vapour form. It then condensates at the surface of the chilled substrate. The second step consists in injecting a radical initiator into the reactor, most often tert-butyl peroxide (TBPO), also in vapour form. As it goes through the heated filament, the initiator is pyrolyzed, thus creating highly reactive radical species. With a filament temperature around 200-250°C, TBPO is cleaved as represented in the first step of Figure 29, forming 2 radicals ($\cdot OC(CH_3)_3$)[123]. When these radicals come into contact with the monomer at the surface of the substrate, the polymerisation is initiated, and propagation then occurs as in radical polymerisation (Figure 29). The time of deposition can be adjusted to tune the thickness of the polymer thin film.

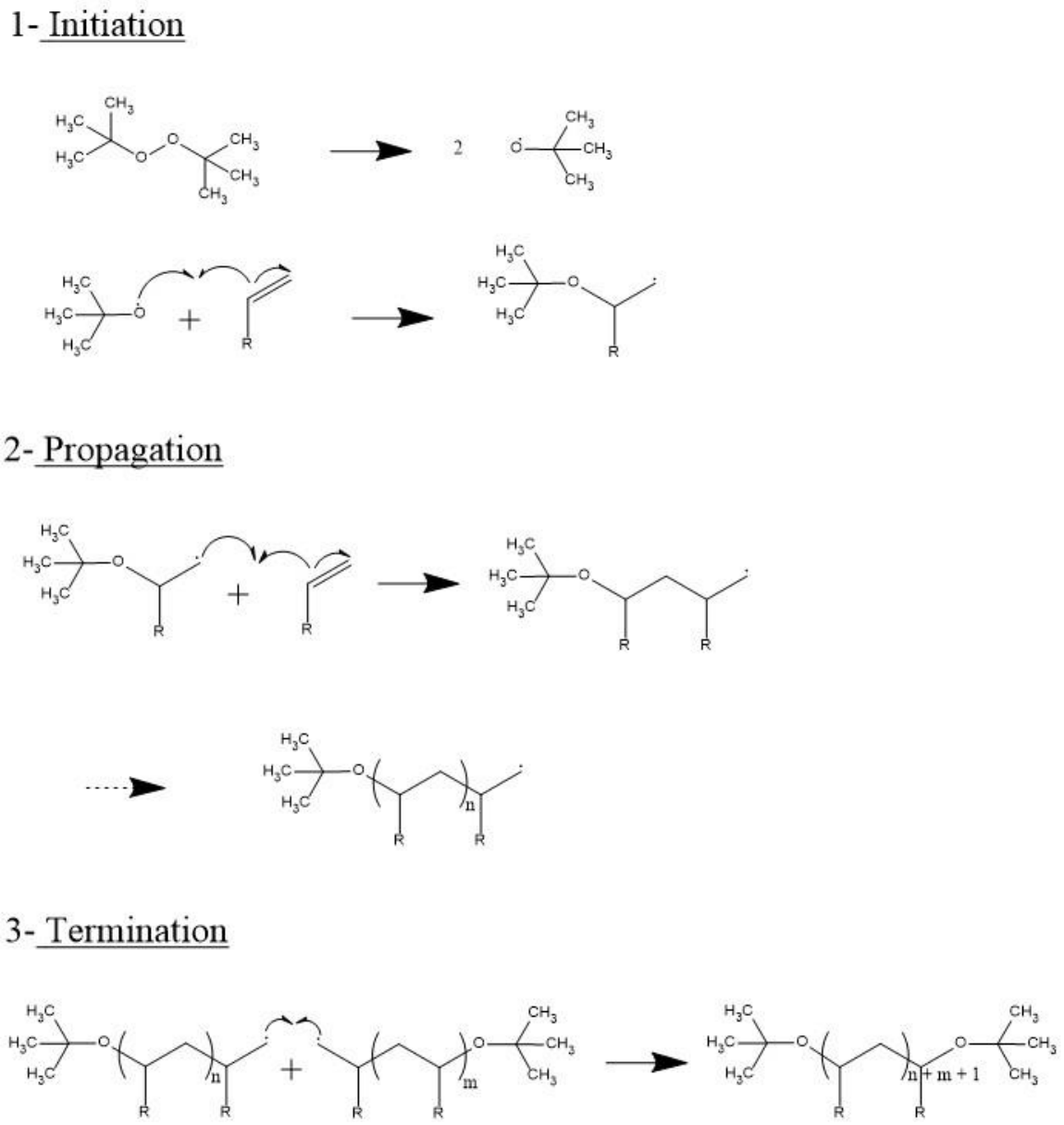

Figure 29: Radical polymerisation mechanism as occurring in iCVD with TBPO as radical initiator. For the initiation step, the cleavage of TBPO occurs as the molecule goes through the heated filament. The second step, forming the radical monomer happens at the surface of the substrate. Termination can occur, as represented here, as two polymer chains react with one another, or as one polymer chain reacts with a TBPO radical.

Unlike other CVD processes such as PECVD or HWCVD, this process thus does not affect the functional groups of the monomer[123]. This can be verified by using Fourier Transform Infrared Spectroscopy (FTIR) as it can be seen in Figure 30. This allows the creation of polymers with many diverse properties. Indeed, these spectra show the resemblance of iCVD-deposited poly(glycidyl methacrylate) (PGMA) with conventional PGMA. However, when using PECVD to deposit this precursor, some of the chemical functions are modified, and the epoxy-related peaks at 907, 848 and 760 cm^{-1} disappear. This example was the first proof-of-concept for iCVD coatings[170].

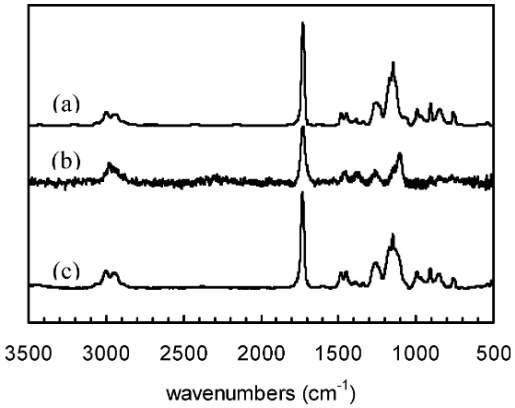

Figure 30: FTIR spectra of (a)PGMA deposited by iCVD with TBPO as radical initiator. (b) Plasma polymer of GMA deposited by PECVD. (c) Conventional polymerized PGMA. Reprinted with permission from Mao and Gleason [170] Copyright © 2004 American Chemical Society.

iCVD has also proven to lead to conformal coatings, even on high aspect ratio structures. This can be seen in Figure 31 which represents iCVD coatings of various polymers on different structures. For example, it has been observed that poly(ethylene glycol acrylate) (PEGDA) can be deposited conformally on silicon trenches with an aspect ratio up to 8.4 (Figure 31a)[171]. A similar study with poly(V3D3) was also carried out. It was shown that in optimal process conditions, the coating was still conformal on trenches with an aspect ratio of 13[172,173] (Figure 31d). Conformal coatings were also obtained with poly (hydroxyethyl methacrylate-co-EGDA) (poly(HEMA-co-EGDA)) on TiO_2 nanotubes (Figure 31b).

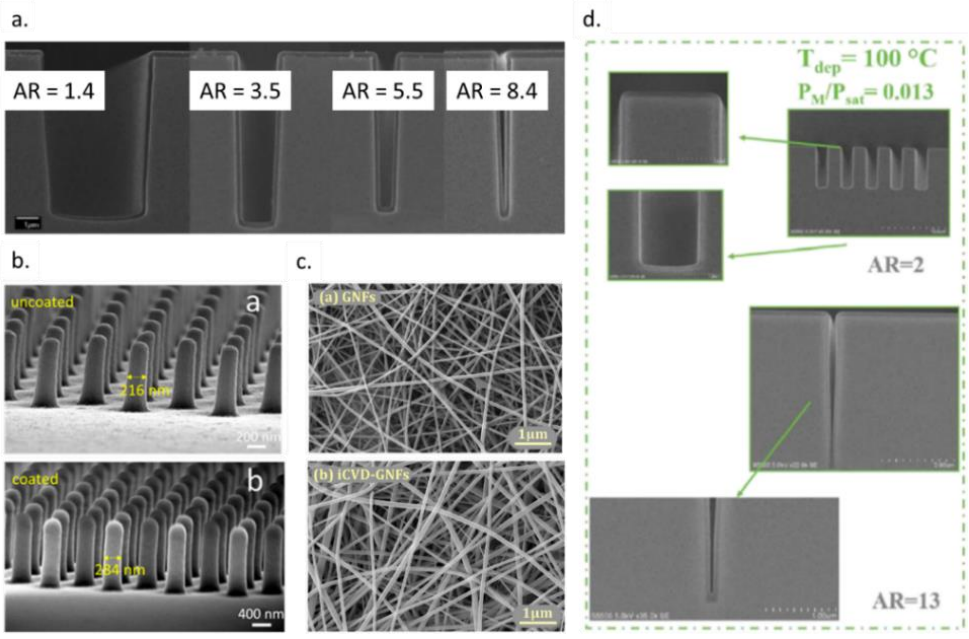

Figure 31: Examples of conformal iCVD coatings observed by SEM a. PEGDA deposited by iCVD onto silicon trenches with different aspect ratios (AR). Adapted from Moni et al.*[171]; b. TiO_2 nanopillars (a) before and (b) after iCVD deposition of poly(HEMA-co-EGDA). Adapted with permission from Li* et al.*[174] Copyright © 2019 American Chemical Society; c. Gelatin nanofibers (a) before and (b) after iCVD deposition of poly(EGDMA). Adapted with permission from Mansurnezhad* et al.*[175] Copyright © 2020 Elsevier; d. ICVD deposited poly(V3D3) on microtrenches with different AR. Adapted from Zavvou.[173]*

For its capability of preserving the functional groups of the monomer and its ability to deposit conformal thin films on complex and fragile substrates, iCVD is a very versatile technique that can be used in many different fields[176,177]. Furthermore, as this process takes place in relatively soft conditions, it is applicable to many different monomers with many different properties[178]. These gentle settings also allow coatings on fragile substrates such as membranes[179,180], textiles[181,182] or even gelatin nanofibers[175]. iCVD has also been used to coat liquid substrates such as silicon oil[183]. Karen Gleason's last literature review underlines the variety of devices that have been functionalized by iCVD[178]. Indeed, iCVD polymers have been used for optical materials[184], for silicon wafer bonding[185], as dielectrics in high voltage capacitors[172], gas sensors[186,187] and many other applications.

In the medical field, for example, sensing devices can benefit from this technique which can provide flexible and functional polymers. Glucose sensing was carried out with an iCVD-deposited boronic acid hydrogel[188]. Another sensor that would benefit healthcare is the pH-sensor. Here again, iCVD was used to deposit a responsive hydrogel for this application. In this case, p(MAA-co-EGDMA) was chosen as its swelling is pH-dependent and can therefore monitor human sweat[189]. This technique has also been used for depositing polymers used to encapsulated and control-release pharmaceuticals[190] such as gentamicin[191] or clotrimazole[192].

As for antibiofouling surfaces, iCVD has been used to synthesize superhydrophobic surfaces by depositing a stacked polymer film composed of poly(V4D4) and poly(perfluorocrylate) (PFDA)[182]. The latter has also been used alone on stainless-steel meshes to impart them with superhydrophobic-superoleophilic properties[193]. Hydrophilic surfaces have also been achieved. For example, copolymer poly(vinyl pyrrolidone-co-EGDMA) (poly(VP-co-EGDMA)) was used to improve biofilm resistance and water permeability on nanofiltration membranes[180].

4. Strategy and objectives of this thesis

As it has been seen in this chapter, while biofilm has negative consequences in many different fields, leading to device failure, contamination and significant costs, there is not yet a universal solution against it. Following biomimetic strategies, many publications have emerged focusing on the combination of chemistry and topography to inhibit biofilm formation. However, due to the novel character of this research, it is still difficult to visualize any convergence to one type of antiadhesive surface.

The objective of this thesis is to contribute to the search for a universal surface combining topography and chemistry aiming to counteract initial bacterial adhesion and, consequently, prevent biofilm formation. This work will more precisely focus on surfaces for medical applications such as implants and will be achieved by investigating the impact of various parameters including the type of chemical precursors deposited, the deposition process employed, and the nature and structure of the substrate. Hydrophobic and hydrophilic organic polymers will be used, in order to test both strategies found in the literature. By depositing these polymers onto micro and/or nanostructured surfaces it is hoped to reach the Cassie-Baxter or Wenzel effect, thus creating superhydrophobic and superhydrophilic surfaces respectively.

CVD-based coatings will be used as they offer versatility and they are also better adapted for conformably depositing functional coatings onto structured surfaces. More precisely, for its promise of conformal coatings, iCVD was chosen, as this technique should allow the conservation of the topography but also of the monomer's functional groups as it is based on free-radical polymerisation. DBD-CAP was also studied in this thesis. Indeed, with its easy set-up and versatility, it offered the

opportunity of comparing deposition techniques with the same monomer. The various deposition processes and the methods used for characterizing the physico-chemical properties of the obtained materials will be presented in chapter 2 of this manuscript.

The chosen monomer to develop hydrophobic coatings was 1,3,5-trivinyl-1,3,5-trimethyltricylcosiloxane (V3D3) (Figure 32) which has previously been used to create fluorine-free hydrophobic plasma polymer pp(V3D3) by PECVD[137] or poly(V3D3) by iCVD[167]. Furthermore, this polymer has previously been used for coating neural probes due to its biocompatibility[137,169].

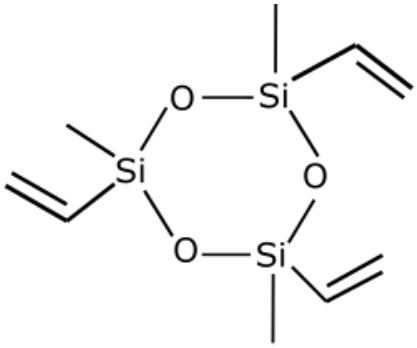

Figure 32: 1,3,5-trivinyl-1,3,5-trimethylcyclotrisiloxane (V3D3).

In this project, conventional polymer poly(V3D3) will be deposited by iCVD but DBD-CAP was also used to create plasma polymer pp(V3D3). This allowed a comparative study on the influence of the choice of process on the resulting thin film and its physico-chemical properties. These results will be presented and discussed in chapter 3.

The hydrophilic polymer that was chosen was polyvinylpyrrolidone (PVP) which is often used for medical applications due to its biocompatibility and its ability to form complexes with many substances[194]. PVP has also been coupled with antibacterial substances such as iodine[195], quaternized chitosan[196], or iodopropyltrimethoxysilane[30]. This polymer can also be deposited by iCVD from the VP monomer (Figure 33)[197]. This is the path that will be studied in this thesis.

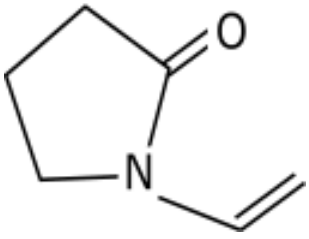

Figure 33: Vinylpyrrolidone (VP).

However, PVP's strong affinity with water makes it soluble in aqueous solutions. To overcome this, codeposition was carried out using V3D3 as a crosslinking agent in the aim of stabilising the coating. The results for both PVP and poly(VP-co-V3D3) thin films on planar substrates will be presented and discussed in chapter 4.

Chapter 5 will concentrate on the combination of these polymers with topography. To do so, substrates with a two-scale micro and nano topography were used. The fabrication of these substrates, developed in the CEA Leti's 200 and 300 mm microsystems platform will be presented in this chapter before focusing on surface properties with and without additional polymer thin film.

Finally, chapter 6 will present the microbiology assays that were carried out to study the impact of the various surfaces created as part of this thesis on bacterial adhesion and biofilm formation.

5. Bibliography

(1) Donlan, R. M. Biofilms: Microbial Life on Surfaces. *Emerging Infectious Diseases.* **2002**, *8* (9), 881–890. https://doi.org/10.3201/eid0809.020063.

(2) Haidar, R. Antoni van Leeuwenhoek. *Photoniques* **2016**, No. 82, 19–24. https://doi.org/10.1051/photon/20168217.

(3) Durand, H.; Whiteley, A.; Mailley, P.; Nonglaton, G. Combining Topography and Chemistry to Produce Antibiofouling Surfaces: A Review. *ACS Applied Bio Materials.* **2022**, acsabm.2c00586. https://doi.org/10.1021/acsabm.2c00586.

(4) Adlhart, C.; Verran, J.; Azevedo, N. F.; Olmez, H.; Keinanen-Toivola, M. M.; Gouveia, I.; Melo, L. F.; Crijns, F. Surface Modifications for Antimicrobial Effects in the Healthcare Setting: A Critical Overview | Elsevier Enhanced Reader. *Journal of Hospital Infections.* **2018**, *99* (3), 239–249. https://doi.org/10.1016/j.jhin.2018.01.018.

(5) *Gram Positive vs Gram Negative*. Immunology & Microbiology from Technology Networks. http://www.technologynetworks.com/immunology/articles/gram-positive-vs-gram-negative-323007 (accessed 2024-04-28).

(6) Humblot, V.; Yala, J.-F.; Thebault, P.; Boukerma, K.; Héquet, A.; Berjeaud, J.-M.; Pradier, C.-M. The Antibacterial Activity of Magainin I Immobilized onto Mixed Thiols Self-Assembled Monolayers. *Biomaterials* **2009**, *30* (21), 3503–3512. https://doi.org/10.1016/j.biomaterials.2009.03.025.

(7) Davidson, I.; Cahill, P.; Hinz, A.; Kluza, D.; Scianni, C.; Georgiades, E. A Review of Biofouling of Ships' Internal Seawater Systems. *Frontiers in Marine Science.* **2021**, *8*, 761531. https://doi.org/10.3389/fmars.2021.761531.

(8) Hopkins, G.; Davidson, I.; Georgiades, E.; Floerl, O.; Morrisey, D.; Cahill, P. Managing Biofouling on Submerged Static Artificial Structures in the Marine Environment – Assessment of Current and Emerging Approaches. *Frontiers in Marine Science.* **2021**, *8*, 759194. https://doi.org/10.3389/fmars.2021.759194.

(9) Bixler, G. D.; Bhushan, B. Biofouling: Lessons from Nature. *Philosophical Transactions of the Royal Society A: Mathematical, Physical and Engineering Science.* **2012**, *370* (1967), 2381–2417. https://doi.org/10.1098/rsta.2011.0502.

(10) Sokol, M., VP Sales and. *What is Industrial Biofouling? (Guide to Process, Problems, and Prevention)*. https://www.adv-polymer.com/blog/biofouling (accessed 2024-03-26).

(11) Jarrell, D. B.; Johnson, A. B.; Zimmerman, P. W.; Gore, M. L. *Nuclear Plant Service Water System Aging Degradation Assessment*; NUREG/CR-5379; Pacific Northwest Laboratory for U.S. Nuclear Regulatory, 1989.

(12) Nunes, S. P. Can Fouling in Membranes Be Ever Defeated? *Current Opinion in Chemical Engineering.* **2020**, *28*, 90–95. https://doi.org/10.1016/j.coche.2020.03.006.

(13) Saget, M.; De Almeida, C. F.; Fierro, V.; Celzard, A.; Delaplace, G.; Thomy, V.; Coffinier, Y.; Jimenez, M. A Critical Review on Surface Modifications Mitigating Dairy Fouling. *Comprehensive Review on Food Science and Food Safety.* **2021**, *20* (5), 4324–4366. https://doi.org/10.1111/1541-4337.12794.

(14) Rather, M. A.; Gupta, K.; Bardhan, P.; Borah, M.; Sarkar, A.; Eldiehy, K. S. H.; Bhuyan, S.; Mandal, M. Microbial Biofilm: A Matter of Grave Concern for Human Health and Food Industry. *Journal of Basic Microbiology.* **2021**, *61* (5), 380–395. https://doi.org/10.1002/jobm.202000678.

(15) Lebeaux, D.; Ghigo, J.-M.; Beloin, C. Biofilm-Related Infections: Bridging the Gap between Clinical Management and Fundamental Aspects of Recalcitrance toward Antibiotics. *Microbiology and Molecular Biology Reviews.* **2014**, *78* (3), 510–543. https://doi.org/10.1128/MMBR.00013-14.

(16) Costerton, J. W.; Stewart, P. S. Battling Biofilms. *Scientific American.* **2001**, *285* (1), 74–81. https://doi.org/10.1038/scientificamerican0701-74.

(17) Kanno, E.; Toriyabe, S.; Zhang, L.; Imai, Y.; Tachi, M. Biofilm Formation on Rat Skin Wounds by Pseudomonas Aeruginosa Carrying the Green Fluorescent Protein Gene. *Experimental Dermatology.* **2010**, *19* (2), 154–156. https://doi.org/10.1111/j.1600-0625.2009.00931.x.

(18) *New report calls for urgent action to avert antimicrobial resistance crisis*. https://www.who.int/news/item/29-04-2019-new-report-calls-for-urgent-action-to-avert-antimicrobial-resistance-crisis (accessed 2024-02-14).

(19) European Commission. AMR: A Major European and Global Challenge. https://ec.europa.eu/health/document/download/87c8d30bd23d- 496f-b0c7-a757102774b3_en (accessed 2024-02-14).

(20) Sanseverino, I.; Navarro, A.; Loos, R.; Marinov, D.; Lettieri, T. *State of the Art on the Contribution of Water to Antimicrobial Resistance*; 2018. https://doi.org/10.2760/771124.

(21) Gupta, P.; Bhatia, M.; Gupta, P.; Omar, B. J. Emerging Biocide Resistance among Multidrug-Resistant Bacteria: Myth or Reality? A Pilot Study. *Journal of Pharmacy and Bioallied Science.* **2018**, *10* (2), 96–101. https://doi.org/10.4103/JPBS.JPBS_24_18.

(22) L. Vega-Jiménez, A.; R. Vázquez-Olmos, A.; Acosta-Gío, E.; Antonio Álvarez-Pérez, M. *In Vitro* Antimicrobial Activity Evaluation of Metal Oxide Nanoparticles. In *Nanoemulsions - Properties, Fabrications and Applications*; Seng Koh, K., Loong Wong, V., Eds.; IntechOpen, 2019. https://doi.org/10.5772/intechopen.84369.

(23) Lam, P.-L.; Wong, R. S.-M.; Lam, K.-H.; Hung, L.-K.; Wong, M.-M.; Yung, L.-H.; Ho, Y.-W.; Wong, W.-Y.; Hau, D. K.-P.; Gambari, R.; Chui, C.-H. The Role of Reactive Oxygen Species in the Biological Activity of Antimicrobial Agents: An Updated Mini Review. *Chemico-Biological Interactions.* **2020**, *320*, 109023. https://doi.org/10.1016/j.cbi.2020.109023.

(24) Lemelle, L.; Rouquette, S.; Mottin, E.; Le Tourneau, D.; Marcoux, P. R.; Thévenot, C.; Maillet, A.; Nonglaton, G.; Place, C. Passive Limitation of Surface Contamination by perFluoroDecylTrichloroSilane Coatings in the ISS during the MATISS Experiments. *Npj Microgravity* **2022**, *8* (1), 1–8. https://doi.org/10.1038/s41526-022-00218-3.

(25) Ghasemlou, M.; Daver, F.; Ivanova, E. P.; Rhim, J.-W.; Adhikari, B. Switchable Dual-Function and Bioresponsive Materials to Control Bacterial Infections. *ACS Applied Materials and Interfaces* **2019**, *11* (26), 22897–22914. https://doi.org/10.1021/acsami.9b05901.

(26) Loyer, F.; Combrisson, A.; Omer, K.; Moreno-Couranjou, M.; Choquet, P.; Boscher, N. D. Thermoresponsive Water-Soluble Polymer Layers and Water-Stable Copolymer Layers Synthesized by Atmospheric Plasma Initiated Chemical Vapor Deposition. *ACS Applied Materials and Interfaces* **2019**, *11* (1), 1335–1343. https://doi.org/10.1021/acsami.8b14806.

(27) Kulaga, E.; Ploux, L.; Balan, L.; Schrodj, G.; Roucoules, V. Mechanically Responsive Antibacterial Plasma Polymer Coatings for Textile Biomaterials. *Plasma Processes and Polymers.* **2014**, *11* (1), 63–79. https://doi.org/10.1002/ppap.201300091.

(28) Děkanovský, L.; Elashnikov, R.; Kubiková, M.; Vokatá, B.; Švorčík, V.; Lyutakov, O. Dual-Action Flexible Antimicrobial Material: Switchable Self-Cleaning, Antifouling, and Smart Drug Release. *Advanced Functional Materials.* **2019**, *29* (31), 1901880. https://doi.org/10.1002/adfm.201901880.

(29) Kaur, R.; Liu, S. Antibacterial Surface Design – Contact Kill. *Progress in Surface Science.* **2016**, *91* (3), 136–153. https://doi.org/10.1016/j.progsurf.2016.09.001.

(30) Bouloussa, H.; Saleh-Mghir, A.; Valotteau, C.; Cherifi, C.; Hafsia, N.; Cohen-Solal, M.; Court, C.; Crémieux, A.-C.; Humblot, V. A Graftable Quaternary Ammonium Biocidal Polymer Reduces Biofilm Formation and Ensures Biocompatibility of Medical Devices. *Advanced Materials and Interfaces* **2021**, *8* (5), 2001516. https://doi.org/10.1002/admi.202001516.

(31) Nicolas, M.; Beito, B.; Oliveira, M.; Tudela Martins, M.; Gallas, B.; Salmain, M.; Boujday, S.; Humblot, V. Strategies for Antimicrobial Peptides Immobilization on Surfaces to Prevent Biofilm Growth on Biomedical Devices. *Antibiotics* **2022**, *11* (1), 13. https://doi.org/10.3390/antibiotics11010013.

(32) Masurier, N.; Tissot, J.-B.; Boukhriss, D.; Jebors, S.; Pinese, C.; Verdié, P.; Amblard, M.; Mehdi, A.; Martinez, J.; Humblot, V.; Subra, G. Site-Specific Grafting on Titanium Surfaces with Hybrid

Temporin Antibacterial Peptides. *Journal of Materials Chemistry. B* **2018**, *6* (12), 1782–1790. https://doi.org/10.1039/C8TB00051D.

(33) Stalet, M. Protections Anti-Microbiennes : Combinaison de La Fonctionnalisation et de La Nano-Structuration Pour Explorer Les Interactions Cellule/Surface, Thèse de doctorat, Université Grenoble Alpes et Université de Sherbrooke, 2024.

(34) Glinel, K.; Thebault, P.; Humblot, V.; Pradier, C. M.; Jouenne, T. Antibacterial Surfaces Developed from Bio-Inspired Approaches. *Acta Biomaterialia* **2012**, *8* (5), 1670–1684. https://doi.org/10.1016/j.actbio.2012.01.011.

(35) Patil, D.; Golia, V.; Overland, M.; Stoller, M.; Chatterjee, K. Mechanobactericidal Nanotopography on Nitrile Surfaces toward Antimicrobial Protective Gear. *ACS Macro Letters.* **2023**, *12* (2), 227–233. https://doi.org/10.1021/acsmacrolett.2c00697.

(36) Cheng, Y.; Ma, X.; Franklin, T.; Yang, R.; Moraru, C. I. Mechano-Bactericidal Surfaces: Mechanisms, Nanofabrication, and Prospects for Food Applications. *Annual Review of Food Science and Technology.* **2023**, *14* (1), 449–472. https://doi.org/10.1146/annurev-food-060721-022330.

(37) Vigué, A.; Vautier, D.; Kaytoue, A.; Senger, B.; Arntz, Y.; Ball, V.; Ben Mlouka, A.; Gribova, V.; Hajjar-Garreau, S.; Hardouin, J.; Jouenne, T.; Lavalle, P.; Ploux, L. Escherichia Coli Biofilm Formation, Motion and Protein Patterns on Hyaluronic Acid and Polydimethylsiloxane Depend on Surface Stiffness. *Journal of Functional Biomaterials.* **2022**, *13* (4), 237. https://doi.org/10.3390/jfb13040237.

(38) Vigué, A. Effets Des Propriétés Mécaniques Sur l'adhésion de Microorganismes: Comportement et Réponse Biologique d'Escherichia Coli et de Candida Albicans Sur Des Biomatériaux Hydratés et Non Hydratés de Différentes Élasticités, Thèse de doctorat, Université de Strasbourg, 2021.

(39) Caro, A.; Humblot, V.; Méthivier, C.; Minier, M.; Salmain, M.; Pradier, C.-M. Grafting of Lysozyme and/or Poly(Ethylene Glycol) to Prevent Biofilm Growth on Stainless Steel Surfaces. *Journal of Physical Chemistry. B* **2009**, *113* (7), 2101–2109. https://doi.org/10.1021/jp805284s.

(40) Kubiak, K. J.; Wilson, M. C. T.; Mathia, T. G.; Carval, Ph. Wettability versus Roughness of Engineering Surfaces. *Wear* **2011**, *271* (3), 523–528. https://doi.org/10.1016/j.wear.2010.03.029.

(41) Marchand, P.; Hassan, I. A.; Parkin, I. P.; Carmalt, C. J. Aerosol-Assisted Delivery of Precursors for Chemical Vapour Deposition: Expanding the Scope of CVD for Materials Fabrication. *Dalton Transactions.* **2013**, *42* (26), 9406. https://doi.org/10.1039/c3dt50607j.

(42) Drelich, J.; Chibowski, E.; Desheng Meng, D.; Terpilowski, K. Hydrophilic and Superhydrophilic Surfaces and Materials. *Soft Matter* **2011**, *7* (21), 9804–9828. https://doi.org/10.1039/C1SM05849E.

(43) Wenzel, R. N. Resistance of solid surfaces to wetting by water. *Industrial and Engineering Chemistry.* **1936**, *28* (8), 988–994. https://doi.org/10.1021/ie50320a024.

(44) Belaud, V.; Valette, S.; Stremsdoerfer, G.; Bigerelle, M.; Benayoun, S. Wettability versus Roughness: Multi-Scales Approach. *Tribology International.* **2015**, *82*, 343–349. https://doi.org/10.1016/j.triboint.2014.07.002.

(45) Ensikat, H. J.; Ditsche-Kuru, P.; Neinhuis, C.; Barthlott, W. Superhydrophobicity in Perfection: The Outstanding Properties of the Lotus Leaf. *Beilstein Journal of Nanotechnology.* **2011**, *2*, 152–161. https://doi.org/10.3762/bjnano.2.19.

(46) Bhushan, B.; Jung, Y. C.; Koch, K. Micro-, Nano- and Hierarchical Structures for Superhydrophobicity, Self-Cleaning and Low Adhesion. *Philosophical Transactions of the Royal Society: Mathematical Physical and Engineering Science.* **2009**, *367* (1894), 1631–1672. https://doi.org/10.1098/rsta.2009.0014.

(47) Sun, M.; Watson, G. S.; Zheng, Y.; Watson, J. A.; Liang, A. Wetting Properties on Nanostructured Surfaces of Cicada Wings. *Journal of Experimental Biology.* **2009**, *212* (19), 3148–3155. https://doi.org/10.1242/jeb.033373.

(48) Feng, X. J.; Jiang, L. Design and Creation of Superwetting/Antiwetting Surfaces. *Advanced Materials.* **2006**, *18* (23), 3063–3078. https://doi.org/10.1002/adma.200501961.

(49) Armstrong, R. E.; Drapeau, M. D.; Loeb, C. A.; Valdes, J. J. *Bio-Inspired Innovation and National Security*; Washington, DC: NDU Press, 2010.

(50) Barthlott, W.; Neinhuis, C. Purity of the Sacred Lotus, or Escape from Contamination in Biological Surfaces. *Planta* **1997**, *202* (1), 1–8. https://doi.org/10.1007/s004250050096.
(51) Lee, H. J.; Willis, C. R.; Stone, C. A. Modeling and Preparation of a Super-Oleophobic Non-Woven Fabric. *Journal of Materials Science.* **2011**, *46* (11), 3907–3913. https://doi.org/10.1007/s10853-011-5314-1.
(52) Koch, K.; Bhushan, B.; Barthlott, W. Multifunctional Surface Structures of Plants: An Inspiration for Biomimetics. *Progress in Materials Science.* **2009**, *54* (2), 137–178. https://doi.org/10.1016/j.pmatsci.2008.07.003.
(53) Bhushan, B. Biomimetics: Lessons from Nature–an Overview. *Philosophical Transactions of the Royal Society Mathematical Physical and Engineering Science.* **2009**, *367* (1893), 1445–1486. https://doi.org/10.1098/rsta.2009.0011.
(54) Bormashenko, E.; Bormashenko, Y.; Stein, T.; Whyman, G.; Bormashenko, E. Why Do Pigeon Feathers Repel Water? Hydrophobicity of Pennae, Cassie–Baxter Wetting Hypothesis and Cassie–Wenzel Capillarity-Induced Wetting Transition. *Journal of Colloid and Interface Science.* **2007**, *311* (1), 212–216. https://doi.org/10.1016/j.jcis.2007.02.049.
(55) Choi, W.; Lee, C.; Yoo, C. H.; Shin, M. G.; Lee, G. W.; Kim, T.-S.; Jung, H. W.; Lee, J. S.; Lee, J.-H. Structural Tailoring of Sharkskin-Mimetic Patterned Reverse Osmosis Membranes for Optimizing Biofouling Resistance. *Journal of Membrane Science.* **2020**, *595*, 117602. https://doi.org/10.1016/j.memsci.2019.117602.
(56) Zhang, L.; Zhao, N.; Xu, J. Fabrication and Application of Superhydrophilic Surfaces: A Review. *Journal of Adhesion Science and Technology.* **2012**, *28* (8–9), 769–790. https://doi.org/10.1080/01694243.2012.697714.
(57) Ueda, E.; Levkin, P. A. Emerging Applications of Superhydrophilic-Superhydrophobic Micropatterns. *Advanced Materials.* **2013**, *25* (9), 1234–1247. https://doi.org/10.1002/adma.201204120.
(58) Wang, S.; Qiu, B.; Shi, J.; Wang, M. Quaternary Ammonium Antimicrobial Agents and Their Application in Antifouling Coatings: A Review. *Journal of Coatings Technology and Research.* **2024**, *21* (1), 87–103. https://doi.org/10.1007/s11998-023-00825-z.
(59) Sakala, G. P.; Reches, M. Peptide-Based Approaches to Fight Biofouling. *Advanced Materials and Interfaces* **2018**, *5* (18), 1800073. https://doi.org/10.1002/admi.201800073.
(60) Moazzam, P.; Razmjou, A.; Golabi, M.; Shokri, D.; Landarani-Isfahani, A. Investigating the BSA Protein Adsorption and Bacterial Adhesion of Al-Alloy Surfaces after Creating a Hierarchical (Micro/Nano) Superhydrophobic Structure. *Journal of Biomedical Materials Research. A* **2016**, *104* (9), 2220–2233. https://doi.org/10.1002/jbm.a.35751.
(61) Mandal, P.; Ivvala, J.; Arora, H. S.; Ghosh, S. K.; Grewal, H. S. Bioinspired Micro/Nano Structured Aluminum with Multifaceted Applications. *Colloids and Surfaces. B Biointerfaces* **2022**, *211*, 112311. https://doi.org/10.1016/j.colsurfb.2021.112311.
(62) Mandal, P.; Shishodia, A.; Ali, N.; Ghosh, S.; Arora, H. S.; Grewal, H. S.; Ghosh, S. K. Effect of Topography and Chemical Treatment on the Hydrophobicity and Antibacterial Activities of Micropatterned Aluminium Surfaces. *Surface Topography: Metrology and Properties.* **2020**, *8* (2), 025017. https://doi.org/10.1088/2051-672X/ab8d86.
(63) Chen, F.; Zhang, D.; Yang, Q.; Yong, J.; Du, G.; Si, J.; Yun, F.; Hou, X. Bioinspired Wetting Surface via Laser Microfabrication. *ACS Applied Materials and Interfaces* **2013**, *5* (15), 6777–6792. https://doi.org/10.1021/am401677z.
(64) Vorobyev, A. Y.; Guo, C. Direct Femtosecond Laser Surface Nano/Microstructuring and Its Applications. *Laser Photonics Reviews.* **2013**, *7* (3), 385–407. https://doi.org/10.1002/lpor.201200017.
(65) Li, S.; Liu, Y.; Zheng, Z.; Liu, X.; Huang, H.; Han, Z.; Ren, L. Biomimetic Robust Superhydrophobic Stainless-Steel Surfaces with Antimicrobial Activity and Molecular Dynamics Simulation. *Chemical Engineering Journal.* **2019**, *372*, 852–861. https://doi.org/10.1016/j.cej.2019.04.200.

(66) Tuo, Y.; Zhang, H.; Chen, L.; Chen, W.; Liu, X.; Song, K. Fabrication of Superamphiphobic Surface with Hierarchical Structures on Metal Substrate. *Colloids and Surfaces A: Physicochemical Engineering Aspects.* **2021**, *612*, 125983. https://doi.org/10.1016/j.colsurfa.2020.125983.

(67) Bao, Y.; Fu, W.; Xu, H.; Chen, Y.; Zhang, H.; Chen, S. Bioinspired Self-Cleaning Surface with Microflower-like Structures Constructed by Electrochemically Corrosion Mediated Self-Assembly. *CrystEngComm* **2022**, *24* (5), 1085–1093. https://doi.org/10.1039/D1CE01267C.

(68) Lee, J.; Jiang, Y.; Hizal, F.; Ban, G.-H.; Jun, S.; Choi, C.-H. Durable Omniphobicity of Oil-Impregnated Anodic Aluminum Oxide Nanostructured Surfaces. *Journal of Colloid and Interface Science.* **2019**, *553*, 734–745. https://doi.org/10.1016/j.jcis.2019.06.068.

(69) Hizal, F.; Rungraeng, N.; Lee, J.; Jun, S.; Busscher, H. J.; van der Mei, H. C.; Choi, C.-H. Nanoengineered Superhydrophobic Surfaces of Aluminum with Extremely Low Bacterial Adhesivity. *ACS Applied Materials and Interfaces* **2017**, *9* (13), 12118–12129. https://doi.org/10.1021/acsami.7b01322.

(70) Chang, X.; Li, M.; Tang, S.; Shi, L.; Chen, X.; Niu, S.; Zhu, X.; Wang, D.; Sun, S. Superhydrophobic Micro-Nano Structured PTFE/WO3 Coating on Low-Temperature Steel with Outstanding Anti-Pollution, Anti-Icing, and Anti-Fouling Performance. *Surface and Coatings Technology.* **2022**, *434*, 128214. https://doi.org/10.1016/j.surfcoat.2022.128214.

(71) Ouyang, Y.; Zhao, J.; Qiu, R.; Hu, S.; Chen, M.; Wang, P. Liquid-Infused Superhydrophobic Dendritic Silver Matrix: A Bio-Inspired Strategy to Prohibit Biofouling on Titanium. *Surface and Coatings Technology.* **2019**, *367*, 148–155. https://doi.org/10.1016/j.surfcoat.2019.03.067.

(72) Chen, T.; Lin, Y.; Chien, C.; Chen, Y.; Yang, Y.; Wang, W.; Chien, L.; Hsueh, H. Fabrication of Frog-Skin-Inspired Slippery Antibiofouling Coatings Through Degradable Block Copolymer Wrinkling. *Advanced Functional Materials.* **2021**, 2104173. https://doi.org/10.1002/adfm.202104173.

(73) Ware, C. S.; Smith-Palmer, T.; Peppou-Chapman, S.; Scarratt, L. R. J.; Humphries, E. M.; Balzer, D.; Neto, C. Marine Antifouling Behavior of Lubricant-Infused Nanowrinkled Polymeric Surfaces. *ACS Applied Materials and Interfaces* **2018**, *10* (4), 4173–4182. https://doi.org/10.1021/acsami.7b14736.

(74) Fang, Y.; Yong, J.; Cheng, Y.; Yang, Q.; Hou, X.; Chen, F. Liquid-Infused Slippery Stainless Steel Surface Prepared by Alcohol-Assisted Femtosecond Laser Ablation. *Adv Materials and Interfaces* **2021**, *8*, 2001334. https://doi.org/10.1002/admi.202001334.

(75) Li, J.; Yuan, T.; Zhou, C.; Chen, B.; Shuai, Y.; Wu, D.; Chen, D.; Luo, X.; Cheng, Y. F.; Liu, Y. Facile Li-Al Layered Double Hydroxide Films on Al Alloy for Enhanced Hydrophobicity, Anti-Biofouling and Anti-Corrosion Performance. *Journal of Materials Science and Technology.* **2021**, *79*, 230–242. https://doi.org/10.1016/j.jmst.2020.10.072.

(76) Selim, M. S.; El-Safty, S. A.; Fatthallah, N. A.; Shenashen, M. A. Silicone/Graphene Oxide Sheet-Alumina Nanorod Ternary Composite for Superhydrophobic Antifouling Coating. *Progress in Organic Coatings.* **2018**, *121*, 160–172. https://doi.org/10.1016/j.porgcoat.2018.04.021.

(77) Selim, M. S.; Yang, H.; Wang, F. Q.; Fatthallah, N. A.; Huang, Y.; Kuga, S. Silicone/ZnO Nanorod Composite Coating as a Marine Antifouling Surface. *Applied Surface Science.* **2019**, *466*, 40–50. https://doi.org/10.1016/j.apsusc.2018.10.004.

(78) Wang, T.; Huang, L.; Liu, Y.; Li, X.; Liu, C.; Handschuh-Wang, S.; Xu, Y.; Zhao, Y.; Tang, Y. Robust Biomimetic Hierarchical Diamond Architecture with a Self-Cleaning, Antibacterial, and Antibiofouling Surface. *ACS Applied Materials and Interfaces* **2020**, *12* (21), 24432–24441. https://doi.org/10.1021/acsami.0c02460.

(79) Bruzaud, J.; Tarrade, J.; Celia, E.; Darmanin, T.; Taffin de Givenchy, E.; Guittard, F.; Herry, J.-M.; Guilbaud, M.; Bellon-Fontaine, M.-N. The Design of Superhydrophobic Stainless Steel Surfaces by Controlling Nanostructures: A Key Parameter to Reduce the Implantation of Pathogenic Bacteria | Elsevier Enhanced Reader. *Materials Science and Engineering C* **2017**, *73*, 40–47. https://doi.org/10.1016/j.msec.2016.11.115.

(80) Lee, Y.; Chung, Y.-W.; Park, J.; Park, K.; Seo, Y.; Hong, S.-N.; Lee, S. H.; Jeon, H.; Seo, J. Lubricant-Infused Directly Engraved Nano-Microstructures for Mechanically Durable Endoscope Lens with

Anti-Biofouling and Anti-Fogging Properties. *Scientific Reports.* **2020**, *10* (1), 17454. https://doi.org/10.1038/s41598-020-74517-8.

(81) Jiang, R.; Hao, L.; Song, L.; Tian, L.; Fan, Y.; Zhao, J.; Liu, C.; Ming, W.; Ren, L. Lotus-Leaf-Inspired Hierarchical Structured Surface with Non-Fouling and Mechanical Bactericidal Performances | Elsevier Enhanced Reader. *Chemical Engineering Journal* **2020**, *398*, 125609. https://doi.org/10.1016/j.cej.2020.125609.

(82) Dolid, A.; Gomes, L. C.; Mergulhão, F. J.; Reches, M. Combining Chemistry and Topography to Fight Biofilm Formation: Fabrication of Micropatterned Surfaces with a Peptide-Based Coating. *Colloids and Surfaces B Biointerfaces* **2020**, *196*, 111365. https://doi.org/10.1016/j.colsurfb.2020.111365.

(83) Yoo, C. H.; Lee, G. W.; Choi, W.; Shin, M. G.; Lee, C.; Shin, J. H.; Son, Y.; Chun, B.; Lee, J.-H.; Jung, H. W.; Lee, J. S. Identifying the Colloidal Fouling Behavior on the Sharkskin-Mimetic Surface: In-Situ Monitoring and Lattice Boltzmann Simulation. *Chemical Engineering Journal* **2021**, *405*, 126617. https://doi.org/10.1016/j.cej.2020.126617.

(84) Choi, W.; Lee, C.; Lee, D.; Won, Y. J.; Lee, G. W.; Shin, M. G.; Chun, B.; Kim, T.-S.; Park, H.-D.; Jung, H. W.; Lee, J. S.; Lee, J.-H. Sharkskin-Mimetic Desalination Membranes with Ultralow Biofouling. *Journal of Materials Chemistry. A* **2018**, *6* (45), 23034–23045. https://doi.org/10.1039/C8TA06125D.

(85) Kefallinou, D.; Ellinas, K.; Speliotis, T.; Stamatakis, K.; Gogolides, E.; Tserepi, A. Optimization of Antibacterial Properties of "Hybrid" Metal-Sputtered Superhydrophobic Surfaces. *Coatings* **2020**, *10* (1), 25. https://doi.org/10.3390/coatings10010025.

(86) Wu, Q.; Liu, D.; Chen, W.; Chen, H.; Yang, C.; Li, X.; Yang, C.; Lin, H.; Chen, S.; Hu, N.; Chen, W.; Xie, X. Liquid-like Layer Coated Intraocular Lens for Posterior Capsular Opacification Prevention. *Applied Materials. Today* **2021**, *23*, 100981. https://doi.org/10.1016/j.apmt.2021.100981.

(87) Zaggia, A.; Ameduri, B. Recent Advances on Synthesis of Potentially Non-Bioaccumulable Fluorinated Surfactants. *Current Opinion in Colloid and Interface Science.* **2012**, *17* (4), 188–195. https://doi.org/10.1016/j.cocis.2012.04.001.

(88) An, R.; Dong, Y.; Zhu, J.; Rao, C. Adhesion and Friction Forces in Biofouling Attachments to Nanotube- and PEG- Patterned TiO2 Surfaces. *Colloids and Surfaces B Biointerfaces* **2017**, *159*, 108–117. https://doi.org/10.1016/j.colsurfb.2017.07.067.

(89) Ren, X.; Guo, M.; Xue, L.; Zeng, Q.; Gao, X.; Xin, Y.; Xu, L.; Li, L. A Self-Cleaning Mucus-like and Hierarchical Ciliary Bionic Surface for Marine Antifouling. *Advanced Engineering Materials.* **2020**, *22* (5), 1901198. https://doi.org/10.1002/adem.201901198.

(90) Lou, T.; Bai, X.; He, X.; Yuan, C. Antifouling Performance Analysis of Peptide-Modified Glass Microstructural Surfaces. *Applied Surface Science.* **2020**, 148384. https://doi.org/10.1016/j.apsusc.2020.148384.

(91) Yu, X.; Yang, W.; Yang, Y.; Wang, X.; Liu, X.; Zhou, F.; Zhao, Y. Subsurface-Initiated Atom Transfer Radical Polymerization: Effect of Graft Layer Thickness and Surface Morphology on Antibiofouling Properties against Different Foulants. *Journal of Materials Science.* **2020**, *55* (29), 14544–14557. https://doi.org/10.1007/s10853-020-05055-x.

(92) Liu, H.; Ma, Z.; Yang, W.; Pei, X.; Zhou, F. Facile Preparation of Structured Zwitterionic Polymer Substrate via Sub-Surface Initiated Atom Transfer Radical Polymerization and Its Synergistic Marine Antifouling Investigation. *European Polymer Journal.* **2019**, *112*, 146–152. https://doi.org/10.1016/j.eurpolymj.2018.07.025.

(93) Zhang, Y.; Hu, H.; Pei, X.; Liu, Y.; Ye, Q.; Zhou, F. Polymer Brushes on Structural Surfaces: A Novel Synergistic Strategy for Perfectly Resisting Algae Settlement. *Biomaterials Science.* **2017**, 8.

(94) Brzozowska, A. M.; Parra-Velandia, F. J.; Quintana, R.; Xiaoying, Z.; Lee, S. S. C.; Chin-Sing, L.; Jańczewski, D.; Teo, S. L.-M.; Vancso, J. G. Biomimicking Micropatterned Surfaces and Their Effect on Marine Biofouling. *Langmuir* **2014**, *30* (30), 9165–9175. https://doi.org/10.1021/la502006s.

(95) Zhao, L.; Chen, R.; Lou, L.; Jing, X.; Liu, Q.; Liu, J.; Yu, J.; Liu, P.; Wang, J. Layer-by-Layer-Assembled Antifouling Films with Surface Microtopography Inspired by Laminaria Japonica. *Applied Surface Science.* **2020**, *511*, 145564. https://doi.org/10.1016/j.apsusc.2020.145564.

(96) Weinman, S. T.; Husson, S. M. Influence of Chemical Coating Combined with Nanopatterning on Alginate Fouling during Nanofiltration. *Journal of Membrane Science.* **2016**, *513*, 146–154. https://doi.org/10.1016/j.memsci.2016.04.025.

(97) Choi, W.; Chan, E. P.; Park, J.-H.; Ahn, W.-G.; Jung, H. W.; Hong, S.; Lee, J. S.; Han, J.-Y.; Park, S.; Ko, D.-H.; Lee, J.-H. Nanoscale Pillar-Enhanced Tribological Surfaces as Antifouling Membranes. *ACS Applied Materials and Interfaces* **2016**, *8* (45), 31433–31441. https://doi.org/10.1021/acsami.6b10875.

(98) Choi, W.; Shin, M. G.; Yoo, C. H.; Park, H.; Park, Y.-I.; Lee, J. S.; Lee, J.-H. Desalination Membranes with Ultralow Biofouling via Synergistic Chemical and Topological Strategies. *Journal of Membrane Sci.* **2021**, *626*, 119212. https://doi.org/10.1016/j.memsci.2021.119212.

(99) Aguilar-Sanchez, A.; Jalvo, B.; Mautner, A.; Rissanen, V.; Kontturi, K. S.; Abdelhamid, H. N.; Tammelin, T.; Mathew, A. P. Charged Ultrafiltration Membranes Based on TEMPO-Oxidized Cellulose Nanofibrils/Poly(Vinyl Alcohol) Antifouling Coating. *RSC Advances.* **2021**, *11* (12), 6859–6868. https://doi.org/10.1039/D0RA10220B.

(100) Lin, B.; Tan, H.; Liu, W.; Gao, C.; Pan, Q. Preparation of a Novel Zwitterionic Striped Surface Thin-Film Composite Nanofiltration Membrane with Excellent Salt Separation Performance and Antifouling Property. *RSC Advances.* **2020**, *10*, 16168.

(101) Sun, M.; Wu, Q.; Xu, J.; He, F.; Brown, A. P.; Ye, Y. Vapor-Based Grafting of Crosslinked Poly(N-Vinyl Pyrrolidone) Coatings with Tuned Hydrophilicity and Anti-Biofouling Properties. Journal of Materials Chemistry. B 2016, 4 (15), 2669–2678. https://doi.org/10.1039/C6TB00076B.

(102) Ma, Z.; Liang, S.; Wang, X.; Xiao, K.; Li, M.; Huang, X. Superhydrophilic Polyvinylidene Fluoride Membrane with Hierarchical Surface Structures Fabricated via Nanoimprint and Nanoparticle Grafting | Elsevier Enhanced Reader. Journal of Membrane Science. 2020, 612, 118332. https://doi.org/10.1016/j.memsci.2020.118332.

(103) Park, H.-H.; Sun, K.; Lee, D.; Seong, M.; Cha, C.; Jeong, H. E. Cellulose Acetate Nanoneedle Array Covered with Phosphorylcholine Moiety as a Biocompatible and Sustainable Antifouling Material. *Cellulose* **2019**, *26* (16), 8775–8788. https://doi.org/10.1007/s10570-019-02681-w.

(104) Park, H.-H.; Sun, K.; Seong, M.; Kang, M.; Park, S.; Hong, S.; Jung, H.; Jang, J.; Kim, J.; Jeong, H. E. Lipid-Hydrogel-Nanostructure Hybrids as Robust Biofilm-Resistant Polymeric Materials. *ACS Macro Letters.* **2019**, *8* (1), 64–69. https://doi.org/10.1021/acsmacrolett.8b00888.

(105) Choi, G.; Song, Y.; Lim, H.; Lee, S. H.; Lee, H. K.; Lee, E.; Choi, B. G.; Lee, J. J.; Im, S. G.; Lee, K. G. Antibacterial Nanopillar Array for an Implantable Intraocular Lens. *Advanced Healthcare Materials.* **2020**, *9* (18), 2000447. https://doi.org/10.1002/adhm.202000447.

(106) Chen, C.; Enrico, A.; Pettersson, T.; Ek, M.; Herland, A.; Niklaus, F.; Stemme, G.; Wagberg, L. Bactericidal Surfaces Prepared by Femtosecond Laser Patterning and Layer-by-Layer Polyelectrolyte Coating | Elsevier Enhanced Reader. *Journal of Colloid and Interface Science.* **2020**, *575*, 286–297. https://doi.org/10.1016/j.jcis.2020.04.107.

(107) González-Henríquez, C. M.; Rodríguez-Umanzor, F. E.; Alegría-Gómez, M. N.; Terraza-Inostroza, C. A.; Martínez-Campos, E.; Cue-López, R.; Sarabia-Vallejos, M. A.; García-Herrera, C.; Rodríguez-Hernández, J. Wrinkling on Stimuli-Responsive Functional Polymer Surfaces as a Promising Strategy for the Preparation of Effective Antibacterial/Antibiofouling Surfaces. *Polymers* **2021**, *13* (23), 4262. https://doi.org/10.3390/polym13234262.

(108) Maan, A. M. C.; Hofman, A. H.; Vos, W. M. de; Kamperman, M. Recent Developments and Practical Feasibility of Polymer-Based Antifouling Coatings. *Advanced Functional Materials.* **2020**, *30* (32), 2000936. https://doi.org/10.1002/adfm.202000936.

(109) Wang, Z.; DeWitt, J. C.; Higgins, C. P.; Cousins, I. T. A Never-Ending Story of Per- and Polyfluoroalkyl Substances (PFASs)? *Environmental Science and Technology.* **2017**, *51* (5), 2508–2518. https://doi.org/10.1021/acs.est.6b04806.

(110) Kobono, A.; Okui, N. Polymer Thin Films Prepared by Vapor Deposition. *Progress in Polymer Science.* **1994**, *19*, 389–438.

(111) Frederichi, D.; Scaliante, M. H. N. O.; Bergamasco, R. Structured Photocatalytic Systems: Photocatalytic Coatings on Low-Cost Structures for Treatment of Water Contaminated with

Micropollutants—a Short Review. *Environmental Science and Pollution Research.* **2021**, *28* (19), 23610–23633. https://doi.org/10.1007/s11356-020-10022-9.

(112) Norrman, K.; Ghanbari-Siahkali, A.; Larsen, N. B. 6 Studies of Spin-Coated Polymer Films. *Annual Reports Section C Physical Chemistry.* **2005**, *101*, 174. https://doi.org/10.1039/b408857n.

(113) H. Rajawasam, C. W.; J. Dodo, O.; N. Weerasinghe, M. A. S.; O. Raji, I.; V. Wanasinghe, S.; Konkolewicz, D.; Watuthanthrige, N. D. A. Educational Series: Characterizing Crosslinked Polymer Networks. *Polymer Chemistry.* **2024**, *15* (4), 219–247. https://doi.org/10.1039/D3PY00914A.

(114) Marshall, J. E.; Zhenova, A.; Roberts, S.; Petchey, T.; Zhu, P.; Dancer, C. E. J.; McElroy, C. R.; Kendrick, E.; Goodship, V. On the Solubility and Stability of Polyvinylidene Fluoride. *Polymers* **2021**, *13* (9), 1354. https://doi.org/10.3390/polym13091354.

(115) *Spin Coating - Fundamentals of Perovskite Oxides: Synthesis, Structure, Properties and Applications*. Ebrary. https://ebrary.net/191967/engineering/spin_coating (accessed 2024-02-21).

(116) Obregón, S.; Rodríguez-González, V. Photocatalytic TiO2 Thin Films and Coatings Prepared by Sol–Gel Processing: A Brief Review. *Journal of Sol-Gel Science and Technology.* **2022**, *102* (1), 125–141. https://doi.org/10.1007/s10971-021-05628-5.

(117) Castagnola, V.; Bayon, C.; Descamps, E.; Bergaud, C. Morphology and Conductivity of PEDOT Layers Produced by Different Electrochemical Routes. *Synthetic Metals.* **2014**, *189*, 7–16. https://doi.org/10.1016/j.synthmet.2013.12.013.

(118) Sanchez-Sanchez, A.; Del Agua, I.; Malliaras, G. G.; Mecerreyes, D. Conductive Poly(3,4-Ethylenedioxythiophene) (PEDOT)-Based Polymers and Their Applications in Bioelectronics. In *Smart Polymers and their Applications*; Elsevier, **2019**; pp 191–218. https://doi.org/10.1016/B978-0-08-102416-4.00006-5.

(119) Mousavi, H.; Ferrari, L. M.; Whiteley, A.; Ismailova, E. Kinetics and Physicochemical Characteristics of Electrodeposited PEDOT:PSS Thin Film Growth. *Advanced Electronic Materials.* **2023**, *9* (9), 2201282. https://doi.org/10.1002/aelm.202201282.

(120) Khan, Z. U.; Bubnova, O.; Jafari, M. J.; Brooke, R.; Liu, X.; Gabrielsson, R.; Ederth, T.; Evans, D. R.; Andreasen, J. W.; Fahlman, M.; Crispin, X. Acido-Basic Control of the Thermoelectric Properties of Poly(3,4-Ethylenedioxythiophene)Tosylate (PEDOT-Tos) Thin Films. *Journal of Materials Chemistry. C* **2015**, *3* (40), 10616–10623. https://doi.org/10.1039/C5TC01952D.

(121) Heinze, J.; Frontana-Uribe, B. A.; Ludwigs, S. Electrochemistry of Conducting Polymers—Persistent Models and New Concepts. *Chemical Reviews.* **2010**, *110* (8), 4724–4771. https://doi.org/10.1021/cr900226k.

(122) Zhao, L.; Ma, Z. Facile Synthesis of Polyaniline-Polythionine Redox Hydrogel: Conductive, Antifouling and Enzyme-Linked Material for Ultrasensitive Label-Free Amperometric Immunosensor toward Carcinoma Antigen-125. *Analytica Chimica Acta* **2018**, *997*, 60–66. https://doi.org/10.1016/j.aca.2017.10.017.

(123) Coclite, A. M.; Howden, R. M.; Borrelli, D. C.; Petruczok, C. D.; Yang, R.; Yagüe, J. L.; Ugur, A.; Chen, N.; Lee, S.; Jo, W. J.; Liu, A.; Wang, X.; Gleason, K. K. 25th Anniversary Article: CVD Polymers: A New Paradigm for Surface Modifi Cation and Device Fabrication. *Advanced Materials.* **2013**, *25* (38), 5392–5423. https://doi.org/10.1002/adma.201301878.

(124) Szwarc, M. Some Remarks on the CH2[Graphic Omitted]CH2 Molecule. *Discussions of the Faraday Society.* **1947**, *2* (0), 46–49. https://doi.org/10.1039/DF9470200046.

(125) Gorham, W. F. A New, General Synthetic Method for the Preparation of Linear Poly- *p* -xylylenes. *Journal of Polymer Science [A1]* **1966**, *4* (12), 3027–3039. https://doi.org/10.1002/pol.1966.150041209.

(126) VSi Parylene. The Complete Guide to Parylene Coatings.

(127) Kuppusami, S.; Oskouei, R. H. Parylene Coatings in Medical Devices and Implants: A Review. *Univers. Journal of Biomedical Engineering.* **2015**, *3* (2), 9–14. https://doi.org/10.13189/ujbe.2015.030201.

(128) Bing, W.; Cai, Y.; Jin, H.; Tian, L.; Tian, L.; Yin, Y.; Teng, Y.; Wang, P.; Hou, Z.; Bai, X. An Antiadhesion and Antibacterial Platform Based on Parylene F Coatings. *Progress on Organic Coatings.* **2021**, *151*, 106021. https://doi.org/10.1016/j.porgcoat.2020.106021.

(129) Han, B.; Wang, H.; Bing, W.; Jin, H. Bacterial Adhesion Properties of Parylene C and D Deposited on Polydimethylsiloxane. *New Journal of Chemistry.* **2022**, *46* (18), 8773–8778. https://doi.org/10.1039/D1NJ06223A.

(130) Takahashi, Y.; Iijima, M.; Inagawa, K.; Itoh, A. Synthesis of Aromatic Polyimide Film by Vacuum Deposition Polymerization. *Journal of Vacuum Science and Technology. A* **1987**, *5* (4), 2253–2256. https://doi.org/10.1116/1.574429.

(131) Salem, J. R.; Sequeda, F. O.; Duran, J.; Lee, W. Y.; Yang, R. M. Solventless Polyimide Films by Vapor Deposition. *Journal of Vacuum Science and Technology. A* **1986**, *4* (3), 369–374. https://doi.org/10.1116/1.573930.

(132) Takahashi, Y.; Iijima, M.; Oishi, Y.; Kakimoto, M.; Imai, Y. Preparation of Ultrathin Films of Aromatic Polyamides and Aromatic Poly(Amide-Imides) by Vapor Deposition Polymerization. *Macromolecules* **1991**, *24* (12), 3543–3546. https://doi.org/10.1021/ma00012a013.

(133) Iijima, M.; Takahashi, Y. Vapor Deposition Polymerization: A Study on Film Formation in Reaction of Pyromellitic Anhydride and Bis(4-Aminophenyl) Ether. *Macromolecules* **1989**, *22* (7), 2944–2946. https://doi.org/10.1021/ma00197a011.

(134) Weaver, M. S.; Bradley, D. D. C. Organic Electroluminescence Devices Fabricated with Chemical Vapour Deposited Polyazomethine Films. *Synthetic Metals.* **1996**, *83* (1), 61–66. https://doi.org/10.1016/S0379-6779(97)80053-7.

(135) Zhao, J.; Gleason, K. K. Solvent-Less Vapor-Phase Fabrication of Membranes for Sustainable Separation Processes. *Engineering* **2020**, *6* (12), 1432–1442. https://doi.org/10.1016/j.eng.2020.05.002.

(136) Irikura, H.; Hasegawa, Y.; Takahashi, Y. Preparation of Antibacterial Polyimide Film by Vapor Deposition Polymerization. *Journal of Photopolymer Science and Technology.* **2003**, *16* (2), 273–276. https://doi.org/10.2494/photopolymer.16.273.

(137) Pryce Lewis, H. G.; Edell, D. J.; Gleason, K. K. Pulsed-PECVD Films from Hexamethylcyclotrisiloxane for Use as Insulating Biomaterials. *Chemistry of Materials.* **2000**, *12* (11), 3488–3494. https://doi.org/10.1021/cm0003370.

(138) Zhianmanesh, M.; Gilmour, A.; Bilek, M. M. M.; Akhavan, B. Plasma Surface Functionalization: A Comprehensive Review of Advances in the Quest for Bioinstructive Materials and Interfaces. *Applied Physics Review.* **2023**, *10* (2), 021301. https://doi.org/10.1063/5.0130829.

(139) Macgregor-Ramiasa, M. N.; Cavallaro, A. A.; Vasilev, K. Properties and Reactivity of Polyoxazoline Plasma Polymer Films. *Journal of Materials Chemistry B* **2015**, *3* (30), 6327–6337. https://doi.org/10.1039/c5tb00901d.

(140) Li, D.; Gautier, N.; Dey, B.; Bulou, S.; Richard-Plouet, M.; Ravisy, W.; Goullet, A.; Choquet, P.; Granier, A. TEM Analysis of Photocatalytic TiO2 Thin Films Deposited on Polymer Substrates by Low-Temperature ICP-PECVD. *Applied Surface Science.* **2019**, *491*, 116–122. https://doi.org/10.1016/j.apsusc.2019.06.045.

(141) Han, L. M.; Pan, J.-S.; Chen, S.-M.; Balasubramanian, N.; Shi, J.; Wong, L. S.; Foo, P. D. Characterization of Carbon-Doped SiO[Sub 2] Low k Thin Films: Preparation by Plasma-Enhanced Chemical Vapor Deposition from Tetramethylsilane. *Journal of the Electrochemical Society.* **2001**, *148* (7), F148. https://doi.org/10.1149/1.1375797.

(142) Supiot, P.; Vivien, C.; Granier, A.; Bousquet, A.; Mackova, A.; Escaich, D.; Clergereaux, R.; Raynaud, P.; Stryhal, Z.; Pavlik, J. Growth and Modification of Organosilicon Films in PECVD and Remote Afterglow Reactors. *Plasma Processes and Polymers.* **2006**, *3* (2), 100–109. https://doi.org/10.1002/ppap.200500154.

(143) Cavallaro, A. A.; Macgregor-Ramiasa, M. N.; Vasilev, K. Antibiofouling Properties of Plasma-Deposited Oxazoline-Based Thin Films. *ACS Applied Materials and Interfaces* **2016**, *8* (10), 6354–6362. https://doi.org/10.1021/acsami.6b00330.

(144) Khider, D.; Rossi-Fedele, G.; Fitzsimmons, T.; Vasilev, K.; Zilm, P. S. Disruption of Enterococcus Faecalis Biofilms Using Individual and Plasma Polymer Encapsulated D-Amino Acids. *Clinical Oral Investigations.* **2021**, *25* (5), 3305–3313. https://doi.org/10.1007/s00784-020-03663-0.

(145) Cavallaro, A.; Vasilev, K. Controlled and Sustained Release of Pharmaceuticals via Single Step Solvent-Free Encapsulation. *Chemical Communications.* **2015**, *51* (10), 1838–1841. https://doi.org/10.1039/C4CC08151J.

(146) Bazaka, K.; Jacob, M. V. Synthesis of Radio Frequency Plasma Polymerized Non-Synthetic Terpinen-4-Ol Thin Films. *Materials Letters.* **2009**, *63* (18–19), 1594–1597. https://doi.org/10.1016/j.matlet.2009.04.025.

(147) Kumar, A.; Al-Jumaili, A.; Prasad, K.; Bazaka, K.; Mulvey, P.; Warner, J.; Jacob, M. V. Pulse Plasma Deposition of Terpinen-4-Ol: An Insight into Polymerization Mechanism and Enhanced Antibacterial Response of Developed Thin Films. *Plasma Chemistry and Plasma Processes.* **2020**, *40* (1), 339–355. https://doi.org/10.1007/s11090-019-10045-2.

(148) Al-Jumaili, A.; Bazaka, K.; Jacob, M. V. Retention of Antibacterial Activity in Geranium Plasma Polymer Thin Films. *Nanomaterials* **2017**, *7* (9), 270. https://doi.org/10.3390/nano7090270.

(149) Romo-Rico, J.; Murali Krishna, S.; Golledge, J.; Hayles, A.; Vasilev, K.; Jacob, M. V. Plasma Polymers from Oregano Secondary Metabolites: Antibacterial and Biocompatible Plant-Based Polymers. *Plasma Processes and Polymers.* **2022**, *19* (7), 2100220. https://doi.org/10.1002/ppap.202100220.

(150) Merche, D.; Vandencasteele, N.; Reniers, F. Atmospheric Plasmas for Thin Film Deposition: A Critical Review. *Thin Solid Films* **2012**, *520* (13), 4219–4236. https://doi.org/10.1016/j.tsf.2012.01.026.

(151) Kogelschatz, U. Dielectric-Barrier Discharges: Their History, Discharge Physics, and Industrial Applications. *Plasma Chemistry and Plasma Processing.* **2003**, *23* (1), 1–46. https://doi.org/10.1023/A:1022470901385.

(152) Morent, R.; De Geyter, N.; Van Vlierberghe, S.; Dubruel, P.; Leys, C.; Gengembre, L.; Schacht, E.; Payen, E. Deposition of HMDSO-Based Coatings on PET Substrates Using an Atmospheric Pressure Dielectric Barrier Discharge. *Progress in Organic Coatings.* **2009**, *64* (2–3), 304–310. https://doi.org/10.1016/j.porgcoat.2008.07.030.

(153) Borek-Donten, J.; Nisol, B.; Filimon, M.; Lopes, M.; Collard, D.; Chassaing, M.; Cauchie, H.-M.; Heyberger, R. The Industrial Process for Virucidal Plasma Coatings on Textiles: From Idea to Upscaling. *Plasma Processes and Polymers.* **2022**, *19* (10), 2100249. https://doi.org/10.1002/ppap.202100249.

(154) Gordeev, I.; Choukourov, A.; Šimek, M.; Prukner, V.; Biederman, H. PEO-like Plasma Polymers Prepared by Atmospheric Pressure Surface Dielectric Barrier Discharge. *Plasma Processes and Polymers.* **2012**, *9* (8), 782–791. https://doi.org/10.1002/ppap.201100213.

(155) Hubert, J.; Mertens, J.; Dufour, T.; Vandencasteele, N.; Reniers, F.; Viville, P.; Lazzaroni, R.; Raes, M.; Terryn, H. Synthesis and Texturization Processes of (Super)-Hydrophobic Fluorinated Surfaces by Atmospheric Plasma. *Journal of Materials Research.* **2015**, *30* (21), 3177–3191. https://doi.org/10.1557/jmr.2015.279.

(156) Abessolo Ondo, D.; Loyer, F.; Boscher, N. D. Influence of Double Bonds and Cyclic Structure on the AP-PECVD of Low-k Organosilicon Insulating Layers. *Plasma Processes and Polymers.* **2021**, *18* (3), 2000222. https://doi.org/10.1002/ppap.202000222.

(157) Abessolo Ondo, D.; Leturcq, R.; Boscher, N. D. Plasma-Initiated Chemical Vapour Deposition of Organosiloxane Thin Films: From the Growth Mechanisms to Ultrathin Low-k Polymer Insulating Layers. *Plasma Processes and Polymers.* **2020**, *17* (7), 2000032. https://doi.org/10.1002/ppap.202000032.

(158) Abessolo Ondo, D.; Loyer, F.; Werner, F.; Leturcq, R.; Dale, P. J.; Boscher, N. D. Atmospheric-Pressure Synthesis of Atomically Smooth, Conformal, and Ultrathin Low-k Polymer Insulating Layers by Plasma-Initiated Chemical Vapor Deposition. *ACS Applied Polymer Materials.* **2019**, *1* (12), 3304–3312. https://doi.org/10.1021/acsapm.9b00759.

(159) Laghi, G.; Franco, D.; Condorelli, G. G.; Gallerani, R.; Guglielmino, S.; Laurita, R.; Morganti, D.; Traina, F.; Conoci, S.; Gherardi, M. Control Strategies for Atmospheric Pressure Plasma

Polymerization of Fluorinated Silane Thin Films with Antiadhesive Properties. *Plasma Processes and Polymers.* **2023**, *n/a* (n/a), e2200194. https://doi.org/10.1002/ppap.202200194.

(160) Duday, D.; Vreuls, C.; Moreno, M.; Frache, G.; Boscher, N. D.; Zocchi, G.; Archambeau, C.; Van De Weerdt, C.; Martial, J.; Choquet, P. Atmospheric Pressure Plasma Modified Surfaces for Immobilization of Antimicrobial Nisin Peptides. *Surface Coating Technology.* **2013**, *218*, 152–161. https://doi.org/10.1016/j.surfcoat.2012.12.045.

(161) Mauchauffé, R.; Moreno-Couranjou, M.; Boscher, N. D.; Weerdt, C. V. D.; Duwez, A.-S.; Choquet, P. Robust Bio-Inspired Antibacterial Surfaces Based on the Covalent Binding of Peptides on Functional Atmospheric Plasma Thin Films. *Journal of Materials Chemistry B* **2014**, *2* (32), 5168–5177. https://doi.org/10.1039/C4TB00503A.

(162) Pryce Lewis, H.; Casserly, T.; Gleason, K. Hot-Filament Chemical Vapor Deposition of Organosilicon Thin Films from Hexamethylcyclotrisiloxane and Octamethylcyclotetrasiloxane. *Journal of the Electrochemical Society - J ELECTROCHEM SOC* **2001**, *148*. https://doi.org/10.1149/1.1415723.

(163) Murthy, S. K.; Olsen, B. D.; Gleason, K. K. Effect of Filament Temperature on the Chemical Vapor Deposition of Fluorocarbon–Organosilicon Copolymers. *Journal of Applied Polymer Science.* **2004**, *91* (4), 2176–2185. https://doi.org/10.1002/app.13342.

(164) Lewis, P.; Gavin), H. G. (Hilton; 1973-. Chemical Vapor Deposition Thin Films as Biopassivation Coatings and Directly Patternable Dielectrics. Thesis, Massachusetts Institute of Technology, 2001. https://dspace.mit.edu/handle/1721.1/28237 (accessed 2024-02-22).

(165) Jousseaume, V.; Yeromonahos, C.; El Sabahy, J.; Altemus, B.; Ladner, C.; Benedetto, K.; Ollier, E.; Faguet, J. Filament Assisted Chemical Vapor Deposited Organosilicate as Chemical Layer for Nanometric Hydrocarbon Gas Sensors. *Sensors and Actuators B Chemistry.* **2018**, *271*, 271–279. https://doi.org/10.1016/j.snb.2018.05.042.

(166) O'Shaughnessy, W. S.; Murthy, S. K.; Edell, D. J.; Gleason, K. K. Stable Biopassive Insulation Synthesized by Initiated Chemical Vapor Deposition of Poly(1,3,5-Trivinyltrimethylcyclotrisiloxane). *Biomacromolecules* **2007**, *8* (8), 2564–2570. https://doi.org/10.1021/bm070242s.

(167) O'Shaughnessy, W. S.; Gao, M.; Gleason, K. K. Initiated Chemical Vapor Deposition of Trivinyltrimethylcyclotrisiloxane for Biomaterial Coatings. *Langmuir* **2006**, *22* (16), 7021–7026. https://doi.org/10.1021/la0607858.

(168) O'Shaughnessy, W. S.; Edell, D. J.; Gleason, K. K. Initiated Chemical Vapor Deposition of Biopassivation Coatings. *Thin Solid Films* **2008**, *516* (5), 684–686. https://doi.org/10.1016/j.tsf.2007.06.112.

(169) O'Shaughnessy, W. S.; Edell, D. J.; Gleason, K. K. Initiated Chemical Vapor Deposition of a Siloxane Coating for Insulation of Neural Probes. *Thin Solid Films* **2009**, *517* (12), 3612–3614. https://doi.org/10.1016/j.tsf.2009.01.192.

(170) Mao, Y.; Gleason, K. K. Hot Filament Chemical Vapor Deposition of Poly(Glycidyl Methacrylate) Thin Films Using Tert-Butyl Peroxide as an Initiator. *Langmuir* **2004**, *20* (6), 2484–2488. https://doi.org/10.1021/la0359427.

(171) Moni, P.; Al-Obeidi, A.; Gleason, K. K. Vapor Deposition Routes to Conformal Polymer Thin Films. *Beilstein Journal of Nanotechnology.* **2017**, *8*, 723–735. https://doi.org/10.3762/bjnano.8.76.

(172) Zavvou, C.; Cluzel, J.; Mariolle, D.; Lefevre, A.; Jousseaume, V. Poly(V3D3), an iCVD Polymer with Promising Dielectric Properties for High Voltage Capacitors. *Solid-State Electronics.* **2021**, *184*, 108057. https://doi.org/10.1016/j.sse.2021.108057.

(173) Zavvou, Z. Dépôt iCVD de Couches Minces de Polymères Pour Des Applications En Électronique de Puissance. These de doctorat, Université Grenoble Alpes, 2023. https://www.theses.fr/s228349 (accessed 2023-12-07).

(174) Li, W.; Bradley, L. C.; Watkins, J. J. Copolymer Solid-State Electrolytes for 3D Microbatteries via Initiated Chemical Vapor Deposition. *ACS Applied Materials and Interfaces* **2019**, *11* (6), 5668–5674. https://doi.org/10.1021/acsami.8b19689.

(175) Mansurnezhad, R.; Ghasemi-Mobarakeh, L.; Coclite, A. M.; Beigi, M.-H.; Gharibi, H.; Werzer, O.; Khodadadi-Khorzoughi, M.; Nasr-Esfahani, M.-H. Fabrication, Characterization and Cytocompatibility Assessment of Gelatin Nanofibers Coated with a Polymer Thin Film by Initiated Chemical Vapor Deposition | Elsevier Enhanced Reader. *Materials Science and Engineering. C* **2020**, *110*, 110623. https://doi.org/10.1016/j.msec.2019.110623.

(176) Bonnet, L. Synthèse de Couches Mindes de Polymères Par iCVD: Mécanisme de Croissance et Application Aux Capteurs de Gaz. Thèse de doctorat, Université de Lyon, 2021.

(177) Van-Straaten, M.; Mabrouk, A. B. H.; Veillerot, M.; Licitra, C.; D'Agosto, F.; Jousseaume, V. Filling of Nanometric Pores with Polymer by Initiated Chemical Vapor Deposition. *Macromolecular Rapid Communications.* **2020**, *41* (14), 2000200. https://doi.org/10.1002/marc.202000200.

(178) Gleason, K. K. Designing Organic and Hybrid Surfaces and Devices with Initiated Chemical Vapor Deposition (iCVD). *Advanced Materials.* **2024**, 2306665. https://doi.org/10.1002/adma.202306665.

(179) Yang, R.; Moni, P.; Gleason, K. K. Ultrathin Zwitterionic Coatings for Roughness-Independent Underwater Superoleophobicity and Gravity-Driven Oil–Water Separation. *Advanced Materials and Interfaces* **2015**, *2* (2), 1400489. https://doi.org/10.1002/admi.201400489.

(180) Liu, W.; Su, C.; Su, P.; Yang, H.; Lu, P.; Du, Z.; Ye, Y. Sub-20 Nm Bilayer Hydrophilic Poly(Vinyl Pyrrolidone) Coatings for Antifouling Nanofiltration Membranes. *Macromolecular Materials and Engineering.* **2021**, *n/a* (n/a), 2100026. https://doi.org/10.1002/mame.202100026.

(181) Song, Q.; Zhao, R.; Liu, T.; Gao, L.; Su, C.; Ye, Y.; Chan, S. Y.; Liu, X.; Wang, K.; Li, P.; Huang, W. One-Step Vapor Deposition of Fluorinated Polycationic Coating to Fabricate Antifouling and Anti-Infective Textile against Drug-Resistant Bacteria and Viruses. *Chemical Engineering Journal.* **2021**, *418*, 129368. https://doi.org/10.1016/j.cej.2021.129368.

(182) Yoo, Y.; You, J. B.; Choi, W.; Im, S. G. A Stacked Polymer Film for Robust Superhydrophobic Fabrics. *Polymer Chemistry.* **2013**, *4* (5), 1664. https://doi.org/10.1039/c2py20963b.

(183) Bradley, L. C.; Gupta, M. Microstructured Films Formed on Liquid Substrates via Initiated Chemical Vapor Deposition of Cross-Linked Polymers. *Langmuir* **2015**, *31* (29), 7999–8005. https://doi.org/10.1021/acs.langmuir.5b01663.

(184) Huo, N.; Rivkin, J.; Jia, R.; Zhao, Y.; Tenhaeff, W. E. Synthesis of High Refractive Index Polymer Thin Films for Soft, Flexible Optics Through Halomethane Quaternization of Poly(4-Vinylpyridine). *Advanced Optical Materials.* **2024**, *n/a* (n/a), 2302201. https://doi.org/10.1002/adom.202302201.

(185) Montméat, P.; Dechamp, J.; Enyedi, G.; Fournel, F.; Zavvou, Z.; Jousseaume, V. Initiated Chemical Vapor Deposition of Polysiloxane as Adhesive Nanolayer for Silicon Wafer Bonding. *Materials Science in Semiconductor Processing.* **2022**, *148*, 106808. https://doi.org/10.1016/j.mssp.2022.106808.

(186) Schröder, S.; Ababii, N.; Lupan, O.; Drewes, J.; Magariu, N.; Krüger, H.; Strunskus, T.; Adelung, R.; Hansen, S.; Faupel, F. Sensing Performance of CuO/Cu2O/ZnO:Fe Heterostructure Coated with Thermally Stable Ultrathin Hydrophobic PV3D3 Polymer Layer for Battery Application. *Materials Today Chemistry.* **2022**, *23*, 100642. https://doi.org/10.1016/j.mtchem.2021.100642.

(187) Schröder, S.; Ababii, N.; Brînză, M.; Magariu, N.; Zimoch, L.; Bodduluri, M. T.; Strunskus, T.; Adelung, R.; Faupel, F.; Lupan, O. Tuning the Selectivity of Metal Oxide Gas Sensors with Vapor Phase Deposited Ultrathin Polymer Thin Films. *Polymers* **2023**, *15* (3). https://doi.org/10.3390/polym15030524.

(188) Unger, K.; Coclite, A. M. Glucose-Responsive Boronic Acid Hydrogel Thin Films Obtained via Initiated Chemical Vapor Deposition. *Biomacromolecules* **2022**, *23* (10), 4289–4295. https://doi.org/10.1021/acs.biomac.2c00762.

(189) Unger, K.; Greco, F.; Coclite, A. M. Temporary Tattoo pH Sensor with pH-Responsive Hydrogel via Initiated Chemical Vapor Deposition. *Advanced Materials Technology.* **2021**, *n/a* (n/a), 2100717. https://doi.org/10.1002/admt.202100717.

(190) Gleason, K. K. Controlled Release Utilizing Initiated Chemical Vapor Deposited (iCVD) of Polymeric Nanolayers. *Frontiers in Bioengineering and Biotechnology.* **2021**, *9*, 632753. https://doi.org/10.3389/fbioe.2021.632753.

(191) Decandia, G.; Palumbo, F.; Treglia, A.; Armenise, V.; Favia, P.; Baruzzi, F.; Unger, K.; Perrotta, A.; Coclite, A. M. Initiated Chemical Vapor Deposition of Crosslinked Organic Coatings for Controlling Gentamicin Delivery. *Pharmaceutics* **2020**, *12* (3), 213. https://doi.org/10.3390/pharmaceutics12030213.

(192) Ghasemi-Mobarakeh, L.; Werzer, O.; Keimel, R.; Kolahreez, D.; Hadley, P.; Coclite, A. M. Manipulating Drug Release from Tridimensional Porous Substrates Coated by Initiated Chemical Vapor Deposition. *Journal of Applied Polymer Science.* **2019**, *136* (33), 47858. https://doi.org/10.1002/app.47858.

(193) Bayram, F.; Mercan, E. S.; Karaman, M. One-Step Fabrication of Superhydrophobic-Superoleophilic Membrane by Initiated Chemical Vapor Deposition Method for Oil–Water Separation. *Colloid Polymer Science.* **2021**. https://doi.org/10.1007/s00396-021-04870-1.

(194) Teodorescu, M.; Bercea, M. Poly(Vinylpyrrolidone) - A Versatile Polymer for Biomedical and Beyond Medical Applications. *Polymer-Plastics Technology and Engineering.* **2015**, *54* (9), 923–943. https://doi.org/10.1080/03602559.2014.979506.

(195) Ignatova, M.; Markova, N.; Manolova, N.; Rashkov, I. Antibacterial and Antimycotic Activity of a Cross-Linked Electrospun Poly(Vinyl Pyrrolidone)–Iodine Complex and a Poly(Ethylene Oxide)/Poly(Vinyl Pyrrolidone)–Iodine Complex. *Journal of Biomaterials Science. Polymer Edition.* **2012**. https://doi.org/10.1163/156856208783721056.

(196) Ignatova, M.; Manolova, N.; Rashkov, I. Novel Antibacterial Fibers of Quaternized Chitosan and Poly(Vinyl Pyrrolidone) Prepared by Electrospinning. *European Polymer Journal.* **2007**, *43* (4), 1112–1122. https://doi.org/10.1016/j.eurpolymj.2007.01.012.

(197) Chan, K.; Kostun, L. E.; Tenhaeff, W. E.; Gleason, K. K. Initiated Chemical Vapor Deposition of Polyvinylpyrrolidone-Based Thin Films. *Polymer* **2006**, No. 47, 6941–6947. https://doi.org/10.1016/j.polymer.2006.07.068.

Chapter 2:
Polymer thin film deposition methods and physico-chemical characterisations

1. Introduction

As mentioned in the previous chapter, two deposition techniques will be used throughout this thesis to functionalise surfaces with a hydrophobic or hydrophilic polymer thin film. These two methods are initiated Chemical Vapour Deposition (iCVD) and Dielectric Barrier Discharge Cold Atmospheric Plasma (DBD-CAP) which will be presented in detail here.

To characterize these thin films, a certain number of analytical techniques were carried out to determine physical-chemical properties such as the film's thickness, morphology and chemical composition. These analytical techniques will also be presented in this chapter.

2. Deposition techniques

2.1.Initiated Chemical Vapour Deposition (iCVD)

2.1.1. The TEL iCVD equipment

The iCVD equipment that was used in this project was the TEL iCVD, which was conceived by Tokyo Electron Limited (TEL) and manufactured by Annealsys. This tool is an industrial-size prototype conceived for taking a 200 mm silicon wafer. For smaller samples, a substrate holder can be used as seen in Figure 1b.

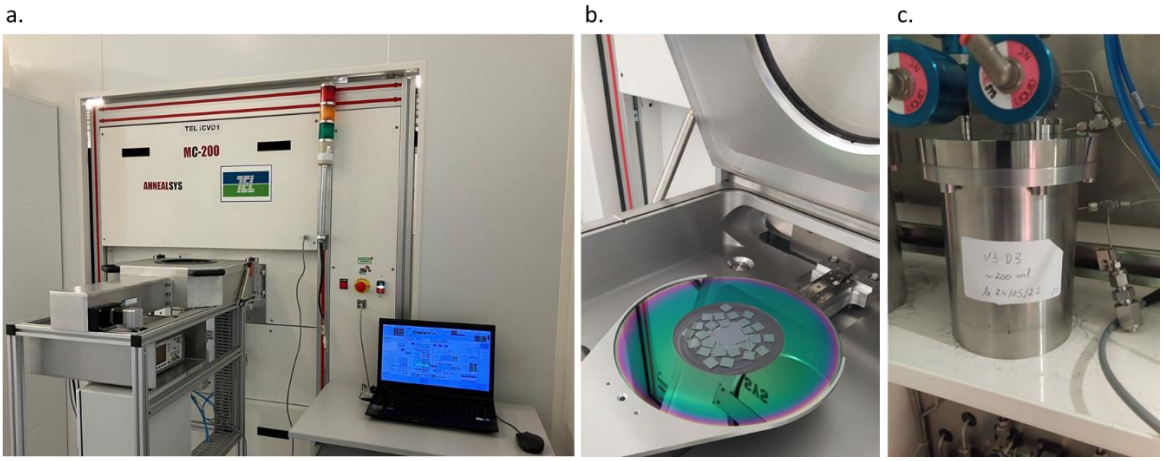

Figure 1: a. The TEL iCVD equipment in the CEA-Leti clean room. b. The open load-lock into which is loaded a 200 mm substrate holder with coupons. c. The monomer canister which can be found at the back of the equipment.

In normal use, only the substrate load-lock and the computer used to control the equipment are accessible from the cleanroom as seen in Figure 1a. The deposition chamber, as well as all chemical canisters are found behind. Moreover, the monomer canisters (Figure 1c) are filled in a glovebox to avoid oxidation and water uptake of the monomers which could lead to unwanted spontaneous polymerisation in the reservoir or the injectors. This makes the process very safe and adapted to an industrial use.

In stand-by mode, the equipment, as well as the load-lock system, are under vacuum ($1x10^{-3}$ Torr for the deposition chamber). Furthermore, in order to inhibit polymerisation occurring on the

chamber walls and inside the injectors, the latter are heated at all times at 125°C. When running the deposition process, the silicon wafer is placed on a substrate holder which is cooled by a closed-circuit oil system circulating beneath it. This temperature difference favours condensation of the molecules.

2.1.2. The iCVD deposition process for poly(V3D3)

The values given in this section were those used for the deposition of poly(1,3,5-trivinyl-1,3,5-trimethylcyclotrisiloxane) (poly(V3D3)) thin films. These values were optimized in previous studies[1]. For other precursors, such as vinyl pyrrolidone (VP) which is also used in this project, these values can be adapted. They will be presented further on.

To carry out a deposition process with the TEL iCVD, after checking the vacuum and temperatures are set in accordance with the recipe, the substrate can be loaded. To do so, the load lock's vacuum must be broken, allowing to insert the silicon wafer (or holder with coupons). The load lock can then be pumped down and when the vacuums in both the chamber and the load lock reach equilibrium, the chamber opens (Figure 2) and an automatic arm takes the substrate into the reactor where it is deposited onto the chilled substrate holder.

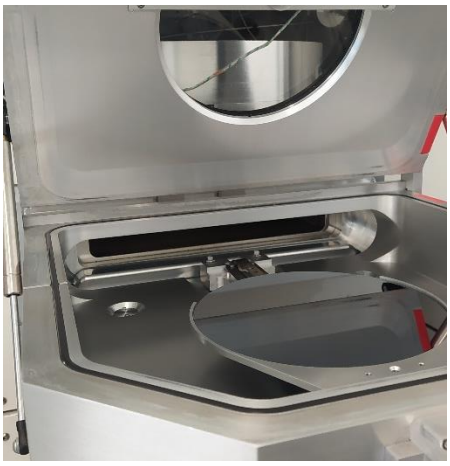

Figure 2: Open chamber corresponding with the load lock. This photography was acquired during a maintenance operation under atmospheric conditions. In working conditions, this opening only occurs when vacuum equilibrium is reached between deposition chamber and load lock.

Before injecting the monomer and initiator, the substrate holder is elevated to reach its position 3.3 centimetres under the heated filament. This filament, which is made from a nickel-chrome alloy, is placed in a serpentine, covering the entire chamber. The recipe pressure, which in this case is 1.5 Torr, is gradually set, and the heated filament is powered by a direct current of 3.5 A in order for it to reach a temperature of around 285°C. The chiller on which the substrate is placed is heated to 100°C, thus remaining under the 125°C of the reaction chamber. The temperature of the silicon wafer is measured during the time of the process by a thermocouple under the substrate. It is always a few degrees higher than the chiller's set temperature as it is heated by the surrounding chamber walls and the heated filament which is 3.3 cm above. In the rest of this document, the temperature that will be referred to is that of the chiller.

Once all these surrounding parameters are reached and stable, the injection of the V3D3 monomer is induced with a flowrate of 0.1 g/min, pushed by argon at 25 standard cubic centimetres per minute (sccm) as carrier gas. The monomer is injected under vapour form through a showerhead at the top of the reactor to insure it is uniformly distributed in the chamber. To allow the saturation of the chilled substrate surface in V3D3, the monomer is injected alone with its carrier gas for 180 s. After this time, the radical initiator, tert-butyl peroxide (TBPO) is also vaporised (by heating the canister to 28°C) and injected with a flowrate of 2 sccm. As it goes through the heated filament, it is pyrolyzed, becoming radicals (Figure 3). As these radicals come into contact with the monomer on the substrate, they initiate the polymerisation of V3D3. The time of deposition can be adjusted, from tens to thousands of seconds, depending on the desired thickness of polymer. When the time of deposition is reached, all injections are stopped and the equipment returns to stand-by mode under vacuum. The substrate holder goes back to its initial position and the silicon wafer, coated with poly(V3D3), can be unloaded through the load-lock chamber.

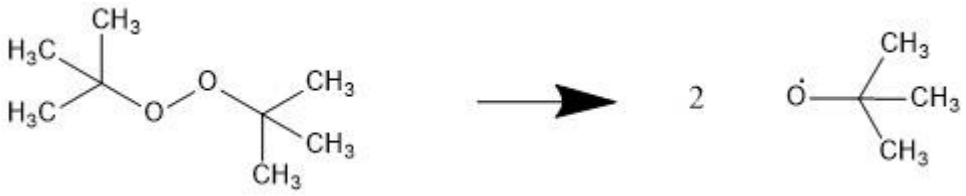

Figure 3: Pyrolysis of TBPO.

Table 1: iCVD process parameters used for depositing poly(V3D3) thin films.

Temperature (°C)			Pressure (Torr)	Vaporisation temperature (°C)		Injection rate	
Chamber	Filament	Chiller		V3D3	TBPO	V3D3 (g/min)	TBPO (sccm)
125	285	100	1.5	125	28	0.1	2

2.1.3. iCVD polymerisation of PVP

A second precursor was used in this thesis and was deposited by iCVD: vinylpyrrolidone (VP). This monomer has previously been deposited by iCVD leading to the obtention of poly(vinylpyrrolidone) (PVP) thin films. The radical initiator that was used was tert-butyl peroxide (TBPO). This is the same initiator that was used for poly(V3D3) and also the only initiator found in the literature for PVP coatings[2–5].

The recipe parameters from the literature on iCVD PVP coatings were used, when possible, as a starting point for developing our own process with the TEL iCVD (Appendix A)[2–8]. This concerns the chamber pressure, the temperatures of the filament and the substrate, the vaporisation temperatures of VP and TBPO, as well as their flowrates.

In our recipe, the chamber pressure was set between 0.5 and 1.5 Torr. The chiller's temperature was set between 30°C and 37°C, which is close to the values found in the literature. As for the temperature of the filament used to pyrolyze the TBPO and create the radical species, it was powered

by a direct current of 3 A, leading to a temperature around 250°C. Concerning the injection parameters of the VP precursor and the radical initiator TBPO, these were adapted from our preceding experience with the TEL iCVD. The VP precursor was injected at 115°C in vapour form with a flowrate of 0.15 g/min, pushed by 120 sccm of argon as carrier gas. The radical initiator, TBPO, was injected in vapour form at 28°C with a flowrate between 2 and 4 sccm. Time of deposition was also modified to study the deposition kinetics.

Table 2: iCVD process parameters used for depositing PVP thin films.

Temperature (°C)			Pressure (Torr)	Vaporisation temperature (°C)		Injection rate		Time (s)
Chamber	Filament	Chiller		VP	TBPO	VP (g/min)	TBPO (sccm)	
125	250	37	1.5	115	28	0.15	2	100 200 400 800 1600 3200 4800 6400
125	250	35	0.5 0.75 1 1.25 1.5	115	28	0.15	4	1200
125	250	30	0.5 0.75 1 1.25 1.5	115	28	0.15	4	1200

2.1.4. Copolymerisation by iCVD

ICVD can also be used for copolymerisation by injecting two monomers simultaneously into the reactor. In this thesis, this is carried out with VP and V3D3 in order to create crosslinked copolymers poly(VP-co-V3D3). TBPO is still used as radical initiator.

In this case, the substrate temperature was set to 40°C and the chamber pressure was set to 1.5 Torr. As for PVP depositions, the filament temperature was powered with a direct current of 3 A leading to a temperature around 250°C, allowing the pyrolysis of TBPO and the formation of radicals. The injection of VP was modified between 0.15 and 0.2 g/min, pushed by 60 sccm of argon. For V3D3, the injection rate was lower as the objective was to use it only as a crosslinking agent. It was varied between 0.03 and 0.1 g/min, pushed by 25 sccm of argon. These variations of the precursor's injection rates led to variations of the injected fractions of each monomer as seen in Table 3. In chapter 4, we will study the impact this has on the thin film properties.

Table 3: iCVD process parameters used for depositing poly(VP-co-V3D3) thin films.

Temperature (°C)	Pressure (Torr)	Injection rate			Time (s)	Injected fractions (%)	
chiller		VP (g/min)	V3D3 (g/min)	TBPO (sccm)		VP	V3D3
40	1.5	0.17	0.1	2	500 1000 1500 2500 3500	62.6	37.4
40	1.5	0.17	0.03	2	500 1000 1500 2500 3500	85.1	14.9
40	1.5	0.17	0.03 0.04 0.06 0.08 0.1	2	2500	85.1 80.6 73.5 68.0 62.6	14.9 19.4 26.5 32.0 37.4
40	1.5	0.15 0.16 0.17 0.18 0.19 0.2	0.03	2	2500	83.5 84.9 85.1 85.9 86.6 87.2	16.5 15.1 14.9 14.1 13.4 12.8

2.1.5. Controlling P_m/P_{sat}

It has previously been shown that many process parameters can impact the polymerisation and growth rate of thin films deposited by iCVD. Indeed, in her thesis, Laetitia Bonnet showed that there are some parameters that impact the concentration of radicals in the chamber[9]. This is the case for: the filament's temperature, the distance between the filament and the substrate, and the initiator's flowrate. Others, such as the pressure, the substrate's temperature and the precursor's flowrate, influence the monomer concentration. While all these factors have a non-negligeable impact on the polymerisation process, one important parameter should be focused on: the saturation ratio P_m/P_{sat}. P_m is the monomer partial pressure and P_{sat} is the monomer saturation vapour pressure. Both are calculated separately.

Monomer partial pressure P_m (Torr) depends on the total pressure in the reactor P_{tot} (Torr) and the fraction of the monomer in the chamber $x_{monomer}$:

$$P_m = P_{tot} \times x_{monomer}$$

with:

$$x_{monomer} = \frac{n_{monomer}}{n_{tot}} = \frac{n_{monomer}}{n_{monomer} + n_{TBPO} + n_{argon}} = \frac{Q_{monomer}}{Q_{monomer} + Q_{TBPO} + Q_{argon}}$$

with $n_{monomer}$ the quantity of monomer (mol), n_{TBPO} the quantity of radical initiator TBPO (mol), n_{argon} the quantity of argon as carrier gas (mol) and $Q_{monomer}$, Q_{TBPO} and Q_{argon} the volume flowrates in sccm of monomer, TBPO and argon respectively.

In the case of a copolymer, this term must take into account both monomers. This equation is given with the two monomers used in this project, VP and V3D3, to determine the fraction of VP:

$$x_{monomer\,VP} = \frac{n_{monomer\,VP}}{n_{tot}} = \frac{n_{monomer\,VP}}{n_{monomer\,VP} + n_{monomer\,V3D3} + n_{TBPO} + n_{argon\,VP} + n_{argon\,V3D3}}$$

As for the monomer saturation vapour pressure P_{sat}, it is calculated using constant A (Torr), enthalpy of vaporisation ΔH_{vap} (J.mol^{-1}), ideal gas constant R (R = 8.314 J.mol^{-1} K^{-1}) and the temperature of the substrate $T_{substrate}$ (K):

$$P_{sat} = Ae^{\frac{-\Delta H_{vap}}{RT_{substrat}}}$$

This value can be obtained using the Clausius-Clapeyron diagram.

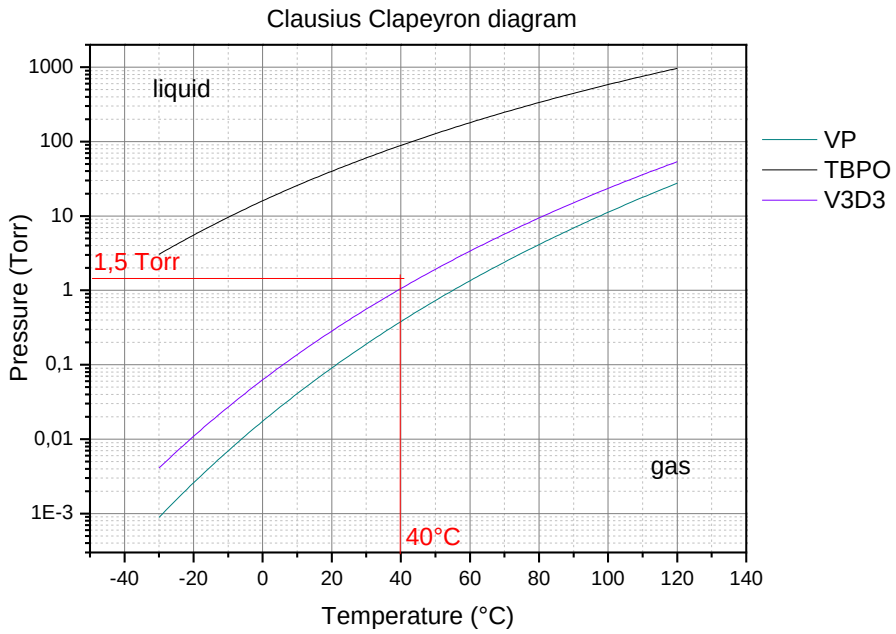

Figure 4: Clausius-Clapeyron Diagram of V3D3, VP and TBPO highlighting the process parameters used for depositing poly(VP-co-V3D3): pressure = 1.5 Torr and substrate temperature = 40°C.

As it can be seen when decomposing the calculation of saturation ratio P_m/P_{sat}, this value takes into account many important process parameters that have an influence on the polymerisation process in iCVD. Moreover, this parameter has a direct impact on the monomer adsorption at the surface of the substrate, showing how important its control is. This can be seen with the Brunauer-Emmett-Teller (BET) equation[10]:

$$V_{ad} = \frac{V_{ml} \times c \times \frac{P_m}{P_{sat}}}{(1 - \frac{P_m}{P_{sat}}) \times (1 - (1 - c)\frac{P_m}{P_{sat}})}$$

with V_{ad} the total adsorbed volume, V_{ml} the adsorbed volume of a monolayer and c the monomer's concentration at the surface of the substrate. However, this BET equation only explains the first step of a two-step regime occurring in iCVD deposition. This will be further discussed in chapter 4.

In this study, we assume that $T_{substrate}$ is underestimated, therefore overestimating P_m/P_{sat}. Indeed, the substrate temperature is controlled with a closed-circuit oil system circulating beneath it in the chiller. However, the surrounding heat from the walls of the chamber and the filament impact the substrate's temperature. Therefore, when calculating the P_m/P_{sat} in this study, the substrate's temperature was used rather than the chiller's.

2.2.Dielectric Barrier Discharge Cold Atmospheric Plasma (DBD-CAP)

In order to deposit plasma polymers from monomer V3D3, Dielectric Barrier Discharge Cold Atmospheric Plasma (DBD-CAP) was carried out using Molecular Plasma Group's (MPG, Luxembourg) Plasmaspot® which is represented in Figure 5a.

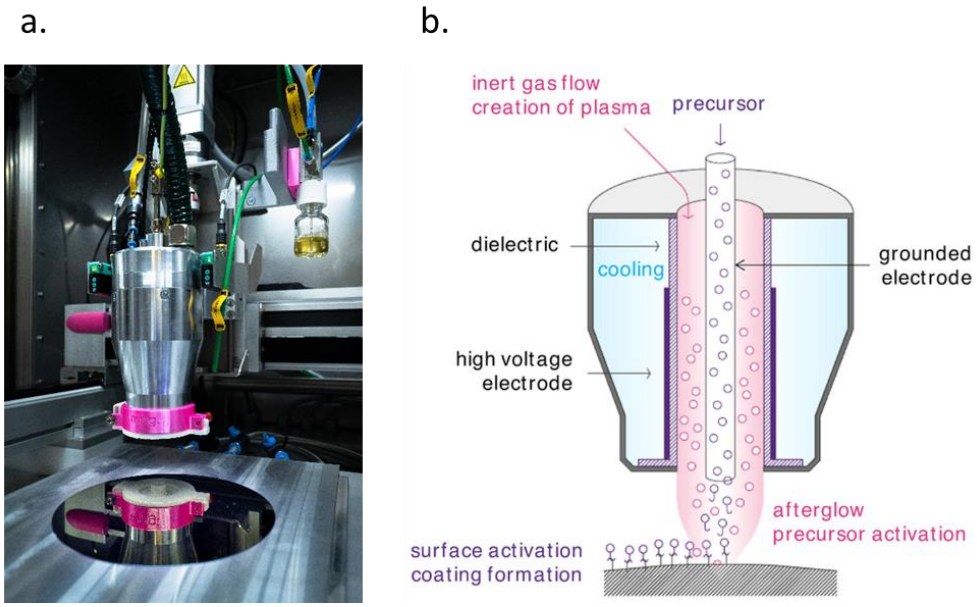

Figure 5: a. Photograph of the Plasmaspot®, Copyright © 2023 CEA Leti, b. Schematic representation of the plasma polymerisation process using the Plasmaspot®[11]. Copyright © 2022 John Wiley & Sons - Books.

The precursor, V3D3, was placed without further dilution or purification into a glass vial and was connected to the plasma torch. During deposition process, the precursor is nebulized and carried in aerosol form alongside nitrogen with a flowrate between 700 and 900 standard centimetres per minute (sccm). These values were chosen to have a reflux of around 1 droplet per second in the precursor flask, as recommended by the manufacturer. The flow of monomer was further diluted with 6 000 sccm of nitrogen. This mixture of nitrogen and monomer microdroplets are injected through the inner circular electrode of the plasma torch, which can be seen in Figure 5b. Simultaneously, nitrogen, which was used as the gas to ignite the plasma, is injected between both circular electrodes with a flowrate of 80 000 sccm which is the recommended operating setting. This allows the plasma to be ignited between both electrodes, with a power between 150 and 250 W. As the V3D3 aerosol comes out of the plasma torch, the precursor is activated by the plasma's afterglow, forming reactive species

such as radicals, ions, electrons. These energetic fragments will then react with one another, creating plasma polymer pp(V3D3) on the substrate's surface.

The Plasmaspot®'s particularity is that the plasma torch can be automated to move over the substrate. Thus, the height of the torch and the movement pattern have to be set before launching the plasma deposition. The height of the torch was set to leave a space of 1 mm between the outlet of the nozzle and the surface of the substrate. This small distance was chosen to limit monomer fragmentation as it has been shown that a small distance allows higher conservation of the monomer structure[12].

The movement of the torch was configured to cover a rectangular surface by moving left over the set width, going down by a fixed step, moving right over the same width, going down by the step, and repeating this scheme until covering the whole length of the substrate. This pattern in represented in Figure 6. The substrates coated in this study were 100 mm silicon wafers. For this reason, the width and length were set to 120 mm. The chosen step was 10 mm and the speed of the torch was 50 mm/s. It is also possible to repeat the movement scheme of the plasma torch. Indeed, once it arrives at the end of the described pattern, it can return to the beginning and start over. This will also be studied in chapter 3.

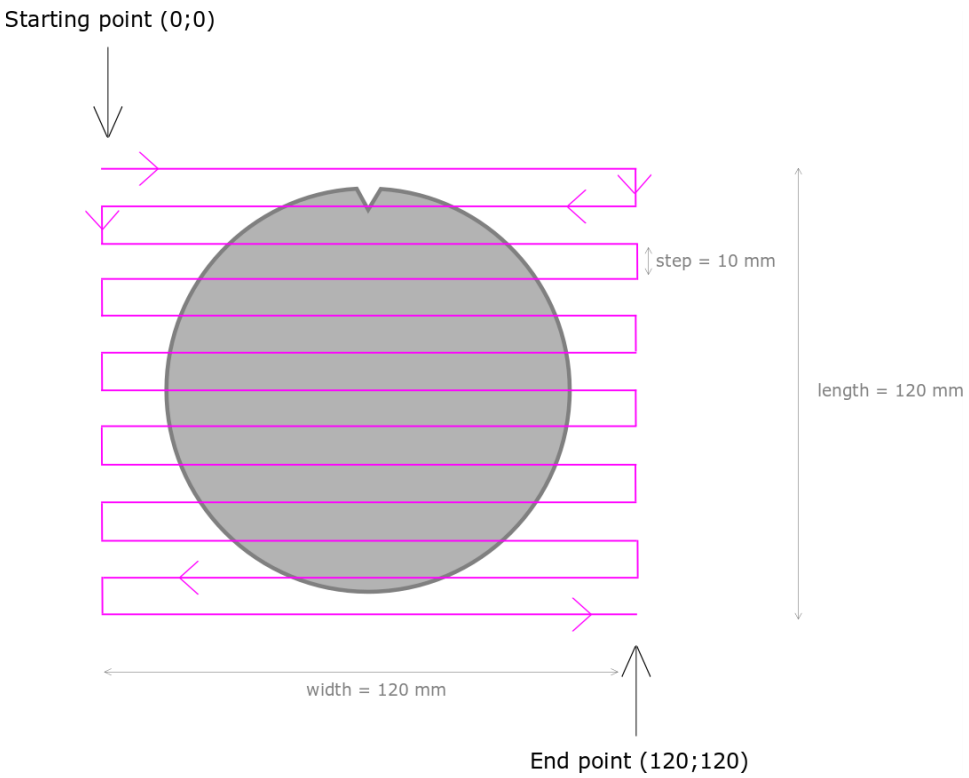

Figure 6: Movement of the plasma torch to cover a 100 mm silicon wafer.

The influence of some parameters will be studied in chapter 3. These are summarized in the following table.

Table 4: Process parameters for DBD-CAP deposition of pp(V3D3).

V3D3 flowrate (sccm)	Dilution (sccm)	Flowrate of plasma gas (sccm)	Plasma power (W)	Number of torch repetitions
700	6	80	150	1 2 3 4 5
700	6	80	150 200 250	1
800	6	80	150 200 250	1
900	6	80	150 200 250	1

3. Physico-chemical characterisation

3.1. Spectroscopic Ellipsometry

Spectroscopic ellipsometry is a non-destructive, optical technique that allows the measurement of thin film and optical properties such as the thickness or the refractive index.

This technique works by emitting a linearly polarized light onto a sample and detecting the change in polarization state of the light as it is reflected off the surface (Figure 7)[14]. Indeed, after reflection, the polarized light becomes elliptical, hence the name of the technique. The electric fields of the incident wave ($\vec{E}$) and the reflective wave ($\overrightarrow{E'}$) can both be decomposed along the s-plane which is perpendicular to the incident plane, and the p-plane which is parallel to it. The amplitudes of the s-plane (E_s and E'_s) and p-plane (E_p and E'_p) then give the reflection coefficients:

$$r_s = \frac{E'_s}{E_s} \text{ and } r_p = \frac{E'_p}{p}$$

Ellipsometry measures the parameters ψ and Δ which correspond to the amplitude and phase shifts between the p and s components of the electric fields, thus describing the resulting ellipse after reflection. These parameters are related to the reflection coefficients according to the following equation:

$$\rho(\theta, \lambda) = \frac{r_p}{r_s} = tan\psi \, e^{i\Delta}$$

where θ and λ are the angle of incidence and the wavelength, respectively.

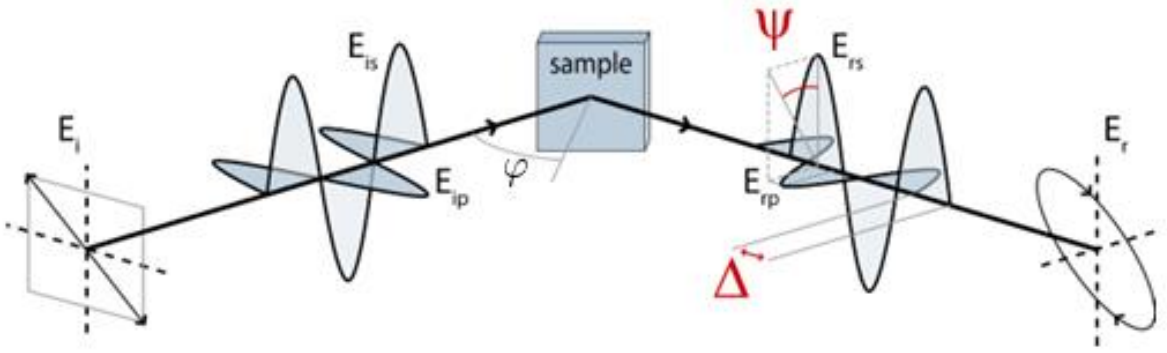

Figure 7: Spectroscopic ellipsometry principal. Reprinted from Van Beekum[13].

The measurement of parameters ψ and Δ, at multiple wavelengths, can then indirectly give physical properties such as thin film thickness, optical index and even roughness, by fitting a model to the experimental data[15]. Two models were used in this thesis: the Tauc-Lorentz model and the Cauchy-Urbach model.

The Cauchy dispersion model is the most common model used in spectroscopic ellipsometry for transparent thin films[16]. It gives the optical index n as a function of wavelength λ using the following equation:

$$n(\lambda) = A + \frac{B}{\lambda^2} + \frac{C}{\lambda^4}$$

with A, B and C the Cauchy fit parameters.

The two-parameter Urbach model can be added to take into consideration any absorption. This gives the extinction coefficient k as a function of wavelength λ as following:

$$k(\lambda) = \alpha e^{\beta(\frac{1}{\lambda} - \frac{1}{\gamma})}$$

with α the extinction coefficient amplitude, β the exponent factor and γ the band edge.

The Tauc-Lorentz model is used for absorbing materials[17]. The Lorentz oscillator is used to describe the absorbance of thin films and can be defined by the following equation:

$$\varepsilon_2(E) = \frac{A}{E_0^2 - E^2 - iBE}$$

with A the amplitude of the function, E_0 the centre energy and B the damping which gives the broadening of the peak.

A second oscillator shape ε1(∞) is determined with the Kramers-Kronig relation which mathematically connects n and k.

The Tauc-Lorentz equation further includes an optical bandgap term. It is given by the following formula:

$$\varepsilon_2(E) = \frac{AE_0C(E-E_g)^2}{(E-E_0)^2+C^2E^2}\frac{1}{E}, E > E_0;\ \varepsilon_2(E) = 0, E \leq E_g$$

with E_g the optical band gap energy, A the amplitude, E_0 the resonant energy, and C the oscillator width (broadening).

For both models, all fit parameters are reached by iteration after generating the model for the experimental data. The Mean Square Error (MSE) between the theoretical and experimental values of ψ and Δ is generally given as an evaluation of the data fit. However, it is also important to check that the model curve is close to the experimental data. Indeed, a low MSE can also be the sign of a local minimum in the algorithm regression, and not the global minimum which is what is being sought[18].

In this work, to evaluate the polymer film thickness, spectroscopic ellipsometry was carried out with J.A. Woollam's M-2000®. A three-angle measurement (65°, 70° and 75°) was carried out at the centre of the silicon wafer before using the CompleteEase® software to generate and fit the adapted model: for PVP and poly(VP-co-V3D3), the Tauc-Lorentz model was used. For poly(V3D3) and pp(V3D3), preliminary results showed that both Tauc-Lorentz and Cauchy-Urbach models could be used. Indeed, as it can be seen in Figure 8, for both models applied to the same measurement carried out on a poly(V3D3) thin film, the model (black dotted line) fits the experiment data for ψ (red line) and Δ (green line) perfectly. Furthermore, the optical index n and extinction coefficient k are identical at 632.8 nm, and very close over the entire measured range. This is also true for the resulting thickness measurements. The Cauchy-Urbach model was therefore chosen for fitting poly(V3D3) and pp(V3D3) as it is the most represented in the literature.

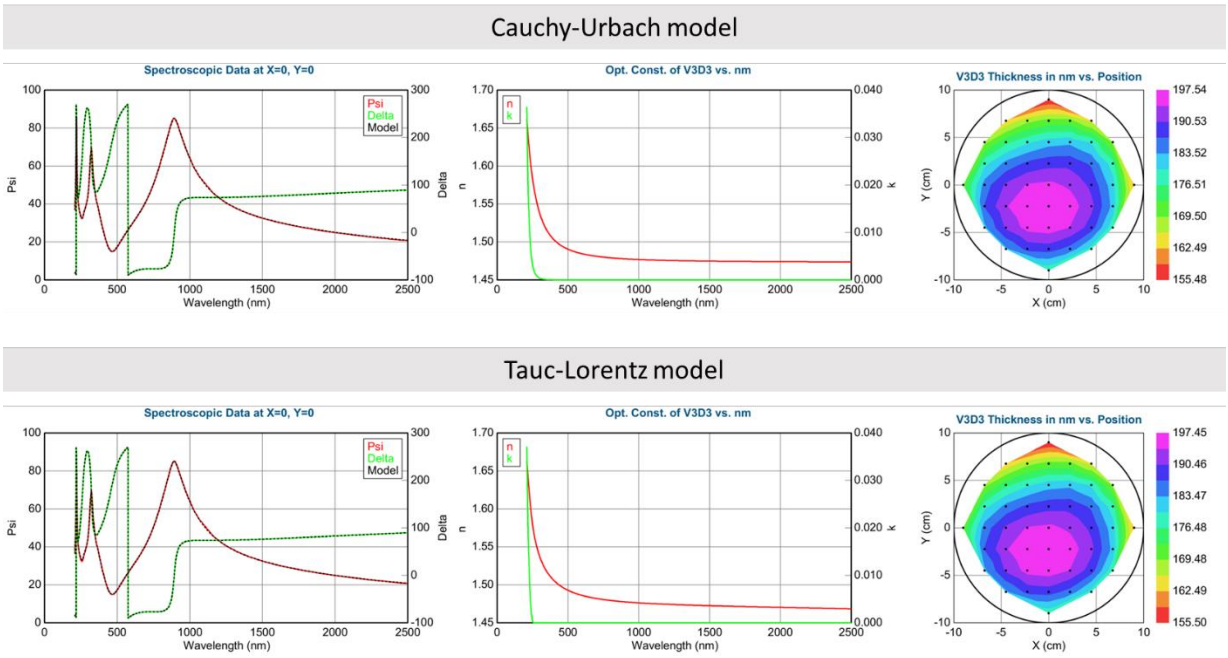

Figure 8: Cauchy-Urbach and Tauc-Lorentz model applied to experimental data from the mapping of a poly(V3D3) thin film.

For a same thin film, the model was fit on a coating with a consequent thickness. The fit parameters were then conserved for all other thinner samples of the same polymer, with the hypothesis that the thickness does not change the nature of the material.

J.A. Woollam's M-2000® was also used to carry out mapping of the silicon wafers (Figure 8) on which a polymer thin film was coated. In this case, forty-nine measurements were made across the wafer. The parameters of the chosen model were then fitted for the measurement at the centre, before being fixed and applied to all other points in order to determine the thickness across the whole surface.

3.2. X-ray Reflectivity (XRR)

X-ray reflectivity (XRR) is a technique used to determine thin film parameters such as thickness, roughness and density. The principle is based on the analysis of X-ray reflection intensity curves obtained from an incident X-ray beam with a grazing incident angle (< 4°).

For an incident angle under the critical angle θ_c, there is total reflectance of the X-rays. This allows the determination of the material's density[1]. This can be seen in Figure 9. Furthermore, the distance between the oscillating fringes determines the thickness of the thin film. The amplitude of these oscillations gives the density contrast between the film and the substrate. The bigger the amplitude, the higher the contrast. Concerning the surface roughness, the higher it is, the faster the oscillation's amplitude decreases. Both surface roughness and interface roughness have an effect on the decay of the oscillations[19].

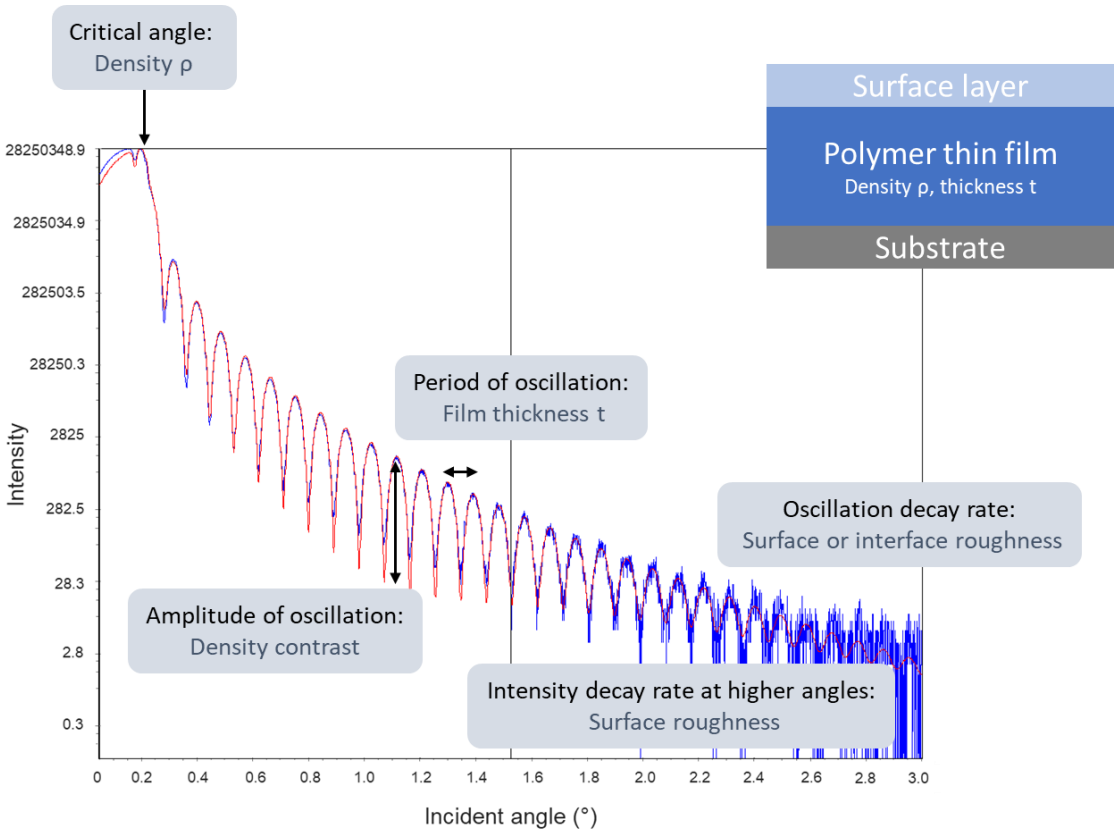

Figure 9: X-ray reflectivity curve of poly(V3D3) deposited by iCVD and the information it can provide. The experimental data is in blue and the model is in red. Inspired by Yasaka[19].

In order to quantify the parameters of the thin film, a model is used and fitted to the data. A surface layer is added to the model to take into account any surface modifications due to contamination. This layer only accounts for a couple of nanometres and is used to provide a better fit to the model.

In this thesis, the experiments were carried out using Malvern Panalytical's Empyrean diffractometer with a wavelength of 1.54 Å.

3.3. Fourier Transform Infrared Spectroscopy (FTIR)

Fourier Transform Infrared Spectroscopy (FTIR) is an analytical method used to determine the nature of the chemical functional groups in a material. The principle is based on the fact that chemical bonds vibrate in different manners (Figure 10) as they absorb infrared radiation. Thus, when exposing a sample to infrared (IR) radiation, the IR spectrum is determined by analysing the absorbtion[20].

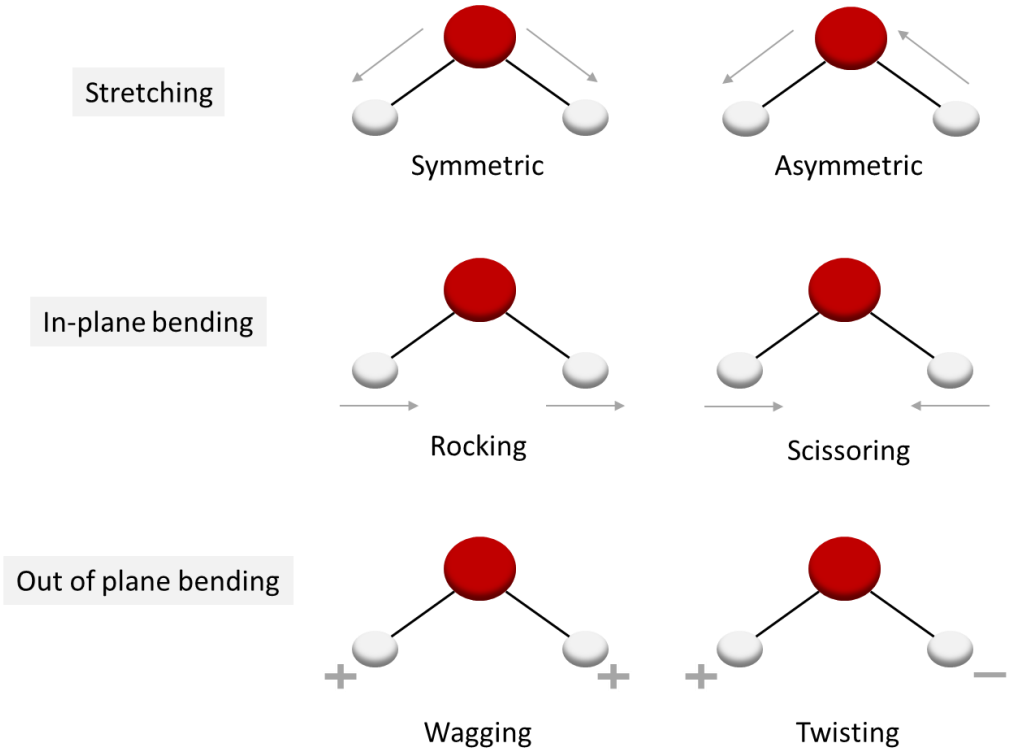

Figure 10: Different vibrational modes that absorb infrared radiation.

In practice, FTIR spectroscopy relies on a Michelson interferometer consisting of two perpendicular mirrors, one of which has a translational movement perpendicular to the incident beam. As the IR source is emitted, it is split by the beam splitter, causing 50 % of the IR light to be reflected off the fixed mirror and 50 % off the sliding mirror. The beams are then recombined, creating an interference pattern and transmitted towards the detector, through the sample. The detected interferogram is then submitted to mathematical transformation Fourier Transform to give the final IR spectrum[1,20,21].

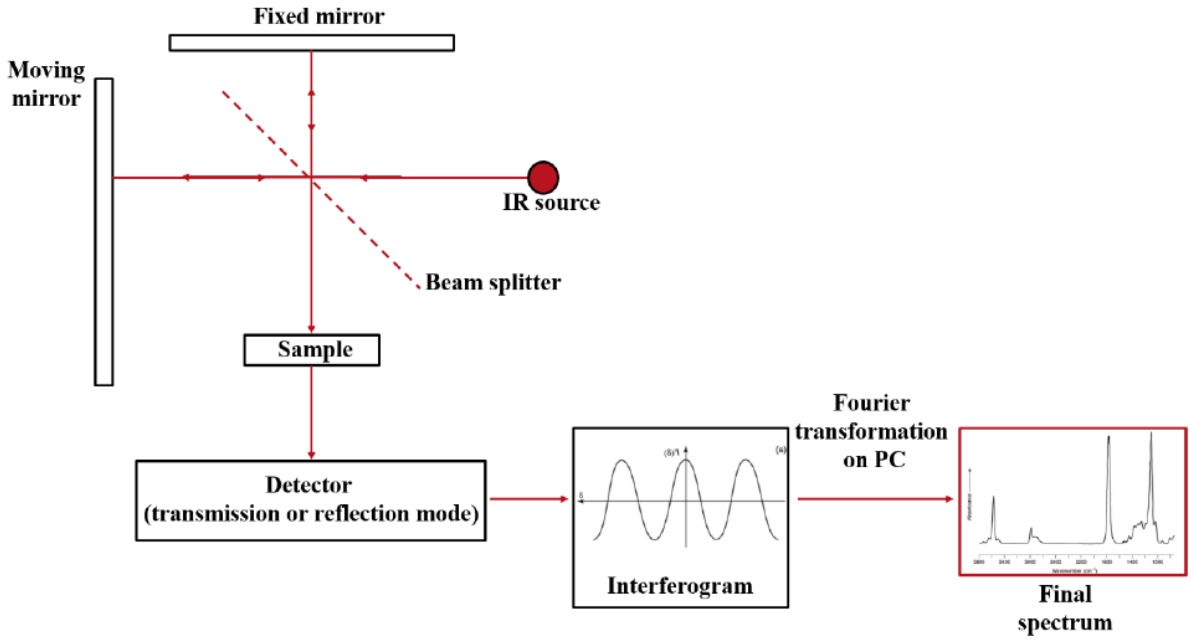

Figure 11: Schematic representation of the experimental process of FTIR spectroscopy. Reprinted from Zavvou[1].

In this case, FTIR spectroscopy was carried out under vacuum with Bruker's Vertex 70v equipment in normal transmission mode. A DTGS detector (Deuterated alanine doped Tri-Glycine Sulphate) was used with a resolution of 4 cm^{-1} over the range 400-5000 cm^{-1}. Measurements were averaged over 32 or 64 scans and the final spectra was baseline corrected.

3.4. X-ray Photoelectron Spectroscopy (XPS)

X-ray Photoelectron Spectroscopy (XPS) is a surface analysis technique allowing elemental quantification in the top few nm of the material.

The principle is to expose the substrate to an X-ray beam, causing photoelectrons to be emitted (Figure 12). The latter will then be detected and by measuring their kinetic energy $E_{kinetic}$, their binding energy E_b can be determined through the following equation:

$$E_{kinetic} = h\nu - E_b$$

where hv is the energy of the incident photons.

The binding energy consequently gives the nature of the emitting atom and the orbital from which the electron comes from[22].

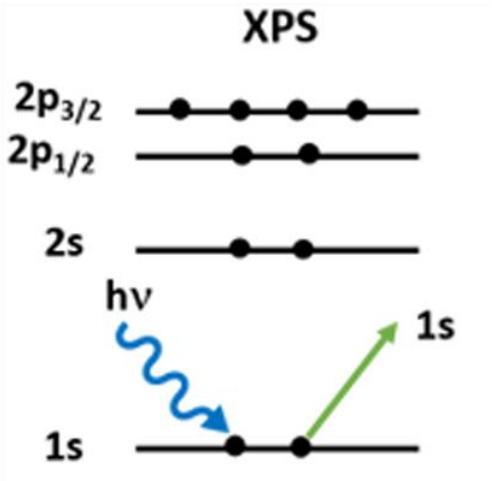

Figure 12: Photoemission process involved in XPS analysis. Adapted with permission from Stevie and Donley[22] Copyright 2020 American Vacuum Society.

XPS data is found in spectra which plot photoelectron counts as a function of binding energy. XPS spectra are often represented in a survey mode (Figure 13a), showing all elements detected at the material's surface. High resolution spectra are then given (Figure 13b) to precisely analyse specific peaks which can be deconvoluted to quantify the presence of chemical bonds[23].

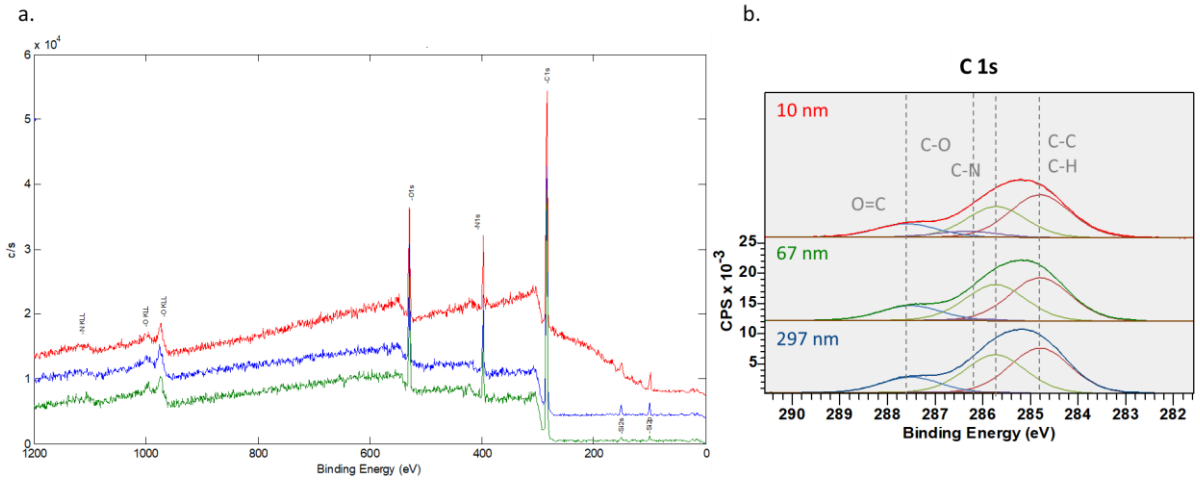

Figure 13: XPS spectra for PVP films of different thickness. a. Survey mode, b. High resolution XPS spectra for C 1s.

In this work, X-ray Photoelectron Spectroscopy (XPS) was carried out using PHI500 VersaProbe II or Quantes X-ray Photoelectron Spectroscope with a monochromatic microfocused X-ray beam with a source energy of 1486,6 eV. The analysis angle is 45°, leading to a penetration into the material of around 6.5 nm. The spectra was then reset by fitting the C-C component to 284.8 eV[24,25] and analysed with Casa XPS to quantify the chemical bonds present at the surface of the sample. Gaussian-Lorentzian curves were used to fit the peaks and the full width half maximum (fwhm) was kept in a range of 1.3 to 1.8 eV. The peak positions should be read ± 0.1 eV although this error will not be indicated in the rest of this manuscript to facilitate reading. The fitting data can be seen in the appendix for all films.

3.5. Atomic Force Microscopy (AFM)

Atomic Force Microscopy (AFM) is a technique used to analyse the topography and determine a material's properties at the nanoscale.

This technique relies on a probing tip at the end of a cantilever to probe the surface of the substrate which is mounted onto a piezoelectric scanner. As the cantilever probes the surface with a resonant frequency, deflections are detected via a laser beam. Indeed, an incident laser beam is reflected off the cantilever, and detected by a photodiode. This is illustrated in Figure 14. The light signal is then converted to an electrical signal[26].

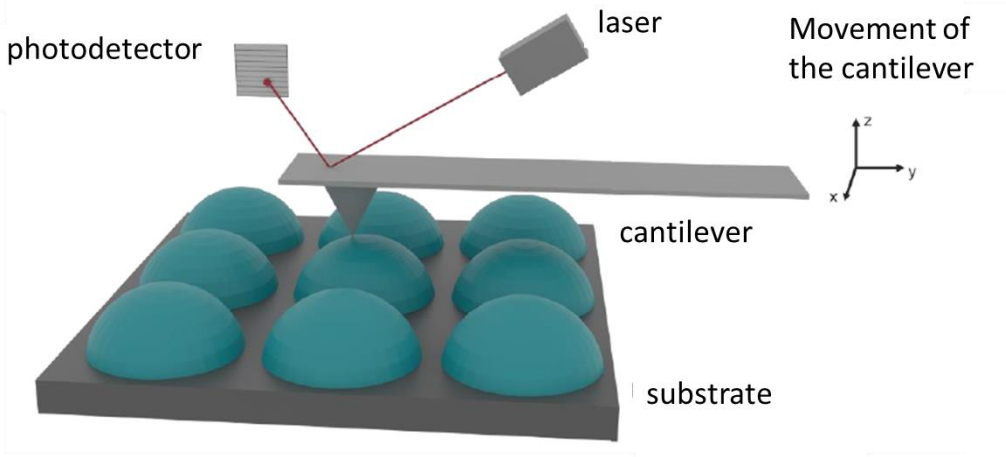

Figure 14: Schematic representation of the operating principle of AFM. Adapated from Feougier[27].

As well as imaging the topography of a surface, AFM can be used to evaluate the thin film roughness. To do so in this project, the Root Mean Square (RMS or Rq) roughness was used. Indeed, this value considers more significantly any large differences between peaks and valleys, than the average roughness R_a which is also often used for discussing surface roughness. This can be seen in the following equations.

$$R_a = \frac{1}{N}\sum_{i=1}^{N} |z_i - \overline{z}|$$

$$RMS = Rq = \sqrt{\frac{1}{N}\sum_{i=1}^{N} (z_i - \overline{z})^2}$$

Two equipment were used in this work: Bruker's Dimension Icon® with either a Bruker Otespa-r3 or a VTESPA-300 tip; and Bruker's Dimension FastScan® with a Bruker FastScan-A tip. Both were used in TappingMode™.

3.6. Water Contact Angle (WCA)

Water Contact Angles (WCAs) are used to determine the wettability of a surface. Indeed, when the WCA is over 150°, the surface is superhydrophobic. It is hydrophobic when WCA > 90°. For WCA < 90°, the surface is hydrophilic and when WCA < 10°, it becomes superhydrophilic and displays perfect wetting[28].

To study the wettability of the various surfaces developed in this thesis, the Kruss Drop Shape Analyser DSA100 was used to measure the WCA. This equipment, complete with an automatic dispenser, deposited 2 µL deionized water droplets onto the surface and a camera was used to image them. ADVANCE software by Kruss, was then used to determine the WCA. A minimum of three droplets were deposited and measured for each sample.

4. Conclusions

This chapter gives a detailed description of the processes used to deposit poly(V3D3), pp(V3D3), PVP and poly(VP-co-V3D3) which were all studied in this thesis and will be presented in the following chapters.

V3D3 based thin films were deposited by both iCVD and DBD-CAP, which, as it was seen in this chapter are quite different polymerisation techniques. This will allow the study of the influence of the process on the final thin film and its physico-chemical properties.

PVP was also deposited using the iCVD technique, and for the first time to our knowledge, copolymerisation was carried out to create crosslinked thin films of copolymer poly(VP-co-V3D3).

In this thesis, surfaces are also modified by Nano Imprint Lithography (NIL) and plasma etching to achieve micro and nanoscale topography. These techniques will be presented in chapter 5. The experimental protocols carried out for the microbiology assays will be detailed and discussed in chapter 6.

All the thin films were analysed to determine properties such as their chemical composition, their morphology, their thickness and their wettability. While the results will be presented in the following chapters, chapter 2 gave a description of the methods which were used.

5. Bibliography

(1) Zavvou, Z. Dépôt iCVD de Couches Minces de Polymères Pour Des Applications En Électronique de Puissance. These de doctorat, Université Grenoble Alpes, 2023. https://www.theses.fr/s228349 (accessed 2023-12-07).

(2) Chan, K.; Kostun, L. E.; Tenhaeff, W. E.; Gleason, K. K. Initiated Chemical Vapor Deposition of Polyvinylpyrrolidone-Based Thin Films. *Polymer* **2006**, No. 47, 6941–6947. https://doi.org/10.1016/j.polymer.2006.07.068.

(3) Janakiraman, S.; Farrell, S. L.; Hsieh, C.-Y.; Smolin, Y. Y.; Soroush, M.; Lau. Kinetic Analysis of the Initiated Chemical Vapor Deposition of Poly(Vinylpyrrolidone) and Poly(4-Vinylpyridine). *Thin Solid Films* **2015**, *595*, 244–250. https://doi.org/10.1016/j.tsf.2015.04.083.

(4) Liu, W.; Su, C.; Su, P.; Yang, H.; Lu, P.; Du, Z.; Ye, Y. Sub-20 Nm Bilayer Hydrophilic Poly(Vinyl Pyrrolidone) Coatings for Antifouling Nanofiltration Membranes. *Macromolecular Materials and Engineering,* **2021**, *n/a* (n/a), 2100026. https://doi.org/10.1002/mame.202100026.

(5) Prasath, V. S.; Lau, K. K. S. Kinetically Limited Bulk Polymerization of Polymer Thin Films by Initiated Chemical Vapor Deposition. *Macromolecules* **2023**, *56* (24), 10111–10118. https://doi.org/10.1021/acs.macromol.3c01868.

(6) Smolin, Y. Y.; Janakiraman, S.; Soroush, M.; Lau, K. K. S. Experimental and Theoretical Investigation of Dye Sensitized Solar Cells Integrated with Crosslinked Poly(Vinylpyrrolidone) Polymer Electrolyte Using Initiated Chemical Vapor Deposition. *Thin Solid Films* **2017**, *635*, 9–16. https://doi.org/10.1016/j.tsf.2016.12.034.

(7) Sun, M.; Qiu, H.; Su, C.; Shi, X.; Wang, Z.; Ye, Y.; Zhu, Y. Solvent-Free Graft-From Polymerization of Polyvinylpyrrolidone Imparting Ultralow Bacterial Fouling and Improved Biocompatibility. *ACS Applied Bio Materials,* **2019**. https://doi.org/10.1021/acsabm.9b00529.

(8) Sun, M.; Wu, Q.; Xu, J.; He, F.; Brown, A. P.; Ye, Y. Vapor-Based Grafting of Crosslinked Poly(N-Vinyl Pyrrolidone) Coatings with Tuned Hydrophilicity and Anti-Biofouling Properties. *Journal of Materials Chemistry B* **2016**, *4* (15), 2669–2678. https://doi.org/10.1039/C6TB00076B.

(9) Bonnet, L. Synthèse de Couches Mindes de Polymères Par iCVD: Mécanisme de Croissance et Application Aux Capteurs de Gaz.

(10) Lau, K. K. S.; Gleason, K. K. Initiated Chemical Vapor Deposition (iCVD) of Poly(Alkyl Acrylates): An Experimental Study. *Macromolecules* **2006**, *39* (10), 3688–3694. https://doi.org/10.1021/ma0601619.

(11) Borek-Donten, J.; Nisol, B.; Filimon, M.; Lopes, M.; Collard, D.; Chassaing, M.; Cauchie, H.-M.; Heyberger, R. The Industrial Process for Virucidal Plasma Coatings on Textiles: From Idea to Upscaling. *Plasma Processes and Polymerisation* **2022**, *19* (10), 2100249. https://doi.org/10.1002/ppap.202100249.

(12) Zabihzadeh Khajavi, M.; Nikiforov, A.; Nilkar, M.; Devlieghere, F.; Ragaert, P.; De Geyter, N. Degradable Plasma-Polymerized Poly(Ethylene Glycol)-Like Coating as a Matrix for Food-Packaging Applications. *Nanomaterials* **2023**, *13* (20), 2774. https://doi.org/10.3390/nano13202774.

(13) Van Beekum, E. R. J. PEALD and PECVD Inorganic Layers Microstructure Characterization and Moisture Permeation Barrier Properties. Master thesis, Eindhoven University of Technology, 2012.

(14) *What is Ellipsometry?*. J.A. Woollam. https://www.jawoollam.com/resources/ellipsometry-tutorial/what-is-ellipsometry (accessed 2024-02-26).

(15) *Spectroscopic Ellipsometry: Basic Concepts - HORIBA*. https://www.horiba.com/gbr/scientific/technologies/spectroscopic-ellipsometry/spectroscopic-ellipsometry/ (accessed 2024-02-27).

(16) Shah, D.; Patel, D.; Hilfiker, J.; Linford, M. A Tutorial on Spectroscopic Ellipsometry (SE), 2. The Cauchy Model. **2019**.

(17) Patel, D.; Shah, D.; Hilfiker, J.; Linford, M. A Tutorial on Spectroscopic Ellipsometry (SE), 5. Using the Tauc-Lorentz and Cody-Lorentz Models to Describe the Absorption Features of Amorphous Silicon (a-Si). **2019**, *20*, 34.

(18) Avval, T.; Johnson, B.; Hilfiker, J.; Linford, M. A Tutorial on Spectroscopic Ellipsometry (SE), 1. Determination of the Thicknesses of Thin Oxide Layers on Semiconductor Substrates. **2019**.
(19) Yasaka, M. X-Ray Thin Film Measurement Techniques . V. X-Ray Reflectivity Measurement. *Rigaku J.* **2010**, *26* (2).
(20) Stuart, B. *Infrared Spectroscopy: Fundamentals and Applications*; Analytical techniques in the sciences; J.Wiley & sons: Chichester, 2004.
(21) Mahadeshwara, M. R. *Fourier Transform Infrared Spectroscopy – About Tribology*. https://www.tribonet.org/wiki/fourier-transform-infrared-spectroscopy/ (accessed 2024-02-27).
(22) Stevie, F. A.; Donley, C. L. Introduction to X-Ray Photoelectron Spectroscopy. *J. Vac. Sci. Technol. Vac. Surf. Films* **2020**, *38* (6), 063204. https://doi.org/10.1116/6.0000412.
(23) Mogk, D. *X-ray Photoelectron Spectroscopy*. Imaging and Chemical Analysis Laboratory, Montana State University. https://serc.carleton.edu/msu_nanotech/methods/xps.html (accessed 2024-02-27).
(24) *Carbon | XPS Periodic Table - FR*. https://www.thermofisher.com/fr/fr/home/materials-science/learning-center/periodic-table/non-metal/carbon.html (accessed 2024-03-05).
(25) Kim, D. H.; Jang, W.; Choi, K.; Choi, J. S.; Pyun, J.; Lim, J.; Char, K.; Im, S. G. One-Step Vapor-Phase Synthesis of Transparent High Refractive Index Sulfur-Containing Polymers. *Science Advances* **2020**, *6* (28), eabb5320. https://doi.org/10.1126/sciadv.abb5320.
(26) Kyeyune, B. Atomic Force Microscopy, 2017. https://doi.org/10.13140/RG.2.2.17356.10887.
(27) Feougier, R. Développement de Procédés de Microstructuration et Nanostructuration Hiérarchique, Thèse de doctorat, Université Grenoble Alpes, 2024.
(28) IGL Coatings. *The Science of Hydrophobicity*. IGL Coatings Blog. https://blog.iglcoatings.com/the-science-of-hydrophobicity/ (accessed 2024-02-28).

Chapter 3: Hydrophobic thin films: two different V3D3 based polymers

1. Introduction

As mentioned in the first chapter, hydrophobic surfaces can be good candidates for inhibiting bacterial adhesion. However, fluor containing compounds, which are the most common superhydrophobic substances, are becoming more and more problematic due to toxicity concerns[1,2]. However, there is a lack of research and development of fluorine-free superhydrophobic compounds[2]. Therefore, developing hydrophobic surfaces without the use of per- and polyfluoroalkyl substances (PFASs) is a challenge thoroughly justified.

In this study, (1,3,5)-trivinyl-(1,3,5)-trimethylcyclotrisiloxane or V3D3 was chosen for its hydrophobic and biocompatible properties. Indeed, although mostly known for its good dielectric properties[3,4], poly(V3D3) is a good candidate for antiadhesive surfaces since, as well as being hydrophobic, the three vinyl moieties of the V3D3 monomer (Figure 1) lead to a highly cross-linked and thus very stable polymer.

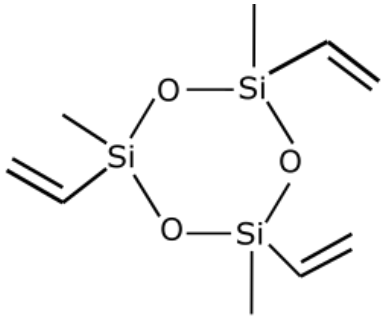

Figure 1 : (1,3,5)-trivinyl-(1,3,5)-trimethylcyclotrisiloxane (V3D3) monomer.

V3D3 based thin films were developed in the microelectronic field as dielectrics and they have been deposited in the past by electrodeposition[5], Plasma Enhanced Chemical Vapour Deposition (PECVD)[4], Hot Filament CVD (HFCVD)[6,7], initiated CVD (iCVD)[8,9] and Atmospheric Pressure Plasma-initiated CVD (AP-PiCVD)[10,11]. The latter vapour-based techniques allow the deposition of thin and conformal polymers, as well as being solvent-free[11].

Sharing some properties with polydimethylsiloxane (PDMS), which is one of the most used materials for biomedical devices[8], V3D3 has also been used for similar applications. Indeed, after studying the potential of PECVD-deposited hexamethylcyclotrisiloxane (D3) as an insulating biomaterial[12], Gleason's group used thin films of poly(V3D3) deposited by iCVD to coat neural implants[8,13,14]. Indeed, along with its electrical resistivity needed for recording neural activity, the flexibility, biocompatibility and stability of poly(V3D3) are essential characteristics for such devices sometimes designed to be used over years. The small size of these devices, and the need for smooth and conformal coatings with a good control over the thickness[13] justifies the use of iCVD. The technique also prevents any functional groups of the monomer being damaged. The devices were tested continuously over two and half years and no stability or functional issues arose during that time[13]. Finally, PC12 neural cells showed normal growth when in contact with poly(V3D3) coatings, therefore confirming the biocompatibility of the thin film[13].

For other applications, where more flexibility can be allowed concerning the chemistry of the coating, plasma-based techniques can be used to deposit thin films from the V3D3 monomer. Plasma

depositions offer other advantages than cannot be achieved with iCVD, such as versatility or working under atmospheric conditions. For instance, Abessolo Ondo *et al*. deposited plasma polymers of V3D3 using AP-PiCVD in order to obtain low-k insulating films[10,11]. Furthermore, plasma-based deposition methods are compatible with aerosol injection of the monomer[15] and do not require a radical initiator.

In this work, two deposition techniques were carried out and compared: initiated Chemical Vapour Deposition (iCVD) which leads to controlled polymer poly(V3D3) and Dielectric Barrier Discharge Cold Atmospheric Plasma (DBD-CAP) which gives plasma polymer pp(V3D3). Both methods are quite different from one another, with iCVD being a process carried out under vacuum with monomer and initiator injected in vapour form, and DBD-CAP taking place under atmospheric conditions and the precursor being injected alone in the form of an aerosol. The obtained thin films will then be compared to see whether the deposition technique has an influence on the coating's properties. More precisely, surface properties such as chemistry, roughness and wettability will be studied as these are some of the most important factors to consider when developing antibiofouling surfaces[16].

2. Poly(V3D3) thin films deposited by iCVD

2.1. Description of the process

Depositing poly(V3D3) had been carried out with the TEL iCVD equipment before this project and the process parameters used for this deposition were optimized in previous studies by our team.

As detailed in chapter 2, the chamber and the injectors were heated to 125°C while the substrate chiller was set to 100°C. Furthermore, in this process, the pressure was set to 1.5 Torr and the heated filament was around 285°C. The injection of the V3D3 monomer was induced with a flow of 0.1 g/min and the radical initiator tert-butyl peroxide (TBPO) was also vaporised and injected with a flow of 2 (standard cubic centimetres per minute) sccm. As it goes through the heated filament, the latter was pyrolyzed forming radicals which initiate the polymerisation of V3D3 when they come into contact with the monomer at the surface of the substrate. The time of deposition was adjusted depending on the desired thickness of polymer.

2.2. Thin films of poly(V3D3)

2.2.1. Kinetics

To evaluate the polymer film thickness, spectroscopic ellipsometry mapping was carried out. A Cauchy-Urbach model was then used to fit the measurements and evaluate the thickness of the coating.

As shown in Figure 2, which represents the average thickness over a 200 mm silicon wafer, in these deposition conditions, with the chiller temperature set to 100°C, the thickness of the thin film increases linearly with time and the calculated deposition rate is 1.4 nm/min. It has previously been shown that the linearity is kept even for much longer deposition times[3]. This figure also shows the low Mean Square Error (MSE) values obtained for the 3-angle measurement at the centre. Indeed, the global minimum is under 6 for all coatings, showing a good match between model and experimental data[17].

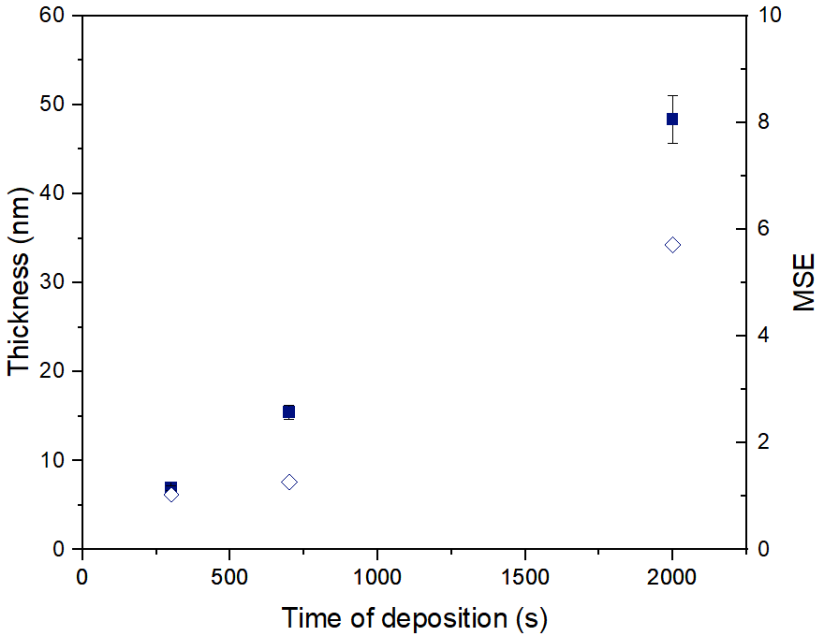

Figure 2 : Average thickness of poly(V3D3) deposited by iCVD onto a 200 mm silicon wafer (right Y axis, full squares). MSE obtained from the measurement at the centre (left Y axis, outlined diamonds).

As seen in Figure 3, spectroscopic ellipsometry mapping illustrates uniformity of poly(V3D3) thickness across the 200 mm silicon wafer. There is a slight edge effect. However, there is only a few nm difference between the maximum and minimum measured thicknesses. Furthermore, the same thickness pattern can be seen for all poly(V3D3) showing good reproducibility of the process.

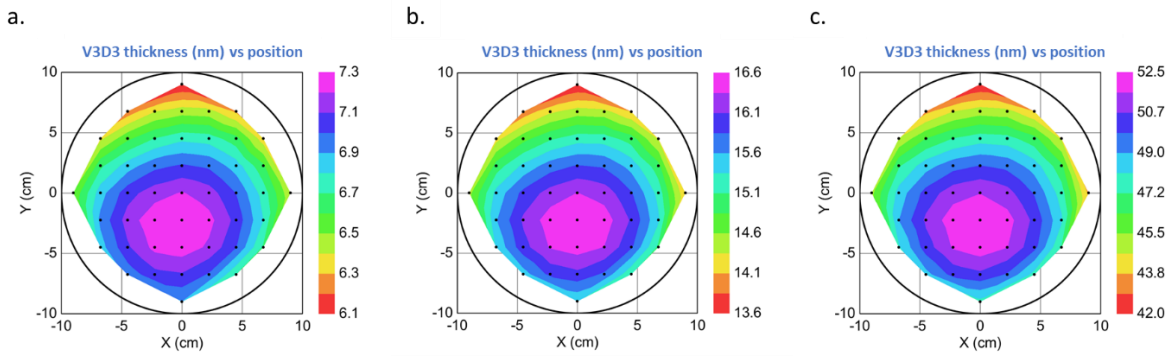

Figure 3 : Spectroscopic ellipsometry mapping of poly(V3D3) thin films deposited by iCVD onto a 200 mm silicon wafer for a time of deposition of a. 300 s b. 700 s c. 2000 s. The orientation of the wafer is always the same for the coatings and the measurements.

The kinetics of poly(V3D3) deposition, and iCVD polymer deposition in general, depend on the process parameters. As discussed in chapter 2, one of the most important parameters for the control of the iCVD polymer deposition is the saturation ratio P_m/P_{sat}, where P_m is the monomer's partial pressure, and P_{sat} is the saturated vapour pressure. This ratio depends on various process parameters such as the substrate temperature, the chamber pressure and the molar fraction of monomer. In these

deposition conditions, the P_m/P_{sat} ratio is around 0.0125 which is low in comparison to the recommended range of 0.4 to 0.7 found in the literature[18].

This can explain the differences in kinetics seen in the literature. Indeed, as each research team adjusts their process to their equipment and their applications, the P_m/P_{sat} ratio can be quickly modified[3,8]. For example, O'Shaughnessy *et al*. explained it was possible to tune the deposition rate of poly(V3D3) from 2 nm/min to 10 nm/min by varying the substrate temperature[8].

2.2.2. Poly(V3D3) chemistry

2.2.2.1. Radical polymerisation of V3D3

To characterize the polymerisation of the V3D3 monomer, Fourier Transform InfraRed (FTIR) spectroscopy can be a first step. Indeed, observing whether there remain any peaks corresponding to vinyl bonds and whether the monomer's functional groups have been conserved, can be a good guide for revealing radical polymerisation.

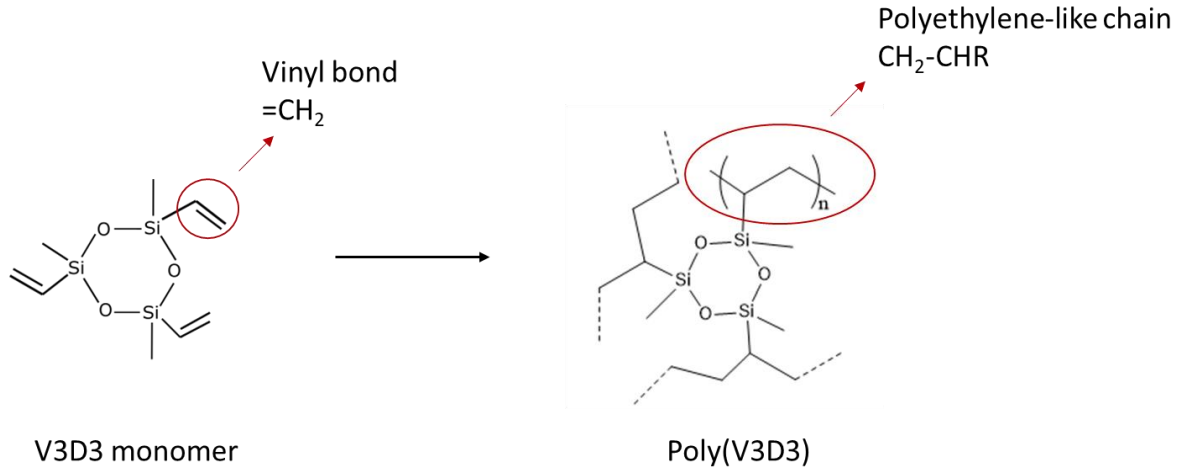

Figure 4 : Schematic representation of the transformation of V3D3 monomer into poly(V3D3).

In the FTIR spectrum of poly(V3D3) (Figure 5), which is similar to the spectra that can be found in the literature[8,9,19], a certain number of specific peaks can be noticed. By comparing it to the spectrum of V3D3 monomer, modifications in chemical bonds can be observed.

To begin, the band centred around 795 cm^{-1} comes from the contribution of various chemical bonds: Si-C, Si-O and $-CH_3$. Indeed, Si-C stretching in $Si-(CH_3)_x$ leads to absorbance peaks between 780 and 890 cm^{-1}, with a significate peak at 800 cm^{-1} for Si-C stretching in $Si-(CH_3)_1$[20]. Furthermore, between 780 and 890 cm^{-1} absorbance bands can come from CH_3 rocking[20]. Symmetric stretching in Si-O-Si also shows contributions around 745 cm^{-1} [20]. The absorbance peak at 995 cm^{-1} is the most specific peak of poly(V3D3) and is characteristic of asymmetric stretching in the Si-O-Si ring[9,10]. This peak appears at slightly lower wavenumbers than in the monomer's FTIR spectra, showing a modification of the strain on the siloxane cycle. However, it also demonstrates the conservation of the siloxane ring, as linear Si-O chains absorb at least 25 cm^{-1} higher[8]. In the monomer spectrum, another peak can be seen at 963

cm^{-1}. This is characteristic of CH_2 wagging in vinyl bonds[9]. The disappearance of this peak in the polymer spectrum shows the vinyl bonds have reacted. A slight shoulder can be seen coming off the Si-O-Si absorbance peak at 970 cm^{-1} in the poly(V3D3) spectrum. This is characteristic of wagging in Si-$(CH_2)_x$-Si[21] and cannot be seen in the monomer spectrum. The peak at 1260 cm^{-1} can be associated with C-H_3 bending in Si(-CH_3)$_x$ bonds[20]. More precisely, with a wavenumber of 1260 cm^{-1}, the Si-CH_3 is found in a conformation where the silicon is di-substituted by oxygen[22]. This configuration is known as D in the literature[12]. Here, we have CH_3-SiO_2C- in both monomer and polymer. The peak which can be seen in the monomer spectra at 1408 cm^{-1} can be attributed to a combination of Si-CH_2 deformation and Si-CH_3 antisymmetric stretching[8]. This peak should be seen in the polymer FTIR spectra as well[9]. However, as it is not a very intense peak it is likely lost in the noise.

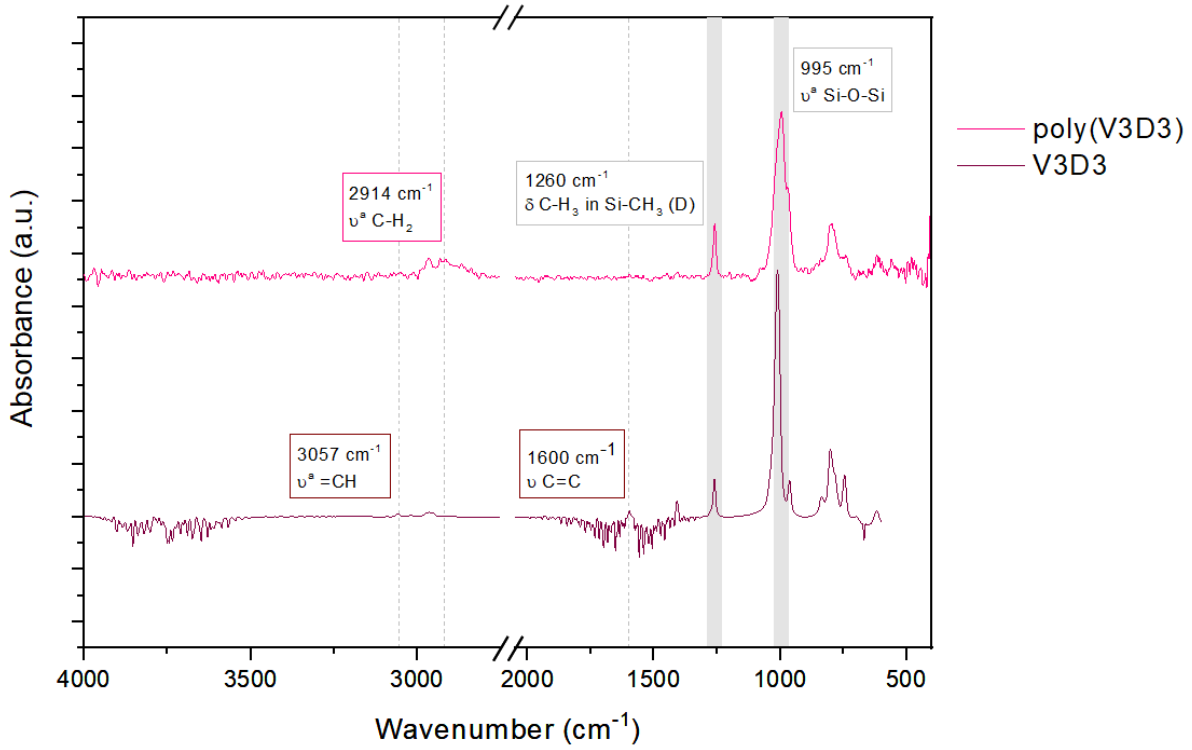

Figure 5 : FTIR spectra of poly(V3D3) deposited by iCVD onto a 200 mm silicon wafer and the V3D3 monomer.

The most important peak which can only be seen in the monomer spectra is the one which appears around 1600 cm^{-1}. This is characteristic of C=C stretching and is therefore visible due to the vinyl bonds in the monomer. In the polymer however, as it is formed by free-radical polymerisation, the vinyl bond disappears and is replaced by a polyethylene-like chain[8,9] (-CH_2-CHR-) (where R is the siloxane group), as it can be seen in Figure 4. To verify this, the CH_x peaks around 3000 cm^{-1} can be analysed (Figure 6).

Around 3000 cm^{-1} various overlapping bands and peaks can be seen for both monomer and polymer (Figure 6). Indeed, asymmetric and symmetric stretching in CH_3 lead to absorbance at 2967 and 2904 cm^{-1} respectively[9,23]. These peaks contribute to both monomer and polymer spectra. Furthermore, asymmetric and symmetric stretching in CH_2 lead to absorbance peaks at 2914 and 2861 cm^{-1} respectively[9]. These bands appear in the polymer spectra. However, in the monomer, the only existing CH_2 bonds are found in vinyl groups =CH_2. Their absorbance can be seen in the monomer's FTIR spectrum at 3057 and 3018 cm^{-1} for asymmetric and symmetric stretching respectively[7,9].

Contributions from CH bonds in vinyl groups are also present at 2974 and 2935 cm^{-1} for asymmetric and symmetric stretching respectively[9]. These changes in absorbance peaks from monomer to polymer spectra, show the transformation of vinyl groups into alkyl CH_2 bonds, which is in accordance with the free-radical polymerisation mechanism[14].

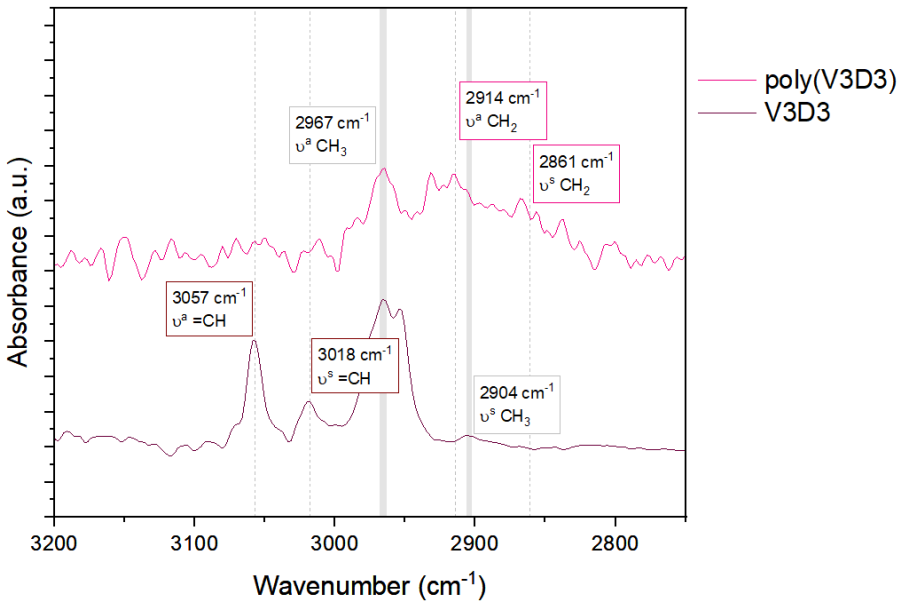

Figure 6 : FTIR spectra zoomed between 2750 and 3200 cm^{-1} of poly(V3D3) deposited by iCVD onto a 200 mm silicon wafer and the V3D3 monomer.

Furthermore, as it can be seen in Figure 7, the chemical composition of poly(V3D3) does not change with the thickness of the deposited thin film.

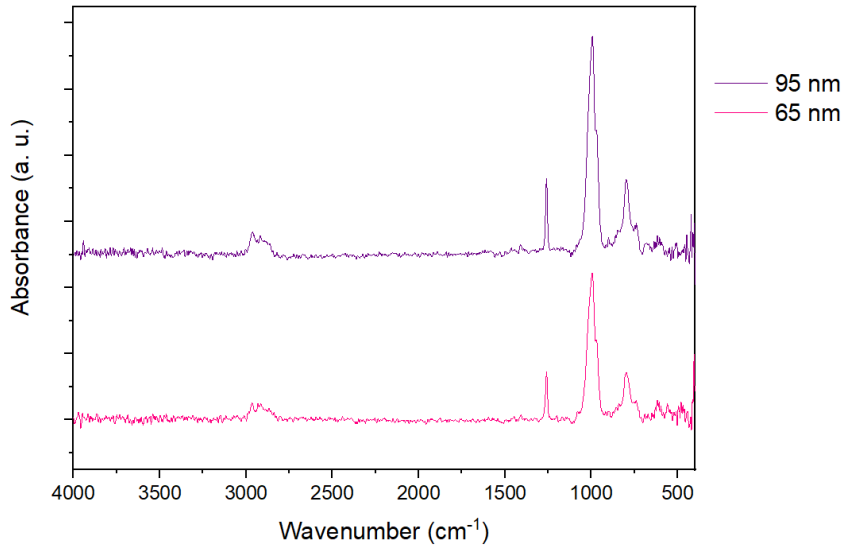

Figure 7 : FTIR spectra of poly(V3D3) of different thicknesses deposited by iCVD.

These results show that iCVD deposition of poly(V3D3) leads to a thin film conserving the functional Si-O-Si rings of the monomer while polymerising through the vinyl bonds, confirming literature data[8,9]. The obtained polymer is therefore constituted of PE-like chains crosslinking the siloxane functional groups.

2.2.2.2. Chemistry at the surface: X-ray Photoelectron Spectroscopy (XPS)

In the previous section, poly(V3D3)'s chemical bonds were analysed by FTIR spectroscopy. This technique allows the study of functional bonds within the bulk of the material. In order to complete the analysis of the polymer's chemistry, and more precisely, of its surface chemistry, X-ray Photoelectron Spectroscopy (XPS) was carried out.

As shown in Table 1, the atomic percentages of carbon (C), oxygen (O) and silicon (Si) at the surface of iCVD-deposited poly(V3D3) are very similar for thin films of different thicknesses. On average, the elemental proportions are: 60%, 23% and 17% respectively. If we compare these proportions to the proportions found in the V3D3 monomer, we can see they are very similar. Indeed, in the V3D3 monomer, there are 3 O atoms, 3 Si atoms and 9 C atoms. Therefore, the oxygen on carbon ratio (O/C) in the monomer is 0.33. According to these XPS results, the O/C ratio at the surface of the polymer is 0.39. The silicon on carbon ratio (Si/C) in the monomer is also 0.33. In the polymer, this Si/C ratio is 0.29. Finally, we can compare the oxygen on silicon ratio (O/Si) ratio in the monomer which is 1, to the O/Si ratio at the surface of the polymer which is 1.35. These differences may come from the presence of TBPO in the polymer film as it is used in the polymerisation process as a radical initiator, or from atmospheric contamination which may also modify the atomic percentages of C and O at the surface of these films.

Table 1 : Atomic percentage of C, O and Si obtained by XPS analysis in poly(V3D3) deposited by iCVD with a substrate temperature of 100°C.

Film thickness (nm)	Atomic percentage		
	C 1s	O 1s	Si 2p
V3D3 monomer	60	20	20
15	59.4	23.5	17.1
48	59.7	23.0	17.4

High resolution XPS spectra shown in Figure 8 highlight the chemical bonds and show only bonds which were expected. Indeed, for C 1s, the highest peak from the deconvolution emerges with a binding energy of 284.8 eV representing a combination of C-C and C-Si bonds[24,25]. Indeed, it has previously been shown that when C/Si > 1.5, the binding energy of C-Si bonds cannot be differentiated from that of C-C bonds[26]. A second, smaller peak can be seen centred at 286.1 eV representing C-O bonds[23]. These bonds can come from the terminating groups issued from the TBPO radicals, as well as organic contamination. This is coherent with radical polymerisation creating polyethylene-like chains between siloxane cycles. For Si 2p, deconvolution leads to a peak at 102.3 eV which corresponds to C-Si-O with di-substituted silicon[23,27]. A smaller peak centered at 103.7 eV shows a small contribution (8 %) of SiO_X. For O 1s, the binding energy at 532.5 eV highlights O-Si bonds[24]. A small contribution of O-C also appears at 533.6 eV[27].

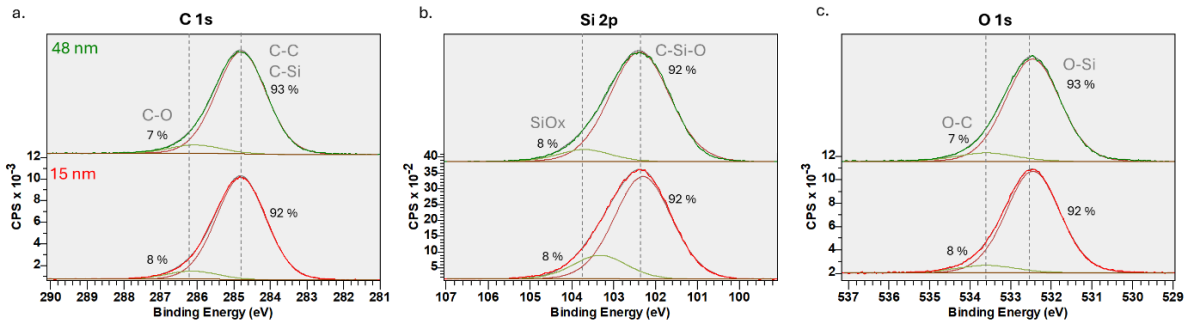

Figure 8 : High resolution X-ray Photoelectron Spectra of a. C 1s, b. Si 2p, c. O 1s for poly(V3D3) deposited by iCVD.

These spectra further demonstrate that no differences can be seen between two polymers of different thicknesses.

2.2.2.3. Estimation of the chain length

In O'Shaughnessy's study of iCVD-deposited poly(V3D3)[8], the elemental ratios obtained by XPS were used to calculate an estimation of the length of the polymer chains.

The equations used by O'Shaughnessy to determine the polymer chain lengths are the following:

$$\frac{Si}{C} = \frac{3M}{9M + 4I}$$

$$V = 3M$$

$$length = \frac{V}{0.5\, I}$$

In these equations, Si and C correspond to the number of silicon and carbon atoms in the polymer, respectively; M represents the number of monomer molecules; I is the number of initiator radicals created through the pyrolysis of TBPO; V is the number of vinyl groups that were transformed and length corresponds to the number of monomer units linked together in the polymer chain[8]. These equations are written with the assumption that all vinyl groups react and that 2 radical initiator groups I are needed for one chain: one to initiate it and one to terminate it[8].

With the atomic percentages measured for our 48 nm thick polymer, as seen in section 2.2.2.2, we have a Si/C ratio of around 0.29.

$$\frac{Si}{C} = 0.29 = \frac{V}{3V + 4\dfrac{V}{0.5\, length}}$$

$$\Longrightarrow length \simeq 17.8$$

According to these equations, our polymerisation process leads to chain lengths of around 18 units. This result is higher than in O'Shaughnessy's publication[8] where the Si/C ratio was 0.26, and the resolution of these equations led to a chain length of 8.9 units. These differences could be caused by different process parameters. Indeed, as seen on the Clausius-Clapeyron diagram in Figure 9, in both

cases the V3D3 monomer is in vapour form but with different pressure and temperature values which would lead to different P_m/P_{sat} ratios. Indeed, with the information given in O'Shaughnessy's article[14], the estimated P_m/P_{sat} is around 0.12, whereas in our conditions, the calculated P_m/P_{sat} is 0.016.

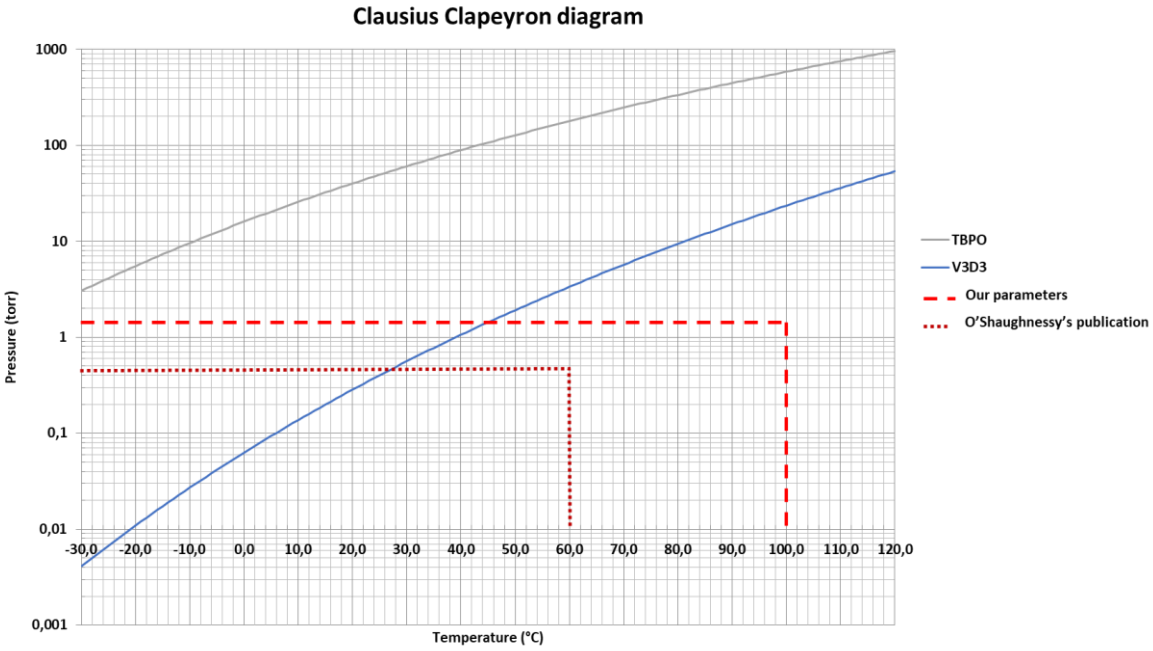

Figure 9 : Clausius-Clapeyron diagram of V3D3 and TBPO showing the pressure and temperature parameters used in our process and for depositing the poly(V3D3) studied by O'Shaughnessy and giving an estimated chain length of 8.9 units[8].

This is contradictory with the theory as when P_m/P_{sat} increases, the concentration of monomer adsorbed at the surface increases[18] and it has been shown that the molecular weight of polymers increases with the monomer concentration and thus with P_m/P_{sat}[28]. Therefore, higher P_m/P_{sat} should lead to higher molecular weight and thus longer chain length. However, the XPS spectra being only representative of the top few nm of the thin film (around 6.5 nm), and atmospheric contamination modifying the exact atomic percentages, it is quite difficult to ascertain the Si/C ratio used in the calculation of the chain length. Furthermore, this equation hypothesizes that all vinyl bonds in the precursor react during polymerisation. However, it has previously been shown that it is not always the case for V3D3 monomers and that this can depend on the process parameters. Indeed, the lower the substrate temperature, the more unreacted vinyl bonds can be found in the final polymer[23]. Therefore, there may be more unreacted vinyl moieties in O'Shaughnessy's poly(V3D3) since it was deposited at lower temperature, leading to shorter chains. However, it is likely that in both cases the thin film is composed of polymer chains of varying lengths.

2.2.2.4. Poly(V3D3) density

X-ray Reflectivity (XRR) was carried out to study the density of the polymer. As well as giving the material's density, XRR also gives the thickness of the coating. Here, the thickness of the poly(V3D3) given by XRR is 46 nm. This value is very close to the 48 nm measured by ellipsometry. Furthermore, the XRR model requires a second layer which takes into account any surface modifications of the

coating from contamination. In this case, the model fits 1.9 nm to this surface layer. Thus, the final thickness is even closer to the value measured by ellipsometry.

Table 2 : Density of poly(V3D3) obtained by X-ray Reflectometry (XRR).

Time of deposition (s)	Thickness (nm) by ellipsometry	Thickness (nm) by XRR		Density (g/cm^3)
		Polymer	Surface layer	
2000	48	46	1.9	1.18

This experiment led to a polymer density of 1.18 g/cm^3 for a 48 nm thick poly(V3D3) film. As a factor of comparison, polydimethylsiloxane (PDMS) has a mass density of 0.97 g/cm^3.[29] The higher value for poly(V3D3) is due to the fact that while PDMS is a linear polymer of siloxanes, in poly(V3D3) the three vinyl groups in the precursor lead to a highly cross-linked matrix. Furthermore, a material density of 1.1 has been noted for similar organosilicon thin films deposited from 1,1,3,3-tetramethyldisiloxane (TMDSO) using a microwave induced remote afterglow[30].

2.2.3. Poly(V3D3) thin film roughness

Atomic Force Microscopy (AFM) was carried out in order to evaluate the surface roughness of poly(V3D3) and see whether it varies with the thin film thickness.

As shown in Figure 10 and Table 3, the iCVD-deposited poly(V3D3) coatings are relatively smooth and the aspect of the topography does not change as the thickness increases. For all poly(V3D3) samples, the coating is fully covering, and no pinholes can be seen, even for the 7 nm thick polymer. Furthermore, the Rq roughness is under 0.4 nm for all coatings (Table 3). It can be seen that although this roughness increases slightly with the thin film thickness, the increase is not significant. The z range which gives the difference between the lowest and highest points also remains low for all thicknesses. Indeed, it is conserved under 4 nm for all samples, even when the polymer has a thickness of 48 nm.

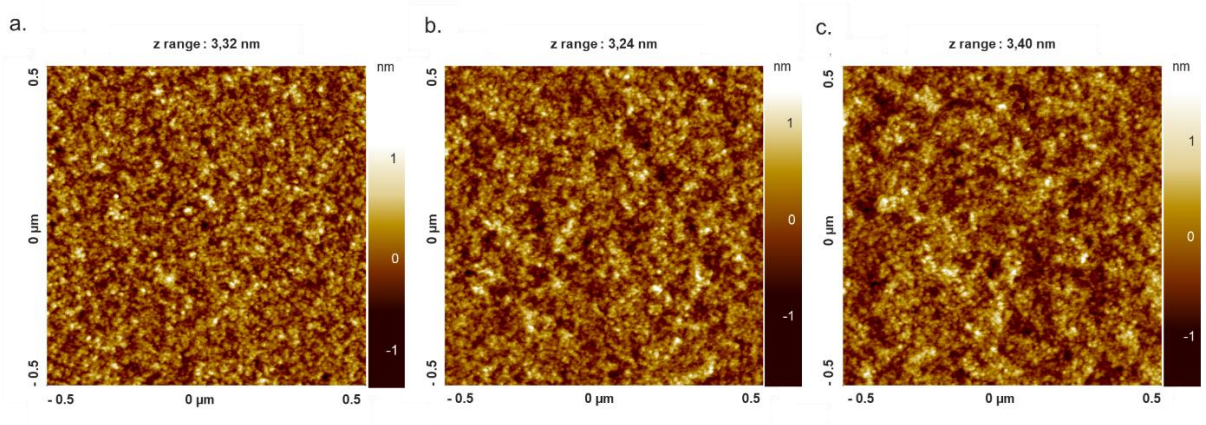

Figure 10 : Atomic Force Microscopy images of poly(V3D3) deposited by iCVD for different times: a. 300 s; b. 700 s; c. 2000 s.

These results are coherent with the literature. Indeed, O'Shaughnessy *et al.* also measured a RMS roughness of 0.4 nm for poly(V3D3) coatings on silicon[13]. They also highlighted the low peak-to-peak distance (< 0.9 nm) of their thin film, demonstrating that the film's roughness is uniform. Sung Gap Im's team also deposited poly(V3D3) with a low RMS roughness (0.6 nm)[31]. Finally, Chara Zavvou's work highlights the conservation of this low surface roughness even for poly(V3D3) coatings of much higher thickness. Indeed, she shows a RMS roughness of 0.37 nm for a 700 nm thick polymer[3].

Table 3 : Root mean square roughness Rq (or RMS) of poly(V3D3) deposited by iCVD for different times.

Time of deposition (s)	Thickness (nm)	Rq (nm)	Z range (nm)
300	7	0.31	3.32
700	15	0.36	3.24
2000	48	0.38	3.40

2.2.4. Hydrophobic thin films

To study the hydrophobicity of poly(V3D3) thin films, water contact angles (WCA) were measured.

The results in Figure 11 show that the polymer is hydrophobic with a WCA of 95° whatever the film thickness. Therefore, as it was already shown for surface chemistry and roughness, the thickness of poly(V3D3) does not influence the wettability of the coating.

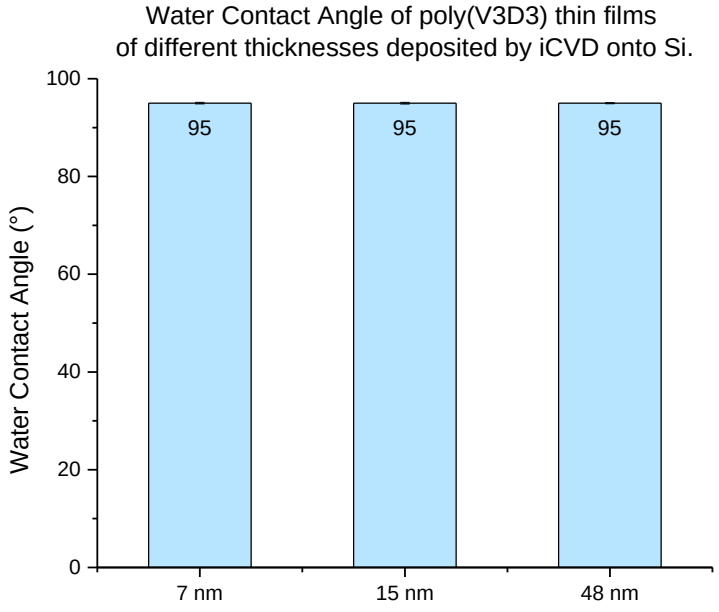

Figure 11 : Water Contact Angle of poly(V3D3) of different thicknesses deposited by iCVD.

In the literature, poly(V3D3) with WCAs of 105° have been recorded[32]. However, this was for poly(V3D3) films deposited using perfluorobutanesulfonyl fluoride (PFBSF) as radical initiator. The fluorine content of PFBSF certainly explains the slightly higher hydrophobicity. For poly(V3D3) thin

films, initiated, as in our case, with radicals issued from TBPO, WCAs of 85° are found in the literature[31]. This value is slightly lower however the wettability behaviour of these films is similar is all three cases.

2.2.5. Stability of poly(V3D3) coatings

2.2.5.1. Stability in toluene, an apolar organic solvent

To evaluate the stability of the poly(V3D3) coating, 2 x 2 cm² samples of the polymer-coated silicon wafers were first dipped into toluene, an apolar organic solvent, for 2 minutes. After this time, they were removed from the solvent and dried by centrifugation. Thickness was then measured by spectroscopic ellipsometry and compared to the thickness measurements before the stability test.

As it can be seen in Figure 12, no significant differences can be seen before and after the stability test. The optical index of the material was not modified either (n = 1.48 at 632.8 nm), further highlighting the stability of the polymer. The insignificant differences between the before and after thickness measurements thus lead to the conclusion that poly(V3D3) deposited with a substrate temperature of 100°C is stable in toluene and thus highly crosslinked.

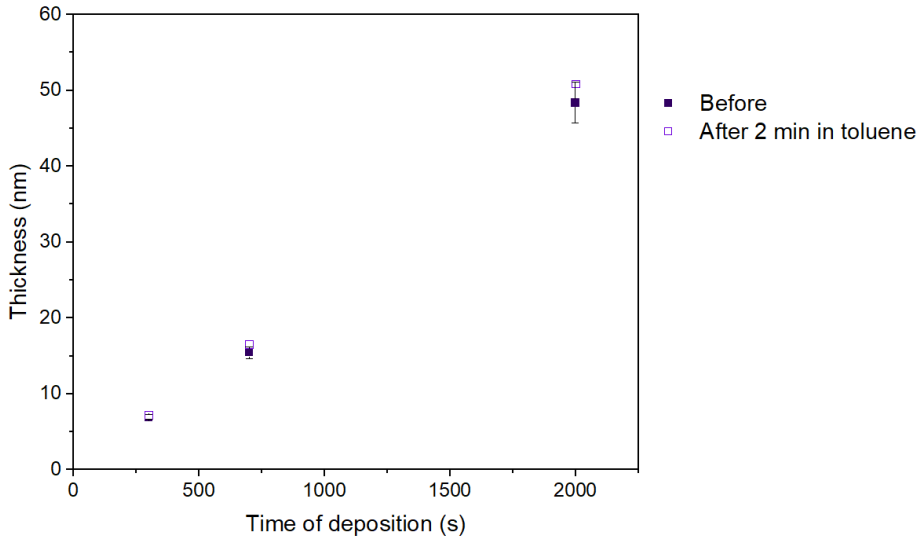

Figure 12 : Thickness of poly(V3D3) before and after 2 min soaking in toluene to test the stability of the polymer.

However, it has previously been shown by Zavvou *et al.* that when depositing this cyclic siloxane with lower substrate temperatures, the thin film can become soluble in toluene. Indeed, it was shown that when the former was 70°C, a 10 % relative thickness loss was observed. When lowering the substrate temperature to 40°C, the thickness loss in toluene was nearly 100 %. This is due to the presence of uncrosslinked small molecules, such as V3D3 monomers or oligomers, in the film, which can be solubilised by the solvent[23]. Depositing poly(V3D3) at 100°C allows to avert this problem.

2.2.5.2. Stability in PBS

For carrying out microbiology assays to test the potential antiadhesive and antibiofouling, as it will be further detailed in chapter 6, coated samples will need to be incubated with bacterial suspensions. These suspensions can be prepared in Phosphate Buffer Saline (PBS), or richer culture

mediums. This buffer solution is standard use in microbiology as it has the same concentration in salts as the human body making it the buffer solution closest to physiological serum.

As in the stability test in toluene, samples were cut to 2 x 2 cm². They were then soaked in PBS 1X for 24 hours and then dried by centrifugation. Spectroscopic ellipsometry was used to measure the thickness of the polymer after the stability test.

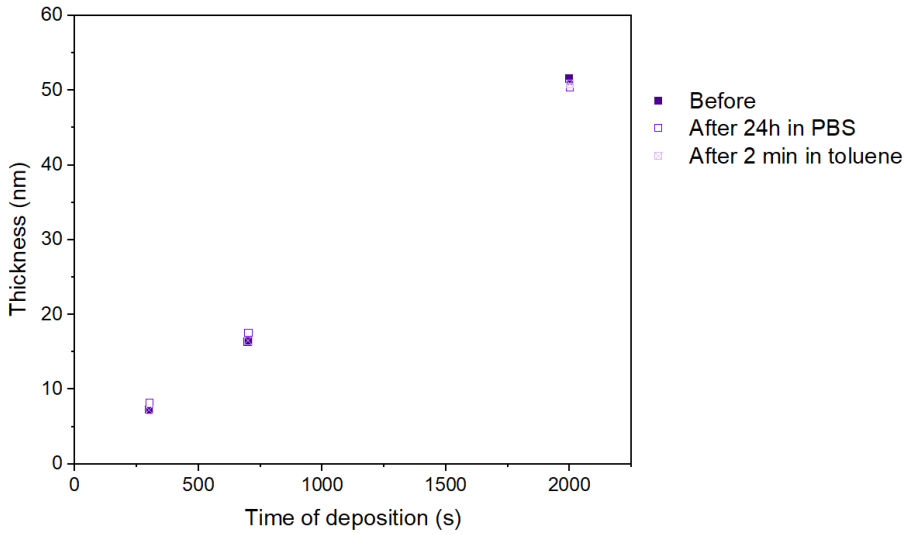

Figure 13 : Thickness of different poly(V3D3) coatings before and after 24 h soaking in PBS to test the stability of the polymer.

Like for the 2 minutes stability test in toluene, after 24 hours in PBS, there are no significant thickness losses observed, no matter the initial film thickness. This could be expected as poly(V3D3) is a highly 3D cross-linked polymer. Furthermore, no change in optical index (n = 1.48 at 632.8 nm) confirmed the integrity of the coating after the stability test.

These stability tests in toluene and PBS confirm the excellent stability of poly(V3D3) which has previously been highlighted in the literature. Indeed, Achyuta *et al*. saw no thickness loss in various solvents[19]. O'Shaughnessy *et al.* also demonstrated that poly(V3D3) can maintain its electrical properties for 2 years while soaking in a solution simulating a biological sample[14].

2.3.Conclusions on poly(V3D3) deposited using iCVD

In this first part, poly(V3D3) deposited using the iCVD technique has been studied. This technique allows the formation of homogeneous and smooth films with a thickness that increases linearly overtime. Higher thickness does not affect the properties of the polymer which remain constant.

Furthermore and in agreement with the literature[8], it was shown that this method of polymerisation leads to the conservation of the V3D3 monomer's siloxane cycle, and that these cycles are linked together through a polyethylene-like backbone chain. However, V3D3 having three vinyl groups which react during polymerisation, the final polymer is not a linear one but rather a highly cross-linked matrix. This explains the high stability of the thin film in aqueous solutions and organic

solvents as well as its good adhesion on silicon. In comparison to PDMS, another siloxane-based polymer which is often used in the biomedical industry, poly(V3D3) shows higher density.

As explained in the introduction, V3D3 is a precursor which offers promising properties with various deposition techniques. In this next section, we will study the plasma polymerisation of V3D3 using DBD-CAP. Indeed, operating in atmospheric conditions has many advantages such as being able to change substrate more easily and reducing costs.

3. Plasma polymer thin films of V3D3 deposited by DBD-CAP

3.1. Process description

In order to deposit plasma polymers, DBD-CAP was carried out using Molecular Plasma Group's Plasmaspot®.

As detailed in chapter 2, in this DBD-CAP process, V3D3 was used in aerosol form carried by nitrogen with a flowrate between 700 and 900 sccm. The flow of monomer was diluted with 6000 sccm of nitrogen. Nitrogen was also used as the plasma gas with a flowrate of 80 000 sccm which is the recommended operating setting. The plasma power was modified between 150 and 250 W. The movement of the torch was configured to cover a 100 mm silicon wafer.

In the first part of this section, plasma polymers obtained with different monomer flowrates and plasma powers will be studied. In the second part, these parameters will be fixed and the torch movement will be repeated to overlap the coatings.

3.2. DBD-CAP thin films of V3D3

3.2.1. Increasing the pp(V3D3)'s thickness

Unlike the iCVD deposition method, where a deposition time can be set to tune the film's thickness, the thickness of the plasma polymer is increased by adjusting the deposition parameters such as the monomer flowrate and the plasma power. These parameters were therefore varied and mapping was carried out by spectroscopic ellipsometry on the deposited plasma polymers. The experimental data was fit with a Cauchy-Urbach model.

Figure 14 shows the thickness mapping images of some of these plasma polymers pp(V3D3) on 100 mm silicon wafers. This highlights the homogeneity of the thickness over the substrate as only a few nanometres difference can be seen between the minimum and maximum thicknesses across the substrate (between 24.8 nm and 26.9 nm for the thickest coating (Figure 14f)).

The average thickness over these wafers is given in Figure 15 which shows an increase in the film thickness with a higher monomer flowrate. Indeed, for a plasma power fixed at 200 W for example, the coating's thickness varies from 14.9 to 20.7 nm as the monomer flowrate is modified from 700 to 900 sccm. Thus, the more monomer injected into the plasma torch, the thicker the thin film can grow. However, this method for increasing the plasma polymer's thickness is limited by the injection of monomer. Indeed, the manufacturer recommends setting the precursor injection leading to a reflux of around 1 droplet per second in its container. With V3D3, these guidelines cannot be followed when increasing the flowrate over 900 sccm.

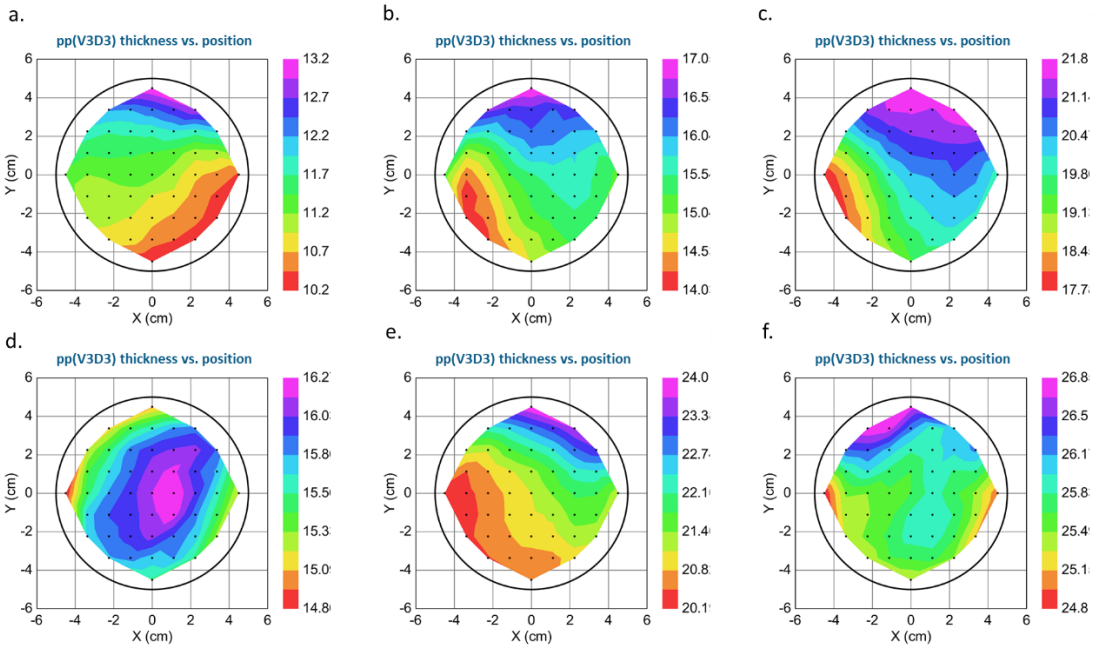

Figure 14 : Spectroscopic ellipsometry mapping of plasma polymers pp(V3D3) deposited by DBD-CAP onto a 100 mm silicon wafer with a monomer flowrate and plasma power respectively of a. 700 sccm and 150 W; b. 700 sccm and 200 W; c. 700 sccm and 250 W; d. 900 sccm and 150 W; e. 900 sccm and 200 W; f. 900 sccm and 250 W. The orientation of the wafer is always the same for the coatings and the measurements.

The second conclusion that can be drawn from Figure 15 is that the plasma polymer's thickness also increases with the plasma power. This can be due to more fragmentation of the monomer by higher powers, thus creating more reactive species which can create bonds with one another. Indeed, the plasma polymerization occurring at atmospheric pressure is thought to be similar to the mechanism for plasma polymerization under vacuum suggested by Yasuda which is based on fragmentation into radicals and recombination[33]. It has been demonstrated that for low powers, the deposition rate increases with the Yasuda parameter W/FM, where W is the discharge power, F is the monomer flowrate and M is the molecular weight of the monomer[33,34].

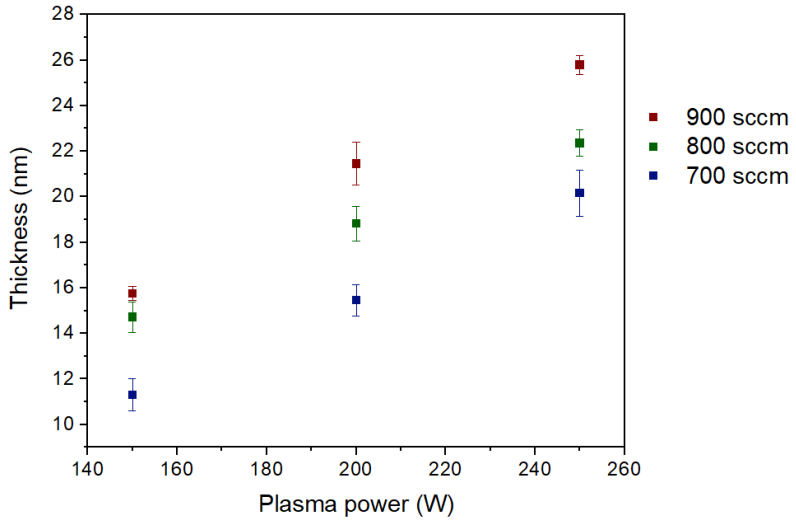

Figure 15 : Average thickness of pp(V3D3) deposited by DBD-CAP with different monomer flows and plasma powers.

These first results show that the thickness of pp(V3D3) can be raised by increasing the amount of precursor injected into the torch or increasing the plasma power used to activate the monomer. However, as the Plasmaspot®'s torch movement can be adjusted, it is also possible to overlap coatings by repeating the pattern of the plasma jet. This was carried out up to 5 repetitions with a monomer flowrate of 700 sccm and a plasma power of 150 W. Spectroscopic ellipsometry was carried out in the same conditions as previously (Figure 16).

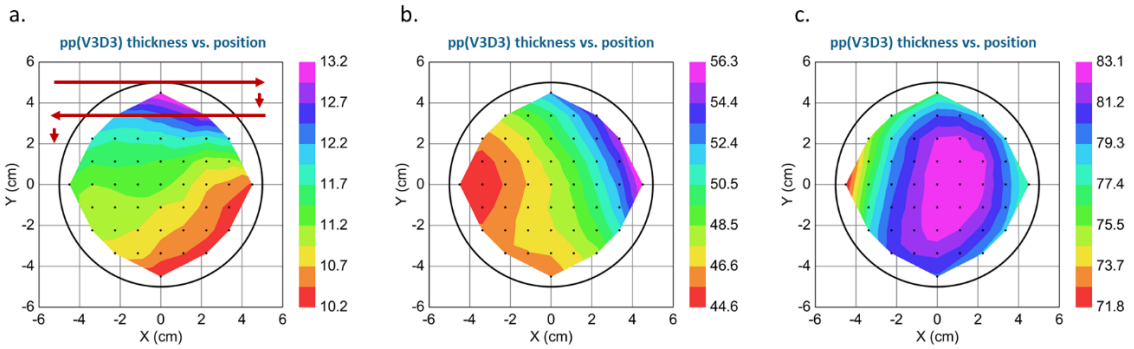

Figure 16 : Spectroscopic ellipsometry mapping of plasma polymers of V3D3 deposited by DBD-CAP onto a 100 mm silicon wafer with a monomer flowrate of 700 sccm and plasma power respectively of 150 W. The plasma torch pattern is overlapped a. once, b. three times and c. five times. The orientation of the wafer is always the same for the coatings and the measurements. The red arrows show the torch movement.

These mapping images show that the thickness of the coating increases as the plasma torch pattern is repeated. The average thickness over the silicon wafer as the torch movement is repeated is shown in the following figure.

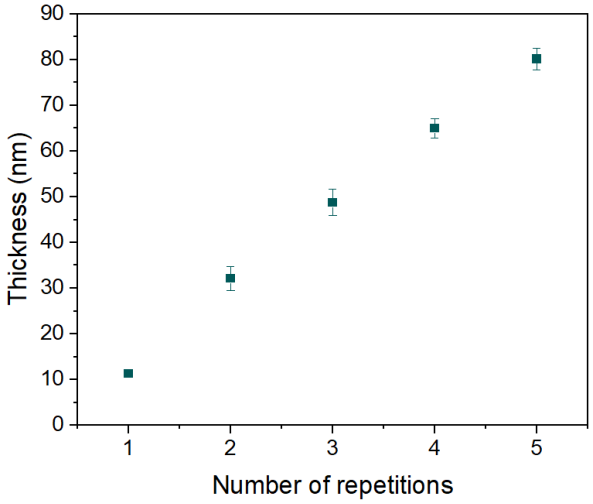

Figure 17 : Thickness of plasma polymers of V3D3 deposited by DBD-CAP with MPG's Plasmaspot® with a monomer flow of 700 sccm, a plasma power of 150 W and by repeating the number of overlapping plasma torch movements.

These measurements show an increase of the polymer film thickness with the number of plasma torch repetitions. Indeed, with these deposition conditions, one coating led to a thickness of 11 nm. This can be increased to 80 nm after 5 repetitions of the plasma torch movement. These

measurements underline the efficiency of this technique for increasing the plasma polymer thickness. However, as the thickness increases, lines appear following the torch's pattern. Although these lines do not appear on the ellipsometry mapping images, this leads to believe that as the thickness increases, thickness inhomogeneities may appear.

Figure 18 : Photo of pp(V3D3) deposition on a silicon wafer, showing the appearance of lines following the plasma torch's movement pattern.

3.2.2. Chemistry of plasma polymers pp(V3D3)

3.2.2.1. Analysis of chemical bonds found in pp(V3D3) by FTIR spectroscopy

Unlike iCVD, the DBD-CAP technique does not require the use of a radical initiator to begin the polymerisation. With this method, the plasma acts directly on the precursor, in this case the V3D3 monomer, breaking it up to make new species. The latter then react with one another to create the plasma polymer coating.

To study how the plasma affects the chemistry of the final thin film in comparison with the iCVD technique, which results in a conventional polymer, FTIR was carried out. Figure 19 shows the spectra for poly(V3D3) and pp(V3D3) thin films, deposited by iCVD and DBD-CAP respectively. Both coatings were 65 nm thick.

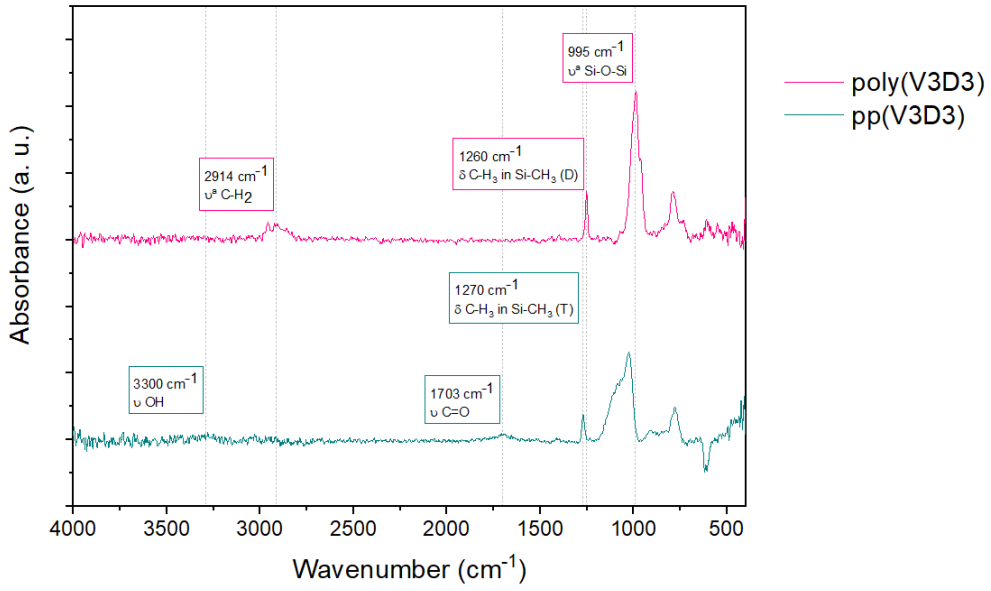

Figure 19 : FTIR spectra of plasma polymer pp(V3D3) deposited by DBD-CAP in comparison to conventional polymer poly(V3D3) deposited by iCVD. Both coatings were 65 nm thick.

The band centred around 795 cm^{-1} can be seen for both polymers. This comes from the contribution of Si-C, Si-O and -CH_3 bonds. The absorbance peak found at 995 cm^{-1} in the spectra of poly(V3D3) is slightly shifted to higher wavenumbers and most importantly broadened for pp(V3D3). This shows that while iCVD conserves the cyclic siloxane group, the plasma-based deposition method alters this ring. Further, the peak found at 1260 cm^{-1} for the iCVD-deposited poly(V3D3) is also shifted to higher wavenumbers and appears at 1270 cm^{-1} for pp(V3D3). This peak is characteristic of C-H_3 bending in Si(-CH_3)$_x$ bonds[20]. The shift in wavenumber underlines a modification of the Si's surrounding environment. Indeed, while the Si is in a D conformation (CH_3-SiO_2C-), di-substituted by O, in the conventional poly(V3D3), it is in a T conformation (CH_3-SiO_3-), tri-substituted by O, in the pp(V3D3) [12,22] (Figure 20). For this conformation to appear and Si to become tri-substituted, ring-opening and recombination must occur.

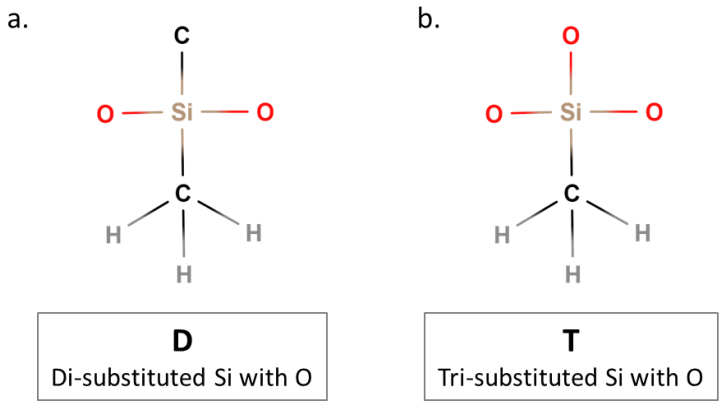

Figure 20 : Schematic representation of silicon in a D and T conformation.

In the spectra of the pp(V3D3) a new absorbance peak can be found at 1703 cm^{-1} which is characteristic of C=O stretching[35]. This chemical bond could be the result of reorganisation of the reactive species created by the plasma's action on the V3D3 monomer. It could also have been created from species found in the surrounding atmosphere as this deposition method is not carried out under vacuum. The band centred around 2900 cm^{-1} which can be seen in the spectra of poly(V3D3) and is the result of a combination of stretching peaks from CH_3 and CH_2, disappears in the pp(V3D3) spectra, despite the presence of CH_3 in Si-CH_3 bonds. This suggests the resulting plasma polymer contains much less carbon than the conventional polymer. Furthermore, it confirms that unlike in iCVD, the polymerisation does not occur through the vinyl bonds leading to polyethylene-like chains. In the FTIR spectra of pp(V3D3), there also seems to be a slight emergence of an absorbance band centred around 3300 cm^{-1}. This would correspond to O-H stretching which could appear from the surrounding environment. In fact, this spectrum resembles the one found in Burkey and Gleason's publication on thin films deposited from V3D3 and water by pulsed plasma CVD[36]. With this comparison, the incorporation of oxygen and/or humidity from the atmosphere seems to be a valid explanation.

Deconvolution of the band around 1000 cm^{-1} corresponding to Si-O-Si bonds should bring more precision concerning the modifications of the siloxane cycle. This deconvolution leads to three peaks centred at 1020, 1051 and 1102 cm^{-1} (Figure 21).

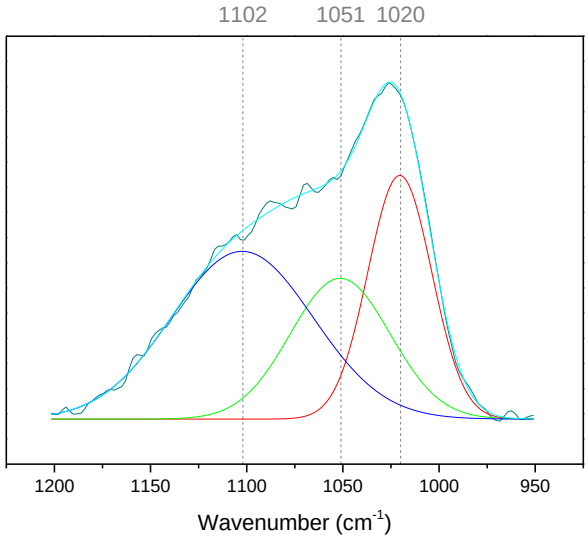

Figure 21 : Deconvolution of the absorbance peak around 1000 cm^{-1} in the FTIR spectra of pp(V3D3) deposited by DBD-CAP.

These peaks can be compared to the peaks obtained in Grill's publication[20], where deconvolutions of the Si-O-Si symmetric stretching absorbance band found in SiCOH films deposited by PECVD of tetramethylcyclotetrasiloxane (TMCTS) were carried out. Indeed, it was shown in this study that deposition and annealing of TMCTS led to broader absorbance bands in the FTIR spectra than for the corresponding monomer. In particular, the Si-O-Si asymmetric stretching band appears at 1063 cm^{-1} for the TMCTS monomer. For the PECVD deposited film, the equivalent band becomes larger and can be deconvoluted into three peaks centred at 1023, 1063 and 1135 cm^{-1}. These peaks, which are close to those in Figure 21, were attributed to asymmetric stretching in Si-O-Si in different conformations[37].

The peak at 1023 cm^{-1} was attributed to the asymmetric stretching of Si-O-Si bonds with a bond angle under 144°, such as found in silicon suboxides[20,37]. We can suggest the same siloxane configurations are responsible for our deconvolution peak at 1020 cm^{-1}. Secondly, the peak centred at 1063 cm^{-1} for annealed TMCTS films is attributed to the stretching of siloxane bonds in a network structure with Si-O-Si angles of around 144°[20]. For our films, we have a peak centred at 1051 cm^{-1} in the case of the plasma polymers. We can therefore hypothesize that DBD-CAP leads to breaking the Si-O-Si cycles and allowing them to form new bonds, creating a larger Si-O-Si network. The last peak from Grill's deconvolution appears at 1135 cm^{-1}, which is slightly higher than for our plasma polymers. This peak is attributed to Si-O-Si stretching in a cage structure, with Si-O-Si angles around 155°[20]. As the initial Si-O-Si cycle is smaller initially with V3D3 than with TMCTS we can expect different angles after plasma polymerisation which may explain the higher wavenumber in the case of TMCTS for the last deconvolution peak.

FTIR spectroscopy analysis of pp(V3D3) thin films showed similarities with the poly(V3D3) spectra obtained after iCVD deposition. However, although the initial monomer was identical in both experiments, and the film's thickness did not seem to effect either type of polymer, the different techniques led to variations in the chemical bonds found in the final coatings.

3.2.2.2. Detailed analysis of the chemical bonds present at the surface of pp(V3D3) coatings

XPS was carried out to bring more precision to the surface chemistry and the existing chemical bonds in this plasma polymer. The atomic percentages of C, O, N and Si are shown in Table 4. These results show similar composition for all thin films demonstrating there does not seem to be an influence of the number of deposition cycles on the surface chemistry of the plasma polymer. We can also note a slight N contamination which can be due to the nitrogen used as a carrier gas in the process[38].

Table 4 : Atomic percentage of C, O, N and Si obtained by XPS analysis of plasma polymers of V3D3 obtained by DBD-CAP with a monomer flowrate of 700 sccm, a plasma power of 150 W and a varying number of repetitions.

Number of repetitions	Film thickness (nm)	Atomic percentage			
		C 1s	O 1s	N 1s	Si 2p
V3D3 monomer		60	20	0	20
1	11	35.9	40.4	0.7	23.0
2	32	37.6	40.9	0.7	20.8
3	49	37.8	40.6	0.9	20.7
4	65	37.2	39.4	1.1	22.3
5	80	38.6	38.6	1.0	21.8

To compare these results with the atomic percentages found in the iCVD-deposited poly(V3D3) and the V3D3 monomer, the atomic ratios were calculated. The elemental proportions used were those for the thin film obtained with 3 repetitions of the torch movement. This gives a 49 nm coating and can be compared to the 48 nm polymer created by iCVD.

Table 5 : Comparison of the atomic ratios O/C, Si/C and O/Si found in the V3D3 monomer, poly(V3D3) and pp(V3D3).

	Atomic ratios		
	O/C	Si/C	O/Si
V3D3 monomer	0.33	0.33	1
Poly(V3D3)	0.39	0.29	1.35
Pp(V3D3)	1.07	0.55	1.96

With these results, the O/C ratio is 1.07. This value is much higher than for the poly(V3D3) coating studied in section 2.2.2.2 and the V3D3 monomer, which are 0.39 and 0.33 respectively. This higher value can be explained by the incorporation of oxygen from the surrounding atmosphere into the deposited polymer. Indeed, the molecules found in the atmosphere can also be activated by the plasma at the interface between the torch outlet and the substrate's surface. The Si/C ratio is 0.55 for the plasma polymer obtained with 3 torch pattern repetitions. This value is also higher than for the iCVD-deposited polymer and the V3D3 monomer: 0.29 and 0.33 respectively. This difference can come from the plasma fragmenting some of the organic functions in the coating. There may also be higher atmospheric contamination as this method is not carried out under vacuum. Lastly the O/Si ratio is also much higher for these plasma polymers than for the poly(V3D3) obtained by free-radical polymerisation or for the monomer: 1.96, 1.35 and 1 respectively. It is thought that here the higher O/Si value can be explained by incorporation of atoms from the surrounding atmosphere. The higher

O content is coherent with the apparition of small absorbance peaks in the FTIR spectra at wavenumbers corresponding to C=O and O-H stretching.

Deconvolution of the high resolution XPS was carried out to further study the chemistry of these plasma polymers, and more specifically at the surface. Figure 22 shows there are no significant differences in surface chemistry between the various pp(V3D3) obtained with different numbers of torch repetitions.

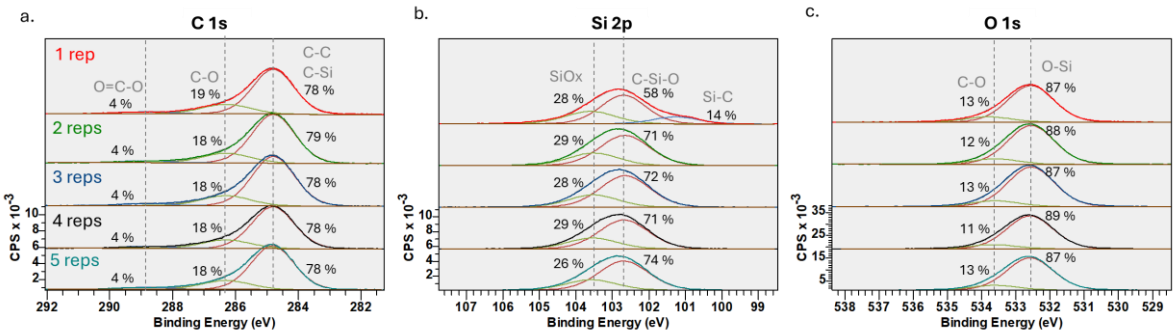

Figure 22 : High resolution X-ray Photoelectron Spectra of a. C 1s, b. Si 2p and c. O 1s in pp(V3D3) obtained with a monomer flowrate of 700 sccm, a plasma power of 150 W and a varying number of repetitions.

Deconvolution of the high resolution XPS spectra of C 1s (Figure 22a) confirms the appearance of carboxyl functions, as suggested by the FTIR spectra, in esters or carboxylic acids. Indeed, this deconvolution highlights the presence of O=C bonds with a binding energy of 288.9 eV[27]. This peak cannot be seen for iCVD deposited poly(V3D3). This may be the result of the incorporation of atmospheric molecules during the deposition process. Indeed, appearance of oxygen containing groups have previously been mentioned in the literature for these types of coatings[38]. A peak centred on 286.3 eV represents C-O bonds[27]. This value is slightly higher than for poly(V3D3) and can be due to the different chemical environment of the carbon in C-O for each material[39]. Lastly C-C, C-Si and C-H bonds can be seen at highest proportion with a binding energy of 284.8 eV[24,25].

For Si 2p (Figure 22b), for the polymer deposited with only one torch movement repetition, Si-C bonds which show a binding energy of 101.3 eV can be found whereas not for the other coatings. This could be due to different bonds at the interface between the silicon wafer and the first nm of polymer. Indeed, the plasma, as well as activating the injected monomer, can slightly activate the surface which is here native SiO_2. The other Si 2p bonds highlighted are O-Si-C which appear at 102.7 eV and represent around 70 % of the Si 2p. This binding energy is higher than for O-Si-C in poly(V3D3) which is coherent with Si being tri-substituted by O[27]. SiO_X is also apparent with a binding energy around 103.6 eV.

Concerning the O 1s, the deconvolution is similar to that of poly(V3D3) with a peak centred at 532.6 eV corresponding to Si-O which corresponds to around 90 % of the O 1s. A smaller peak around 533.7 eV can be attributed to C-O[27].

XPS spectra confirms the differences between poly(V3D3) and pp(V3D3), notably the higher oxidation of the thin film. Furthermore, this analysis shows the plasma has a negative effect on the organic bonds present in the coating. Indeed, the atomic percentage of C is much lower for the pp(V3D3) than for poly(V3D3) which showed similar elemental composition to the V3D3 monomer.

3.2.2.3. Film density

X-ray Reflectivity (XRR) was carried out to study the density of the plasma polymer and see whether this density evolved with the number of overlapped coatings.

Three samples were tested: the ones obtained with 1, 3 and 5 torch movement repetitions. As it can be seen in Table 6, the density is similar for all samples at around 1.28 g/cm^3. Therefore, it seems that overlapping the plasma polymer coatings by repeating the torch movements does not lead to any variations in the density of the coating.

Table 6 : Plasma polymer pp(V3D3) density obtained by X-ray Reflectometry (XRR) in comparison to poly(V3D3)'s density.

Number of repetitions	Thickness (nm) by ellipsometry	Thickness (nm) by XRR		Density (g/cm^3)
		Polymer	Surface layer	
Poly(V3D3) iCVD	48	46	1.9	1.18
1	11	8	2.4	1.28
3	46	44	1.4	1.29
5	77	71	2.5	1.28

Furthermore, as it was with iCVD poly(V3D3), the pp(V3D3) thickness given by XRR is very close to the thickness measured by ellipsometry (Table 6), comforting those results.

In comparison to iCVD deposited poly(V3D3) however, the density seems to be slightly higher when using DBD-CAP (1.29 g/cm^3 instead of 1.18 g/cm^3). This can be due to the fewer CH_x bonds found in the plasma polymer. Indeed, the steric hindrance brought by these moieties can decrease the material's density[40,41]. Similar differences have been noted for organosilicon thin films using different plasma deposition processes with hexamethyldisiloxane (HMDSO) and TMDSO as monomers. Indeed, Supiot *et al.* obtained coatings with a density between 1.1 and 1.45[30].

3.2.3. Pp(V3D3) thin film roughness

As it was for poly(V3D3) coatings, the film's roughness was analysed by AFM. As the thickness increases more with the plasma power than with the monomer flow, it was chosen to study the film roughness with the plasma power increase rather than when increasing the monomer flow, to check higher thickness does not induce a non-desired film roughness. Here the monomer flow was fixed at 700 sccm.

As seen in Figure 23, the aspect of the surface topography does not change when increasing the plasma power. The values in Table 7 confirm that the Rq roughness stays low for all the studied plasma powers. Indeed, it reaches 0.3 nm for the coating deposited with a monomer flowrate of 700 sccm and a 250 W plasma power.

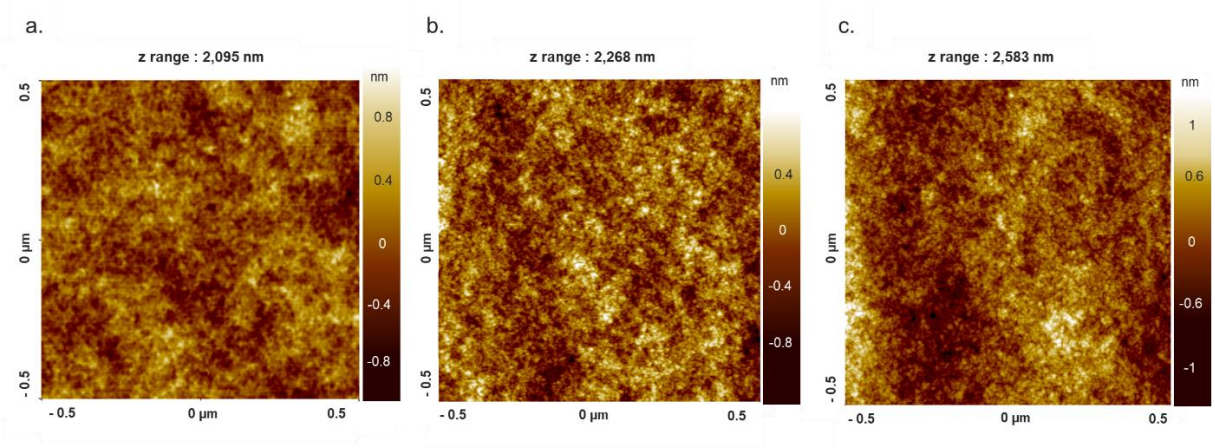

Figure 23 : AFM images of pp(V3D3) deposited by DBD-CAP with a plasma power of a. 150 W, b. 200 W, c. 250 W.

In comparison to the poly(V3D3) deposited by iCVD, the surface roughness is very similar. Indeed, for thin films with a 15 nm thickness, we have an Rq roughness of 0.36 nm for the iCVD polymer and 0.27 nm for the plasma polymer. We can conclude that for both poly(V3D3) and pp(V3D3) coatings under 20 nm, the deposition method, in the studied conditions, does not have an influence on the surface roughness. This smoothness has previously been observed in the literature[3,42,43]. For example, in their study of AP-PiCVD depositions of V3D3, Abessolo Ondo *et al*. showed roughness does not exceed 0.7 nm for the plasma polymers[10].

Table 7 : Rq roughness of pp(V3D3) deposited by DBD-CAP with a flowrate of 700 sccm and different plasma powers.

Plasma power	Thickness (nm)	Rq (nm)
Poly(V3D3) iCVD	15	0.36
150	11	0.25
200	15	0.27
250	20	0.32

AFM images were also taken to study the surface roughness as the number of torch repetitions increases. These images are reported in Figure 24 where it can be seen that the overall aspect of the surface stays the same as the number of torch repetitions increases.

Furthermore, the Rq roughness does not vary significantly with the increase in number of torch repetitions, staying below 0.5 nm as noted in Table 8. This value is close to those previously observed, for plasma polymers deposited with just 1 coating. The surface roughness is also very similar to that of poly(V3D3) deposited by iCVD.

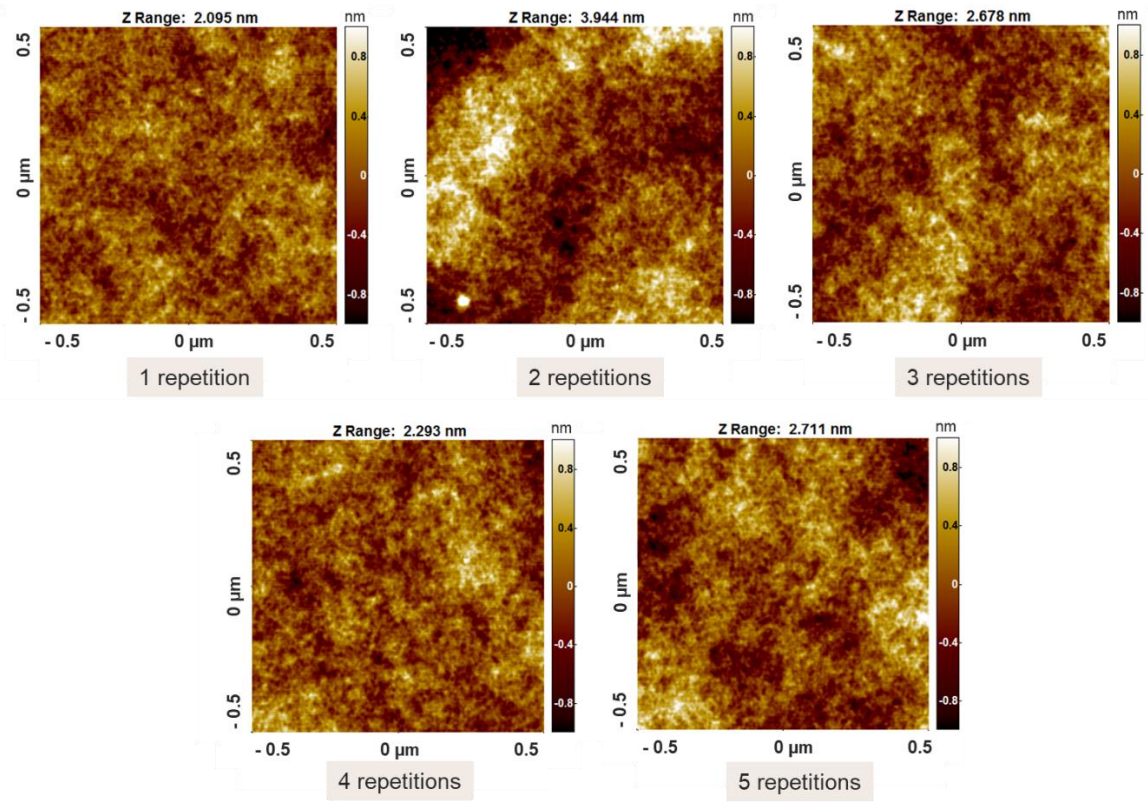

Figure 24 : AFM images of pp(V3D3) obtained by DBD-CAP with the Plasmaspot® changing the number of plasma torch repetitions over a 100 mm silicon wafer. All coatings were deposited with a monomer flowrate of 700 sccm and a plasma power of 150 W.

Table 8 : Rq roughness of plasma polymers pp(V3D3) deposited by DBD-CAP onto a 100 mm silicon wafer, using the Plasmaspot® and changing the number of plasma torch repetitions.

Number of torch repetitions	Thickness (nm)	Rq (nm)
Poly(V3D3) iCVD	15	0.36
Poly(V3D3) iCVD	48	0.38
1	11	0.25
2	30	0.43
3	46	0.31
4	62	0.27
5	77	0.34

These results show that when changing the plasma power or the number of plasma torch repetitions, surface roughness remains very low for pp(V3D3) coatings. In fact, in the studied conditions, there are no significant differences in roughness between iCVD poly(V3D3) and pp(V3D3) deposited by DBD-CAP.

3.2.4. Appearance of a coffee ring effect

In the previous section, it was shown that the surface roughness remained very low when increasing the number of plasma torch repetitions. However, optical microscopy revealed the

appearance of spherical shapes, with an increasing number and size as the torch movement is overlapped.

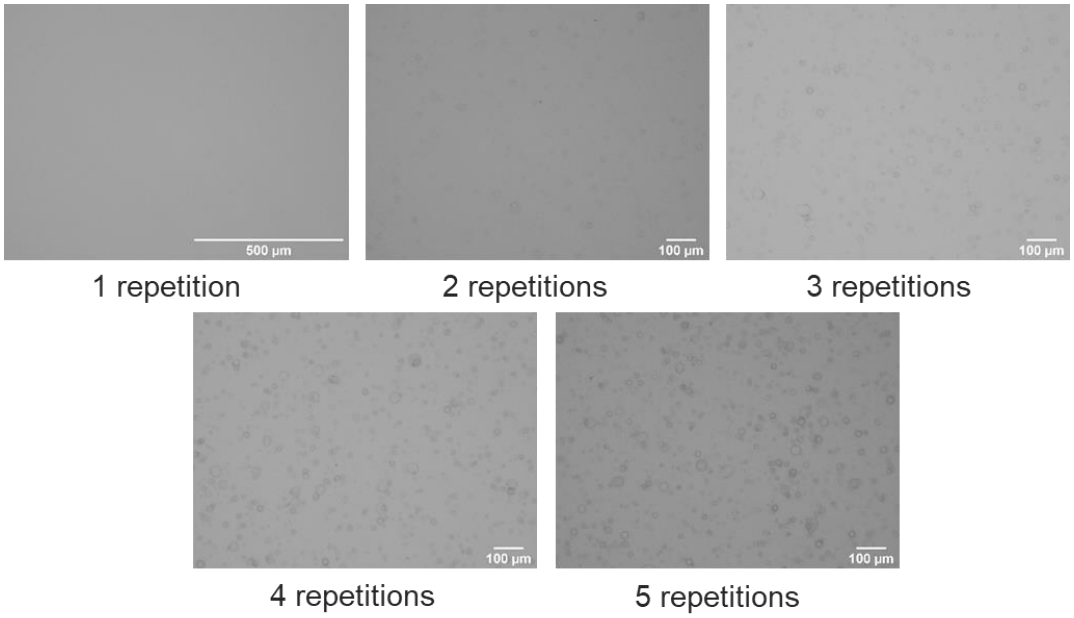

Figure 25 : Optical microscopy images of the surface of plasma polymers pp(V3D3) obtained by DBD-CAP using the Plasmaspot® and changing the number of plasma torch repetitions over a 100 mm silicon wafer. All coatings were deposited with a monomer flowrate of 700 sccm and a plasma power of 150 W.

As the model used to calculate the thickness from the spectroscopic ellipsometry measurements fits all experimental values, we can eliminate the hypothesis that these shapes are actually air bubbles. Indeed, the optical index of air being very different to that of the polymer, if bubbles were trapped inside the thin film, we would not be able to fit the data correctly. Furthermore, the material's density would decrease. However, as seen in section 3.2.2.3, it is the same with 1, 3 and 5 plasma torch repetitions.

To further understand the nature of these circular shapes, AFM imaging was carried out over a 50 x 50 µm² surface as seen in Figure 26. This image shows that the spherical shapes are in fact ringlets with a higher edge than centre. This is called the coffee-ring effect and occurs with evaporation. Indeed, as the droplet dries, the liquid flows from the centre towards the perimeter, leaving a ring around the edge[44]. This phenomenon has been shown to influence processes such as ink-jet printing, coating and washing[44,45].

It has been shown that the substrate temperature and the frequency of the precursor drops can have a significant effect on the coffee-ring effect[45,46]. Here, the substrate temperature cannot be adjusted without altering the equipment. However, the frequency of the droplets reaching the surface can be reduced by decreasing the monomer flowrate and/or accelerating the movement of the torch. This could be tested in future to try and optimise these thin film coatings.

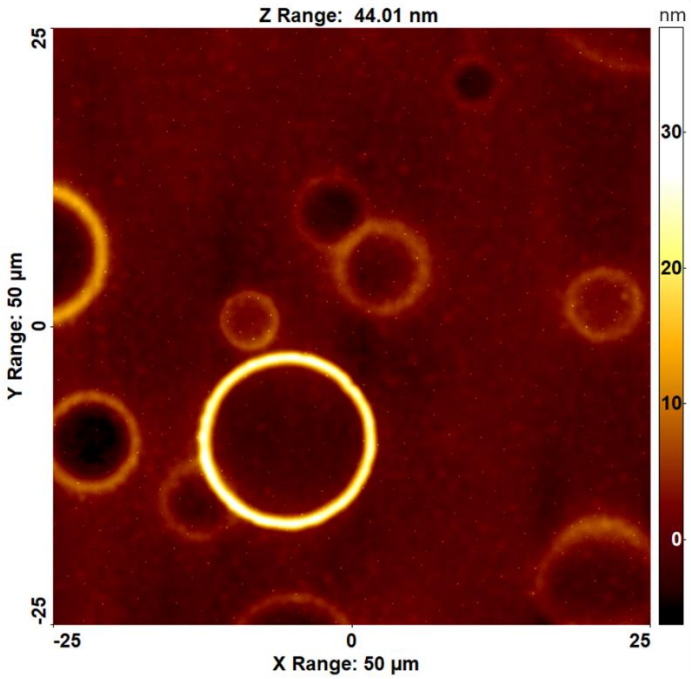

Figure 26 : AFM image of plasma polymer of V3D3 deposited by DBD-CAP with a monomer flow of 700 sccm, a plasma power of 150 W and 5 repetitions of the plasma torch movement.

However, despite the appearance of more and more ring shapes as the pp(V3D3) coatings are overlapped, as seen previously, the low-scale roughness and density of the film do not show significant variations.

3.2.5. Evaluating the wettability of plasma polymers of V3D3

As one of the most important surface properties for the antibiofouling application these polymers are destined to, wettability of the plasma polymers pp(V3D3) was studied. To do so, WCA were measured. The plasma polymers whose wettability is presented in this section are coatings deposited by DBD-CAP with varying monomer flowrates (700, 800 and 900 sccm) and a varying plasma power (150, 200 and 250 W).

These results represented in Figure 27 show that neither the monomer flowrate nor the plasma power have an impact on the wettability on these surfaces. For all cases, the measured WCA is between 75 and 80°. These values are lower than for iCVD-deposited poly(V3D3) which showed a WCA of 95° as shown in Figure 11. This difference in hydrophobicity may be explained by the incorporation of polar hydroxyl and carbonyl groups into the coating[47] which was seen when studying the chemical composition of pp(V3D3) (section 3.2.2).

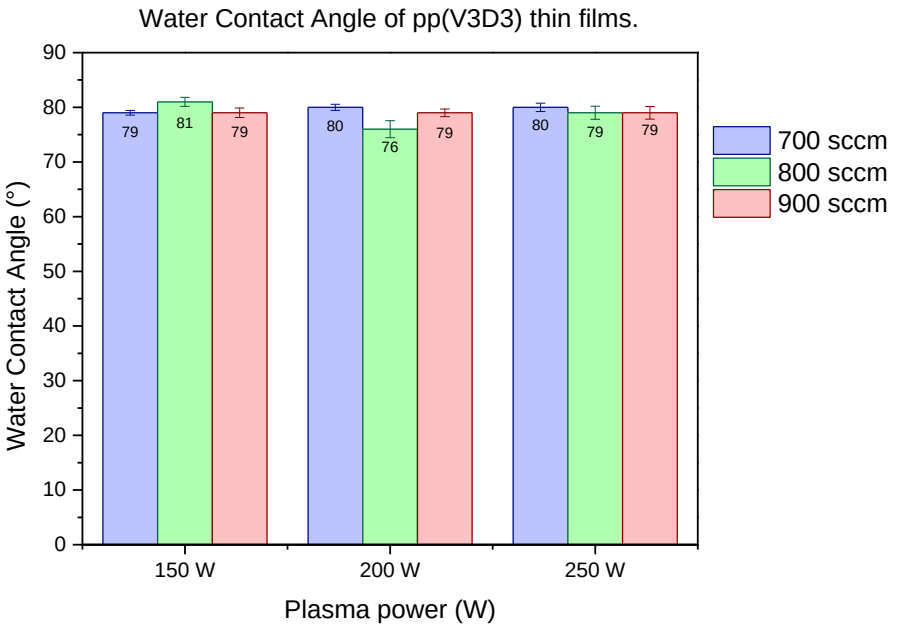

Figure 27 : WCA of pp(V3D3) deposited by DBD-CAP with different process parameters.

Furthermore, the higher hydrophobicity of poly(V3D3) is conserved over a month although slight changes can be seen for both polymers (Figure 28).

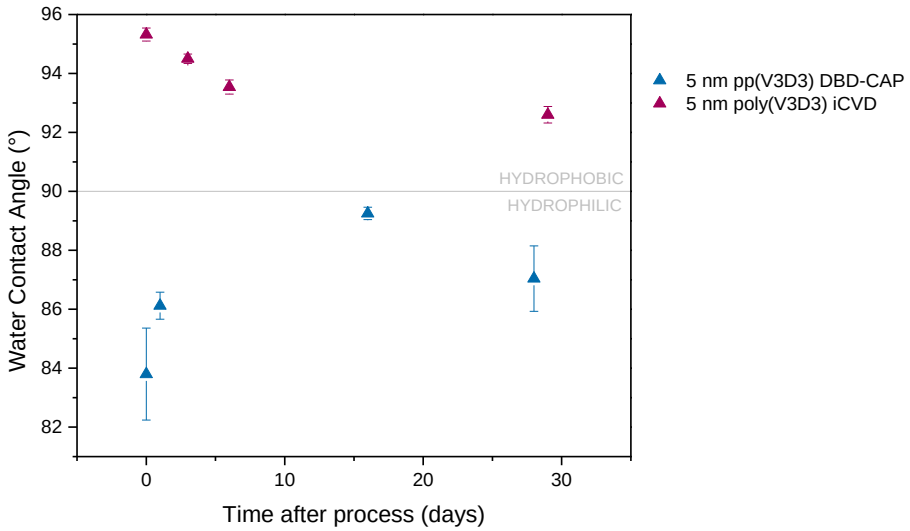

Figure 28 : WCA over time of poly(V3D3) deposited by iCVD and pp(V3D3) deposited by DBD-CAP.

Indeed, for iCVD-deposited polymers, the WCA decreases from 95° to 92° over a period of one month. This could be due to absorption of humidity from the atmosphere. For the DBD-CAP deposited plasma polymers, the WCA is 84° just after deposition. This value reaches 89° after 16 days before decreasing again to 87°. This change in wettability can be compared to that of PDMS when activated by oxygen plasma. Indeed, it has been suggested that the polar groups at the surface get buried in the bulk when in contact with air over long periods of time[47]. This can lead to the recovery of higher hydrophobicity[48]. We can imagine a similar rearrangement occurs when depositing V3D3 with a plasma-based technique.

3.2.6. Stability of plasma polymers of V3D3

3.2.6.1. Evaluating the crosslinking of pp(V3D3) by soaking in toluene

In order to study the stability of plasma polymers pp(V3D3), the same test was carried out as with the iCVD-deposited poly(V3D3): samples were soaked in toluene for 2 min before being dried by centrifuge. The thickness of these samples was measured after the soaking test and compared to the measurements beforehand. The results are represented in Figure 29.

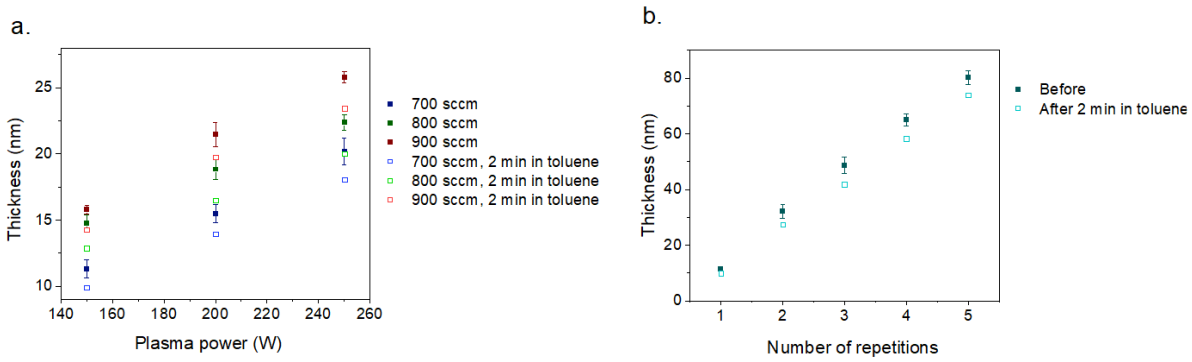

Figure 29 : Thickness measurements before and after soaking of pp(V3D3) in toluene for 2 minutes. a. Plasma polymers deposited by DBD-CAP while varying the plasma power and monomer flowrate. b. Plasma polymers deposited by DBD-CAP at a plasma power of 150 W, with a monomer flowrate of 700 sccm and by varying the number of torch repetitions.

For the coatings deposited without repeating the number of plasma torch repetitions, a thickness loss of around 2 nm can be seen for all coatings after 2 minutes soaking in toluene. We can hence suggest the toluene removes unreacted small molecules that are present in the coating[9]. When repeating the number of plasma torch repetitions, the relative thickness loss seems to decrease from 14 to 8 %. This could result from the plasma reactivating uncrosslinked species as the torch goes over them again forming new radicals which could then create bonds with one another, thus decreasing the solubility of pp(V3D3).

In comparison to iCVD-deposited poly(V3D3) thin films, the plasma polymers show slightly higher thickness loss in toluene. We can hypothesise that, even if plasma polymers are known for being well crosslinked and forming 3D structures[49], in this case, with its 3 vinyl bonds allowing reaction propagation, radical polymerisation of V3D3 leads to less soluble coatings. It is also possible that DBD-CAP leads to more unreacted moieties in the coating which can easily be solubilised.

3.2.6.2. V3D3 plasma polymers' stability in PBS

For proving the possibility of carrying out microbiology assays on these plasma polymers pp(V3D3), stability tests were also carried out in PBS as they were with poly(V3D3) deposited by iCVD. Like for the previous stability tests, thickness measurements were taken before and after using spectroscopic ellipsometry.

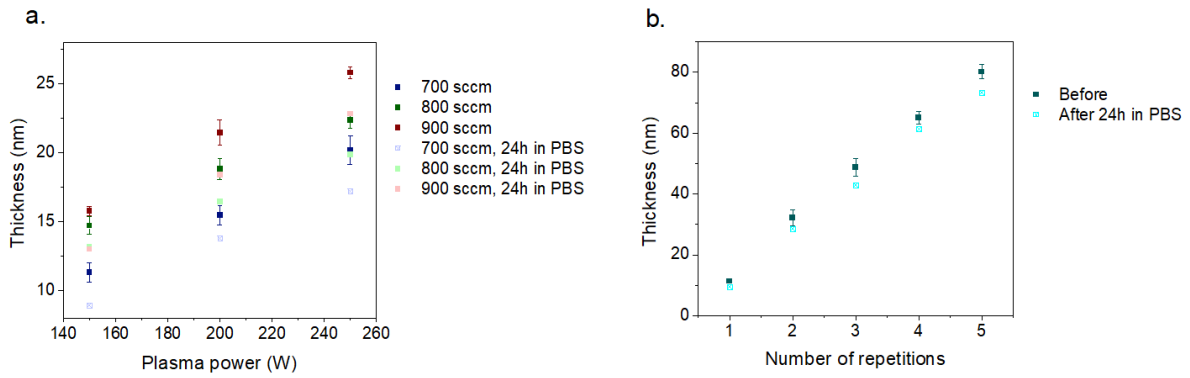

Figure 30 : Thickness measurements before and after soaking of pp(V3D3) in PBS for 24 hours. a. Plasma polymers deposited by DBD-CAP while varying the plasma power and monomer flowrate. b. Plasma polymers deposited by DBD-CAP at a plasma power of 150 W, with a monomer flowrate of 700 sccm and by varying the number of torch repetitions.

For the plasma polymers deposited with only one torch repetition, the average thickness loss after a day soaking in PBS is 2 nm (Figure 30a). For the coatings created by repeating the torch movements and overlapping the depositions, as it was seen for the stability testing in toluene, the relative thickness loss again seems to decrease with the number of torch repetitions.

These results confirm that the thickness loss remains low for pp(V3D3), especially when overlapping the coatings, comforting literature results that demonstrate the stability of similar PECVD deposited hexamethylcyclotrisiloxane (D3) in saline solution for up to a year[12].

3.3.Conclusions on pp(V3D3) plasma polymers

As it has been observed in this section, pp(V3D3) plasma polymers have been deposited by DBD-CAP using the Plasmaspot®. With this method, it was shown that thin films between 10 and 100 nm can be deposited. The thickness can be tuned by modifying the plasma power or the monomer flowrate. However, the most efficient way of increasing the thickness is by overlapping the coatings.

These plasma polymers pp(V3D3) show low roughness at a small scale. However, overlapping the coatings did lead to some differences in the homogeneity of the coating as droplet shapes appear due to the coffee-ring effect.

As for the chemical structure of the obtained thin film, we observed a modification of the siloxane cycle from the V3D3 monomer as it was deposited by DBD-CAP. In parallel, FTIR spectroscopy highlighted the presence of Si tri-substituted by oxygen in the resulting pp(V3D3) coatings. This result, along with XPS spectroscopy showed a consumption of the organic groups in the material. Analysis of the material's chemical composition also showed the presence of hydroxyl and carbonyl groups, which brought polarity to the coating, thus decreasing the WCA[47].

All in all, plasma polymerisation being known for its good crosslinking capabilities and V3D3 being well inclined to crosslinking, plasma polymers show good stability in PBS and toluene.

4. Comparison of both V3D3-based polymers

As it has been seen throughout this chapter, V3D3 can be deposited by iCVD and DBD-CAP. The choice of technique leads to different materials: poly(V3D3) and pp(V3D3) respectively, which show different properties (Table 9).

Table 9 : Summary of the properties of poly(V3D3) and pp(V3D3).

	Poly(V3D3)	Pp(V3D3)
Chemical structure	PE-like chain between siloxane rings	crosslinked films
Si configuration	di-substituted by O (D)	tri-substituted by O (T)
Density	1.2 g/cm^3	1.3 g/cm^3
Roughness	< 0.5 nm	< 0.5 nm
WCA	95°	80°
Solubility in PBS	insoluble	insoluble

Indeed, as seen by carrying out FTIR and XPS spectroscopy, both polymers show different chemical compositions. ICVD, which is a method based on free-radical polymerisation leads to a polymer which conserves the functional groups of the monomer, in this case, the siloxane rings of V3D3. These rings are linked together through a carbon polyethylene-like backbone, as represented in Figure 31a. The Plasmaspot® on the other hand, which is a cold atmospheric plasma created by DBD, is a technique which provides less control over the polymerisation of the precursor. The monomer, V3D3, is activated by the plasma at the outlet of the torch which hovers over the substrate surface. This leads to modifications of the monomer, cycle opening and the creation of new Si-O-Si bonds with various conformations (Figure 31b). Furthermore, the configuration of the Si atom is different from one polymer to the other. Indeed, while it is di-substituted with oxygen in the conventional poly(V3D3), it becomes tri-substituted with oxygen in the pp(V3D3). The resulting plasma polymer thus contains fewer organic functions than the conventional polymer.

This highlights the possibilities of obtaining thin film variations from the same monomer by using a different technique. In one case a polymer true to the definition of “a repetition of monomer units” is created. In the other, a polymer-like cross-linked structure is formed. It is common use to call these thin films “plasma polymers”, and it has been throughout this work, although the term polymer as such is not actually representative and can be confusing.

As it was seen by measuring the density of both types of polymer, V3D3-based polymers have high density in comparison to other common siloxane polymers[50]. Furthermore, it was shown that DBD-CAP led to even higher density coatings than iCVD. This can be explained by the chemical structure of each polymer. Indeed, for the poly(V3D3) obtained by free-radical polymerisation, we have a polyethylene-like backbone chain linking the Si-O-Si bonds which show the same conformation as in the V3D3 monomer. With DBD-CAP, the plasma activation leads to a reorganisation of the siloxane bonds, creating a highly cross-linked cage-like network with fewer CH_x bonds[40,41]. The steric hindrance from the latter resulting in vacant space, the density can increase when decreasing their number and consequently the space around them.

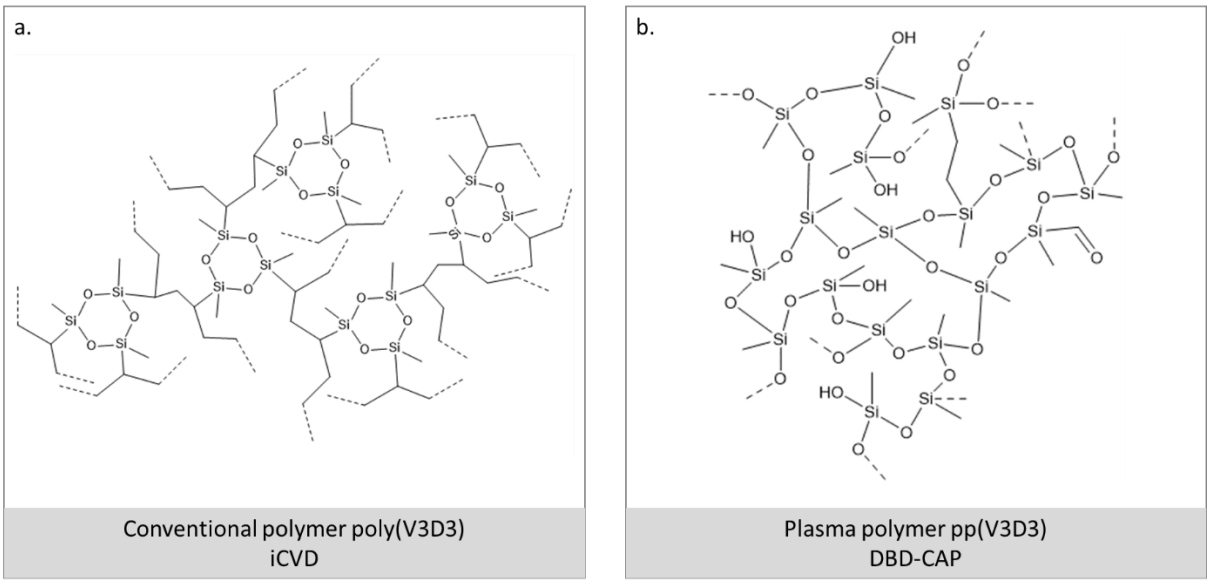

Figure 31 : Schematic representation of a. Conventional polymer poly(V3D3) obtained by iCVD. B. Plasma polymer pp(V3D3) obtained by DBD-CAP.

Stability tests in an organic solvent revealed the presence of unreacted small molecules in the pp(V3D3) coatings, as their thickness decreased after dipping in toluene. However, it seems that by overlapping the coatings, the relative thickness loss can be decreased. This may be due to the plasma torch reactivating the already deposited polymer, which can then be further crosslinked.

Furthermore, for both poly(V3D3) and pp(V3D3) thin films, the surface roughness R_q remains under 0.5 nm for all tested conditions. However, a coffee-ring effect does appear for the DBD-CAP deposited coatings. It may be possible to remove this effect by adjusting parameters such as the monomer flowrate or the speed of the torch movement.

Concerning the wettability of these films, conventional poly(V3D3) appeared to be more hydrophobic. It is thought that the lower WCA for pp(V3D3) may come from the incorporation of hydroxyl and carbonyl groups into the polymer[47]. These functions may be a consequence of atmospheric contamination.

Soaking in PBS for 24 hours did not lead to the removal of either polymer, showing their promise for microbiology testing. Furthermore, as the optical index of the material did not change significantly after this time, we can conclude that the polymers were not modified by the PBS.

5. Conclusions

This work has highlighted the possibilities of using V3D3-based polymers as fluorine-free hydrophobic coatings. Indeed, this precursor has been used to create two types of polymers: a conventional poly(V3D3) obtained by free-radical polymerisation in the iCVD process and a plasma polymer pp(V3D3) deposited by DBD-CAP with a moving plasma jet. While poly(V3D3) has previously been deposited by iCVD[3,51,52] and other techniques based on plasma polymerisation[10], to our knowledge it is the first time V3D3 was deposited using a DBD-CAP configuration with a continuous plasma jet.

For iCVD polymers, radical polymerisation was confirmed with the conservation of the siloxane cycles and the appearance of a polyethylene-like backbone chain. The thickness of this polymer can be increased with deposition time and does not affect other properties such as the chemical composition of the film, its roughness or its wettability.

On the other hand, to increase the thickness of plasma polymers using the Plasmaspot® which is a DBD-CAP based technique, the most efficient method is overlapping the coatings by repeating the plasma torch's movement. This does not influence the surface roughness or wettability although more and more ring shapes appear as more precursor droplets are injected onto the same area.

In comparison to one another, the plasma polymer's structure is less controlled than conventional poly(V3D3). Indeed, in the pp(V3D3) the siloxane bonds are found in various conformations, there are fewer CH_x groups and hydroxyl and carbonyl functions appear. These differences in chemical composition led to higher density for the pp(V3D3) as well as lower hydrophobicity.

Stability tests carried out in PBS showed the possibility of using both of these polymers for microbiology assays. With their high WCA, these polymer coatings should be good candidates for repelling bacteria and act as fluorine-free antibiofouling surfaces.

6. Bibliography

(1) Zaggia, A.; Ameduri, B. Recent Advances on Synthesis of Potentially Non-Bioaccumulable Fluorinated Surfactants. *Current Opinion in Colloid & Interface Science* **2012**, *17* (4), 188–195. https://doi.org/10.1016/j.cocis.2012.04.001.

(2) Wang, Z.; DeWitt, J. C.; Higgins, C. P.; Cousins, I. T. A Never-Ending Story of Per- and Polyfluoroalkyl Substances (PFASs)? *Environmental Science & Technology* **2017**, *51* (5), 2508–2518. https://doi.org/10.1021/acs.est.6b04806.

(3) Zavvou, C.; Cluzel, J.; Mariolle, D.; Lefevre, A.; Jousseaume, V. Poly(V3D3), an iCVD Polymer with Promising Dielectric Properties for High Voltage Capacitors. *Solid-State Electronics* **2021**, *184*, 108057. https://doi.org/10.1016/j.sse.2021.108057.

(4) Razmik Malkhasyan, N. Chemical Vapor Deposition of Low-Dielectric Constant Organosilicon-Based Thin Films. April 14, 2009.

(5) Sassin, M. B.; Long, J. W.; Wallace, J. M.; Rolison, D. R. Routes to 3D Conformal Solid-State Dielectric Polymers: Electrodeposition versus Initiated Chemical Vapor Deposition. *Materials Horizons* **2015**, *2* (5), 502–508. https://doi.org/10.1039/C5MH00057B.

(6) Murthy, S. K.; Olsen, B. D.; Gleason, K. K. Effect of Filament Temperature on the Chemical Vapor Deposition of Fluorocarbon–Organosilicon Copolymers. *Journal of Applied Polymer Science* **2004**, *91* (4), 2176–2185. https://doi.org/10.1002/app.13342.

(7) Murthy, S. K.; Olsen, B. D.; Gleason, K. K. Initiation of Cyclic Vinylmethylsiloxane Polymerization in a Hot-Filament Chemical Vapor Deposition Process. *Langmuir* **2002**, *18* (16), 6424–6428. https://doi.org/10.1021/la025815v.

(8) O'Shaughnessy, W. S.; Gao, M.; Gleason, K. K. Initiated Chemical Vapor Deposition of Trivinyltrimethylcyclotrisiloxane for Biomaterial Coatings. *Langmuir* **2006**, *22* (16), 7021–7026. https://doi.org/10.1021/la0607858.

(9) Aresta, G.; Palmans, J.; van de Sanden, M. C. M.; Creatore, M. Initiated-Chemical Vapor Deposition of Organosilicon Layers: Monomer Adsorption, Bulk Growth, and Process Window Definition. *Journal of Vacuum Science & Technology A* **2012**, *30* (4), 041503. https://doi.org/10.1116/1.4711762.

(10) Abessolo Ondo, D.; Loyer, F.; Werner, F.; Leturcq, R.; Dale, P. J.; Boscher, N. D. Atmospheric-Pressure Synthesis of Atomically Smooth, Conformal, and Ultrathin Low-k Polymer Insulating Layers by Plasma-Initiated Chemical Vapor Deposition. *ACS Applied Polymer Materials.* **2019**, *1* (12), 3304–3312. https://doi.org/10.1021/acsapm.9b00759.

(11) Abessolo Ondo, D.; Leturcq, R.; Boscher, N. D. Plasma-Initiated Chemical Vapour Deposition of Organosiloxane Thin Films: From the Growth Mechanisms to Ultrathin Low-k Polymer Insulating Layers. *Plasma Processes and Polymers* **2020**, *17* (7), 2000032. https://doi.org/10.1002/ppap.202000032.

(12) Pryce Lewis, H. G.; Edell, D. J.; Gleason, K. K. Pulsed-PECVD Films from Hexamethylcyclotrisiloxane for Use as Insulating Biomaterials. *Chemistry of Materials.* **2000**, *12* (11), 3488–3494. https://doi.org/10.1021/cm0003370.

(13) O'Shaughnessy, W. S.; Murthy, S. K.; Edell, D. J.; Gleason, K. K. Stable Biopassive Insulation Synthesized by Initiated Chemical Vapor Deposition of Poly(1,3,5-Trivinyltrimethylcyclotrisiloxane). *Biomacromolecules* **2007**, *8* (8), 2564–2570. https://doi.org/10.1021/bm070242s.

(14) O'Shaughnessy, W. S.; Edell, D. J.; Gleason, K. K. Initiated Chemical Vapor Deposition of Biopassivation Coatings. *Thin Solid Films* **2008**, *516* (5), 684–686. https://doi.org/10.1016/j.tsf.2007.06.112.

(15) Palumbo, F.; Lo Porto, C.; Fracassi, F.; Favia, P. Recent Advancements in the Use of Aerosol-Assisted Atmospheric Pressure Plasma Deposition. *Coatings* **2020**, *10* (5), 440. https://doi.org/10.3390/coatings10050440.

(16) Balaure, P. C.; Grumezescu, A. M. Recent Advances in Surface Nanoengineering for Biofilm Prevention and Control. Part I: Molecular Basis of Biofilm Recalcitrance. Passive Anti-Biofouling Nanocoatings. *Nanomaterials* **2020**, *10* (6), 1230. https://doi.org/10.3390/nano10061230.
(17) *Ellipsometry Data Analysis*. J.A. Woollam. https://www.jawoollam.com/resources/ellipsometry-tutorial/ellipsometry-data-analysis (accessed 2024-02-08).
(18) Lau, K. K. S.; Gleason, K. K. Initiated Chemical Vapor Deposition (iCVD) of Poly(Alkyl Acrylates): An Experimental Study. *Macromolecules* **2006**, *39* (10), 3688–3694. https://doi.org/10.1021/ma0601619.
(19) Achyuta, A. K. H.; White, A. J.; Pryce Lewis, H. G.; Murthy, S. K. Incorporation of Linear Spacer Molecules in Vapor-Deposited Silicone Polymer Thin Films. *Macromolecules* **2009**, *42* (6), 1970–1978. https://doi.org/10.1021/ma802330s.
(20) Grill, A.; Neumayer, D. A. Structure of Low Dielectric Constant to Extreme Low Dielectric Constant SiCOH Films: Fourier Transform Infrared Spectroscopy Characterization. *Journal of Applied Physics*. 94th ed. 2003, pp 6697–6707.
(21) Coclite, A. M.; Ozaydin-Ince, G.; d'Agostino, R.; Gleason, K. K. Flexible Cross-Linked Organosilicon Thin Films by Initiated Chemical Vapor Deposition. *Macromolecules* **2009**, *42* (21), 8138–8145. https://doi.org/10.1021/ma901431m.
(22) Abessolo Ondo, D.; Loyer, F.; Boscher, N. D. Influence of Double Bonds and Cyclic Structure on the AP-PECVD of Low-k Organosilicon Insulating Layers. *Plasma Processes and Polymers* **2021**, *18* (3), 2000222. https://doi.org/10.1002/ppap.202000222.
(23) Zavvou, Z. Dépôt iCVD de Couches Minces de Polymères Pour Des Applications En Électronique de Puissance. These en préparation, Université Grenoble Alpes, 2019. https://www.theses.fr/s228349 (accessed 2023-12-07).
(24) Kim, D. H.; Jang, W.; Choi, K.; Choi, J. S.; Pyun, J.; Lim, J.; Char, K.; Im, S. G. One-Step Vapor-Phase Synthesis of Transparent High Refractive Index Sulfur-Containing Polymers. *Science Advances* **2020**, *6* (28), eabb5320. https://doi.org/10.1126/sciadv.abb5320.
(25) Posseme, N.; Chevolleau, T.; Joubert, O.; Vallier, L.; Rochat, N. Etching of Porous SiOCH Materials in Fluorocarbon-Based Plasmas. *Journal of Vacuum Science & Technology B: Microelectronics and Nanometer Structures Processing, Measurement, and Phenomena* **2004**, *22* (6), 2772–2784. https://doi.org/10.1116/1.1815316.
(26) Charles-Alfred, C. Mise Au Point de Matériaux Barrières Diélectriques de Type A-SiC:H à Faible Permittivité Déposés Par PECVD Pour Réduire La Capacité Intermétallique Dans Les Interconnexions Avancées Des Circuits Intégrés. Thèse de doctorat, Université de Nantes, 2009.
(27) Kuchakova, I.; Ionita, M. D.; Ionita, E.-R.; Lazea-Stoyanova, A.; Brajnicov, S.; Mitu, B.; Dinescu, G.; De Vrieze, M.; Cvelbar, U.; Zille, A.; Leys, C.; Yu Nikiforov, A. Atmospheric Pressure Plasma Deposition of Organosilicon Thin Films by Direct Current and Radio-Frequency Plasma Jets. *Materials* **2020**, *13* (6), 1296. https://doi.org/10.3390/ma13061296.
(28) Lau, K. K. S. Growth Mechanism, Kinetics and Molecular Weight. In *CVD Polymers: Fabrication of Organic Surfaces and Devices*; Wiley-VCH-Verlag GmBH & Co. KGaA., 2015; pp 15–44.
(29) *PDMS*. https://www.mit.edu/~6.777/matprops/pdms.htm (accessed 2023-12-11).
(30) Supiot, P.; Vivien, C.; Granier, A.; Bousquet, A.; Mackova, A.; Escaich, D.; Clergereaux, R.; Raynaud, P.; Stryhal, Z.; Pavlik, J. Growth and Modification of Organosilicon Films in PECVD and Remote Afterglow Reactors. *Plasma Processes and Polymers* **2006**, *3* (2), 100–109. https://doi.org/10.1002/ppap.200500154.
(31) Choi, J.; Seong, H.; Pak, K.; Im, S. G. Vapor-Phase Deposition of the Fluorinated Copolymer Gate Insulator for the p-Type Organic Thin-Film Transistor. *Journal of Information Display* **2016**, *17* (2), 43–49. https://doi.org/10.1080/15980316.2016.1171803.
(32) Schröder, S.; Ababii, N.; Lupan, O.; Drewes, J.; Magariu, N.; Krüger, H.; Strunskus, T.; Adelung, R.; Hansen, S.; Faupel, F. Sensing Performance of CuO/Cu2O/ZnO:Fe Heterostructure Coated with Thermally Stable Ultrathin Hydrophobic PV3D3 Polymer Layer for Battery Application. *Materials Today Chemistry* **2022**, *23*, 100642. https://doi.org/10.1016/j.mtchem.2021.100642.

(33) Merche, D.; Vandencasteele, N.; Reniers, F. Atmospheric Plasmas for Thin Film Deposition: A Critical Review. *Thin Solid Films* **2012**, *520* (13), 4219–4236. https://doi.org/10.1016/j.tsf.2012.01.026.
(34) Hegemann, D.; Körner, E.; Guimond, S. Plasma Polymerization of Acrylic Acid Revisited. *Plasma Processes & Polymers* **2009**, *6* (4), 246–254. https://doi.org/10.1002/ppap.200800089.
(35) Smith, B. C. The Carbonyl Group, Part I: Introduction. **2017**, *32*, 31–36.
(36) Burkey, D. D.; Gleason, K. K. Structure and Mechanical Properties of Thin Films Deposited from 1,3,5-Trimethyl-1,3,5-Trivinylcyclotrisiloxane and Water. *Journal of Applied Physics* **2003**, *93* (9), 5143–5150. https://doi.org/10.1063/1.1562744.
(37) Pai, P. G.; Chao, S. S.; Tagagi, Y. Infrared Spectroscopic Study of Siox Films Produced by Plasma Enhanced Chemical Vapor-Deposition. *Journal of Vaccum Science and Technology* **1986**.
(38) Zabihzadeh Khajavi, M.; Nikiforov, A.; Nilkar, M.; Devlieghere, F.; Ragaert, P.; De Geyter, N. Degradable Plasma-Polymerized Poly(Ethylene Glycol)-Like Coating as a Matrix for Food-Packaging Applications. *Nanomaterials* **2023**, *13* (20), 2774. https://doi.org/10.3390/nano13202774.
(39) Nisol, B.; Reniers, F. Challenges in the Characterization of Plasma Polymers Using XPS. *Journal of Electron Spectroscopy and Related Phenomena* **2015**, *200*, 311–331. https://doi.org/10.1016/j.elspec.2015.05.002.
(40) Gourhant, O. Élaboration et Caractérisation de Matériaux à Très Faible Constante Diélectrique de Type A-SiOCH Élaborés Par PECVD: Application Aux Interconnexions Des Circuits Intégrés. Thèse de doctorat, Université Joseph Fourier, 2008.
(41) Wu, Z.-C.; Shiung, Z.-W.; Chiang, C.-C.; Wu, W.-H.; Chen, M.-C.; Jeng, S.-M.; Chang, W.; Chou, P.-F.; Jang, S.-M.; Yu, C.-H.; Liang, M.-S. Physical and Electrical Characteristics of Methylsilane- and Trimethylsilane-Doped Low Dielectric Constant Chemical Vapor Deposited Oxides. *Journal of the Electrochemical Society* **2001**, *148* (6), F127. https://doi.org/10.1149/1.1369373.
(42) Abessolo Ondo, D. Plasma Initiated CVD -from the Growth Mechanisms to Ultrathin Low-k Polymer Insulating Layers.
(43) Montméat, P.; Dechamp, J.; Enyedi, G.; Fournel, F.; Zavvou, Z.; Jousseaume, V. Initiated Chemical Vapor Deposition of Polysiloxane as Adhesive Nanolayer for Silicon Wafer Bonding. *Materials Science in Semiconductor Processing* **2022**, *148*, 106808. https://doi.org/10.1016/j.mssp.2022.106808.
(44) Deegan, R. D.; Bakajin, O.; Dupont, T. F.; Huber, G.; Nagel, S. R.; Witten, T. A. Capillary Flow as the Cause of Ring Stains from Dried Liquid Drops. *Nature* **1997**, *389* (6653), 827–829. https://doi.org/10.1038/39827.
(45) Soltman, D.; Subramanian, V. Inkjet-Printed Line Morphologies and Temperature Control of the Coffee Ring Effect. *Langmuir* **2008**, *24* (5), 2224–2231. https://doi.org/10.1021/la7026847.
(46) Sliz, R.; Czajkowski, J.; Fabritius, T. Taming the Coffee Ring Effect: Enhanced Thermal Control as a Method for Thin-Film Nanopatterning | Langmuir. *Langmuir* **2020**, No. 36, 9562−9570. https://doi.org/10.1021/acs.langmuir.0c01560.
(47) Drelich, J.; Chibowski, E.; Desheng Meng, D.; Terpilowski, K. Hydrophilic and Superhydrophilic Surfaces and Materials. *Soft Matter* **2011**, *7* (21), 9804–9828. https://doi.org/10.1039/C1SM05849E.
(48) Morra, M.; Occhiello, E.; Marola, R.; Garbassi, F.; Humphrey, P.; Johnson, D. On the Aging of Oxygen Plasma-Treated Polydimethylsiloxane Surfaces. *Journal of Colloid and Interface Science* **1990**, *137* (1), 11–24. https://doi.org/10.1016/0021-9797(90)90038-P.
(49) Macgregor, M.; Vasilev, K. Perspective on Plasma Polymers for Applied Biomaterials Nanoengineering and the Recent Rise of Oxazolines. *Materials* **2019**, *12* (1), 191. https://doi.org/10.3390/ma12010191.
(50) Campanale, C.; Savino, I.; Pojar, I.; Massarelli, C.; Uricchio, V. F. A Practical Overview of Methodologies for Sampling and Analysis of Microplastics in Riverine Environments. *Sustainability* **2020**, *12* (17), 6755. https://doi.org/10.3390/su12176755.

(51) O'Shaughnessy, W. S.; Gao, M.; Gleason, K. K. Initiated Chemical Vapor Deposition of Trivinyltrimethylcyclotrisiloxane for Biomaterial Coatings. *Langmuir* **2006**, *22* (16), 7021–7026. https://doi.org/10.1021/la0607858.

(52) O'Shaughnessy, W. S.; Edell, D. J.; Gleason, K. K. Initiated Chemical Vapor Deposition of a Siloxane Coating for Insulation of Neural Probes. *Thin Solid Films* **2009**, *517* (12), 3612–3614. https://doi.org/10.1016/j.tsf.2009.01.192.

Chapter 4: Depositing a hydrophilic polymer by iCVD

1. Introduction

Less intuitive than hydrophobicity, but still as effective, hydrophilic surfaces also show good repellence to bacterial adhesion and biofouling. Indeed, rather than leading to the formation of an air barrier at the surface of the substrate of interest, a film of water is created and acts as an obstacle towards bacterial adhesion.

As highlighted in the first chapter of this manuscript, there are many options for creating hydrophilic surfaces with good antifouling properties. In this study, the focus was set on poly(vinylpyrrolidone) (PVP). Indeed, this hydrophilic polymer can be found in many studies in the literature where it is used as an antibiofouling coating. It has been used for fighting against protein[1,2], marine[3] and bacterial[1,2,4] biofouling. As well as being highly hydrophilic and therefore a good candidate for an antibiofouling coating, PVP has been used as a blood plasma substitute[5,6] as it is bio and hemocompatible. This makes it an interesting polymer to use in medical devices. As highlighted by Liu *et al*. in their review published in 2013 and entitled 'Poly(N-vinylpyrrolidone)-Modified Surfaces for Biomedical Applications'[5].

In addition to its antibiofouling and biocompatible properties, PVP is a polymer that can be obtained by free-radical polymerisation of vinylpyrrolidone. This, as well as its compatible vapour and glass transition temperatures, allows it to be deposited by iCVD. Indeed, Gleason's team was the first to publish work on iCVD deposited PVP in 2006[7] and this work was then continued by Kenneth Lau[8,9]. Sun *et al.* also used iCVD to graft PVP onto surfaces of interest[10,11].

However, high solubility often leads to PVP being crosslinked with a second precursor such as ethylene glycol diacrylate (EGDA)[7,9] or ethylene glycol dimethacrylate (EGDMA)[12]. By simultaneously injecting monomer and crosslinking agent, iCVD has shown good results for creating copolymers[13–15]. However, with their high reactivity, control over the deposition of acrylates can be difficult. Therefore, in this work, previously studied V3D3 will be used as it is able to create 3D matrices due to its 3 vinyl bonds. While V3D3 has previously been used as a crosslinking agent[16–18], to our knowledge it is the first time it has been codeposited with VP.

The first section of this chapter will focus on iCVD deposition of PVP as a hydrophilic polymer. The second part will highlight copolymers poly(VP-co-V3D3) which are both hydrophilic and insoluble.

2. PVP deposition by iCVD

2.1. Recipe development and process

As mentioned in the introduction, PVP has previously been deposited by iCVD. The radical initiator that was used was tert-butyl peroxide (TBPO). This is the same initiator that was used for poly(V3D3) and also the only initiator found in the literature for PVP coatings[7,8,12,19].

As mentioned in chapter 2, the recipe parameters from the literature on iCVD PVP coatings were used, when possible, as a starting point for developing our own process with the TEL iCVD equipment.

Some parameters such as pressure and chiller temperature were modified, between 0.5 and 1.5 Torr and between 30 and 37°C respectively, to study their influence on the process. Concerning the injection parameters of the VP precursor and the radical initiator TBPO, the VP precursor was injected at 115°C in vapour form with a flowrate of 0.15 g/min, which corresponds to around 30 sccm.

The radical initiator, TBPO, was injected in vapour form at 28°C with a flowrate between 2 and 4 sccm. Different times of deposition were also carried out to evaluate the kinetics of PVP thin film deposition in these iCVD conditions.

2.2.Poly(vinylpyrrolidone) thin films

2.2.1. Polymerisation of vinylpyrrolidone

2.2.1.1. FTIR spectroscopy to verify radical polymerisation

As explained previously, iCVD is based on free radical polymerisation. Therefore, when depositing PVP using this technique, the polymerisation should propagate through the vinyl bonds without affecting the functional group of the monomer, as schematized in Figure 1.

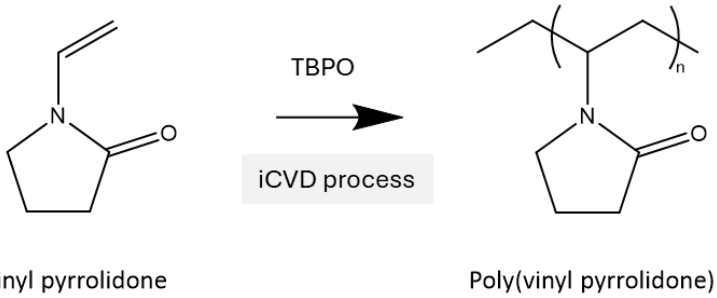

Figure 1: Schematic representation of the polymerisation of N-vinyl pyrrolidone.

To verify the radical polymerisation of vinyl pyrrolidone when depositing it by iCVD, FTIR was carried out to study the chemical bonds present in the final film. Figure 2a represents the FTIR spectra of VP monomer and Figure 2b represents the spectra obtained for PVP deposited by iCVD and for commercial PVP. The latter was diluted in water, a droplet was then deposited on silicon and left to dry before being analysed.

The spectra of the PVP polymers both show 4 distinct bands and the main difference between these two spectra is the broad band around 3400 cm^{-1} for the commercial polymer. This can be recognized as O-H or N-H bonds which appear because the PVP powder was diluted in water.[20]. A broad peak centred around 2900 cm^{-1} is characteristic of CH_X stretching. The presence of CH_X groups is confirmed by the peak at 1427 cm^{-1} which corresponds to CH_X bending. These peaks, also found for the commercial polymer, are expected from the radical polymerisation leading to CH_2-CHR moieties with R the pyrrolidone cycle, which also contains CH_2 bonds. For the commercial PVP, a shoulder appears at 1500 cm^{-1}. This peak could be due to N-H bending appearing as the molecule interacts with water when diluted[20]. A sharp peak appears at 1681 cm^{-1} and can be attributed to C=O stretching in the amide group. This peak appears at a slightly higher wavenumber than for the commercial polymer and is close to what can be found in the literature on iCVD PVP coatings[7,8]. Indeed, for the commercial PVP, this peak is centred around 1657 cm^{-1}. It is thought that the lower wavenumbers could be due to hydrogen bonds created between the C=O group and water molecules[21]. Furthermore, a peak appearing at 1288 cm^{-1} for both spectra can be attributed to C-N stretching[22].

Finally, the absence of a peak at 1631 cm^{-1}, which can be seen in the spectra of the VP monomer, shows the absence of C=C stretching and thus confirms the disappearance of the vinyl bond[7,8]. This agrees with a free radical polymerisation mechanism.

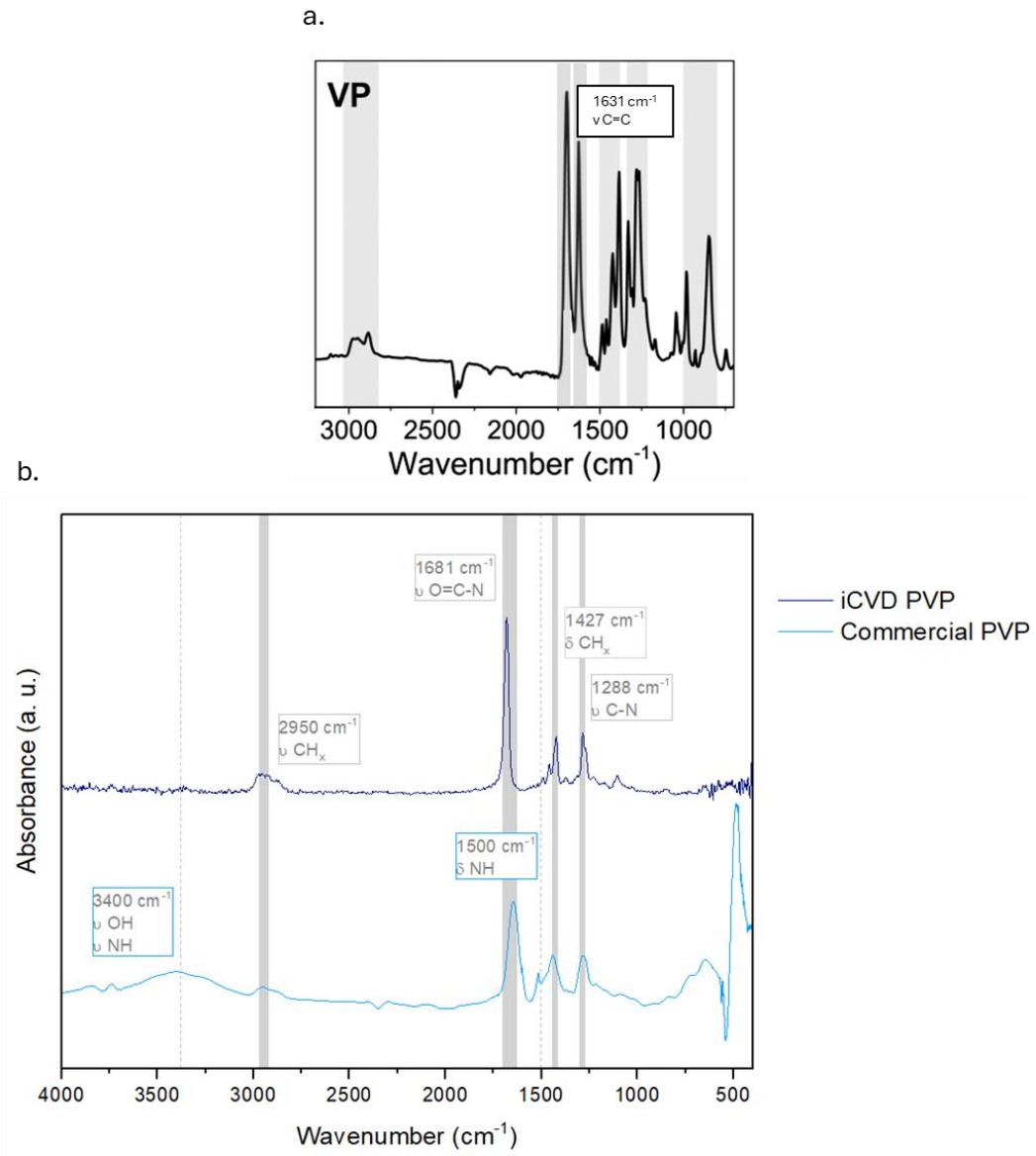

Figure 2: FTIR spectra of a. VP monomer, adapted with permission from Janakiraman et al.[8] *Copyright © 2024 Elsevier, b. PVP from a commercial powder diluted in deionised water (light blue) and deposited by iCVD (dark blue).*

The analysis of the FTIR spectrum of iCVD deposited PVP which shows no peaks corresponding to vinyl bonds, and also shows the conservation of functional groups such as the amide, indicates PVP was formed by free radical polymerisation of the VP monomer.

2.2.1.2. Analysis of the surface chemistry by XPS

XPS was also carried out to bring more precision concerning the chemical bonds present at the surface of our deposited PVP.

Table 1: Atomic percentages of C, O, N and Si of PVP of different thicknesses deposited by iCVD.

Film thickness (nm)	Atomic percentage			
	C 1s	O 1s	N 1 s	Si 2p
9.6	71.0	13.7	11.4	3.9
67.4	73.6	13.0	12.4	1.0
296.7	74.4	12.4	12.6	0.6

Three samples were analysed with different thicknesses: 10, 67 and 297 nm. The atomic percentages of C 1s, O 1s, N 1s and Si 2p were very similar for all coatings. The presence of Si could be due to cleavage residues. Indeed, as the X-ray beam only penetrates around 6.5 nm, even for the thinnest coating, no contributions from the silicon substrate should be seen.

The atomic composition can be compared to that of the VP monomer. In a single molecule of the latter, there is 1 oxygen atom, 1 nitrogen atom and 6 carbon atoms. This leads to an O/N ratio of 1, and O/C and N/C ratios of 0.167. For the PVP coating measuring 297 nm thick, these ratios become: O/N = 0.98; O/C = 0.17 and N/C = 0.17. The proximity of these atomic percentage ratios confirms the conservation of the monomer's structure (Table 2).

Table 2: Comparison of the atomic ratios O/N, O/C and N/C found in the VP monomer and PVP.

	Atomic ratios		
	O/N	O/C	N/C
VP monomer	1	0.17	0.17
PVP	0.98	0.17	0.17

Deconvolution of high resolution XPS spectra was carried out to study the bonds present in these PVP thin films (Figure 3).

For C 1s, the first thing that can be noticed is that the carbon's chemical environment does not depend on the film thickness. Indeed, for all studied films of PVP, deconvolution leads to four peaks. The first one, centred at 284.8 eV corresponds to C-C/C-H bonds[23,24]. Another peak can be seen at 285.7 eV and corresponds to C-N bonds[11]. There is also a peak which can be attributed to C=O bonds which can be seen at 287.6 eV[7,25]. All these bonds are found in VP and confirm the deposition process did not modify the monomer's functional group. A fourth peak, corresponding to C-O bonds can be found at 286.2 eV. The latter shows a very small contribution of C-O bonds (under 6 %) which is coherent with the presence of these bonds in only the TBPO molecule. A single peak emerges for N 1s and is centred around 399.6 eV which corresponds to C-N bonds[7]. Concerning O 1s, Figure 3c highlights the fact that it is mostly found in C=O bonds with a binding energy of 531 eV[7]. However, there is also a small amount which can be attributed to Si-O bonds with a binding energy around 532.4 eV. However, the silicon and any SiO_2 moieties could be due to cleavage residues.

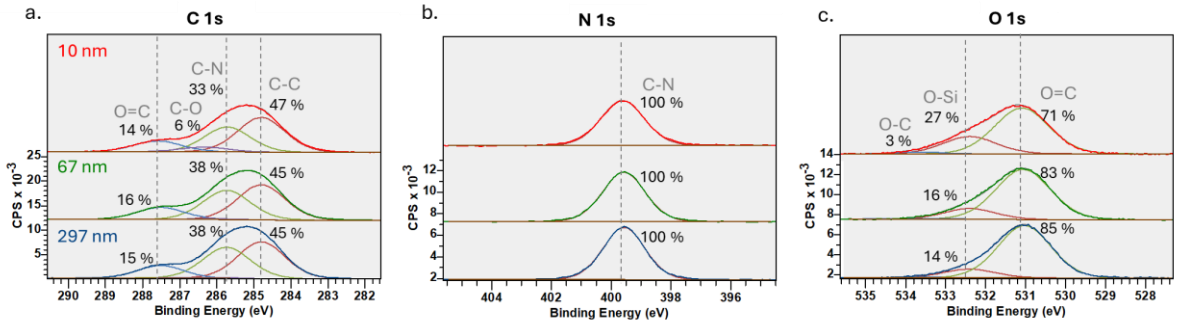

Figure 3: High resolution XPS spectra of a. C 1s, b. N 1s and c. O 1s for PVP of different thicknesses (10 nm in red, 67 nm in green and 297 nm in blue) deposited by iCVD.

This analysis of the surface chemistry of PVP thin films by XPS shows that the monomer's functional group is conserved intact in the thin film. This confirms polymerisation occurs through the vinyl bonds.

2.2.2. Thin film growth of PVP

2.2.2.1. Kinetics

In order to evaluate the kinetics of PVP growth with our iCVD equipment, various coatings were carried out using the same parameters and only modifying the deposition time. The pressure of the reactor was set to 1.5 Torr and the substrate temperature was regulated at 37°C which gave a saturation ratio P_m/P_{sat} of 0.77. Spectroscopic ellipsometry was carried out to evaluate the thickness of the coatings. More precisely, as the PVP was deposited onto 200 mm silicon wafers, mapping was carried out to evaluate the thickness over the whole surface. Figure 4a shows that the average value over the entire surface of the substrate and the thickness at the centre of the wafer are not significantly different from one another. This study shows that the coating thickness can be tuned between a few nanometres and hundreds of nanometres by increasing the deposition time. However, as the thickness increases, the standard deviation becomes quite significant, underlining a non-uniformity of the coating thickness on the 200 mm silicon wafer. Optimization of the process should allow to obtain polymer coatings with better thickness homogeneity, as found for poly(V3D3) (chapter 3).

At first glance, Figure 4a seems to show linearity between film thickness and time of deposition. However, if the deposition rate is studied more precisely, it seems to rise with the time of deposition before stabilising. Indeed, as it can be seen in Figure 4b, the apparent deposition rate increases from around 1 nm/min at minor times of deposition to 2.8 nm/min after 1 hour. This two regime behaviour has been seen previously when depositing poly(methacrylate) by iCVD[26,27]. It should be noted that this apparent deposition rate is an average over the total deposition time and does not consider the change in kinetics, hence the term *apparent*.

Indeed, in their study of poly(*neo*-pentyl methacrylate) (PnPMA) deposited by iCVD, Bonnet *et al*. showed that for polymers deposited under stable process conditions, two growth regimes could be noticed when increasing the deposition time[26,27]. They hypothesized that the kinetics are limited by the adsorption of the monomer on the substrate at the beginning of the process. This gives slow kinetics at the start of the polymerisation. Once the first polymer chains are created, they help accelerate the deposition rate as they can act as a monomer reservoir and increase the quantity of available precursors. As the polymer thickness further increases, reaching a critical thickness, only the

monomers found at the surface of this reservoir can react. A steady-state is then reached, with the monomer concentration involved in propagation, and consequently the deposition rate, becoming constant. For PnPMA, the critical thickness was estimated to be around 40-80 nm[26].

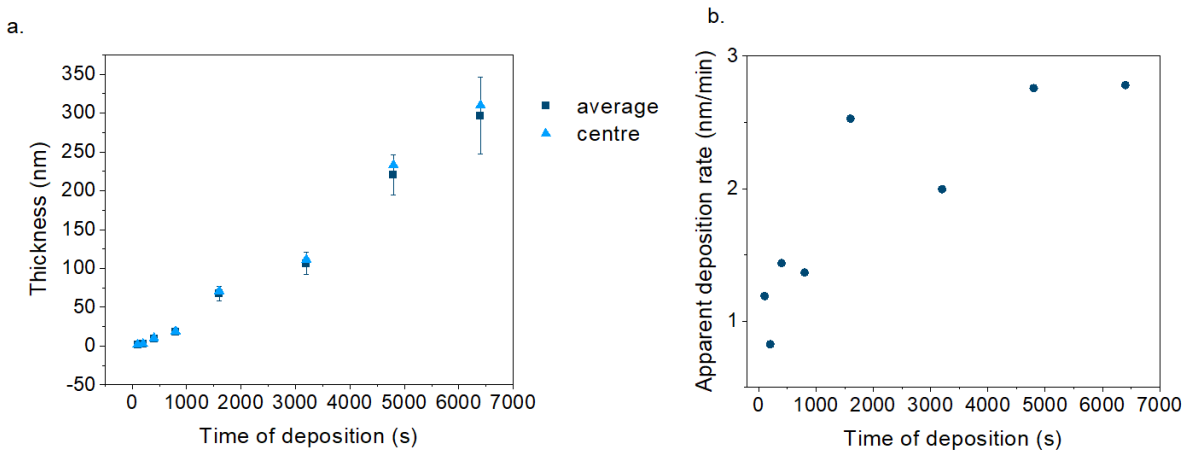

Figure 4: a. Average thickness and centre thickness of PVP deposited by iCVD onto a 200 mm silicon wafer for different times of deposition. For all coatings, the pressure was set at 1.5 Torr and the substrate's temperature was 37°C. b. Apparent deposition rate for these same coatings. The deposition rate was calculated by dividing the average thickness by the deposition time.

From the observations of the growth rate increase with the time of deposition, this hypothesis of a two-regime growth mechanism seems to fit well with our experimental results for a PVP thin film with process conditions leading to a P_m/P_{sat} ratio equal to 0.77. The critical thickness in these conditions seems to be between 50 and 100 nm.

2.2.2.2. Influence of the saturation ratio on PVP growth

To further understand the growth of PVP deposited by iCVD, the P_m/P_{sat} ratio was modified by varying the chamber pressure (between 0.5 and 1.5 Torr) and the substrate temperature (30 or 35°C). All depositions in this study were carried out with the same process time: 1200 s. The thickness measurements led to Figure 5 which shows the apparent deposition rate increases with the saturation ratio. It is commonly accepted for iCVD depositions that the deposition rate increases with P_m/P_{sat} [28] and this has previously been shown for PVP depositions[7,8].

However, as the P_m/P_{sat} increases over 0.6, it seems that the deposition rate increases faster when the substrate temperature is higher. This is not expected for iCVD depositions, as it is often reported that the deposition rate is inversely proportional to the substrate temperature[8,29]. However, Prasath and Lau also highlight this observation for PVP depositions under certain conditions in a recent publication[19]. They show the kinetics are different for PVP deposited in subsaturated conditions where $P_m/P_{sat} = 0.5$ and saturated conditions where $P_m/P_{sat} = 1$. Indeed, in their study, the temperature of the substrate was modified while keeping the P_m/P_{sat} ratio fixed. For $P_m/P_{sat} = 0.5$, the deposition rate stays stable whereas, for $P_m/P_{sat} = 1$, the deposition rate increases with the substrate temperature[19]. This is what seems to be happening in our study.

Therefore, it is believed, that, as well as showing a two-regime growth for a fixed saturation, like shown in the previous section, the kinetics of PVP deposition also depend on the P_m/P_{sat} ratio.

Indeed, it seems that for a low P_m/P_{sat}, kinetics are limited by the monomer adsorption on the substrate and thus deposition is faster with a lower substrate temperature. At high P_m/P_{sat} however, it seems that thermally activated bulk polymerisation becomes the limiting reaction once the critical thickness has been reached.[19]

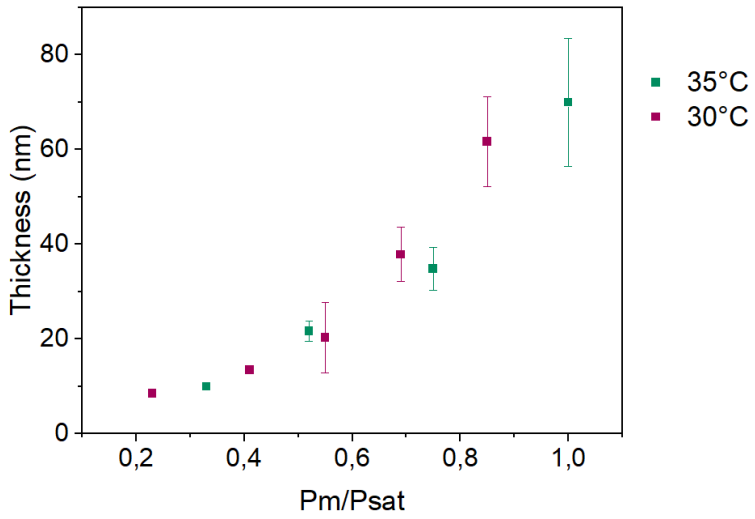

Figure 5: Average apparent deposition rate of PVP deposited by iCVD onto a 200 mm silicon wafer with various substrate temperatures and chamber pressures.

However, it may be possible that the saturation ratio changes the critical thickness discussed previously. For a more accurate study, kinetics should be evaluated for different P_m/P_{sat} ratios in order to determine the critical thickness after which the apparent deposition rate becomes constant. Comparing the apparent deposition rates reached after the critical thickness would be more precise.

2.2.2.3. Influence of an increased thickness on the PVP thin films roughness

In order to evaluate the roughness of the PVP coating, AFM was carried out. The samples analysed were deposited under the same conditions (chamber pressure = 1.5 Torr, substrate temperature = 37°C) and only the time of deposition was modified to obtain thin films with different thicknesses.

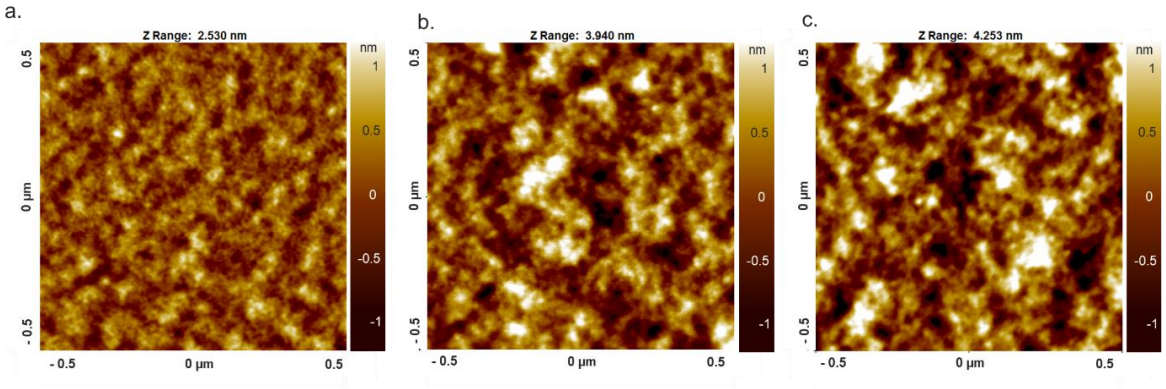

Figure 6: AFM images of PVP with a thickness of a. 9.6 nm, b. 67.4 nm, c. 296.7 nm. All coatings were deposited by iCVD onto silicon wafers.

As it can be seen in the AFM images above, the aspect of the polymer changes slightly as the thickness of the coating increases from 10 nm to nearly 300 nm. This leads to differences in the film's roughness. Indeed, the Rq roughness increases from 0.35 nm for the film 10 nm thick, to 0.6 nm for the 297 nm thick coating as summarized in Table 3. However, for all analysed samples the thin film's roughness remains under 1 nm which is coherent with other iCVD polymers[28]. Furthermore, these results are close to those published by Sun *et al.* for their PVP crosslinked with EGDA (poly(VP-co-EGDA)) for which the Rq roughness is 0.8 nm[10]. Poly(VP-co-EGDMA) also led to smooth surfaces when deposited by iCVD[12].

Table 3: Rq roughness values for PVP thin films deposited by iCVD.

Time of deposition (s)	Thickness of the PVP coating (nm)	Rq (nm)
400	9.6	0.35
1600	67.4	0.5
6400	296.7	0.6

Furthermore, as the thickness of the PVP coating increased, optical microscopy revealed the apparition of dendritic shapes as it can be seen in Figure 7. Similar fractal dendrites have previously been observed for iCVD depositions of poly(1H,1H,2H,2H-perfluorodecylacrylate) (pPFDA) and poly(acrylic acid) (pAA) and are thought to be the result of accumulation of oligomers in the reaction chamber from previous depositions. It has been suggested by Shindler *et al.* that these defects can be removed by beginning the process with a high substrate temperature before lowering it to the desired conditions[30]. It would be interesting to see whether this solution is applicable to PVP thin films deposited by iCVD.

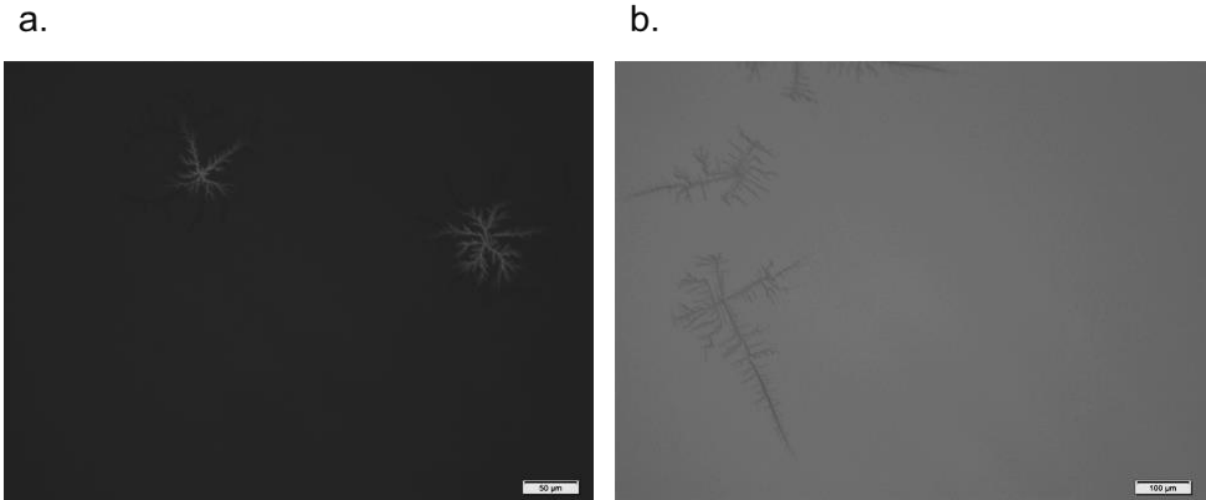

Figure 7: Optical microscopy images of PVP coatings with a thickness of a. 67 nm and b. 297 nm.

2.3.A highly hydrophilic material and its limits

2.3.1. Hydrophilicity of the thin film

As explained in the introduction, PVP was chosen in this study for its hydrophilic properties. To verify the hydrophilicity of the thin films deposited using our iCVD equipment, WCAs were measured. Fifteen water droplets were deposited over the diameter of the coated silicon wafer. The WCA was measured 1 s and 10 s after the droplets were deposited.

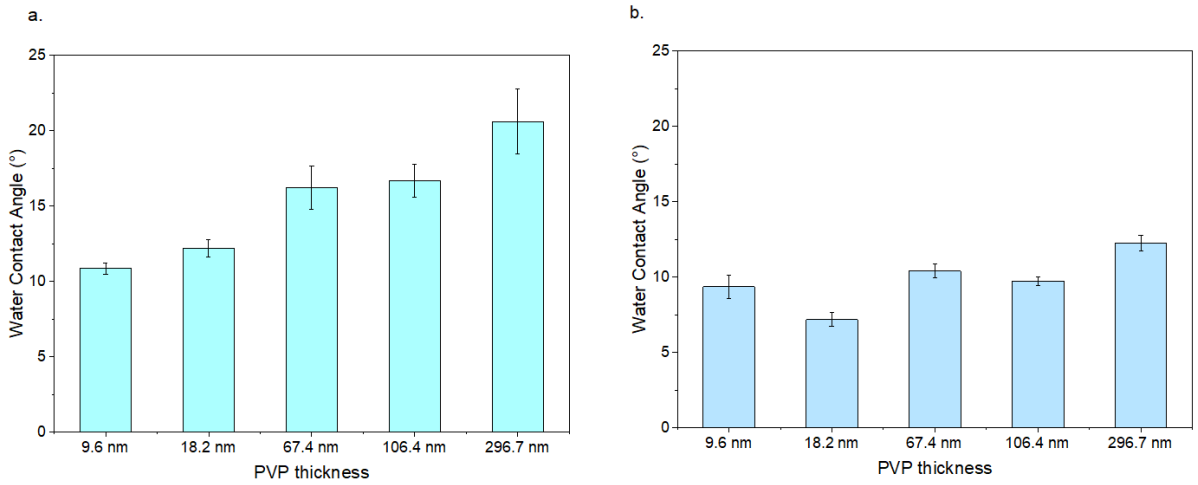

Figure 8: WCAs measured after a. 1 s and b. 10 s, on PVP thin films. Each measurement was averaged over 15 droplets deposited over the diameter of the 200 mm silicon wafer.

Figure 8 proves the hydrophilicity of the PVP films as the WCA is under 25° for all coatings. After 10 s, the WCA is around 10° for all coatings due to the water droplet spreading on the surface of the superhydrophilic polymer.

2.3.2. Solubility of PVP

The WCA measurements however, underlined a problematic issue. Indeed, once the droplets dried, it was evident they had led to the dissolution of some or all of the polymer. This can be seen in the photo in Figure 9. Nevertheless, to be able to use PVP as antibiofouling coatings, it needs to be stable in aqueous solutions.

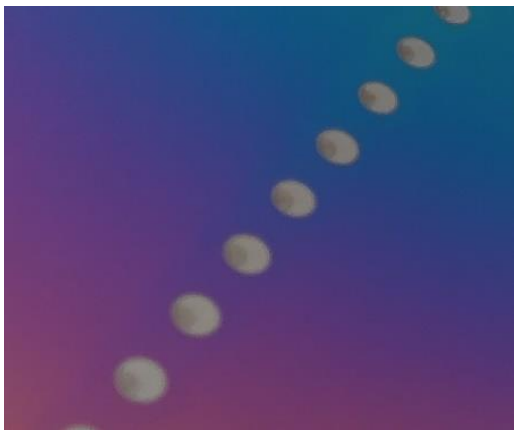

Figure 9: Photo representing the dissolution of the PVP by the water droplets used for measuring the WCAs.

To verify whether the dissolution of the polymer was complete, stability tests were carried out in PBS. The thickness of the films was measured by spectroscopic ellipsometry before and after 24h soaking in PBS 1X. Figure 10 shows the complete removal of the polymer coating after this time, for all substrates.

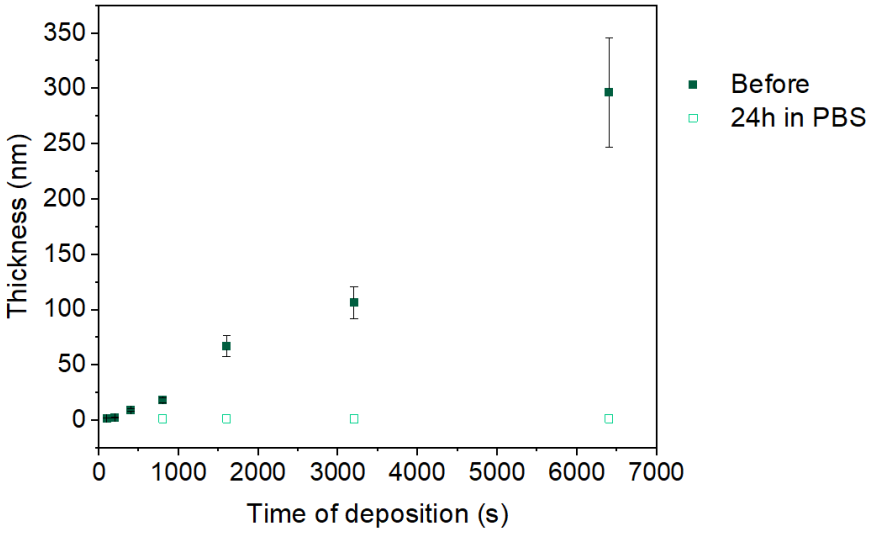

Figure 10: Thickness of PVP coatings before and after 24h soaking in PBS.

These results show the need to stabilise our PVP polymer in order to use it for antibiofouling applications. This can be done by crosslinking the polymer with another precursor to form a crosslinked polymer matrix.

2.4.Conclusions on PVP thin films

In this section, we have shown the possibility of depositing PVP by iCVD, leading to its free radical polymerisation and the formation of PVP. While controlling the deposition parameters can lead to different kinetics, it also seemed that for fixed criterions, the film growth occurred in a two-step regime, as it has previously been seen for P(nPMA). It was also shown that while some dendritic shapes can appear through self-assembly of the polymer chains, the thin film's roughness remains under 0.6 nm which is coherent with other iCVD polymers.

This polymer shows good potential as a superhydrophilic coating, yet it should need stabilising in order to prevent its dissolution in aqueous solutions such as PBS. Crosslinking of PVP has already been mentioned in the literature in order to bring stability[7,12]. This will be studied in the next section of this chapter.

3. Poly(VP-co-V3D3)

In the literature, PVP has been codeposited by iCVD with various precursors to achieve crosslinking and consequently stabilise the polymer. Ethylene glycol diacrylate (EGDA) has been used

for its two C=C bonds and its compatibility with the process conditions[7,9]. Ethylene glycol dimethacrylate (EGDMA) has also been codeposited with VP to bring higher stability[12].

In this study, for the first time to our knowledge, V3D3 was used as a crosslinking agent for PVP. Indeed, this monomer, studied in chapter 3 of this manuscript, contains three vinyl bonds, and is therefore an ideal candidate for stabilising the PVP coating. Moreover, V3D3 has been used previously in iCVD technology as a crosslinker[16–18]. Its slower kinetics in comparison to acrylates, will allow better control over the deposition process.

3.1. Process

For depositing copolymers by iCVD, the process was the same as for one precursor, except that two monomers were injected simultaneously into the chamber. As previously, TBPO was used as the radical initiator.

In this case, to ensure a P_m/P_{sat} ratio under 1 for both monomers, the substrate temperature was set to 40°C and the chamber pressure was set to 1.5 Torr. The filament temperature was around 250°C, allowing the pyrolysis of TBPO and the formation of radicals.

The injection of VP was modified between 0.15 and 0.2 g/min, pushed by 60 sccm of Argon. For V3D3, the injection rate was lower as the objective was to use it only as a crosslinking agent. It was varied between 0.03 and 0.1 g/min, pushed by 25 sccm of Argon. By varying the injection rates of each monomer, the injection mass fraction of VP varies between 63 and 87 %. The injection fraction of V3D3 thus varies between 13 and 37 %. The influence of these different monomer injection fractions on the copolymer will be studied in the following sections. The different parameters are summarized in chapter 2.

3.2. Poly(VP-co-V3D3) copolymers

3.2.1. Adjusting the monomer injection fraction to adjust the monomer fractions in the copolymers

3.2.1.1. FTIR spectroscopy to verify the copolymerisation

FTIR spectroscopy was carried out on copolymer coatings obtained by varying the injection fractions of VP and V3D3 to see whether this had an influence on the final chemistry of the copolymer. The deposition time was 2500 s for all coatings.

Figure 11 represents these FTIR spectra, as well as spectra of poly(V3D3) and PVP obtained by iCVD depositions carried out in the same process conditions: pressure = 1.5 Torr, substrate temperature = 40°C and time of deposition = 2500 s. All are normalised by thickness.

This figure shows that the FTIR spectra of the copolymers result in the overlapping of the spectra of both PVP and poly(V3D3). To better visualise this, specific bonds for each polymer have been highlighted by vertical lines on the spectra. For poly(V3D3), the peak at 1005 cm^{-1} is representative of the Si-O-Si bond found in the cyclic siloxane of V3D3. At this wavenumber, no peaks can be seen on the PVP spectrum which means that any bands appearing at 1005 cm^{-1} in the copolymers come from the presence of V3D3. For PVP, the peak emerging at 1682 cm^{-1} is specific to O=C-N bonds. This is a good peak for confirming contributions of VP in the spectra of copolymers as nothing emerges for poly(V3D3) at this wavenumber. Both these peaks, among others, appear for all copolymers, with more

or less intensity. And, logically, the higher the proportion of injected VP, the higher the intensity of the peak specific to VP, emerging at 1682 cm^{-1}. The contrary is also true with the Si-O-Si peak at 1005 cm^{-1}.

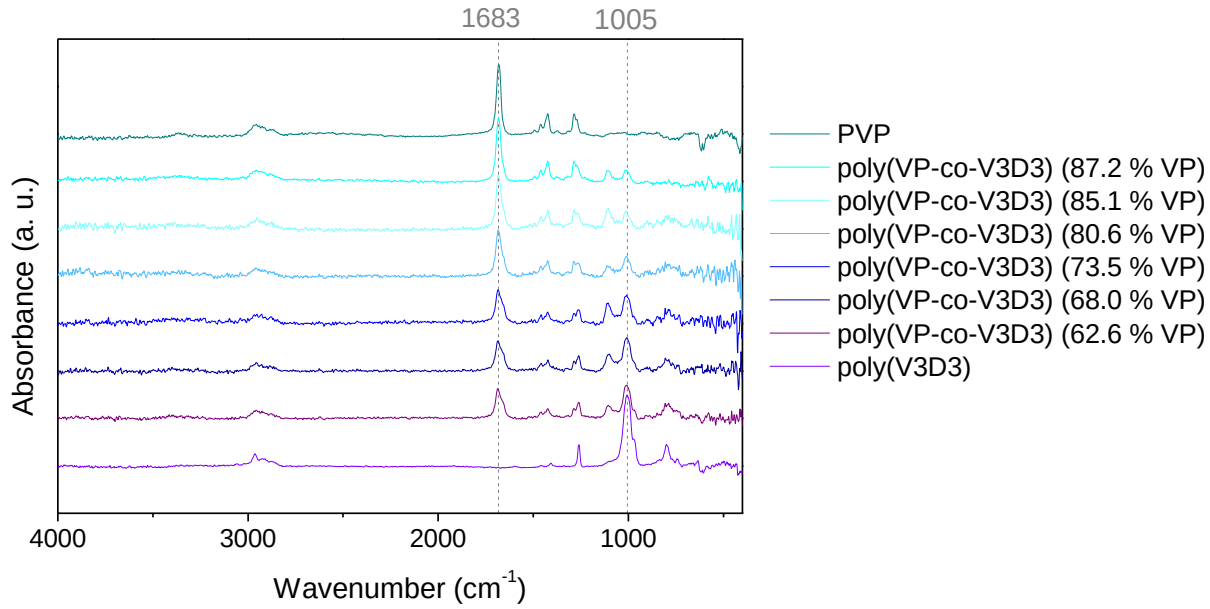

Figure 11: FTIR spectra of poly(VP-co-V3D3) deposited by iCVD with varying injection fractions of VP. The peak at 1005 cm^{-1} is representative of the Si-O-Si bond. The peak at 1682 cm^{-1} is specific to O=C-N bonds.

Of course, the other peaks present on the individual polymers can also be seen for the copolymers. The large band centred around 2900 cm^{-1}, specific to CH_X stretching, is present for all polymers, including PVP and poly(V3D3). The PVP specific bonds emerging at 1427 cm^{-1} and 1288 cm^{-1} correspond to CH_X bending and C-N stretching respectively. Their intensity is stronger with a higher proportion of injected VP. Intervening with the peak at 1288 cm^{-1} and making it appear as a doublet, is the peak representative of Si-CH_3 bonds in poly(V3D3) which emerges at 1260 cm^{-1}. As expected, this has more intensity when more V3D3 was injected. Last but not least, for the copolymers obtained by injecting a higher proportion of V3D3, a large band around 795 cm^{-1} emerges. This corresponds to a mix of Si-C, Si-O and CH_3 bands.

Complete polymerisation is shown from the absence of a peak around 1630 cm^{-1} which would be representative of residual vinyl bonds. Along with the conservation of the functional groups from each precursor and the presence of CH_x bonds, this strongly points to a free radical copolymerisation of VP and V3D3 leading to crosslinked poly(VP-co-V3D3).

3.2.1.2. Estimating the monomer fractions in the copolymer

As it can be seen in the FTIR spectra studied above, as the injection fraction of VP increases, the peak specific to PVP around 1682 cm^{-1} increases. On the other hand, the peak specific to poly(V3D3) around 1005 cm^{-1} decreases. By calculating the area beneath these peaks, we can quantify these differences.

To do so, specific zones were selected: for calculating the area beneath the PVP specific peak, the data points between 1600 and 1750 cm^{-1} were selected; for the area beneath the poly(V3D3)

specific peak, the data points between 950 and 1050 cm^{-1} were selected. Then Origin's integrate function was used to calculate the absolute area under the curve. The area was also calculated following the same method for the spectra of the corresponding polymer. This value was then used to normalise the data. The results show that as the injection fraction of VP increases, the area under the peak specific to PVP increases linearly and the area under the peak specific to poly(V3D3) decreases linearly (Figure 12).

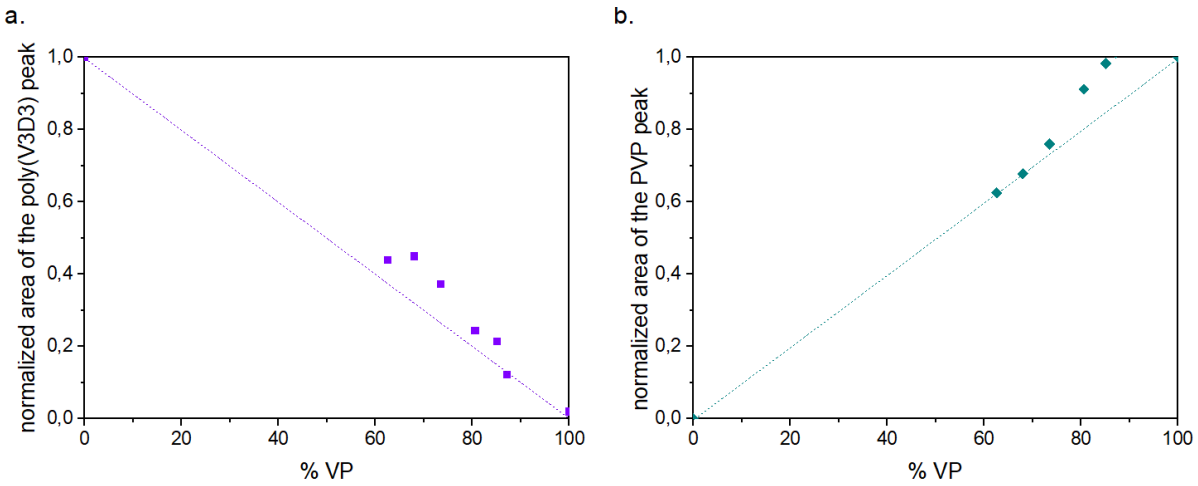

Figure 12: Normalised area under the FTIR spectra a. for the specific PVP peak at 1682 cm^{-1} (area considered between 1600 and 1750 cm^{-1}), b. for the specific poly(V3D3) peak at 1005 cm^{-1} (area considered between 950 and 1050 cm^{-1}).

The areas can then be used to determine the fraction of each monomer in the copolymer[9]. Rigorously, these areas should be corrected by the absorption coefficients of the respective peaks Si-O-Si and O=C-N. In this study, the hypothesis that these absorption coefficients are of the same magnitude will be made. With this hypothesis, the fraction of VP in the copolymer F_{VP} is given by:

$$F_{VP} = \frac{A_{PVP}}{A_{PVP} + A_{pV3D3}}$$

with A_{PVP} the area under the FTIR spectrum of the copolymer between 1600 and 1750 cm^{-1} normalised by the area under the PVP FTIR spectrum in the same range, and A_{pV3D3} the area under the FTIR spectrum of the copolymer between 950 and 1050 cm^{-1} normalised by the area under the poly(V3D3) FTIR spectrum in the same range.

In the same way, the fraction of V3D3 in the copolymer can be determined by:

$$F_{V3D3} = \frac{A_{pV3D3}}{A_{pV3D3} + A_{PVP}}$$

The injected monomer fractions f_{VP} and f_{V3D3} as well as the monomer fractions in the copolymer F_{VP} and F_{V3D3} are summarised in the following table.

Table 4: Injected monomer fractions and monomer fractions in the copolymer as calculated using the FTIR spectra.

Injected monomer fraction		Monomer fraction in the copolymer	
f_{VP}	f_{V3D3}	F_{VP}	F_{V3D3}
0	1	0	1
0,63	0,37	0,59	0,41
0,68	0,32	0,60	0,40
0,74	0,27	0,67	0,33
0,81	0,19	0,79	0,21
0,85	0,15	0,82	0,18
0,87	0,13	0,89	0,11
1	0	1	0

When plotting the fraction of VP found in the copolymer F_{VP} as a function of the monomer fraction f_{VP} (Figure 13), it can be seen that the evolution increases linearly. This has previously been seen for copolymers poly(VP-co-EGDA) studied by Smolin *et al.* and explained by the fact that the polymerisation process in iCVD is adsorption limited[9]. However, as it was seen for the PVP thin films previously, the adsorption of the monomer on the substrate is not the only impacting parameter for iCVD deposition. Furthermore, this explanation implies that injected monomer fractions are equivalent to the adsorbed monomer fractions on the surface. This is unlikely because VP is more volatile than V3D3 as it can be seen in the Clausius-Clapeyron diagram (chapter 2, figure 4).

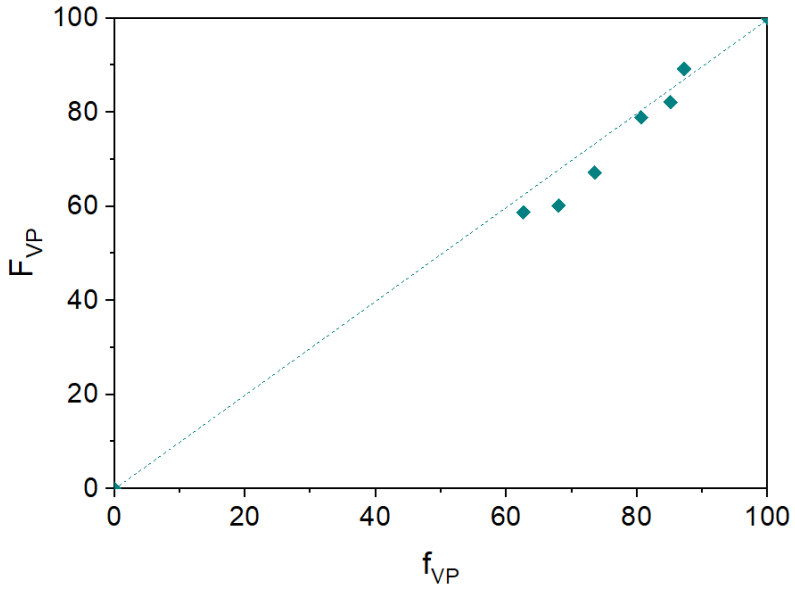

Figure 13: Plot of the fraction of VP (F_{VP}) in the deposited copolymer as a function of the injected fraction of VP (f_{VP}).

However, for the following section, we will make the hypothesis that the fraction of adsorbed monomer at the surface is equal to the injected fraction of monomer.

3.2.1.3. Determining the reactivity ratios using the Fineman-Ross equation

The monomer fractions f_{VP} and f_{V3D3} and the monomer fractions in the final copolymer F_{VP} and F_{V3D3} can be used to solve the Fineman-Ross equation to determine the reactivity ratios r_{VP} and r_{V3D3}[9,31–33]. The Fineman-Ross equation is the following:

$$Y = r_{VP} \times X + r_{V3D3}$$

with:

$$X = \frac{f_{VP}^2(F_{VP} - 1)}{F_{VP}(1 - f_{Vp})^2}$$

and:

$$Y = \frac{f_{VP}(1 - 2F_{VP})}{F_{VP}(1 - f_{VP})}$$

These reactivity ratios can give an idea of the distribution of both monomers in the final copolymer. Indeed, when both reactivity ratios r_A and r_B for monomers A and B are close to 0, monomer A will react preferentially with monomer B, forming an alternating copolymer. When r_A and r_B are close to 1, each monomer will react to A and B with the same preference, leading to a random copolymer. Finally, if r_A is higher than 1, it will preferably react with another monomer A. Therefore, if both r_A and r_B are much higher than 1, block copolymers will form[9].

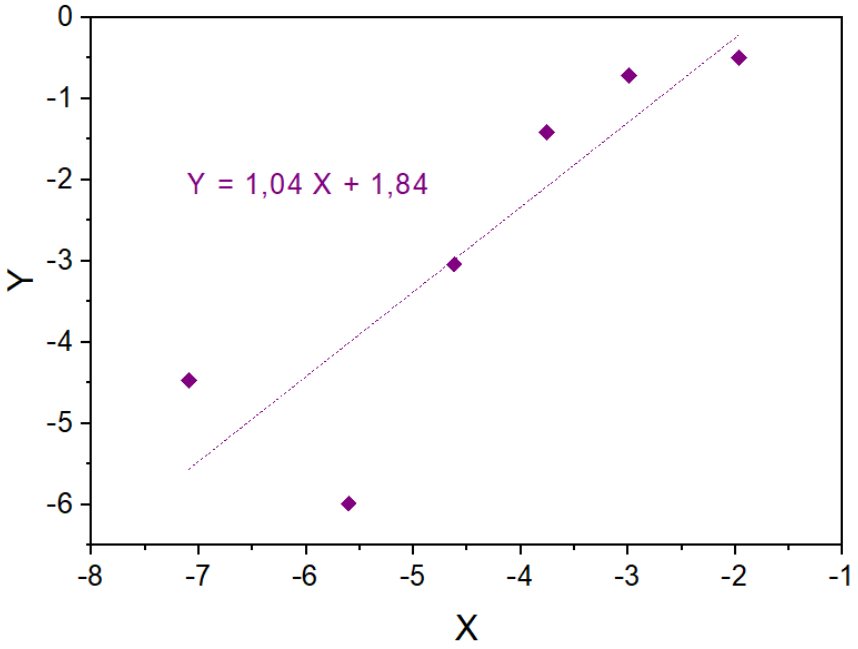

Figure 14: Fineman-Ross plot for poly(VP-co-V3D3) injected with a chamber pressure of 1.5 Torr and a chiller temperature of 40°C.

In this case, plotting the data as it can be seen in Figure 14, gives the following reactivity ratios: r_{VP} = 1.04 and r_{V3D3} = 1.84. These reactivity ratios suggest that while VP reacts equally to another VP monomer and to V3D3, V3D3 has a very slight preference for reacting with another V3D3 molecule. Overall, both reactivity ratios being close to 1, this suggest that the copolymers poly(VP-co-V3D3) created in these conditions are random copolymers. A possible representation can be seen in Figure 15. However, it should be kept in mind that these results are based on the approximation that the monomer fraction absorbed at the surface is equivalent to the injected monomer fraction and on the hypothesis that the adsorption coefficients of Si-O-Si and O=C-N bonds are of equivalent magnitudes.

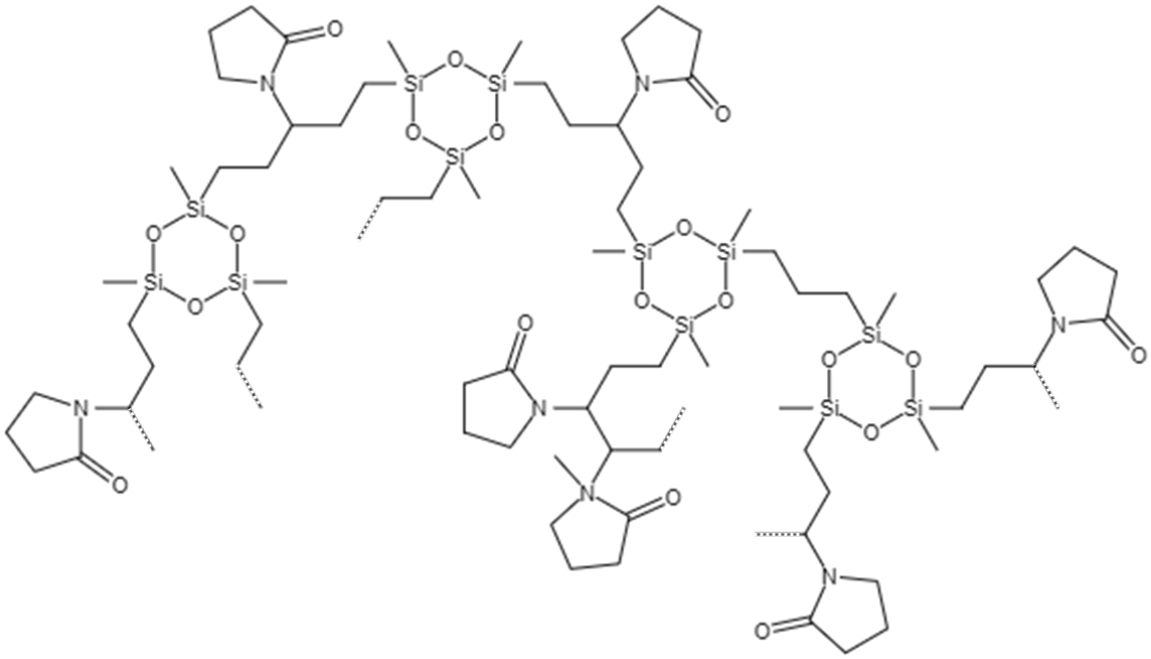

Figure 15: Schematic representation of a possible structure for the crosslinked random copolymer poly(VP-co-V3D3).

3.2.1.4. XPS to study the surface chemistry of these copolymers

For further understanding of the evolution of the chemistry of these copolymers with the variation of the injection fractions of VP, XPS analysis was carried out. Three samples were characterised, each with a different mass percentage of injected VP: 62.6, 80.6 and 87.2 %.

Firstly, XPS confirms the presence of both precursors in the coatings as it reveals the presence of N, specific to the VP monomer, and Si, specific to the V3D3 precursor. Indeed, although some Si traces were found in the PVP thin films they are believed to be due to from cleavage residues as no Si is found in either the VP monomer or the TBPO radical initiator. C and O are found in both monomers, making their attribution less evident.

Table 5: Atomic percentages of C 1s, O 1s, N 1s and Si 2p in poly(VP-co-V3D3) deposited by iCVD with varying mass percentage of VP. Atomic percentages of poly(V3D3) (48 nm) and PVP (67.4 nm) have been added to facilitate comparison.

Polymer	% VP injected	Atomic percentage			
		C 1s	O 1s	N 1 s	Si 2p
poly(V3D3)	0	59.7	23.0	0	17.4
Poly(VP-co-V3D3)	62.6	64.3	20.7	4.5	10.4
	80.6	67.5	18.7	6.6	7.2
	87.2	69.7	16.6	9.0	4.6
PVP	100	73.6	13.0	12.4	1.0

High-resolution XPS spectra allowed us to determine the chemical bonds present in the copolymer. To begin, this spectrum highlights that for all atoms, the injection fraction of each precursor does not have an effect on the presence or absence of certain bonds, only on their proportion. This is coherent with other work on iCVD copolymers[17]. Moreover, the same bonds as in each individual polymer can be seen.

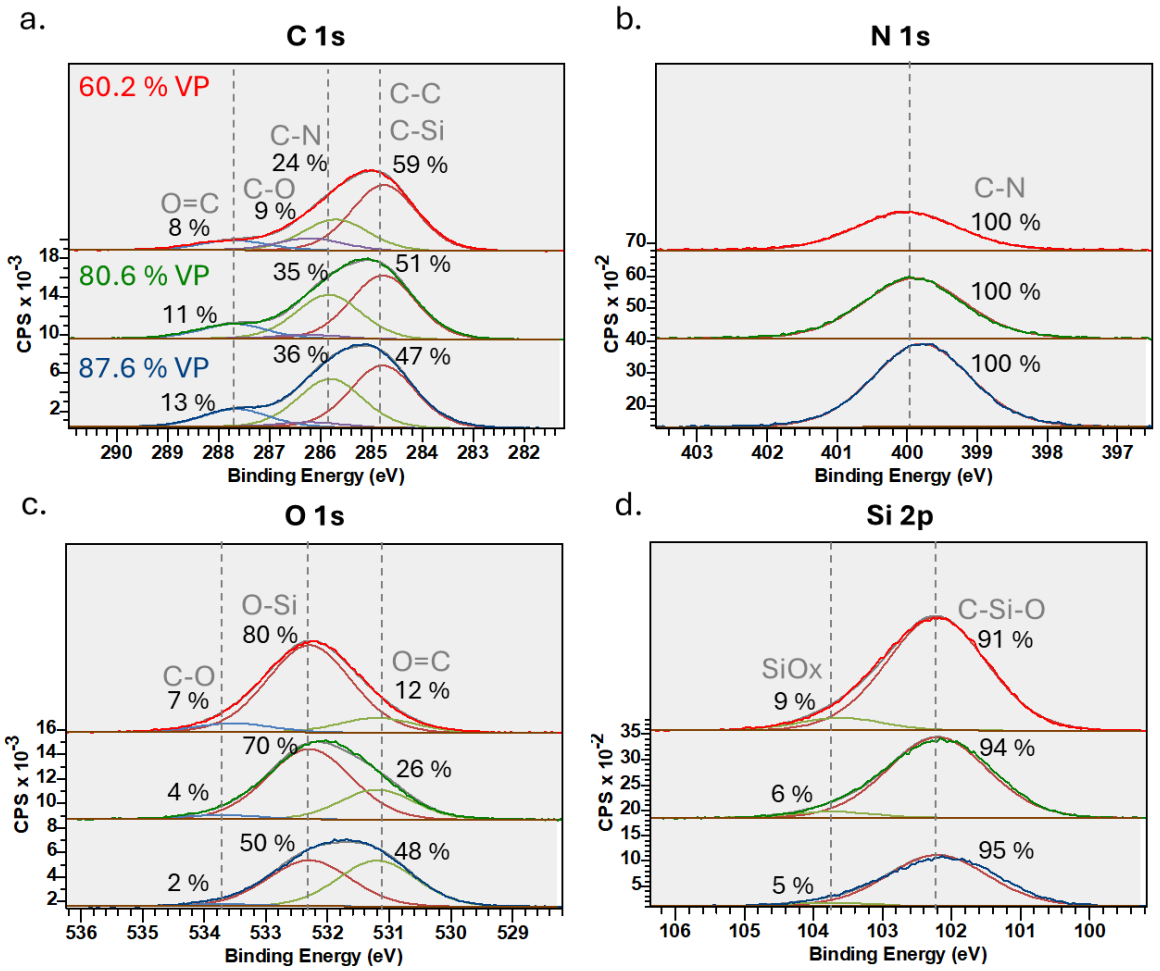

Figure 16: Deconvolution of high resolution XPS spectra of a. C 1s, b. N 1s, c. O 1s and d. Si 2p for poly(VP-co-V3D3) copolymers deposited by iCVD onto 200 mm silicon wafers with a varying mass percentage of VP.

For C 1s, as shown in Figure 16a, four deconvolution peaks can be seen. More precisely, the peak with a binding energy of 284.8 eV corresponds to a combination of C-C and C-Si bonds as it was seen for poly(V3D3) and pp(V3D3)[34]. At 285.5 eV, there is a peak corresponding to C-N bonds for which the proportion increases (from 24 % to 36 %) with the injection fraction of VP[11]. This is because the N atoms can only be found in VP molecules. Similarly, the proportion of C=O bonds, which can be seen at 287.7 eV, increases from 8 to 13 % as the injection fraction of VP increases from 60.2 to 87.6 %[7]. At 286.2 eV, there is a peak which shows the presence of C-O bonds. However, as the injection fraction of VP increases, their proportion decreases from 9 % to 3 %. As for PVP, a single peak can be seen for N 1s with a binding energy of 399.9 eV. This corresponds to C-N bonds[7]. Its intensity increases with the amount of VP. For O 1s, as the injection fraction of VP increases, the proportion of O=C bonds increases from 12 to 48 %. Lastly, for Si 2p, the same two peaks can be seen as in poly(V3D3): C-Si-O with a binding energy of 102.2 eV and SiO_X with a binding energy of 103.7 eV.

Therefore, the XPS spectra confirms that increasing the proportion of injected VP results in increasing the proportion of bonds specific to the VP precursor in the final copolymer. It also shows bonds specific to both individual polymers, such as the O-Si-C bonds found in poly(V3D3) and the O=C-N bond found in PVP.

3.2.2. Effect of the precursor ratio on the refractive index of the copolymer

These chemical differences likely have an impact on the optical index of the material. To check this hypothesis, the latter was evaluated by spectroscopic ellipsometry.

Figure 17 shows the evolution of the refractive index at 632.8 nm with the injection fraction of VP. It demonstrates that for the copolymers with a high content of VP, the optical index is close to that obtained for iCVD deposited PVP films without crosslinking. Indeed, when over 75 % of the injected mass of precursors corresponds to the VP monomer, the associated refractive index is around 1.52, which is very close to n_{PVP} = 1.52. A lower proportion of VP leads to copolymers with a lower optical index around 1.51. This value remains much higher that the optical index of poly(V3D3) which is $n_{poly(V3D3)}$ = 1.48.

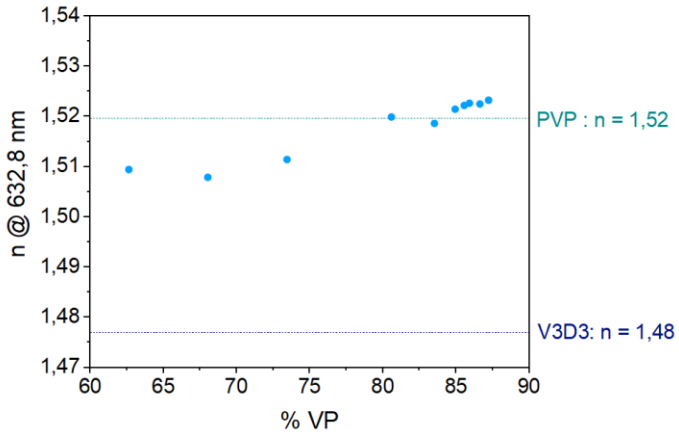

Figure 17: Optical index of poly(VP-co-V3D3) deposited by iCVD with varying injection fraction of VP.

Here again, the measurement of the refractive index of the copolymer thin films shows variations with the proportion of injected precursors. It is possible that the density of the films also evolves with the composition of the coatings.

3.2.3. Kinetics of copolymer deposition

As well as giving an approximation of the optical index of the copolymers, spectroscopic ellipsometry was used to measure their thickness. Two sets of copolymers were studied: one with a VP injection fraction of 60.6 % and the other with a VP injection fraction of 85.6 %. The thickness of these thin films was measured at different points over the 200 mm silicon wafer on which the coatings were deposited and the resulting mapping images can be seen Figure 18.

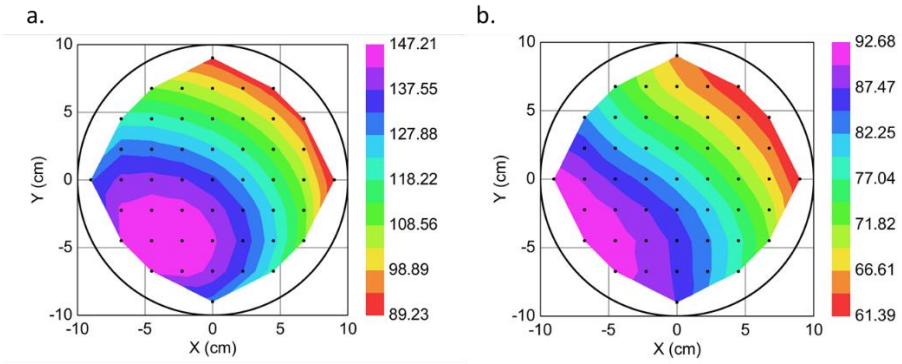

Figure 18: Mapping images of poly(VP-co-V3D3) coatings deposited by iCVD onto a 200 mm silicon wafer with a reactor pressure of 1.5 Torr and a substrate temperature of 40°C with an injection fraction of VP of a. 62.6 % and b. 85.6 %. Time of deposition was 3500 s for both coatings.

They reveal a thickness gradient which evolves with the VP injection fraction, which itself evolves by varying the injection rates of each precursor. There seems to be more of a centred dome shape for copolymers with a lower fraction of VP. Moreover, these images show that for a same deposition time (3 500 s), the average thickness depends on the injected mass percentage of VP.

Figure 19 represents the average thickness over the entire wafer as a function of time for different injection fractions of VP. It can be seen that the thickness varies with the proportion of injected VP. Indeed, when this value is 62.6 %, for a same deposition time, the thickness is nearly twice as high as when the injected fraction of VP is 85.6 %.

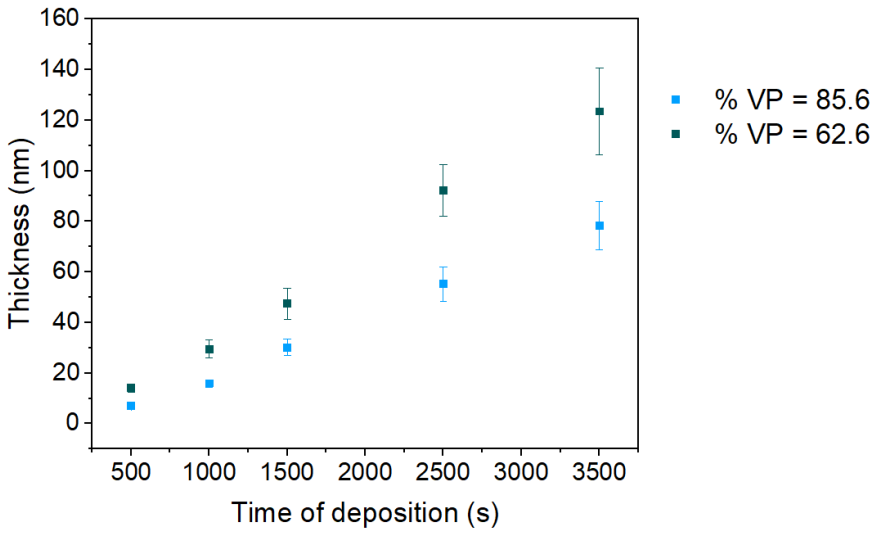

Figure 19: Thickness of poly(VP-co-V3D3) thin films deposited by iCVD with a varying injection fraction of VP.

While a two-regime growth mechanism was observed for PVP thin films, for these poly(VP-co-V3D3) copolymers, the thickness of the thin films seems to grow linearly with deposition time as for poly(V3D3). One hypothesis that can be made is that crosslinked polymers do not undergo a two-regime growth during iCVD process as linear polymers seem to do.

To further understand the evolution of the apparent deposition rate with the precursor injection ratio, the thickness was evaluated for copolymers deposited with a VP injection fraction varying between 60 and 90 % (Figure 20).

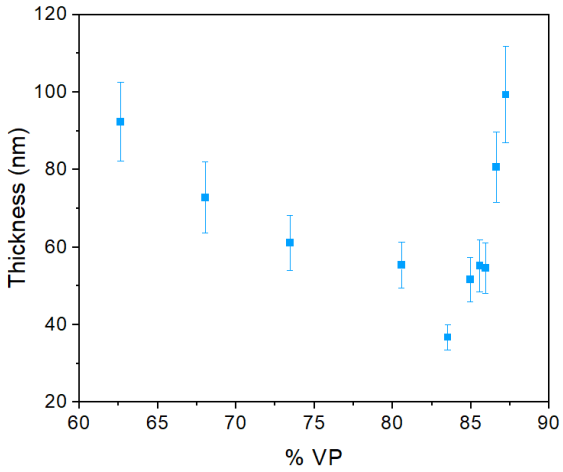

Figure 20: Thickness of poly(VP-co-V3D3) copolymers deposited by iCVD at 1.5 Torr and 40°C. All depositions were carried out for 2500 s.

This figure shows that the apparent deposition rate varies between 0.9 and 2.4 nm/min depending on the injection fraction of VP. However, as these ratios were modified by varying the injection rates of each precursor (between 0.15 and 0.2 g/min for VP and between 0.03 and 0.1 g/min for V3D3), it may be possible that this is the cause of a varying growth rate. To verify this hypothesis, the apparent deposition rate was traced as a function of each monomer flow rate, with the other precursor injection rate at a fixed value. This is represented in Figure 21.

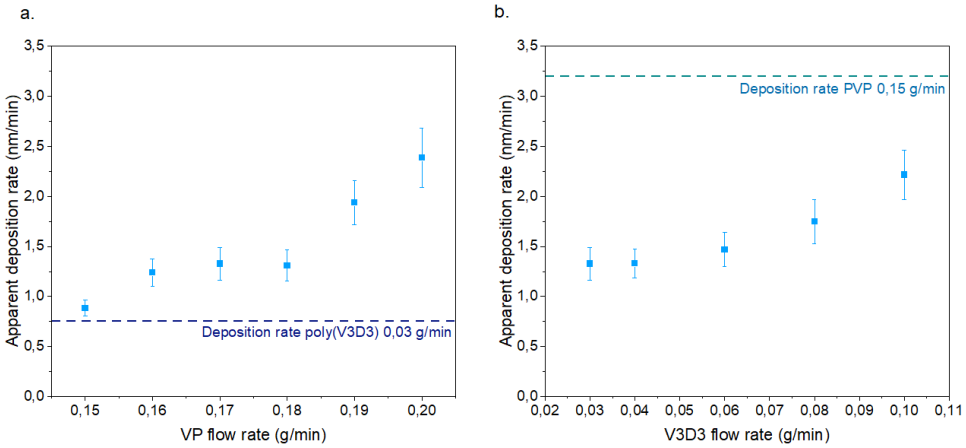

Figure 21: Deposition rate of poly(VP-co-V3D3) deposited by iCVD at 37°C and 1.5 Torr with a. a V3D3 flowrate fixed at 0.03 g/min and a varying flowrate of VP, b. a VP flowrate fixed at 0.17 g/min and a varying flowrate of V3D3.

More precisely, Figure 21a represents the copolymer apparent growth rate when the deposition was carried out with V3D3 injection regulated at 0.03 g/min and a varying flowrate of VP. Figure 21b, on the other hand, corresponds to copolymers deposited with a varying flowrate of V3D3 and VP injection rate fixed at 0.17 g/min. These figures show that the flowrate of the precursors influences the apparent deposition rate of the copolymers. Furthermore, a lower propagation rate constant k_p for V3D3, which also imparts larger steric hindrance, could also reduce the apparent deposition rate of the copolymer thin films.

3.2.4. Disappearance of coating heterogeneities through crosslinking

To study the effect of the proportion of injected monomers on the thin film roughness and overall aspect, AFM was carried out. Copolymers with different VP injection fractions (62.6, 80.6 and 87.2 %) were analysed and, as shown in Figure 22, it seems that as the injection fraction of VP increases, the aspect of the coating varies, and the grain size increases.

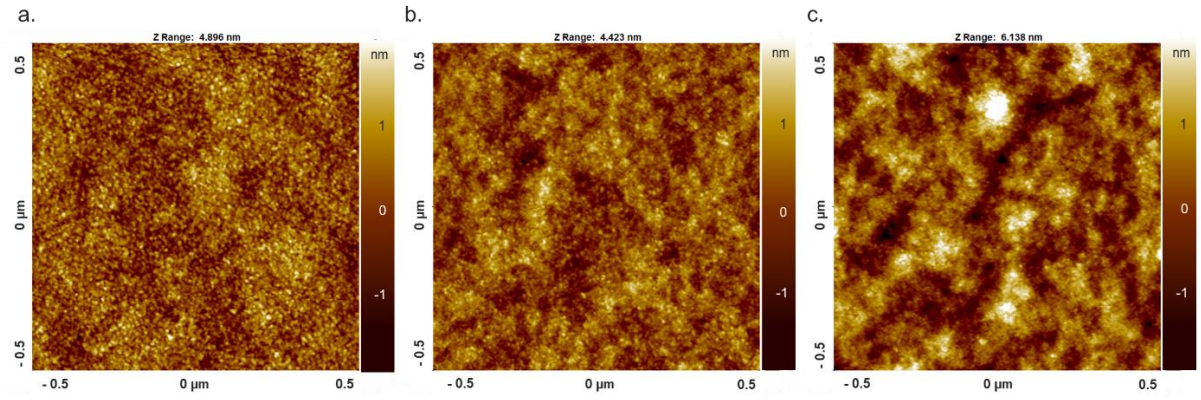

Figure 22: AFM images for poly(VP-co-V3D3) copolymers deposited by iCVD with an injection mass percentage of VP of a. 62.6 % (film thickness = 92.3 nm), b. 80.6 % (film thickness = 55.3 nm), c. 87.2 % (film thickness = 99.3 nm).

However the Rq roughness of these copolymer films is under 0.8 nm for all tested conditions (Table 6). This is comparable to the PVP thin films studied in section 2.2.2.3 (Rq < 0.6 nm). Furthermore, there does not seem to be an effect of the thickness on the roughness or the aspect of the films. Indeed, copolymers created with a VP injection fraction of 62.6 and 80.6 % both have an Rq roughness around 0.5 nm. However, their thickness varies from 92 to 55 nm respectively. Analysis of copolymer thin films with a larger thickness should be carried out to consolidate these observations.

Table 6: Rq roughness values for poly(VP-co-V3D3) thin films deposited by iCVD.

VP/V3D3 injection ratio	Time of deposition (s)	Thickness of the PVP coating (nm)	Z range (nm)	Rq (nm)
62.6	2500	92.3	4.896	0.54
80.6	2500	55.3	4.423	0.52
87.2	2500	99.3	6.138	0.71

Lastly, it was observed, as mentioned in section 2.2.2.3, that dendritic shapes appeared for PVP coatings. No such shapes could be observed on any of the copolymers we developed. This could be a result of the slightly higher substrate temperature used for the deposition of these copolymers[30].

3.3.A hydrophilic but insoluble surface

3.3.1. Wettability

WCAs were measured on poly(VP-co-V3D3) to check whether the coating still conserves PVP's hydrophilic property after crosslinking. As before, 15 droplets were deposited across the diameter of the coated silicon wafer. WCAs were measured 1 s and 10 s after the droplets were deposited onto the surface.

Figure 23 shows that, like for PVP (Figure 8), the droplets spread slightly after their deposition onto the surface. Indeed, the WCA is lower after 10 s for all coatings.

Furthermore, the wettability of the copolymers largely depends on the proportion of VP in the copolymer. Indeed for a VP injection fraction of 62.6%, the WCA is around 85° which is close to that of poly(V3D3) ($WCA_{poly(V3D3)}$ = 95°). However, when increasing this proportion to 87.2 %, the WCA decreases to around 50°.

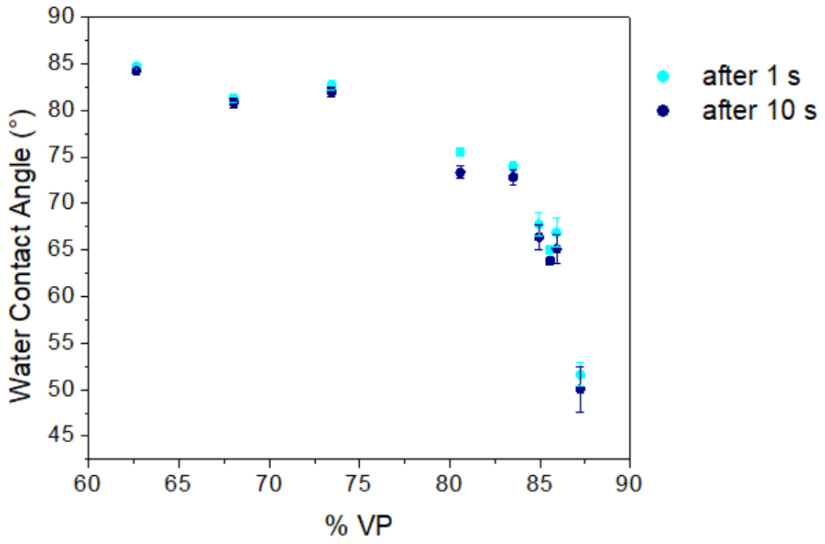

Figure 23: Water Contact Angle on poly(VP-co-V3D3) deposited by iCVD with varying injected fractions of VP.

This hydrophilicity is encouraging for the development of antibiofouling surfaces. Nevertheless, in the studied conditions, superhydrophilicity as it can be seen for PVP (WCA_{PVP} < 20°) was not yet achieved.

Unlike on PVP coatings, the WCA measurements on poly(VP-co-V3D3) did not leave droplet traces showing the dissolution of the thin film. This is promising for the stability of these crosslinked polymers.

3.3.2. Stability of poly(VP-co-V3D3)

To evaluate the solubility of these copolymers, samples were soaked in PBS 1X for 24 hours and the thickness of the copolymer was measured before and after.

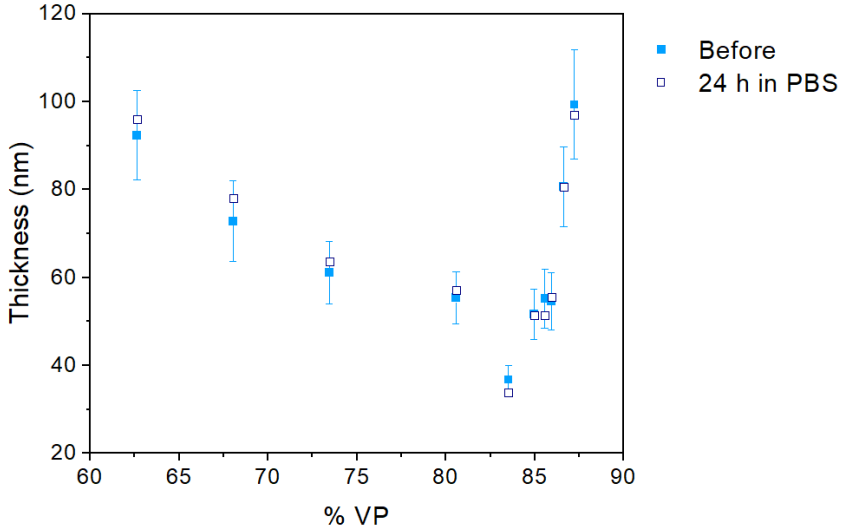

Figure 24: Thickness of poly(VP-co-V3D3) before and after soaking in PBS for 24 hours.

Figure 24 shows that no thickness removal can be seen after 24 hours soaking in PBS, even for the copolymers with a high proportion of VP. This is very promising as all PVP was removed when it was coated without a crosslinking agent. Therefore, as it was suggested in the literature, crosslinking PVP does lead to it becoming insoluble in aqueous solutions[35]. Furthermore, it seems that even a small amount of crosslinking agent is enough to induce such insolubility.

4. Conclusions

In this chapter, smooth hydrophilic coatings obtained using iCVD were highlighted. First, PVP thin films were developed. Study of the kinetics of this thin film deposition highlighted a two-regime mechanism such as the one found for P(nPMA) coatings[26]. However, for a saturation ratio $P_m/P_{sat} > 0.6$, it also seemed that the deposition rate was limited by thermally activated bulk polymerisation. These PVP thin films demonstrated superhydrophilicity but also showed solubility in PBS, therefore impeding their use for antibiofouling applications.

To counter this limitation, for the first time, V3D3 was successfully used as a crosslinking agent to bring stability to the PVP polymers by creating copolymers poly(VP-co-V3D3). The proportion of each monomer in the final coating can be tuned by adjusting the injection flowrates of each precursor. By studying the areas under the FTIR curves, it was shown that the fraction of VP in the copolymer was proportional to the injected fraction of VP. Furthermore, with the hypothesis that this injected fraction was equivalent to the fraction of monomer at the surface, the Fineman-Ross equation was applied. This allowed the estimation of the reactivity ratios of each monomer in the copolymer: $r_{VP} = 1.04$ and $r_{V3D3} = 1.84$. As these reactivity ratios are both close to 1, the copolymer poly(VP-co-V3D3) deposited by iCVD in these conditions is most likely a random copolymer

Study of the apparent deposition rates of these copolymer thin films showed that the variation of injection flowrates had a significant impact on the kinetics of the thin films. Furthermore, adding V3D3 as a cross-linking agent significantly slowed the apparent deposition rate. This can be due to a lower propagation rate constant k_p and could also be impacted by the steric hindrance of this larger molecule.

These poly(VP-co-V3D3) copolymers showed good hydrophilicity although in these conditions the WCA stayed above 50°. However, after 24 hours soaking in PBS, no significant thickness loss could be noted, confirming the effectiveness of crosslinking PVP with V3D3 to make it insoluble. The codeposition also seemed to lead to more homogeneous thin films than when depositing PVP alone.

The work presented in this chapter shows the advantages of using iCVD for depositing thin films. Indeed, as it was also highlighted in chapter 3, this technique is based on free radical polymerisation of the monomer(s), allowing conservation of the functional groups and good control over the thin film properties. It is also the only deposition method which can create thin films of crosslinked polymer. This allows tuning of the final coating by adjusting the proportion of monomer and crosslinking agent. In this work, it was possible to create insoluble hydrophilic thin films which conserve the functional groups of both VP and V3D3.

5. Bibliography

(1) Guo, H.; Wen, C.; Tian, S.; Zhang, X.; Ma, Y.; Liu, X.; Yang, J.; Zhang, L. Universal Intraductal Surface Antifouling Coating Based on an Amphiphilic Copolymer. *ACS Applied Materials and Interfaces*, **2021**, 13 (18), 21051-21059, https://doi.org/10.1021/acsami.1c04579

(2) Jiang, J.; Zhu, L.; Zhu, L.; Zhang, H.; Zhu, B.; Xu, Y. Antifouling and Antimicrobial Polymer Membranes Based on Bioinspired Polydopamine and Strong Hydrogen-Bonded Poly(*N* -Vinyl Pyrrolidone). *ACS Applied Materials and Interfaces* **2013**, *5* (24), 12895–12904. https://doi.org/10.1021/am403405c.

(3) Guo, H.; Liu, X.; Zhao, W.; Xie, C.; Zhu, Y.; Wen, C.; Li, Q.; Sui, X.; Yang, J.; Zhang, L. A Polyvinylpyrrolidone-Based Surface-Active Copolymer for an Effective Marine Antifouling Coating. *Progress in Organic Coatings* **2021**, *150*, 105975. https://doi.org/10.1016/j.porgcoat.2020.105975.

(4) Su, C.; Hu, Y.; Song, Q.; Ye, Y.; Gao, L.; Li, P.; Ye, T. Initiated Chemical Vapor Deposition of Graded Polymer Coatings Enabling Antibacterial, Antifouling, and Biocompatible Surfaces. *ACS Applied Materials and Interfaces* **2020**, *12* (16), 18978–18986. https://doi.org/10.1021/acsami.9b22611.

(5) Liu, X.; Xu, Y.; Wu, Z.; Chen, H. Poly(N-Vinylpyrrolidone)-Modified Surfaces for Biomedical Applications. *Macromolecular Bioscience* **2013**, *13* (2), 147–154. https://doi.org/10.1002/mabi.201200269.

(6) Li, Z.; Wang, S.; Yang, X.; Liu, H.; Shan, Y.; Xu, X.; Shang, S.; Song, Z. Antimicrobial and Antifouling Coating Constructed Using Rosin Acid-Based Quaternary Ammonium Salt and N-Vinylpyrrolidone via RAFT Polymerization | Elsevier Enhanced Reader. *Applied Surface Science* **2020**, *530*, 147193. https://doi.org/10.1016/j.apsusc.2020.147193.

(7) Chan, K.; Kostun, L. E.; Tenhaeff, W. E.; Gleason, K. K. Initiated Chemical Vapor Deposition of Polyvinylpyrrolidone-Based Thin Films. *Polymer* **2006**, No. 47, 6941–6947. https://doi.org/10.1016/j.polymer.2006.07.068.

(8) Janakiraman, S.; Farrell, S. L.; Hsieh, C.-Y.; Smolin, Y. Y.; Soroush, M.; Lau. Kinetic Analysis of the Initiated Chemical Vapor Deposition of Poly(Vinylpyrrolidone) and Poly(4-Vinylpyridine). *Thin Solid Films* **2015**, *595*, 244–250. https://doi.org/10.1016/j.tsf.2015.04.083.

(9) Smolin, Y. Y.; Janakiraman, S.; Soroush, M.; Lau, K. K. S. Experimental and Theoretical Investigation of Dye Sensitized Solar Cells Integrated with Crosslinked Poly(Vinylpyrrolidone) Polymer Electrolyte Using Initiated Chemical Vapor Deposition. *Thin Solid Films* **2017**, *635*, 9–16. https://doi.org/10.1016/j.tsf.2016.12.034.

(10) Sun, M.; Qiu, H.; Su, C.; Shi, X.; Wang, Z.; Ye, Y.; Zhu, Y. Solvent-Free Graft-From Polymerization of Polyvinylpyrrolidone Imparting Ultralow Bacterial Fouling and Improved Biocompatibility. *ACS Applied Bio Materials* **2019**. https://doi.org/10.1021/acsabm.9b00529.

(11) Sun, M.; Wu, Q.; Xu, J.; He, F.; Brown, A. P.; Ye, Y. Vapor-Based Grafting of Crosslinked Poly(N-Vinyl Pyrrolidone) Coatings with Tuned Hydrophilicity and Anti-Biofouling Properties. *Journal of Materials Chemistry B* **2016**, *4* (15), 2669–2678. https://doi.org/10.1039/C6TB00076B.

(12) Liu, W.; Su, C.; Su, P.; Yang, H.; Lu, P.; Du, Z.; Ye, Y. Sub-20 Nm Bilayer Hydrophilic Poly(Vinyl Pyrrolidone) Coatings for Antifouling Nanofiltration Membranes. *Macromolecular Materials and Engineering* **2021**, *n/a* (n/a), 2100026. https://doi.org/10.1002/mame.202100026.

(13) Lau, K. K. S.; Gleason, K. K. Initiated Chemical Vapor Deposition (iCVD) of Copolymer Thin Films. *Thin Solid Films* **2008**, *516* (5), 678–680. https://doi.org/10.1016/j.tsf.2007.06.046.

(14) Yılmaz, K.; Şakalak, H.; Gürsoy, M.; Karaman, M. Vapor Deposition of Stable Copolymer Thin Films in a Batch iCVD Reactor. *Journal of Applied Polymer Science* **2021**, *138* (13), 50119. https://doi.org/10.1002/app.50119.

(15) Petruczok, C. D.; Yang, R.; Gleason, K. K. Controllable Cross-Linking of Vapor-Deposited Polymer Thin Films and Impact on Material Properties. *Macromolecules* **2013**, *46* (5), 1832–1840. https://doi.org/10.1021/ma302566r.

(16) Ryu, J.; Oh, M. S.; Yoon, J.; Kang, M.; You, J. B.; Lee, H.; Im, S. G. One-Step Synthesis of a Robust, Ultrathin, Stretchable Antifogging Copolymer Film. *Journal of Materials Chemistry C* **2023**, *11* (13), 4318–4327. https://doi.org/10.1039/D2TC04838H.
(17) Pak, K.; Seong, H.; Choi, J.; Hwang, W. S.; Im, S. G. Synthesis of Ultrathin, Homogeneous Copolymer Dielectrics to Control the Threshold Voltage of Organic Thin-Film Transistors. *Advanced Functional Materials* **2016**, *26* (36), 6574–6582. https://doi.org/10.1002/adfm.201602585.
(18) Jeong, J.; Kim, M. J.; Hwang, W. S.; Cho, B. J. Copolymer-Based Flexible Resistive Random Access Memory Prepared by Initiated Chemical Vapor Deposition Process. *Advanced Electronic Materials*, 2100375. **2021** https://doi.org/10.1002/aelm.202100375.
(19) Prasath, V. S.; Lau, K. K. S. Kinetically Limited Bulk Polymerization of Polymer Thin Films by Initiated Chemical Vapor Deposition. *Macromolecules* **2023**, *56* (24), 10111–10118. https://doi.org/10.1021/acs.macromol.3c01868.
(20) Wang, F. C.; Feve, M.; Lam, T. M.; Pascault, J.-P. FTIR Analysis of Hydrogen Bonding in Amorphous Linear Aromatic Polyurethanes. I. Influence of Temperature. *Journal of Polymer Science Part B: Polymer Physics* **1994**, *32* (8), 1305–1313. https://doi.org/10.1002/polb.1994.090320801.
(21) Zhu, X.; Lu, P.; Chen, W.; Dong, J. Studies of UV Crosslinked Poly(N-Vinylpyrrolidone) Hydrogels by FTIR, Raman and Solid-State NMR Spectroscopies. *Polymer* **2010**, *51* (14), 3054–3063. https://doi.org/10.1016/j.polymer.2010.05.006.
(22) Ahn, M.-Y.; Hwang, I.-T.; Jung, C.-H.; Nho, Y.-C.; Choi, J.-H.; Huh, K. M. Cell Patterning on a Poly(N-Vinyl Pyrrolidone)-Patterned Polystyrene Substrate by Using Ion Implantation. *Journal of Industrial Engineering and Chemistry* **2010**, *16* (1), 87–90. https://doi.org/10.1016/j.jiec.2010.01.015.
(23) Kuchakova, I.; Ionita, M. D.; Ionita, E.-R.; Lazea-Stoyanova, A.; Brajnicov, S.; Mitu, B.; Dinescu, G.; De Vrieze, M.; Cvelbar, U.; Zille, A.; Leys, C.; Yu Nikiforov, A. Atmospheric Pressure Plasma Deposition of Organosilicon Thin Films by Direct Current and Radio-Frequency Plasma Jets. *Materials* **2020**, *13* (6), 1296. https://doi.org/10.3390/ma13061296.
(24) *Carbon | XPS Periodic Table - FR*. https://www.thermofisher.com/fr/fr/home/materials-science/learning-center/periodic-table/non-metal/carbon.html (accessed 2024-03-05).
(25) Han, L. M.; Timmons, R. B. Pulsed-Plasma Polymerization of 1-Vinyl-2-Pyrrolidone: Synthesis of a Linear Polymer. *Journal of Polymer Science Part A: Polymer Chemistry* **1998**, *36* (17), 3121–3129. https://doi.org/10.1002/(SICI)1099-0518(199812)36:17<3121::AID-POLA14>3.0.CO;2-Q.
(26) Bonnet, L.; Altemus, B.; Scarazzini, R.; Veillerot, M.; D'Agosto, F.; Faguet, J.; Jousseaume, V. Initiated-Chemical Vapor Deposition of Polymer Thin Films: Unexpected Two-Regime Growth. *Macromolecular Materials and Engineering* **2017**, *302* (12), 1700315. https://doi.org/10.1002/mame.201700315.
(27) Bonnet, L. Synthèse de Couches Mindes de Polymères Par iCVD: Mécanisme de Croissance et Application Aux Capteurs de Gaz, Thèse de doctorat, Université de Lyon, **2017**
(28) Gleason, K. K. Designing Organic and Hybrid Surfaces and Devices with Initiated Chemical Vapor Deposition (iCVD). *Advanced Materials*, 2306665. **2024** https://doi.org/10.1002/adma.202306665.
(29) Ozaydin-Ince, G.; Coclite, A. M.; Gleason, K. K. CVD of Polymeric Thin Films: Applications in Sensors, Biotechnology, Microelectronics/Organic Electronics, Microfluidics, MEMS, Composites and Membranes. *Reports on Progress in Physics* **2012**, *75* (1), 016501. https://doi.org/10.1088/0034-4885/75/1/016501.
(30) Shindler, S.; Franklin, T.; Yang, R. Prevention and Characterization of Thin Film Defects Induced by Contaminant Aggregates in Initiated Chemical Vapor Deposition. *The Journal of Chemical Physics* **2024**, *160* (14), 144904. https://doi.org/10.1063/5.0195014.
(31) Lau, K. K. S.; Gleason, K. K. Initiated Chemical Vapor Deposition (iCVD) of Copolymer Thin Films. *Thin Solid Films* **2008**, *516* (5), 678–680. https://doi.org/10.1016/j.tsf.2007.06.046.
(32) Yagüe, J. L.; Gleason, K. K. Systematic Control of Mesh Size in Hydrogels by Initiated Chemical Vapor Deposition. *Soft Matter* **2012**, *8* (10), 2890. https://doi.org/10.1039/c2sm07137a.

(33) Petruczok, C. D.; Yang, R.; Gleason, K. K. Controllable Cross-Linking of Vapor-Deposited Polymer Thin Films and Impact on Material Properties. *Macromolecules* **2013**, *46* (5), 1832–1840. https://doi.org/10.1021/ma302566r.
(34) Posseme, N.; Chevolleau, T.; Joubert, O.; Vallier, L.; Rochat, N. Etching of Porous SiOCH Materials in Fluorocarbon-Based Plasmas. *Journal of Vacuum Science & Technology B: Microelectronics and Nanometer Structures Processing, Measurement, and Phenomena* **2004**, *22* (6), 2772–2784. https://doi.org/10.1116/1.1815316.
(35) Tenhaeff, W. E.; Gleason, K. K. Initiated and Oxidative Chemical Vapor Deposition of Polymeric Thin Films: iCVD and oCVD. *Advanced Functional Materials* **2008**, *18* (7), 979–992. https://doi.org/10.1002/adfm.200701479.

Chapter 5: Combining polymers and topography

1. Introduction

Extensive research is being conducted in the realm of combatting microbial contamination. While some teams focus on altering surface chemistry, others draw inspiration from nature's designs, particularly its topological features.

As it was developed in the first chapter, many works have been carried out on developing structures mimicking these natural strategies[1], by combining topography and chemistry[2]. These synergetic approaches can lead to efficient antibiofouling surfaces by multiplying the antibacterial effects. For example, by combining polymers known for being antifouling and structures that can mechanically damage the bacterial cells[3]. In other cases, bactericidal chemistry and topography that creates circulating flows have been combined for their complementary properties against biofilm formation[4]. It has also been proven that in some cases, adding nanotopography to hydrophilic or hydrophobic surfaces can enhance the wettability either way[5], following the Cassie-Baxter or Wenzel effect[6].

In this chapter, a novel multiscale structuration method will be presented, based on NanoImprint Lithography (NIL) and plasma etching. This creates surfaces with perfectly controlled micrometric and nanometric structures, called hierarchical structures (Figure 1). Some of the surface properties of these hierarchical structures, such as chemistry, roughness and wettability will be presented. The polymers studied previously: poly(V3D3), pp(V3D3) and poly(VP-co-V3D3) were then deposited onto these structures to see how this further affected the surfaces.

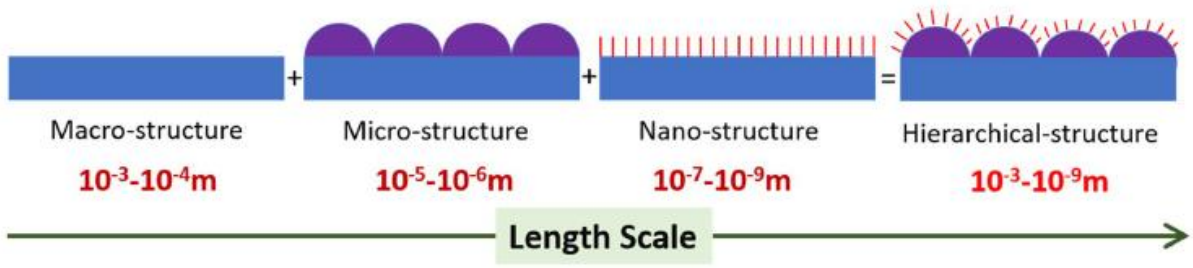

Figure 1: Schematic representation of hierarchical structures. Reprinted from Amini et al.[7]

2. Hierarchical surfaces with two scales of topography

2.1. Fabrication of hierarchical structures

The multiscale topography that was studied in this work was a combination of micro sized structures and nanoscale roughness obtained by Nano Imprint Lithography (NIL) and plasma etching of a polymer resist. The work was carried out on the CEA Leti's 200 and 300 mm microsystems platform.

The polymer resist that was used for this work was a commercial resist chosen for its part organic/part mineral composition, allowing roughness modulation by plasma etching, as well as being UV-curable as the imprinting technique used here is UV-NIL. More precisely, this polymer resist

contains around 4 % of Si/SiO_2 [8]. However, the exact chemical composition of this commercial product is not known.

2.1.1. Nanoimprint Lithography for lines and pillars

The first step of UV-NIL is coating the substrate, in this case a silicon wafer, with the UV-curable polymer resist. This corresponds to step 1 of Figure 2. Here, it is done by spin-coating onto a 200 mm silicon wafer.

The second step is pressing the mould which contains microstructures into the polymer resist and applying UV light to crosslink the polymer and immobilize the topography. The mould can then be removed (step 3) and reused on another substrate[9]. The moulds were designed before this thesis and independently of the subject.

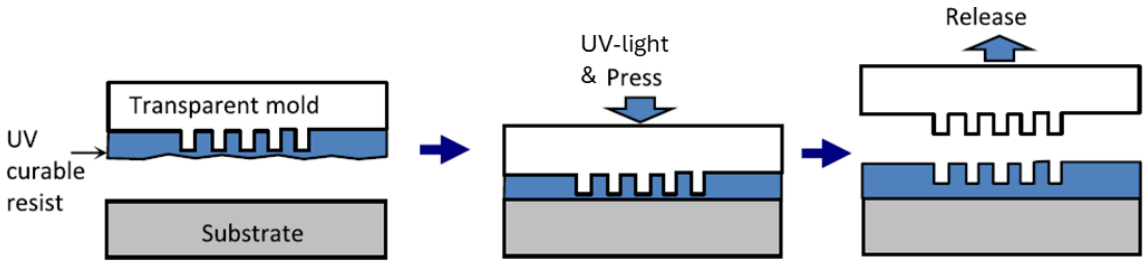

Figure 2: Scheme representing the different steps of Nano Imprint Lithography (NIL). Reprinted with permission from Mohamed[10] Copyright© 2024 Elsevier.

Two types of structures were created: lines and pillars which are all around 500 nm high. After the process, any areas without structures stayed covered with resist, as visible in step 3 of Figure 2. This ensures the same chemistry at the top and bottom of the structures.

The 200 mm silicon wafer is then covered with repetition of a global pattern which is 1 cm². In each 1 cm² zone, the sizes of the created structures vary every 10 µm, creating a pattern of various densities over the surface. The width of the lines changes between 270 nm and 1 062 nm, while the space between two lines varies between 651 nm and 5 233 nm, as it can be seen in Figure 3. For the pillars, their diameter is between 275 nm and 443 nm. The pitch, which is the distance between the centres of two adjacent pillars, is between 2 336 nm and 10 072 nm. These dimensions reaching µm scale justifies the appellation of microstructures[8]. These values are specifications given to create the structures and may not correspond perfectly to the real sizes. Some examples of lines and pillars of different sizes can be seen in the following figure.

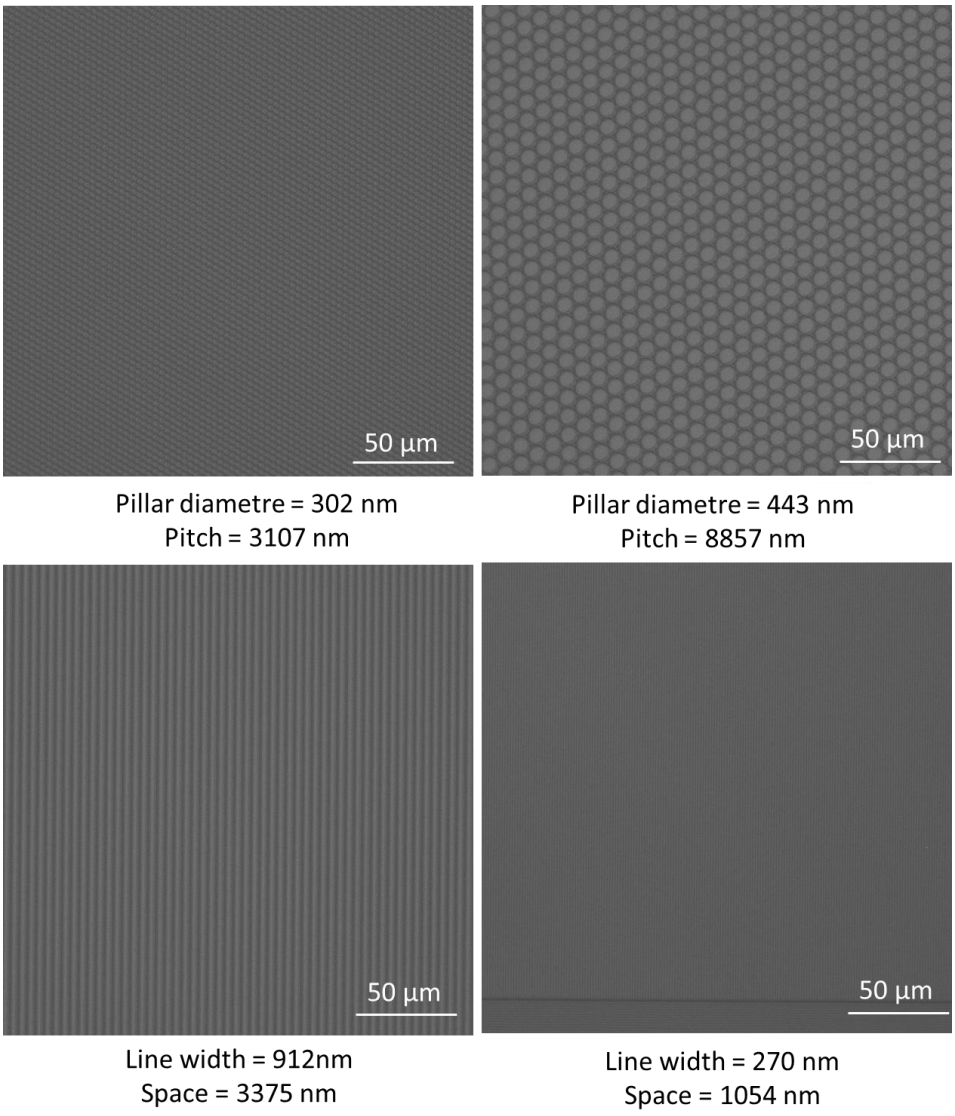

Figure 3: Microscopy images of some lines and pillars with varying sizes created by NIL.

2.1.2. Plasma etching to roughen the surface

In this study, two types of plasma were used to etch the microstructured polymer resist: a hydrogen bromide-based plasma (O_2/Ar/HBr) and a sulphur hexafluoride-based plasma ($N_2/O_2/SF_6$). The latter was studied with two different flowrates of SF_6: 2 and 6 sccm, as it has been previously shown that the flowrate of SF_6 is a very important parameter to control the etch rate of polymer photoresist[11]. Oxygen was added to the SF_6 plasma because it has been shown to reduce lateral etching of this otherwise chemical and isotropic plasma by passivating the sidewalls of the structures with a fluorinated silicon-oxide layer[12]. This is important so to not destroy the microstructures created by NIL. All plasmas were applied to the surface for 30 s with no bias. The process is linked to a CEA-LETI patent[8].

For the rest of this chapter, the plasmas will be designated by their active elements: HBr, and SF_6 (2 sccm) or SF_6 (6 sccm). Each plasma was applied to a substrate on which the polymer resist had been structured by NIL, as well as a substrate on which the resist was just spin coated and crosslinked. This allowed to have a set of surfaces with various roughness, and a set of substrates which had a combination of microstructures and nanoscale roughness. Scanning electron microscopy (SEM) was

used to image some microstructures with and without plasma etching (Figure 4). The lines and pillars appear with very neat and precise shapes in all conditions. The plasma etching gives a uniform roughness over the microstructures without modifying their shape or size. It can also be seen that the HBr plasma (Figure 4c, d) has little effect on the surface roughness whereas the SF_6 plasma leads to a higher surface modification. This is further enhanced as the flowrate of SF_6 is increased from 2 to 6 sccm (Figure 4g, h).

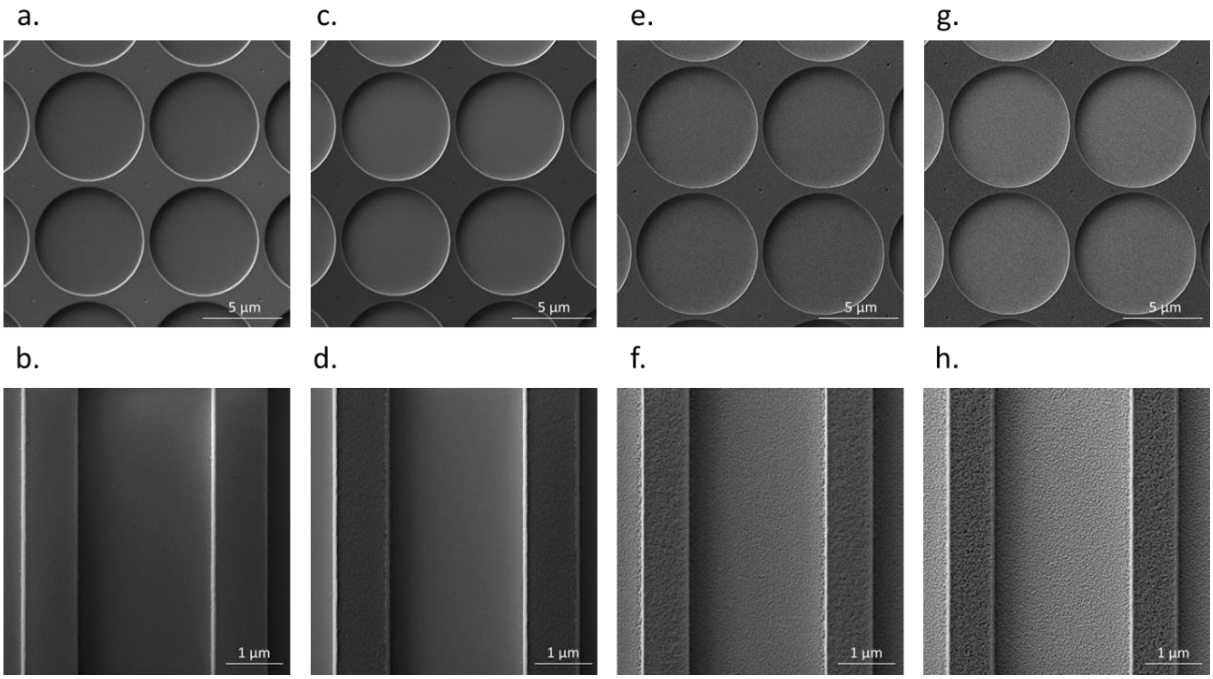

Figure 4: SEM images of polymer resist structured by NIL a., b. without additional plasma etching, c., d. with HBr plasma etching, e., f. with SF6 (2 sccm) plasma etching, g., h. with SF6 (6 sccm) plasma etching.

The plasma etching of the polymer resist which was initially spin-coated onto the silicon wafers, led to a decrease in thickness which was evaluated by spectroscopic ellipsometry. These measurements estimated the initial thickness of the polymer resist to be around 200 nm. The HBr plasma decreased the thickness to around 150 nm. Concerning the SF_6 plasma, when applying 2 sccm of SF_6, the total thickness was around 145 nm, including an estimated 45 nm of very rough and porous resist. When increasing the flow of SF_6 to 6 sccm, the thickness of the resist decreases to approximately 135 nm with roughly 50 nm of it being rough and porous. These first results show the efficiency of the plasma etching for obtaining surfaces with high roughness, especially when applying the SF_6 plasma.

In the following section, the effect of plasma etching and NIL will be studied on some of the surface properties of the material. More precisely, the roughness, chemistry and wettability will be considered as these characteristics have significant importance on bacterial adhesion.

2.2.Some surface properties of plasma etched polymer resist

2.2.1. Nanoscale roughness created by plasma etching

To further understand the effect of the plasma etching on the polymer resist, and evaluate the roughness that it led to, AFM images were taken (Figure 5).

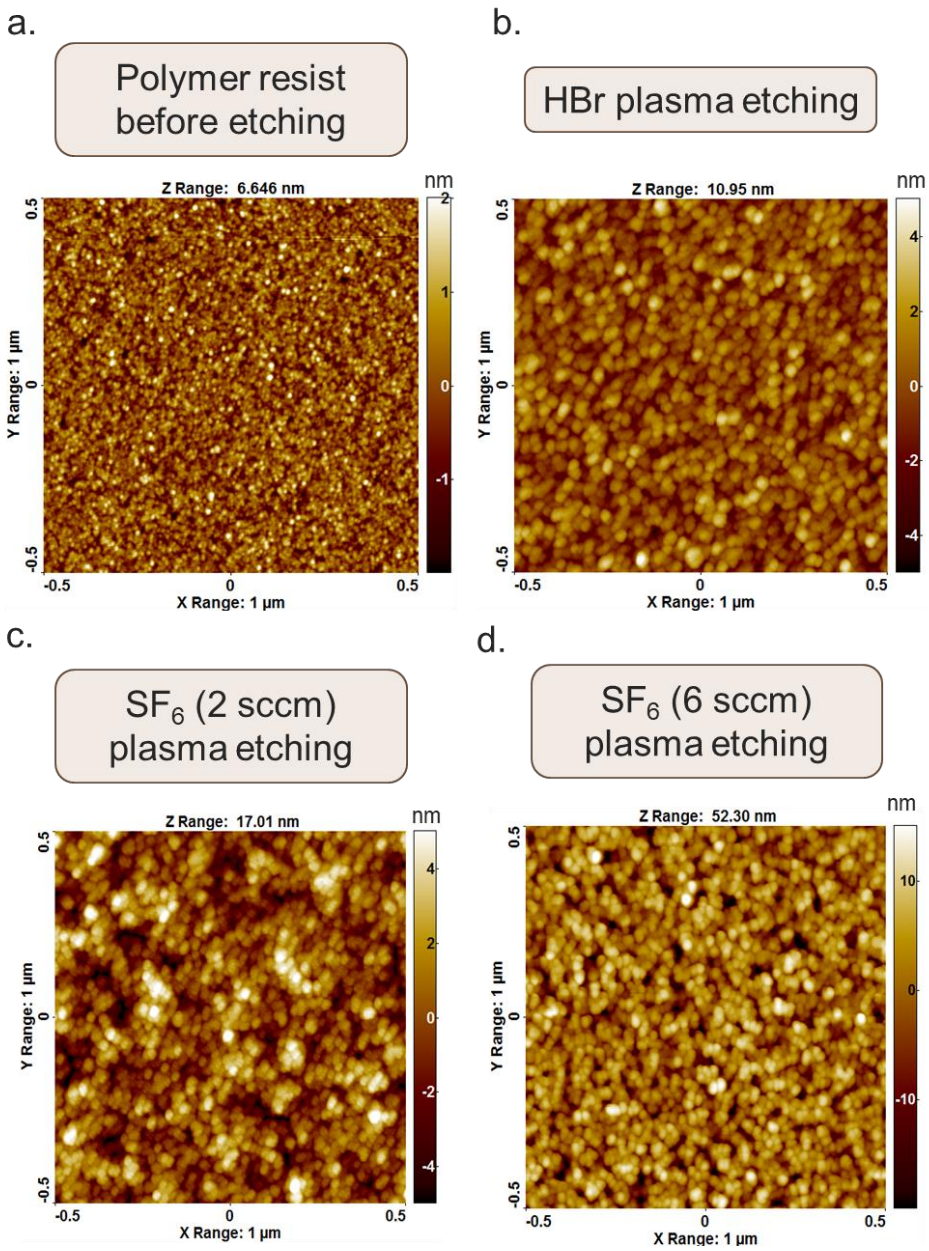

Figure 5: AFM images of polymer resist a. before plasma etching, after plasma etching with b. HBr, c. SF_6 (2 sccm), d. SF_6 (6 sccm).

These AFM images reveal a granular and porous topography induced by the plasma etching. However, the three different plasmas do not seem to affect the size and shape of these granular structures. It appears that only the depth (Z range) of the nanostructuration is modified. Indeed, when measuring the quadratic roughness Rq, variabilities can be highlighted. The polymer resist initially has an Rq roughness of 0.6 nm. When applying the HBr plasma, this roughness increases to 1.3 nm. With the SF_6 plasma, the roughness is further enhanced, and even more so with a higher quantity of SF_6 injected. Indeed, with 2 sccm of SF_6, the Rq roughness is increased to 2 nm, and with 6 sccm of SF_6, the Rq roughness reaches 6.1 nm. These values are summarized in Table 1.

The lower roughness obtained with the HBr plasma is coherent with the literature that mentions that Br atoms have much lower etch rates than F atoms[12,13]. However, in all conditions used in this study, the etching rate and the Rq roughness remain quite low[14].

Table 1: Thickness, Rq roughness and Z range of polymer resist before and after different plasma etching.

Substrate	Thickness (nm)	Rq (nm)	Z range (nm)
Polymer resist	202	0.6	6.6
Polymer resist + HBr	155	1.3	11.0
Polymer resist + SF_6 (2 sccm)	147	2	17.0
Polymer resist + SF_6 (6 sccm)	134	6.1	52.3

The surfaces modified by both NIL and plasma etching were also imaged by AFM to see how the plasma etching performed on structured surfaces (Figure 6).

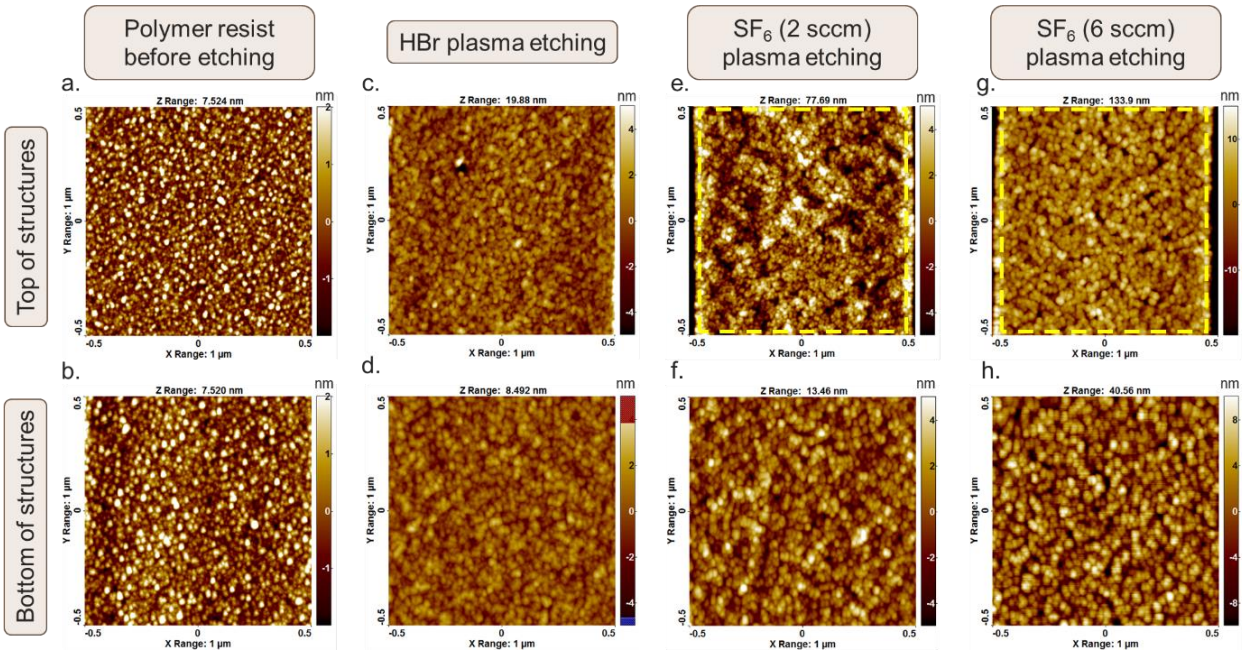

Figure 6: AFM images of polymer resist microstructured by NIL before plasma etching a. at the top, b. at the bottom of the structures, after plasma etching with HBr c. at the top, d. at the bottom of the structures, after plasma etching with SF_6 (2 sccm) e. at the top, f. at the bottom of the structures, after plasma etching with SF_6 (6 sccm) g. at the top, h. at the bottom of the structures. The colour bar scale is in nm. The yellow dotted lines in e. and f. show the areas used for calculating the Rq roughness.

These images show the efficiency of the various plasma etching on both top and bottom of the NIL structured substrates. Furthermore, the aspect of the etched surfaces is very similar than after plasma etching on planar polymer resist. Indeed, the granular structure can still be seen at the top and the bottom of the microstructures. However, when considering the Rq roughness values (Table 2), some differences can be seen between the top and bottom of the structures.

Table 2: Rq roughness (nm) at the top and bottom of NIL structures on polymer resist, with and without plasma etching. The first column is the Rq roughness (nm) of the same polymer resist, with and without plasma etching, but with no structuration by NIL.

Substrate	Rq (nm) without NIL	Rq (nm) top of structures	Rq (nm) bottom of structures
Polymer resist	0.6	0.9	0.9
Polymer resist + HBr	1.3	1.3	1.1
Polymer resist + SF_6 (2 sccm)	2.0	2.4	1.6
Polymer resist + SF_6 (6 sccm)	6.1	5.4	3.9

For the polymer resist without plasma etching, the Rq values stay under 1 nm before and after NIL, at both the top and bottom of the structures. However, there is a very slight increase from 0.6 nm to 0.9 nm. This could be a result of imprinting roughness from the mould used in the NIL process.

With the HBr plasma, the roughness is very similar at the top and bottom of the structures: 1.3 nm and 1.1 nm respectively. The similarities in roughness are due to the low anisotropic chemical etching of Br atoms[12]. Furthermore, the HBr plasma etched planar polymer resist also showed a surface roughness of 1.3 nm. This shows that the plasma appears to act equally on planar and structured polymer resist.

With the SF_6 plasma, the differences between top and bottom of the structures are bigger. Indeed, with 2 sccm of SF_6, the Rq roughness at the top of the structures is 2.4 nm, whereas it is 1.6 nm at the bottom. The same can be said for the SF_6 plasma with 6 sccm of SF_6. Indeed, here the Rq roughness goes from 5.4 nm at the top of structures to 3.9 nm at the bottom. This is due to the SF_6 plasma being isotropic and chemically etching the polymer resist laterally as well as vertically[12]. This can be seen in Figure 7 where the width of the line is smaller after SF_6 plasma etching.

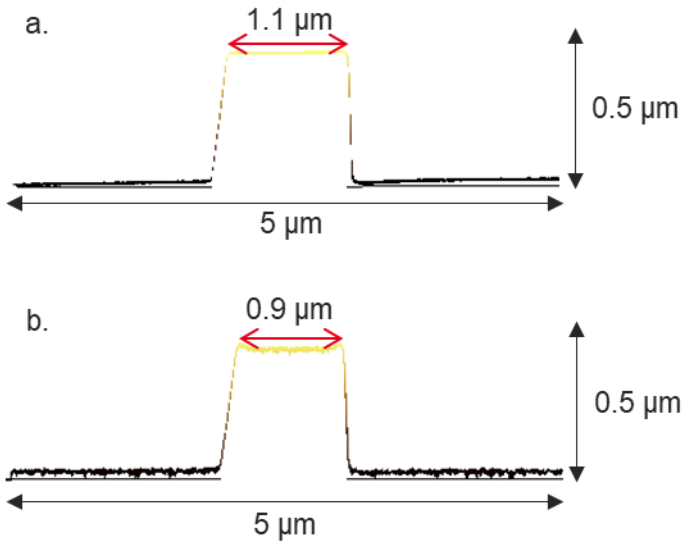

Figure 7: 3D profile of polymer resist microstructured by NIL a. before plasma etching, b. after SF_6 (6 sccm) plasma etching. Both images were taken on structures with the same design width (1.1 µm).

Furthermore, the bigger roughness difference between the top and bottom of these structures with the higher flowrate of SF_6, can be explained by the increase in SF_6/O_2 ratio. Indeed, it has been documented in the literature that a higher O_2 content with a constant flowrate of SF_6 can lead to enhanced vertical etching of Si due to passivation of the sidewalls and focusing of the neutrals[15]. In the conditions studied here, while increasing the SF_6 flowrate from 2 to 6 sccm gives a higher roughness on planar substrates, the decrease in SF_6/O_2 ratio may have impacted the vertical etching, as the bottom of the structures show lower roughness than the top.

These results show the possibility of tuning the roughness of a polymer resist by using different gases for plasma etching. Furthermore, by combining plasma etching with NIL it is possible to obtain surfaces on which microstructures and a nanoscale roughness can be found.

2.2.2. Chemical composition of the photoresist surface before and after plasma etching

As enhancing the surface roughness of the polymer resist relies on a plasma composed of different molecular species, the chemical composition of the photoresist surface was analysed before and after the plasma etching. More precisely, XPS was carried out to analyse the surface chemistry, which is more likely to have an effect on wettability and from an applicative point of view on the adhesion of bacteria and the formation of biofilm.

Table 3 shows the atomic percentages found at the surface of the polymer resist before and after plasma etching. According to this analysis, the initial polymer resist contains C, O and Si at 60 %, 32 % and 8 % respectively. We can thus consider this resist is close to an organosilicon polymer. When applying a plasma to etch the surface, a slight variation of the chemical composition appears. Indeed, with the HBr plasma, Br can be found at 0.1 %. With the SF_6 plasma, F can also be found in traces. This variation is due to contamination by reactive plasma species. In all cases, slight N contamination can be noted.

Table 3: Atomic percentage of C 1s, O 1s, Si 2p, N 1s, Br 3d and F 1s obtained by XPS analysis of polymer resist before and after plasma etching.

Substrate	Atomic percentage					
	C 1s	O 1s	Si 2p	N 1s	Br 3d	F 1s
Polymer resist	60.1	32.0	7.9			
HBr treated polymer resist	24.4	56.6	18.3	0.7	0.1	
SF_6 (2 sccm) treated polymer resist	5.6	67.4	25.2	0.2		1.6
SF_6 (6 sccm) treated polymer resist	7.4	66.9	24.2	0.4		1.2

Furthermore, it can also be noted that the plasma etching leads to a removal of the C at the surface of the resist. Indeed, from 60 % of C in the initial polymer resist, after HBr etching, its proportion decreases to 24 %. With SF_6 etching, its percentage decreases further to 5.6 and 7.4 respectively for 2 sccm and 6 sccm of SF_6. In parallel of the C removal, an increase of O can be noticed. Indeed, oxygen content increases from 32 % to around 57 % after HBr plasma etching and up to 67 % after SF_6 plasma etching.

This selective removal of carbon in SiOCH polymers by SF_6 plasma has previously been seen in the literature. Indeed, Eon *et al.* suggested that ion bombardment and chemical reactions lead to the

replacement of C by O and/or F in methylsilsesquioxane SiOCH[16]. Here, the low percentage of F that can be seen in the plasma etched substrates implies that most vacant bonds are filled with O atoms.

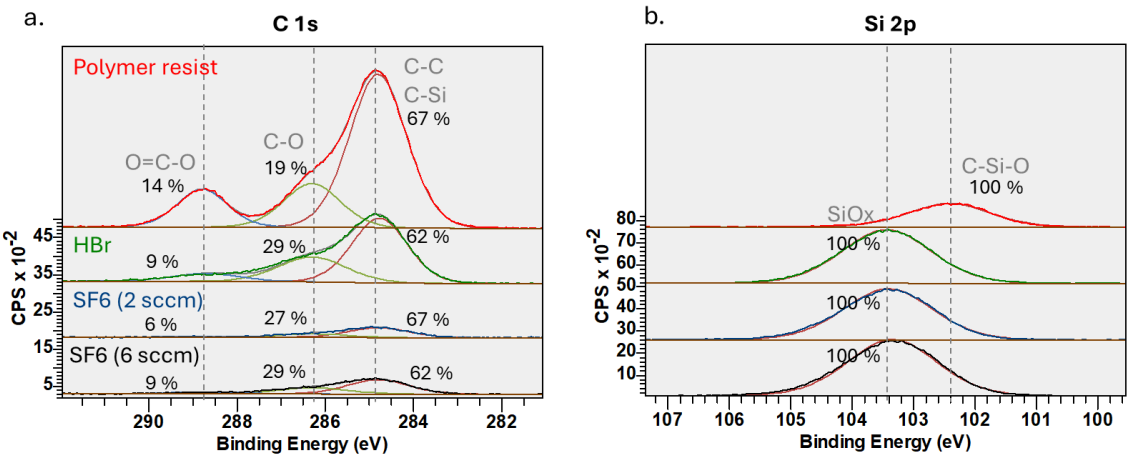

Figure 8: High resolution X-ray Photoelectron Spectra of a. C 1s, b. Si 2p of polymer resist before and after plasma etching.

The high resolution XPS spectra in Figure 8 give an idea of the chemical bonds found at the surface of the polymer resist before and after plasma etching. For C 1s, it can be seen that, even though the atomic percentage of C decreases, it is still involved in the same bonds. Indeed, before and after modification by plasma treatment, between 61 % and 66 % of C is found in C-C, C-Si and C-H bonds which have a binding energy around 284.8 eV. Furthermore, C 1s is found in C-O and O=C-O bonds with binding energies of 286.3 eV and 288.8 eV respectively. Before plasma etching, around 14 % of C 1s is found in O=C-O bonds and 19 % in C-O bonds. After plasma etching, the ratio of O=C-O bonds decreases to between 9 % and 6 %. On the other hand, the proportion of C-O bonds rises to between 27 % and 29 %. The high resolution XPS spectra of Si 2p also underlines the removal of C after plasma etching. Indeed, in the polymer resist before etching, Si 2p can only be found in the form of O-Si-C with a binding energy of 102.4 eV[17]. After plasma etching it becomes SiO_x and shows a binding energy of 103.4 eV. Similar results have been seen when applying an O_2 plasma to PDMS[18].

These XPS results confirm the plasma etching mechanism and the removal of the organic compounds found in the polymer resist. Therefore, from a polymer resist containing a small proportion of Si/SiO_2, after plasma etching, the silicon oxide moieties become predominant at the surface of the structures.

2.2.3. Wettability of the structured surfaces

As surface wettability is an important property for antibiofouling surfaces, WCAs were measured on the polymer resist before and after being modified by NIL and plasma etching.

2.2.3.1. Wettability of plasma-etched surfaces

First, the WCA was measured after stabilisation on the plasma etched surfaces which had not been structured by NIL. As shown in Figure 9, before plasma treatment, the polymer resist had a WCA

around 85°. This value decreases to under 33° after an HBr plasma treatment. With the SF_6 plasma, the WCA decreases to 44° or 34° with 2 sccm or 6 sccm of SF_6 respectively.

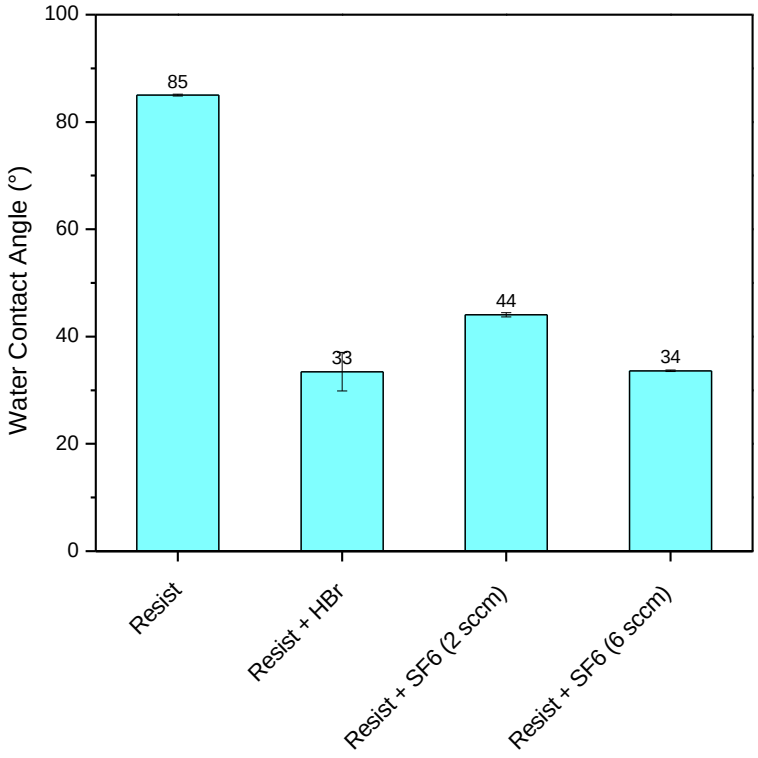

Figure 9: WCAs of plasma etched polymer resist.

Similar results have been seen for SiOCH films treated with an O_2 plasma. Vinogravoda *et al*. showed a WCA decrease from 88° to 34° after 20 s O_2 plasma treatment of a CVD SiOCH porous film. They attributed this change to a combination of topography and replacement of methyl bonds by hydrophilic silanols and oxygen bridges[19]. This explanation is coherent with the observations carried out from the XPS spectra analysis or the plasma etched polymer resist used in this thesis.

As for the difference in wettability induced by the two different types of plasma, the slightly higher WCA observed for the surfaces etched with SF_6 could be due to the presence of fluorine residues on the surface as shown by XPS. Indeed, fluorine is known for its hydrophobicity[20] but as it is present in very low proportion and is combined with surface roughness, it must only have a marginal influence on the overall apparent hydrophilicity.

2.2.3.2. Effect of NIL on the wettability

In the literature, it has been shown that adding topography to a surface can modify its wettability, depending on the shape and size of the created structures by reaching the Wenzel or the Cassie-Baxter effect[5,21]. Therefore, as well as studying the effect of nanoscale roughness on the wettability of the polymer resist, the latter was also evaluated for surfaces modified by NIL.

Figure 10 shows that the WCA on the polymer resist surfaces modified by NIL and/or plasma etching. It can be seen that for the polymer resist without plasma etching, adding microstructures

leads to a hydrophobic surface. For the photoresist which has both NIL and high roughness/porosity bought by SF_6 etching (6 sccm), superhydrophilicity can be achieved. In this case, we can hypothesize that the Wenzel effect is reached, allowing an enhancement of the hydrophilic character of the same substrate without NIL, and that the water droplet can infiltrate the structures.

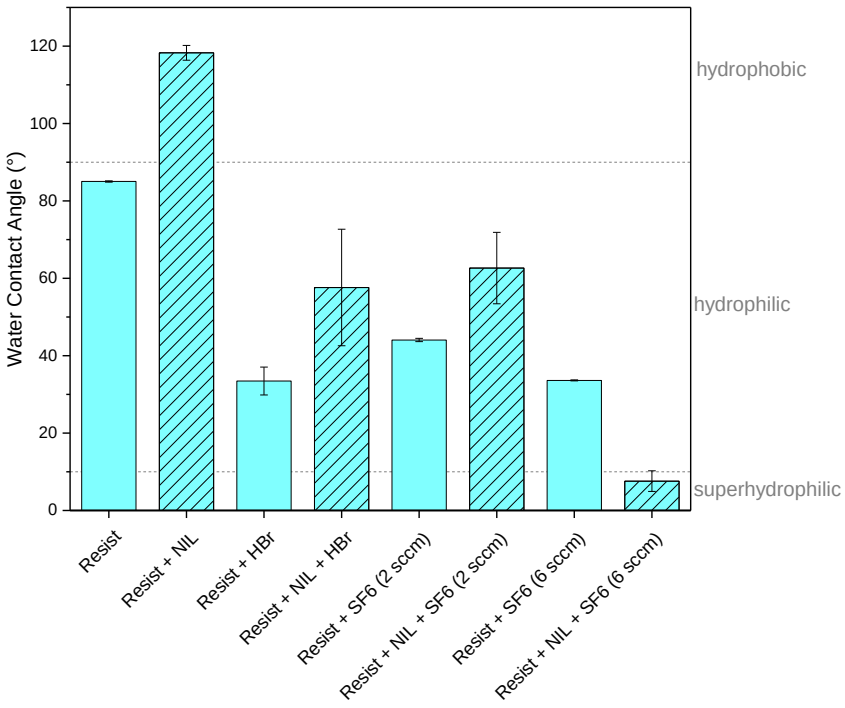

Figure 10: WCAs of polymer resist modified by NIL and plasma etching.

However the values obtained on the microstructured substrates should only be considered qualitatively as the linear patterns lead to the directional spreading of the droplets[22] when deposited on the surfaces (Figure 11).

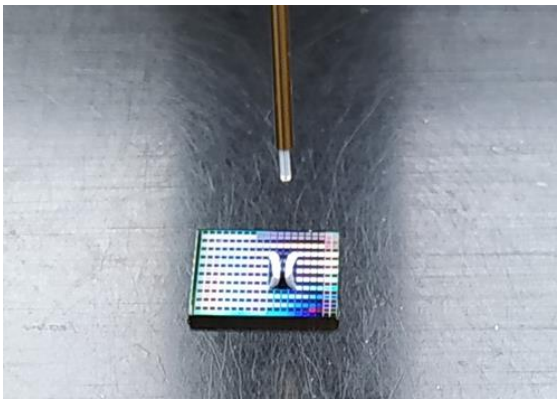

Figure 11: Photo of directional spreading of a water droplet on polymer resist structured by NIL.

This study confirms the possibility of tuning the wettability of surfaces by modifying the topography. Overall, it seems that the roughness bought by plasma etching leads to higher hydrophilicity. This is a consequence of the replacement of carbon groups in the polymer resist by

oxygen bridges after plasma etching[19] and the creation of a granular and porous structure that can allow the water droplets to infiltrate, leading to a low apparent WCA. On the other hand, the topography given by microstructures seems to enhance hydrophobicity. This may be due to air bubbles being trapped in the microstructures, impeding infiltration and spreading of the water droplet.

Overall this study highlights that the relationship between surface roughness and hydrophobicity or hydrophilicity is complex and depends on many factors. There is no single roughness threshold beyond which a surface automatically becomes hydrophobic or hydrophilic, but rather a complex interaction between surface structure, chemical composition and the properties of the liquid concerned.

3. Combining hydrophobic and hydrophilic polymers with structured surfaces

As mentioned in the introduction, it has also been shown in the literature that combining hydrophobic or hydrophilic chemistry with various topography can lead to superhydrophobic or superhydrophilic surfaces[6].

Thus, the iCVD and plasma polymers studied in the previous chapters were deposited on these surfaces to see how this modified the surface properties, and more importantly the wettability.

3.1. Depositing V3D3-based hydrophobic coatings onto substrates with controlled topography

The first set of coatings that were deposited onto these substrates with particular topography were the V3D3-based hydrophobic thin films. Both poly(V3D3) deposited by iCVD and pp(V3D3) deposited by DBD-CAP were studied. It was shown in chapter 3 that these polymers had an Rq roughness under 0.4 nm on planar silicon wafers. Therefore, they should not induce further roughness on these plasma etched surfaces.

3.1.1. Modification of the surface roughness

3.1.1.1. Influence of the poly(V3D3) thickness on the surface roughness

To begin, poly(V3D3) of different thicknesses (6, 13 and 38 nm) were deposited by iCVD onto substrates of polymer resist etched with SF_6 (6 sccm), to see whether there was a limit before erasing the topography. The thickness measurements were taken on planar silicon, which was coated alongside the structured polymer resist during the same process so it only gives an estimation.

As it can be seen in Figure 12, the aspect of the surface changes with the thickness of the poly(V3D3) coating. Indeed, as the latter increases, the grain size seems to increase, leading to a surface which appears to be overall smoother.

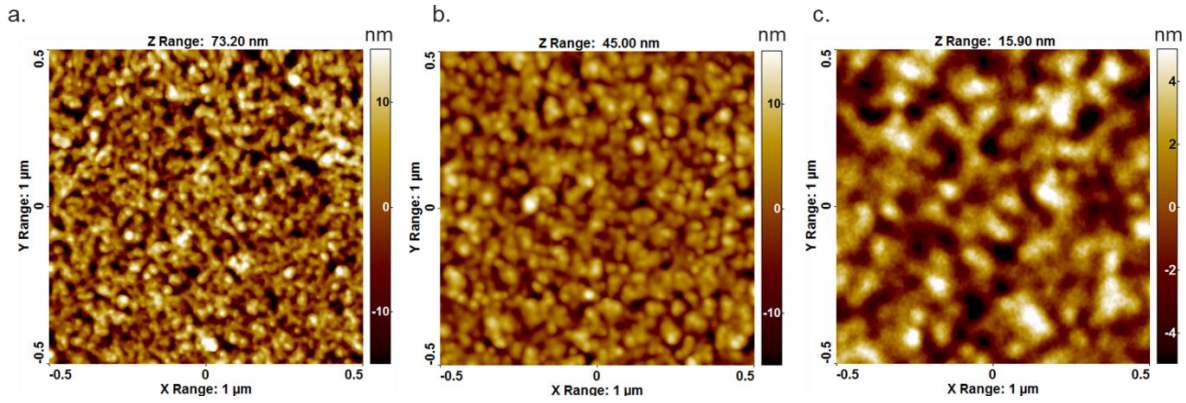

Figure 12: Atomic Force Microscopy (AFM) images of poly(V3D3) deposited by iCVD onto SF_6 (6 sccm) plasma etched polymer resist. The poly(V3D3)'s thickness is around a. 6 nm, b. 13 nm, c. 38 nm.

When comparing the Rq roughness of these plasma-etched surfaces with and without poly(V3D3), it can be seen that the Rq roughness goes from 6.1 nm before coating, to 7.3 nm with around 6 nm of poly(V3D3). The z range is also increased from 52 nm to 73 nm. We can hypothesize that here, the polymer is conformably deposited onto the structured surface, enhancing the roughness of the initial substrate. With a polymer thickness of 13 nm, the Rq roughness decreases to 4.9 nm, and with 38 nm of poly(V3D3), the surface roughness is further decreased, reaching 2.3 nm. The z range is also decreased from 52 nm to 45 and 15.9 nm, respectively.

Table 4: Rq roughness of SF_6 (6 sccm) plasma etched polymer resist onto which poly(V3D3) has been deposited by iCVD.

Presence of polymer	Time of deposition (s)	Thickness of poly(V3D3) on control Si (nm)	Rq (nm)	z range (nm)
Without poly(V3D3)	--	--	6.1	52.3
With poly(V3D3)	300	6	7.3	73.2
	700	13	4.9	45.0
	2000	38	2.3	15.9

Above a certain thickness, it is probable that the iCVD coatings planarize the plasma etched substrates. Indeed, the plasma etching leads to a nanoscale granular structure with pores. However, it has previously been shown that iCVD can be used as a mechanism to fill nanometric pores with polymer[22,23]. Therefore, this study shows that when combining chemistry and topography by coating substrates with enhanced roughness, it is important to control the thickness of the deposition in order to avoid cancelling out the effect of the nanostructuration.

3.1.1.2. Effect of the deposition technique

In the previous section, it was shown that, when combining poly(V3D3) coatings and plasma-etched surfaces, if the polymer thickness is too high, the roughness can be erased. Therefore, in this section, when comparing iCVD-deposited poly(V3D3) with DBD-CAP-deposited pp(V3D3), small thicknesses will be evaluated. Indeed, here the poly(V3D3) had a thickness of around 6 nm and the pp(V3D3) had a thickness of around 8 nm.

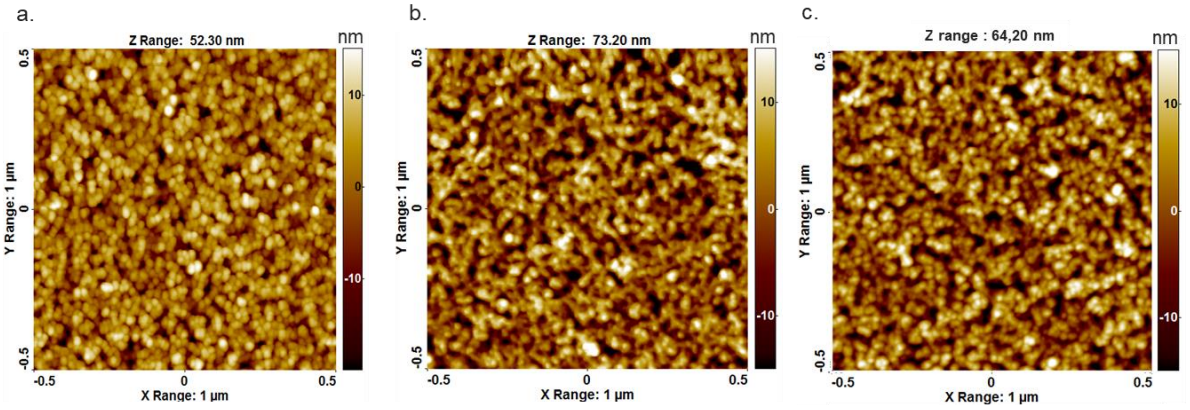

Figure 13: AFM images of SF_6 (6 sccm) plasma etched polymer resist a. without an additional polymer coating, b. with 6 nm of poly(V3D3) deposited by iCVD, c. with 8 nm of pp(V3D3) deposited by DBD-CAP.

As it can be seen in Figure 13, the deposition of V3D3-based coatings of similar thicknesses onto plasma-etched substrates, leads to surfaces with very similar aspects. Furthermore, the Rq roughness seems to be similar for comparable thicknesses of V3D3-based coatings, no matter the technique of deposition. Indeed, for an iCVD-deposited poly(V3D3) with a thickness of 6 nm, the Rq roughness is around 7.3 nm. When the thickness of this coating is increased to 13 nm, the roughness decreases to 4.9 nm. For the DBD-CAP pp(V3D3) of 8 nm, the Rq roughness is also found to be 4.9 nm.

Table 5: Rq roughness of SF_6 (6 sccm) plasma etched polymer resist onto which poly(V3D3) or pp(V3D3) has been deposited by iCVD or DBD-CAP respectively.

Presence of polymer	Technique of polymer deposition	Thickness of V3D3 polymer on control Si (nm)	Rq (nm)	Z range (nm)
Without polymer	--	--	6.1	52.3
With polymer	iCVD	6	7.3	73.2
	DBD-CAP	8	4.9	64.2
	iCVD	13	4.9	45.0

These results show that the poly(V3D3) thin film deposited by iCVD allowed better maintain of the surface roughness obtained by plasma etching. However, the previous section highlighted the fact that the roughness decreased with the thickness of the film. Adjusting the Plasmaspot®'s parameters to deposit a plasma polymer with a thickness of 6 nm would allow a more precise comparison.

3.1.1.3. Combined effect of microstructures, nanoscale roughness and hydrophobic polymers

Hydrophobic poly(V3D3) and pp(V3D3) coatings were also deposited onto substrates which were microstructured by NIL before plasma etching. As it was done in section 2.2.1 on polymer resist plasma-etched substrates, the surface roughness was compared at the top and bottom of the structures. The images that were obtained (Figure 14) show similar properties to the plasma-etched polymer resist coated with poly(V3D3) or pp(V3D3) but without NIL, including the evolution of the grain size as the iCVD poly(V3D3)'s thickness increases (Figure 14g, h).

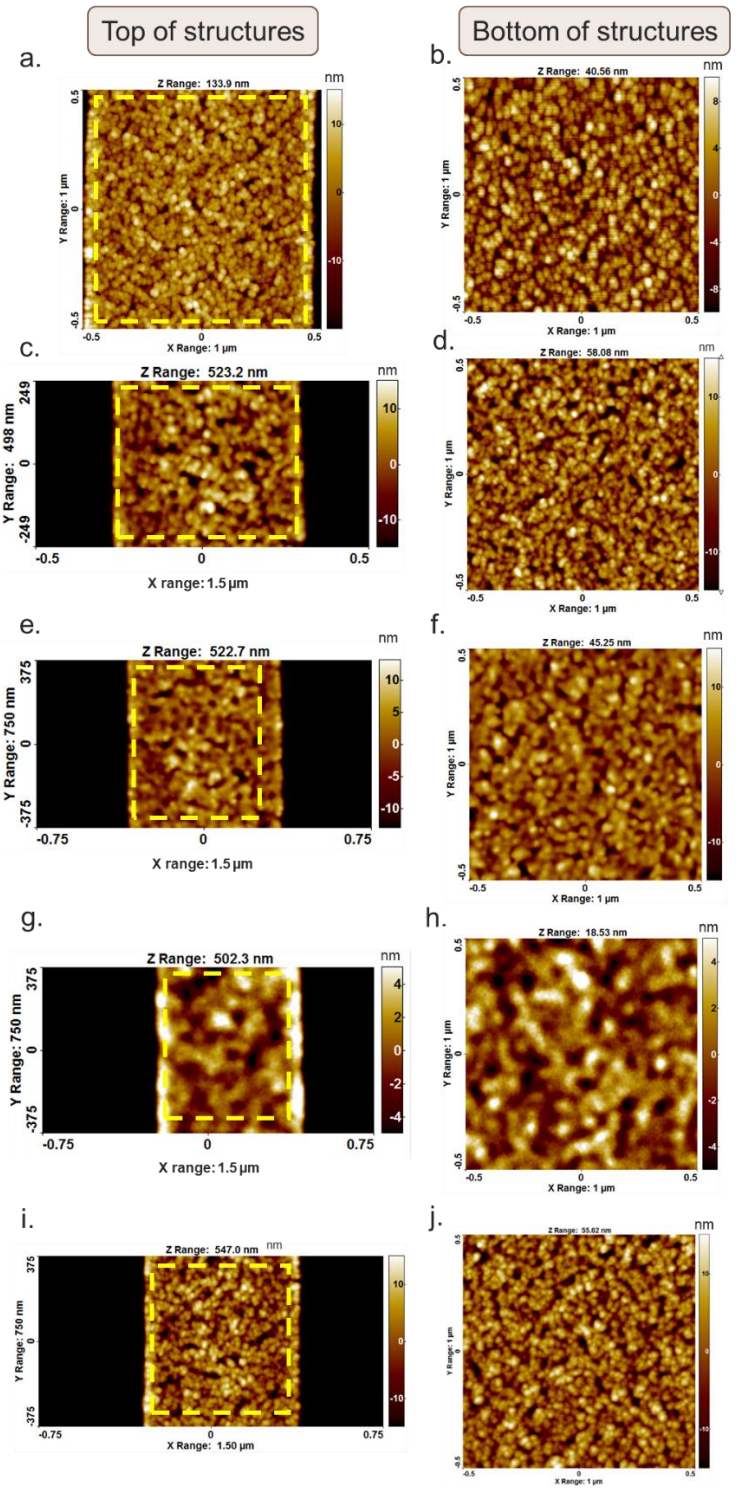

Figure 14: AFM images of polymer resist microstructured by NIL and treated by SF6 (6 sccm) plasma etching a. at the top, b. at the bottom of the structures, after coating with 6 nm of poly(V3D3) c. at the top, d. at the bottom of the structures, after coating with 13 nm of poly(V3D3) e. at the top, f. at the bottom of the structures, after coating with 38 nm of poly(V3D3) g. at the top, h. at the bottom of the structures, after coating with 8 nm of pp(V3D3) i. at the top, j. at the bottom of the structures. The colour bar scale is in nm. The yellow dotted lines in a, b, c, d and f show the areas used for calculating the Rq roughness.

The results in Table 6 show that no significant differences in Rq roughness appear between the top and bottom of the microstructures when these are coated with poly(V3D3) or pp(V3D3).

Moreover, it appears that coating the structured surfaces with either poly(V3D3) or pp(V3D3) standardises the roughness at the top and bottom of the microstructures. For each polymer thickness, the values of the Rq roughness at the top and bottom of the microstructures are very similar to the roughness on the planar surface.

Table 6: Rq roughness (nm) at the top and bottom of NIL structures on polymer resist, with and without an additional polymer coating of poly(V3D3) or pp(V3D3).

Presence of polymer	Technique of polymer deposition	Thickness of V3D3 polymer on control Si (nm)	Rq (nm) without NIL	Rq (nm) top of structures	Rq (nm) bottom of structures
Without polymer	--	--	6.1	5.4	3.9
With polymer	iCVD	6	7.3	6.1	6
	iCVD	13	4.9	4.2	4.8
	iCVD	38	2.3	2.0	2.2
	DBD-CAP	8	4.9	5.8	5.9

These AFM results show the conservation of the surface topography after coating with poly(V3D3) or pp(V3D3). However, to preserve the surface roughness, the thin film's thickness must remain low.

3.1.2. Evolution of the chemical composition of the substrate surface when adding poly(V3D3) or pp(V3D3) thin films

XPS analysis was used to study the surface chemistry of SF_6 (6 sccm) plasma etched substrates coated with iCVD-deposited poly(V3D3) or DBD-CAP-deposited pp(V3D3). The deconvolutions of high-resolution XPS spectra of C 1s and Si 2p are shown in Figure 15.

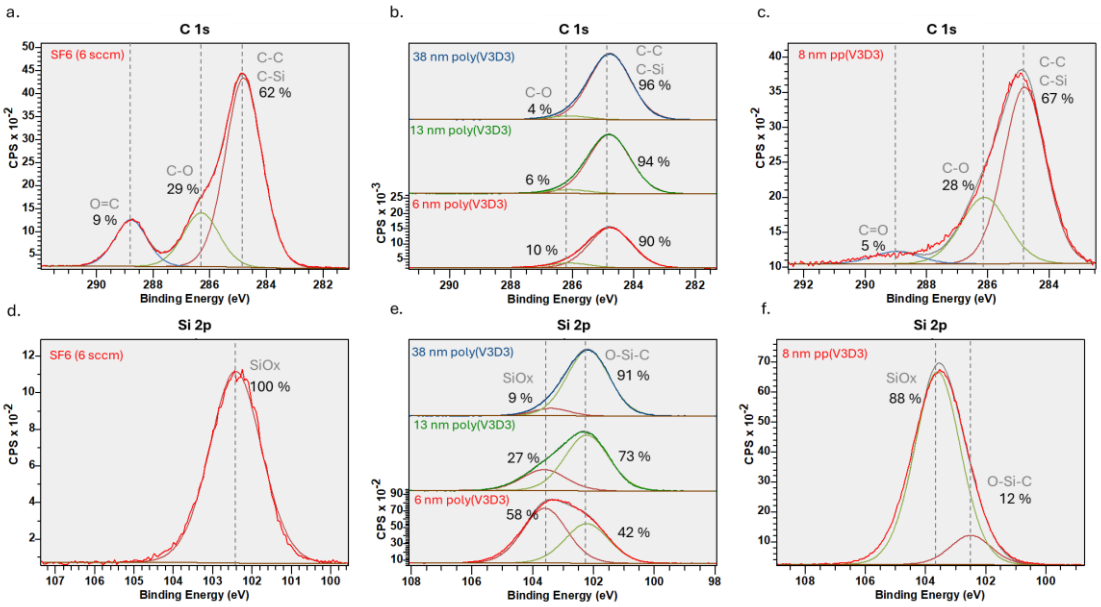

Figure 15: High resolution XPS spectra of C 1s (a., b., c.) and Si 2p (d., e., f.) of polymer resist treated by SF_6 (6 sccm) plasma a., d. Without additional coating, b., e. With poly(V3D3) deposited by iCVD, c., f. With pp(V3D3) deposited by DBD-CAP.

Concerning the C 1s high resolution XPS spectra, the plasma-etched polymer resist before coating shows the presence of C-C/C-Si bonds which have a binding energy of 284.8 eV, C-O bonds (286.1 eV) and C=O bonds (289 eV). When the plasma etched substrate is coated with poly(V3D3) (Figure 15b), it seems that no C=O can be detected. It is found in very small quantities (0.5 %) for the substrate coated with around 6 nm of poly(V3D3). However, as XPS analysis in these conditions allows probing a depth around 6.5 nm, the polymer resist below the poly(V3D3) is detectable. Therefore, the bonds revealed in this case come from a combination of the polymer resist and the poly(V3D3). With the pp(V3D3) deposited by DBD-CAP, the same bonds composing C 1s as on the plasma-etched substrate are visible. However, C-C, C-Si, C-O and O=C-O bonds are also visible in pp(V3D3) as it was seen in chapter 3. It is therefore difficult to determine whether the polymer resist is being probed or not.

For high-resolution XPS spectra of Si 2p, only SiO_X bonds can be seen for the polymer resist etched by SF_6 plasma. With a poly(V3D3) deposited by iCVD coating, O-Si-C bonds appear with a binding energy of 102.2 eV, conform to poly(V3D3) XPS spectra. Their proportion increases from 42 to 92 % with the thickness of the deposited thin film as the substrate becomes undetectable. For the DBD-CAP-deposited pp(V3D3), the high proportion of SiO_X bonds which can be seen shows a strong detection of the substrate in these conditions.

3.1.3. Adding topography to enhance hydrophobicity

3.1.3.1. Effect of plasma etching on the surface hydrophobicity

To find out whether the combination of topography and a hydrophobic polymer could improve water repellency, WCAs were measured on the different samples. Figure 16 shows the WCA measurement of poly(V3D3) and pp(V3D3) on HBr treated polymer resist. Figure 17 corresponds to the WCA of poly(V3D3) and pp(V3D3) on SF_6 (6 sccm) plasma etched polymer resist. In both graphs, the WCA obtained for poly(V3D3) and pp(V3D3) on planar silicon are also represented for comparison.

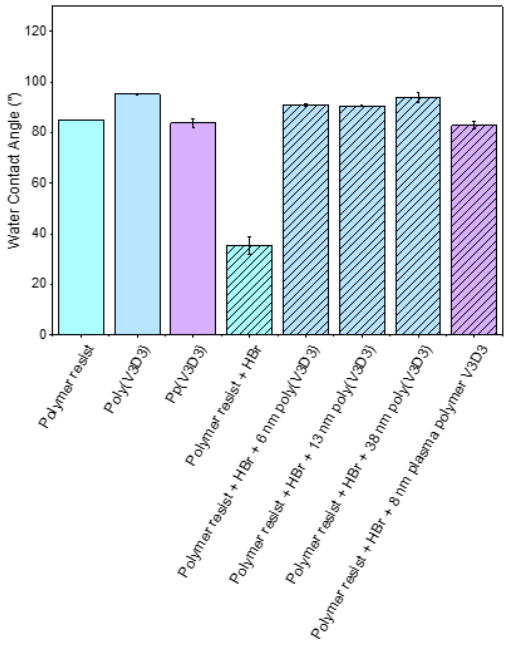

Figure 16: WCA of polymer resist, with and without HBr plasma etching and with or without a coating of 6, 13 and 38 nm of poly(V3D3) deposited by iCVD or 8 nm of pp(V3D3) deposited by DBD-CAP.

It can be seen in Figure 16 that although HBr etching reduces the WCA of the polymer resist before additional thin film deposition, the wettability of the surfaces after the poly(V3D3) and pp(V3D3) coating are all very similar, whether it is on planar Si or HBr etched polymer resist. We can suggest that HBr plasma etching does not modify the roughness enough for poly(V3D3) or pp(V3D3) to have a significant influence on the wettability. Indeed, the roughness of the HBr etched polymer resist is just over 1 nm. Therefore, if the thin film of polymer smoothens the surface even very slightly, the roughness will be close to that of the polymer on planar silicon.

With SF_6 plasma etching on the other hand (Figure 17), with 6 sccm of SF_6, which led to the highest roughness, some changes can be observed when adding the hydrophobic polymer. Indeed, whereas the plasma etching on the polymer resist decreases the WCA from around 85° to 34°, hydrophobic poly(V3D3) becomes more hydrophobic with the additional roughness. Indeed, poly(V3D3) deposited by iCVD onto a planar silicon substrate has a WCA around 95°. When it is deposited with a thickness of around 6 nm onto the plasma-etched polymer resist, the WCA nearly reaches 120°, thus becoming more hydrophobic, following the Wenzel effect. However, increasing the thickness of the polymer to 13 nm and 38 nm, leads to a drop in hydrophobicity with WCAs of 98° and 89°, respectively. We can assume that, as the roughness decreases with a higher thickness of poly(V3D3) (Table 4) the wettability decreases to finally reach the one found on the planar substrate.

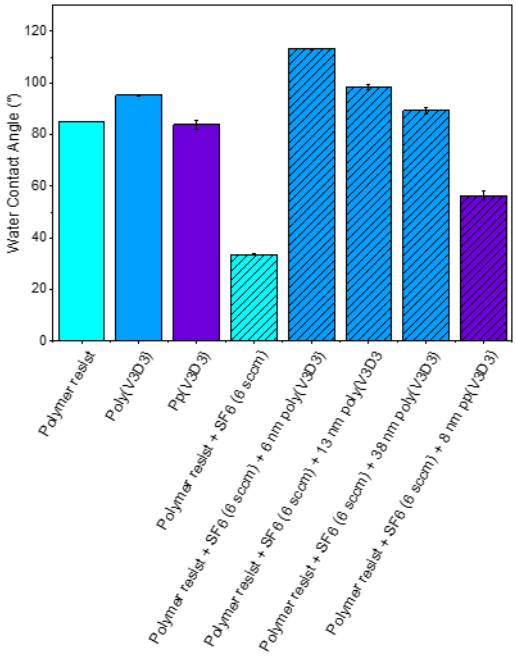

Figure 17: WCA of polymer resist, with and without SF_6 (6 sccm) plasma etching and with or without a coating of 6, 13 and 38 nm of poly(V3D3) deposited by iCVD or 8 nm of pp(V3D3) deposited by DBD-CAP.

These results show that, when depositing hydrophobic polymers (WCA > 90°), higher surface roughness on the initial substrate can lead to higher hydrophobicity. This follows the predictions of the Wenzel theory[22] that stipulates that a hydrophobic coating with high roughness becomes superhydrophobic. However, if the additional coating is too thick and thus covers the initial roughness (Rq decreases from 7 to 2 nm as the poly(V3D3) thickness increases), it seems that the enhancement of the hydrophobic effect can be cancelled out.

For the pp(V3D3) coated SF_6 (6 sccm) plasma etched polymer resist, the WCA (56°) is between the WCA measured for pp(V3D3) and the plasma etched polymer resist: 84° and 34° respectively. This could result from the coating not fully covering the rough substrate and the latter consequently influencing the wettability.

The WCA measured on substrates treated with SF_6 (2 sccm) plasma and coated with poly(V3D3) or pp(V3D3) can be found in the appendix. In this case, it was not possible to reach WCA as high as it was with the SF_6 (6 sccm) plasma. We assume this is due to the lower surface roughness achieved with the plasma etching.

3.1.3.2. Effect of microstructures on the hydrophobicity of the surface

Poly(V3D3) and pp(V3D3) were also deposited on NIL modified polymer resist. As mentioned previously, the WCA on these microstructured substrates should only be taken as an idea of the wettability due to the directional droplet spreading. It can be seen (Figure 18) that the hydrophobicity is increased with the 6 nm coating of iCVD-deposited poly(V3D3), reaching WCA over 120°. On the contrary, hardly any differences can be seen between the WCA on pp(V3D3) on planar silicon and on the NIL imprinted polymer resist as it stays around 90°.

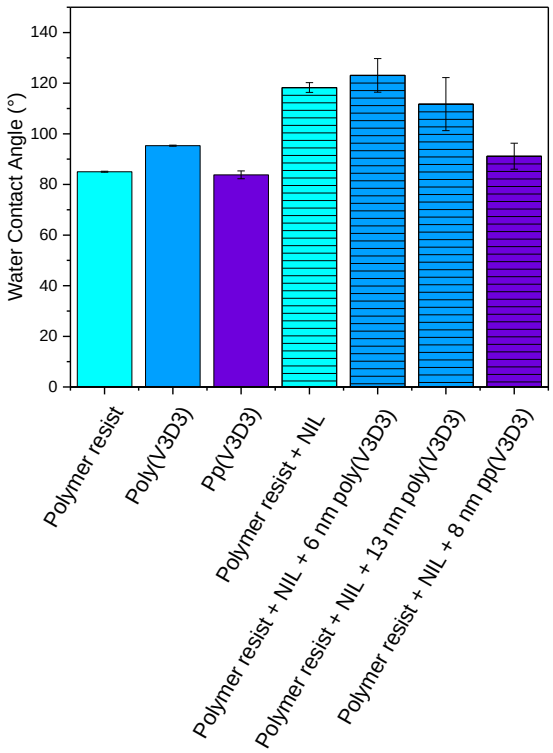

Figure 18: WCAs of polymer resist, with and without NIL modification and with or without a coating of poly(V3D3) deposited by iCVD or pp(V3D3) deposited by DBD-CAP.

3.1.3.3. Combined effect of hydrophobic polymer, nanoscale roughness and microstructures

This WCA difference is further enhanced with the combined effect of the microstructures and surface roughness. Indeed, for the polymer resist modified by NIL and SF_6 (6 sccm) and coated with poly(V3D3), when carrying out the WCA measurement process with the automatic dispenser, the water droplet did not stay on the surface and bounced back with the needle as it returned to its initial position. The lack of affinity to water of these substrates underlines their high hydrophobicity. Some paused images captured from videos of the droplet coming into contact with the microstructured and rough surface coated with various thicknesses of poly(V3D3) during the attempt to measure the WCA can be seen in Figure 19. It can be seen that for all three thicknesses, the droplet stays very round shaped, highlighting the hydrophobic property of these surfaces. It is likely that this is due to air bubbles trapped in the hierarchical structures, causing the Cassie-Baxter effect[21].

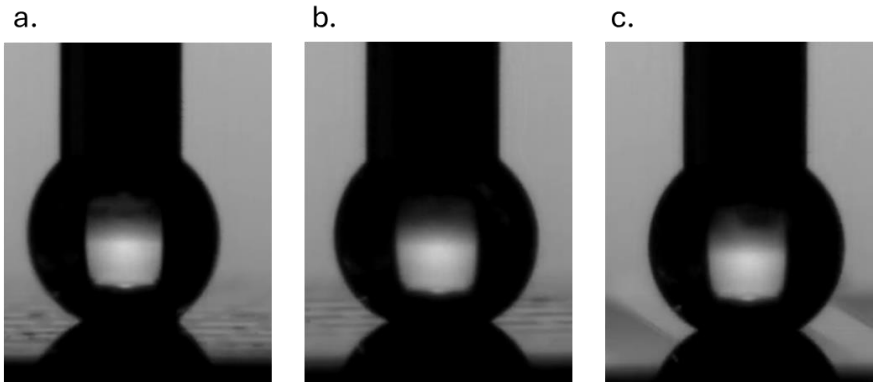

Figure 19: Paused images from the videos of a water droplet as it comes into contact with a substrate of polymer resist microstructured by NIL, etched by SF_6 (6 sccm) plasma and coated with poly(V3D3) with a thickness of a. 6 nm, b. 13 nm and c. 38 nm. The droplets do not spread on the surface but bounce back up with the needle as it goes back to its initial position.

On the other hand, for 8 nm pp(V3D3) deposited onto the same micro and nanostructured surfaces, the WCA is around 80°, not showing any significant differences to the same coating on planar silicon. Again, this could come from the polymer resist substrate if it is not entirely covered by the pp(V3D3) coating.

These results show the efficiency of combining hydrophobic fluorine-free poly(V3D3) and micro/nanostructures to enhance the hydrophobicity of a surface. Furthermore, this study highlights the importance of both the surface topography and the chemistry of any additional coating. Indeed, even for the same precursor, in this case V3D3, a different deposition technique, consequently leading to a different polymer exhibiting different density, structure and functional groups, can have a significate effect on the wettability of the coating.

3.2. Depositing poly(VP-co-V3D3) onto substrates with controlled topography

3.2.1. Effect of plasma etching on the surface wettability

Similarly, poly(VP-co-V3D3) was deposited onto these structured surfaces to study the effects of combining topography with a hydrophilic coating. The copolymer was deposited by iCVD, following the process parameters from chapter 4. In this case, the monomer injection rates were set to reach the copolymer with the highest proportion of VP we managed to achieve (fraction of injected VP = 87.2

%). Two copolymer thicknesses were tested: 5 nm and 11 nm (measured on planar Si coated in the same run).

WCA were then measured on these various samples to qualify their wettability. Figure 20a shows the WCA obtained when combining poly(VP-co-V3D3) with HBr etched polymer resist. Although the HBr etching leads to more hydrophilic surfaces than the untreated polymer resist, the WCA measured on poly(VP-co-V3D3) coatings are very similar whether the substrate was HBr plasma-treated polymer resist or planar silicon. This was also seen with poly(V3D3) on HBr-etched substrates (Figure 16a).

However, whereas for poly(V3D3) on SF_6 (6 sccm) plasma etched substrates, the hydrophobicity was enhanced, in the case of poly(VP-co-V3D3), the WCA are, again, very similar on both planar and rough surfaces (Figure 20b).

Furthermore, whereas in chapter 4, poly(VP-co-V3D3) coatings deposited in these conditions are led to a WCA around 50°, here the WCA on planar silicon is around 66°. This could be due to the very low thickness studied here, or the slight process differences. Indeed, here these measurements were taken on a silicon wafer coupon placed on a substrate holder leading to less control over the substrate's temperature as in chapter 4.

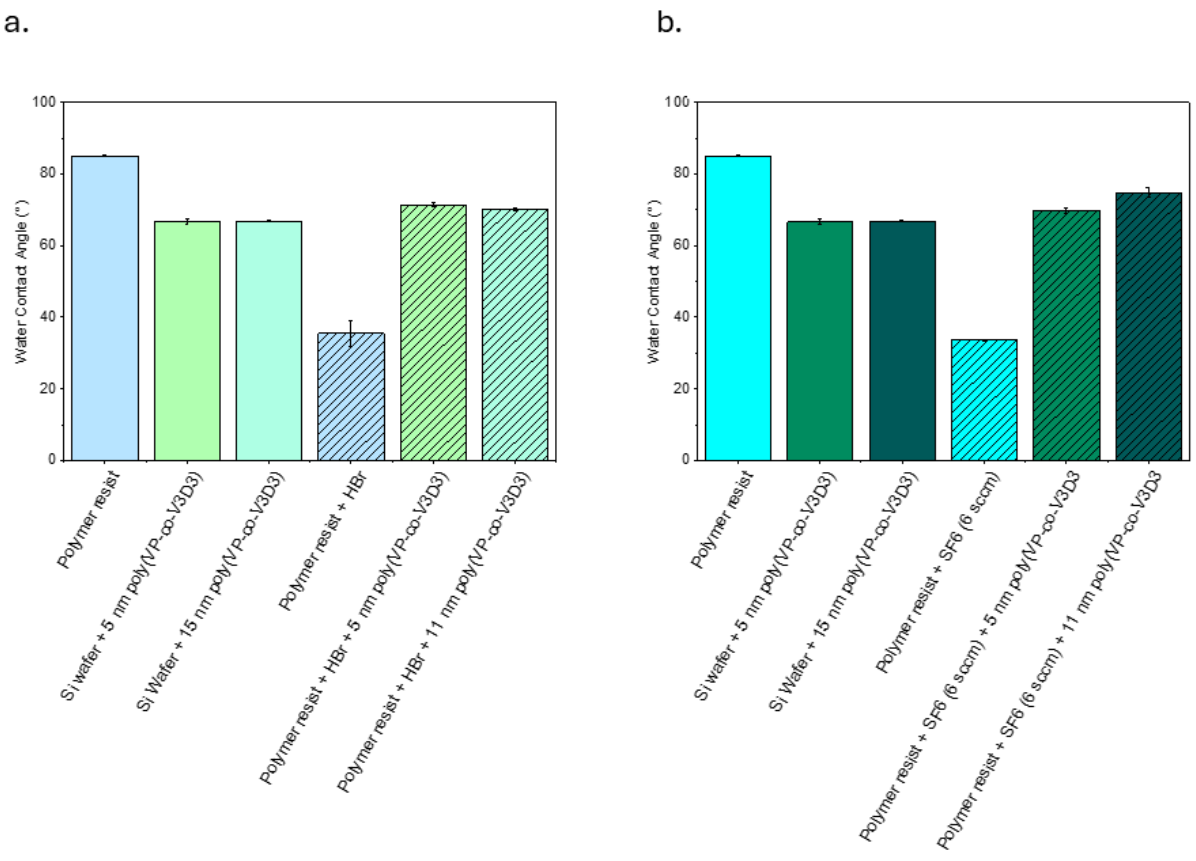

Figure 20: WCAs of polymer resist, with and without a. HBr plasma etching and b. SF_6 (6 sccm) plasma etching, and with or without a coating of poly(VP-co-V3D3) deposited by iCVD.

These combinations of poly(VP-co-V3D3) and surface roughness do not lead to the Wenzel effect. This could be because the polymer is not hydrophilic enough or the roughness is not high

enough. Studying the effect of combining NIL microstructures and poly(VP-co-V3D3) could give a first answer to the second part of this hypothesis.

3.2.2. *Effect of microstructures on the wettability of the surface*

Measurements of the WCAs on microstructured substrates coated with poly(VP-co-V3D3) show the wettability is similar on these surfaces and on planar poly(VP-co-V3D3), in fact it is slightly more hydrophobic. This leads to believe that higher surface topography cannot lead to the Wenzel effect with this copolymer, although it does initially have a WCA <90°.

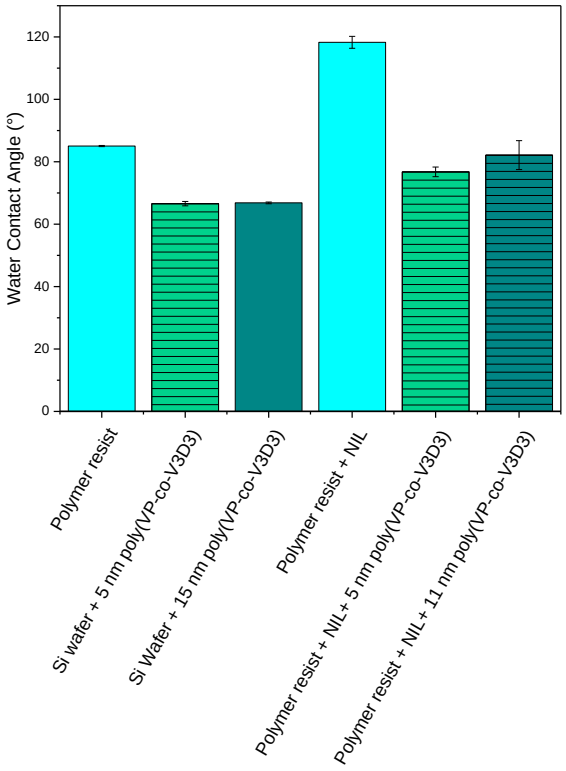

Figure 21: Water Contact Angles of polymer resist, with and without microstructures achieved by NIL and with or without a coating of 5 or 11 nm of poly(VP-co-V3D3) deposited by iCVD.

These results again highlight the complexity of tuning the wettability of a given surface. Indeed, to do so, control over the topography shape and size is required as well as the adequate chemical coating, deposited to the right thickness.

4. Conclusions

This chapter presented the fabrication of complex structured surfaces functionalised with polymers using iCVD and DBD-CAP.

A CEA-Leti patented technique for creating hierarchical structures by NIL and plasma etching was described. It was shown that the choice of active species for the plasma (HBr or SF_6 in this case)

had a significant impact on the resulting roughness. Furthermore, the surface roughness was also influenced by the flowrate of SF_6. Moreover, plasma etching induced variations in surface wettability due to changes in the chemical composition of the polymer resist.

Coating these hierarchical structures with fluorine-free hydrophobic poly(V3D3) was possible using iCVD. It was shown that the thickness of the coating had a significant impact on the roughness and the wettability of the combined surface. Furthermore, using a different deposition method, which led to plasma polymer pp(V3D3), which, as seen previously has different chemical composition and density than poly(V3D3), also impacts the final roughness and wettability of the functionalized surfaces.

When depositing a coating of poly(V3D3) thin enough to not decrease the surface roughness created by plasma etching, the hydrophobicity was enhanced, as predicted by the Wenzel theory[22]. The hydrophobicity was further increased on hierarchical structures with both nanoscale roughness and microstructures. It can be assumed that air bubbles can get trapped between the latter, thus reaching the Cassie-Baxter effect[21] and impeding spreading of the water droplet which showed no affinity to the surfaces.

As for the hydrophilic poly(VP-co-V3D3), in these conditions, its deposition onto plasma etched or microstructured polymer resist did not lead to the creation of superhydrophilic surfaces as predicted by the Wenzel theory. However, by increasing the proportion of VP in the copolymer, it may be possible to achieve more hydrophilic polymers which could react differently on these hierarchical structures.

While this study highlights the complexity of these combinations of structuration and chemistry, these results show the potential of tuning surface properties such as the roughness, wettability and chemical composition by depositing polymers. This is encouraging for the development of antibiofouling surfaces in the current scope of biomimicking surfaces with specific chemistry and topography, as it creates robust surfaces which do not rely on the use of any toxic compounds such as fluorine or nanoparticles.

5. Bibliography

(1) Vellwock, A. E.; Yao, H. Biomimetic and Bioinspired Surface Topographies as a Green Strategy for Combating Biofouling: A Review. *Bioinspiration & Biomimetics* **2021**, *16* (4), 041003. https://doi.org/10.1088/1748-3190/ac060f.

(2) Durand, H.; Whiteley, A.; Mailley, P.; Nonglaton, G. Combining Topography and Chemistry to Produce Antibiofouling Surfaces: A Review. *ACS Applied Bio Materials* **2022**, acsabm.2c00586. https://doi.org/10.1021/acsabm.2c00586.

(3) Brzozowska, A. M.; Parra-Velandia, F. J.; Quintana, R.; Xiaoying, Z.; Lee, S. S. C.; Chin-Sing, L.; Jańczewski, D.; Teo, S. L.-M.; Vancso, J. G. Biomimicking Micropatterned Surfaces and Their Effect on Marine Biofouling. *Langmuir* **2014**, *30* (30), 9165–9175. https://doi.org/10.1021/la502006s.

(4) Choi, W.; Shin, M. G.; Yoo, C. H.; Park, H.; Park, Y.-I.; Lee, J. S.; Lee, J.-H. Desalination Membranes with Ultralow Biofouling via Synergistic Chemical and Topological Strategies. *Journal of Membrane Science* **2021**, *626*, 119212. https://doi.org/10.1016/j.memsci.2021.119212.

(5) Wenzel, R. N. RESISTANCE OF SOLID SURFACES TO WETTING BY WATER. *Industrial Engineering Chemistry* **1936**, *28* (8), 988–994. https://doi.org/10.1021/ie50320a024.

(6) MacGregor-Ramiasa, M. N.; Vasilev, K. Questions and Answers on the Wettability of Nano-Engineered Surfaces. *Advanced Materials Interfaces* **2017**, *4* (16), 1700381. https://doi.org/10.1002/admi.201700381.

(7) Amini, S.; Seche, W.; May, N.; Choi, H.; Tavousi, P.; Shahbazmohamadi, S. Femtosecond Laser Hierarchical Surface Restructuring for next Generation Neural Interfacing Electrodes and Microelectrode Arrays. *Scientific Reports* **2022**, *12* (1), 13966. https://doi.org/10.1038/s41598-022-18161-4.

(8) Teyssedre, H.; Posseme, N.; Mehrez, Z.; May, M. Procédé de structuration de surface hybride par gravure plasma. EP 4 083 706 A1, November 2, 2022.

(9) Voisin, P. Lithographie de nouvelle génération par nanoimpression assistée par UV: étude et développement de matériaux et procédés pour l'application microélectronique. 172.

(10) Mohamed, K. Nanoimprint Lithography for Nanomanufacturing. In *Comprehensive Nanoscience and Nanotechnology*; Elsevier, 2019; pp 357–386. https://doi.org/10.1016/B978-0-12-803581-8.10508-9.

(11) Hong, G.; Holmes, A. S.; Heaton, M. E. SU8 Resist Plasma Etching and Its Optimisation. In *Symposium on Design, Test, Integration and Packaging of MEMS/MOEMS 2003.*; 2003; pp 268–271. https://doi.org/10.1109/DTIP.2003.1287050.

(12) Belen, R. J.; Gomez, S.; Kiehlbauch, M.; Aydil, E. S. Feature Scale Model of Si Etching in SF6/O2/HBr Plasma and Comparison with Experiments. *Journal of Vacuum Science & Technology A: Vacuum, Surfaces, and Films* **2006**, *24* (2), 350–361. https://doi.org/10.1116/1.2173268.

(13) Gul, B.; Aman-ur-Rehman. Numerical Study of HBr/He Discharges in Capacitive Coupled Plasma Reactor. *Plasma Chemistry & Plasma Processing* **2016**, *36* (3), 857–868. https://doi.org/10.1007/s11090-015-9689-7.

(14) Osipov, A. A.; Iankevich, G. A.; Speshilova, A. B.; Osipov, A. A.; Endiiarova, E. V.; Berezenko, V. I.; Tyurikova, I. A.; Tyurikov, K. S.; Alexandrov, S. E. High-Temperature Etching of SiC in SF6/O2 Inductively Coupled Plasma. *Scientific Reports* **2020**, *10* (1), 19977. https://doi.org/10.1038/s41598-020-77083-1.

(15) Belen, R. J.; Gomez, S.; Cooperberg, D.; Kiehlbauch, M.; Aydil, E. S. Feature-Scale Model of Si Etching in SF6/O2 Plasma and Comparison with Experiments. *Journal of Vacuum Science & Technology A* **2005**, *23* (5), 1430–1439. https://doi.org/10.1116/1.2013317.

(16) Eon, D.; Raballand, V.; Cartry, G.; Cardinaud, C. High Density Fluorocarbon Plasma Etching of Methylsilsesquioxane SiOC(H) Low- *k* Material and SiC(H) Etch Stop Layer: Surface Analyses and Investigation of Etch Mechanisms. *Jiurnal of Physics. D: Applied Physics* **2007**, *40* (13), 3951–3959. https://doi.org/10.1088/0022-3727/40/13/007.

(17) Alfonsetti, R.; Lozzi, L.; Passacantando, M.; Picozzi, P.; Santucci, S. XPS Studies on SiOx Thin Films. *Applied Surface Science* **1993**, *70–71*, 222–225. https://doi.org/10.1016/0169-4332(93)90431-A.
(18) Tserepi, A.; Cordoyiannis, G.; Patsis, G. P.; Constantoudis, V.; Gogolides, E.; Valamontes, E. S.; Eon, D.; Peignon, M. C.; Cartry, G.; Cardinaud, Ch.; Turban, G. Etching Behavior of Si-Containing Polymers as Resist Materials for Bilayer Lithography: The Case of Poly-Dimethyl Siloxane. *Journal of Vacuum Science & Technology B: Microelectronics and Nanometer Structures Processing, Measurement, and Phenomena* **2003**, *21* (1), 174–182. https://doi.org/10.1116/1.1535929.
(19) Vinogradova, E.; Osei-Yiadom, E.; Smith, C. E.; Mueller, D. W.; Reidy, R. F. Effects of Plasmas on Porous Low Dielectric Constant CVD SiOCH Films. *Microelectronic Engineering* **2009**, *86* (2), 176–180. https://doi.org/10.1016/j.mee.2008.10.018.
(20) Mertz, G.; Delmée, M.; Bardon, J.; Martin, A.; Ruch, D.; Fouquet, T.; Garreau, S.; Airoudj, A.; Marguier, A.; Ploux, L.; Roucoules, V. Atmospheric Pressure Plasma Co-Polymerization of Two Acrylate Precursors: Toward the Control of Wetting Properties. *Plasma Processes and Polymers* **2018**, *15* (10), 1800073. https://doi.org/10.1002/ppap.201800073.
(21) Belaud, V.; Valette, S.; Stremsdoerfer, G.; Bigerelle, M.; Benayoun, S. Wettability versus Roughness: Multi-Scales Approach. *Tribology International* **2015**, *82*, 343–349. https://doi.org/10.1016/j.triboint.2014.07.002.
(22) Jothi Prakash, C. G.; Prasanth, R. Approaches to Design a Surface with Tunable Wettability: A Review on Surface Properties. *Journal of Materials Science* **2021**, *56* (1), 108–135. https://doi.org/10.1007/s10853-020-05116-1.

Chapter 6:
Evaluating bacterial adhesion on functionalised surfaces

1. Introduction

For evaluating their potential as antibiofouling coatings, microbiology assays were carried out on the various thin films and structured surfaces developed in this work. The aim of these experiments was to determine which surface parameters studied in this thesis (wettability, roughness, chemistry) seemed to be the most important for limiting bacterial adhesion and therefore biofilm formation. Several surfaces were studied: planar hydrophobic poly(V3D3) and pp(V3D3) surfaces and planar hydrophilic poly(VP-co-V3D3) surfaces; plasma-etched polymer resist without additional coating and functionalised with poly(V3D3), pp(V3D3) or poly(VP-co-V3D3). Then the influence of microstructures obtained by NIL was evaluated. To quantify the bacterial adhesion, fluorescent microscopy was carried out after staining the bacteria which were then counted. This technique permits to assess the viability of the cells as well as their adsorption onto the surfaces.

The bacterial specie most studied in this work was Gram-negative *Escherichia coli*. These rod-shaped bacteria can be found in the intestinal tract of warm-blooded animals, including humans. While certain strains can be enteropathogenic[1] or can cause urinary tract infections after biofilm formation[2], biosafety level 1 strains are often used in microbiology labs as model specie. This is the case for the strain used in this thesis: *E. coli* ATCC 8739, which is recommended for use in many different applications[3].

A second bacterial specie was also studied in this work: *Staphylococcus epidermidis.* These Gram-positive spherical bacteria, present in the human microbiota are mainly found on skin and in mucous membranes. Generally harmless, this specie can cause infections in immunodeficient patients, or after the implantation of a medical device[4,5]. In this work, biosafety level 1 *S. epidermidis* ATCC 14990 was used[6].

In this chapter, the experimental protocols are described before presenting and discussing the results of these microbiology assays.

2. Experimental protocols

Evaluating the antimicrobial effect of surfaces relies on carrying out microbiology assays. However, the development of these assays is an ongoing field of research in itself. Indeed, there does not yet exist a standard protocol and the industrial methods tend to not specify the antimicrobial mechanism of action taking place[7]. The protocols which were developed in this thesis were inspired from different studies found in the literature.

The microbiology tests that are the most suitable for evaluating the adhesion of bacteria on surfaces, which is the first step in biofilm formation, are adhesion tests which consist in leaving the surface of interest in a bacterial suspension for 1 to 4 hours under static or agitated conditions[7,8]. This is the method of choice in this thesis, combined with fluorescence microscopy which enables quantification of viable and non-viable cells.

2.1. Preparation of bacterial suspensions

The first step for the adhesion tests was preparing the bacterial suspension of *E. coli* or *S. epidermidis.*

In order to ensure that the bacterial colonies used in these experiments were fresh, a renewed agar plate was systematically prepared the day before. To do so, one isolated colony of the strain of interest was taken from the strain bank and spread onto a sterile tryptic soy agar (TSA) plate using an inoculation loop. This TSA plate was then incubated overnight at 37°C. This step ensures the colonies used in the assay are fresh and will grow efficiently. These colonies were then used to prepare bacterial suspensions of *E. coli* of around 2.10^5 colony forming units (CFU)/mL. For *S. epidermidis*, the concentration was around 2.10^4 CFU/mL. These suspensions were prepared in two different ways to evaluate the impact of the preparation on the bacterial growth and the dispersity of the results.

In the first method, an isolated colony was taken from the fresh culture plate with an inoculation loop and placed into Biomerieux's API® suspension media. Extra isolated colonies were then added until the optical density at 600 nm (measured with an OD600 DiluPhotometer) of the bacterial suspension was 0.5 McFarland (McF). This corresponds to around 2.10^8 CFU/mL for *E. coli* and around 2.10^7 CFU/mL for *S. epidermidis*. The suspension was then diluted in Mueller Hinton culture media[9] to obtain a concentration of around 2.10^5 CFU/mL for *E. coli* and 2.10^4 CFU/mL for *S. epidermidis*.

The second method is inspired by the protocol developed by Marion Stalet in her thesis to ensure that the bacteria were found in exponential growth phase.[8] This method was only used for inoculating *E. coli* in this study. Here, an isolated colony of *E. coli* was taken from the fresh agar plate with a sterile inoculation loop and added to 5 mL of Mueller Hinton culture media in a Falcon tube. This preculture was then incubated overnight at 37°C. Once the preculture was ready, 300 µL were pipetted and placed into 9 mL of Mueller Hinton culture media. This suspension was then incubated for 2h at 37°C and 100 rpm in an Infors HT Ecotron incubator shaker. The optical density of the suspension was then measured before diluting in Mueller Hinton culture media to obtain a concentration of around 2.10^5 CFU/mL. This final *E. coli* suspension was then used for the microbiology assays.

The concentration of the bacterial suspensions was checked by carrying out cascade dilutions and spreading the resulting solutions onto TSA agar plates. After incubating at 37°C overnight, the colonies formed can be manually counted to verify the initial concentration of the bacterial suspension.

2.2.Incubating the prepared surfaces

To carry out the bacterial adhesion assays on the functionalised surfaces developed in this thesis, the latter were cut into 1 cm^2 samples and placed into a 24-well plate. One mL of the prepared bacterial suspension was then added to each well containing a sample. For the adhesion assays presented in this work, the well plate was incubated for 3 h at 37°C[10]. This time was chosen because it is long enough for irreversible adsorption of bacteria onto the surface[7], without yet the formation of biofilm. This allows quantification of the cells on the surface which becomes more difficult for longer times due to the bacteria agglomerating.

Some time-dependent bacterial adhesion experiments were carried out with different incubation times (3, 6, 24 and 48 h) and will be presented in sections 3.1.1.2 and 3.1.1.3. For the 48 h experiment, the saturated bacterial suspension was removed after 24 h and fresh culture media was added to the wells in which the substrates were placed, bringing nutrients to the bacteria[11].

After the incubation time, the bacterial suspension was removed with a pipette and the samples were placed into clean wells into which 1 mL of sterile Phosphate Buffer Saline (PBS)[12] was added for rinsing to remove the non-adhered bacteria. The well-plate was then very gently shaken at 20 rpm for 5 min at room temperature in the incubator shaker. After this time, the PBS was removed and the samples placed into clean wells.

2.3.LIVE/DEAD staining and fluorescent microscopy

In order to quantify the adhered bacteria on the tested surfaces, Invitrogen™'s LIVE/DEAD™ BacLight™ bacterial viability kit was used. Two fluorescent nucleic acid stains allowed the visualisation of both live and dead bacteria on the surface. Indeed, green fluorescent nucleic acid stain SYTO™9 stains all bacteria, no matter their viability. Red fluorescent propidium iodide (PI) on the other hand, only penetrates bacteria with damaged membranes[8,10]. These dyes have an excitation/emission maxima of 480/500 nm and 490/635 nm for SYTO™9 and PI respectively[8,13]. When used together, the PI can cause a reduction of the SYTO™9 staining fluorescence[13]. For this reason, preliminary experiments were conducted to determine the best ratio of both fluorescent stains for carrying out *E. coli* and *S. epidermidis* adhesion assays. The chosen solutions consisted of 1 µL of SYTO™9 and 1.5 µL of PI for *E. coli*, and 1.5 µL of both stains for *S. epidermidis*, diluted in 1 mL of PBS.

Once the solution is prepared, and the samples rinsed, 0.5 mL of the staining solution was added to each well. The samples were then left to incubate for 15 min in the dark. After this time, the solution was removed and the samples were gently rinsed with PBS before being left to dry in the dark. When dry, fluorescent microscopy was carried out on the samples to visualise both the live and dead bacteria by using different filters: standard filter cube FITC for SYTO™9 and a custom-made filter similar to TexasRed® (TXRED) for PI[13].

For each type of surface, 3 samples were incubated, and 10 or 15 images were taken for each sample. Silicon dioxide (SiO_2) was used as a control sample to verify the customary activity of the bacteria.

2.4.Counting the bacteria on the surface

After acquiring the microscopy images, the bacteria were counted using a python programme developed by Clément Douarre (CEA Leti, DTBS) or using ImageJ software. In both cases, the threshold was adjusted for the software to be able to detect the bacteria on the surface. The number of bacteria per image were then translated into number of bacteria per mm². In cases where the total number of bacteria (stained in green) was lower than the number of dead bacteria (stained in red), the results were eliminated as this is an impossible situation.

2.5.Overcoming the dispersion of the results

Results of these adhesion tests on SiO_2 control samples can be seen in Figure 1 which represents the number of cells/mm² after 3 h incubation in Mueller Hinton culture media. Each box in Figure 1a represents one experiment but takes into account all images on all SiO_2 samples tested that day. These boxplots give a vision of the median (the horizontal line in the box), the average (represented by □) as well as the range of values. Figure 1b details the number of live and dead cells on these surfaces. Each individual green and red point respectively corresponds to the value of live

and dead cells/mm² counted from one microscopy image. The * marks the experiments where the bacterial suspension was prepared from a preculture, while the other experiments used the protocol in which the suspension was directly prepared from the fresh colonies on the agar plate.

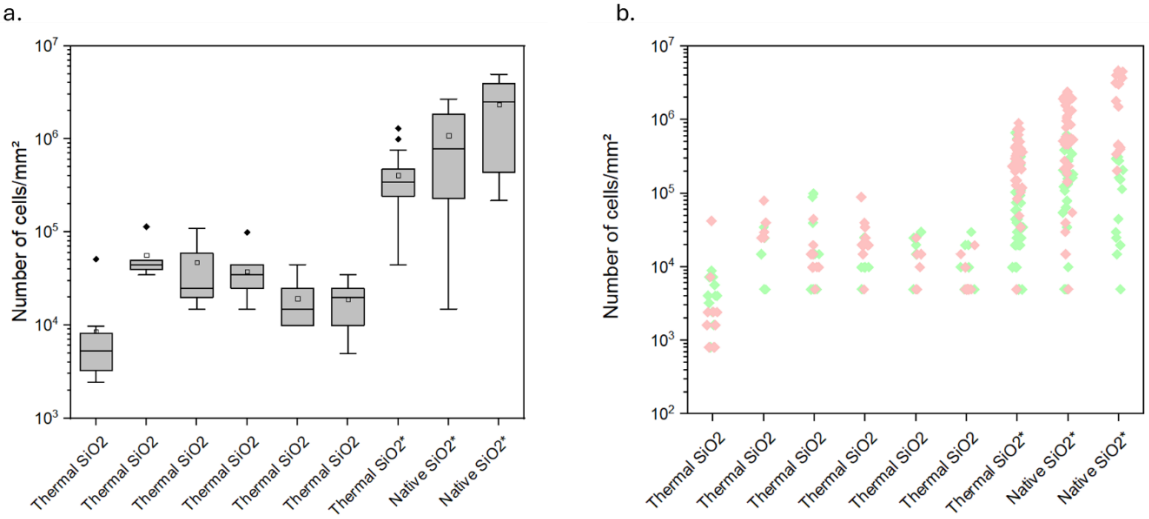

Figure 1: Number of E. coli *cells on thermal or native SiO_2 after 3 h incubation in a bacterial suspension with an initial concentration of around 2.10^5 CFU/mL. a. Boxplot representation of the total number of cells. Each individual boxplot represents one experiment. b. Number of live (green) and dead (red) bacteria on the SiO_2 surface. The * correspond to the experiments where a preculture step was added.*

Representation in boxplot form highlights the dispersity of the results, even for samples carried out on the same day and thus incubated in exactly the same bacterial suspension. Furthermore, this shows that for these adhesion tests, the bacterial suspensions prepared with the preculture step do enhance the growth of *E. coli*, however, it also increases the range of values. There does not seem to be any significant differences between the number of bacteria found on native or thermal SiO_2 incubated in the same conditions. Figure 1b shows that there are as many dead cells on these SiO_2 substrates after 3 h incubation than live bacteria. However, by collecting the bacterial suspension after 3 h, and incubating it on a TSA plate at 37°C overnight, growth of *E. coli* colonies confirmed the viability of the cells in the bacterial suspension during the protocol.

To overcome these differences from day-to-day results, the average values of cells/mm² on functionalised surfaces were divided by the average number of cells/mm² on SiO_2 giving a ratio of cells on specific surface/cells on SiO_2. This method seemed to be the best way of comparing results from one experiment to another.

3. Results and discussion

The fluorescent microscopy images represented in this section were selected out of the 30 to 45 images taken over the three samples of specific functionalised surface. The image was chosen to try and give the best average representation of the bacterial adhesion and viability over all taken images for one surface.

For all graphical results, the green and red colours respectively represent the number of live bacteria and the number of dead bacteria.

3.1. Bacterial adhesion on planar surfaces functionalised by thin film deposition

3.1.1. Bacterial adhesion on hydrophobic thin films

3.1.1.1. *E. coli* adhesion on poly(V3D3) and pp(V3D3) thin films

Both conventional polymer poly(V3D3) and plasma polymer pp(V3D3) deposited by iCVD and DBD-CAP respectively onto planar silicon wafers were studied to evaluate their potential against *E. coli* colonisation.

The fluorescent microscopy images (Figure 2) show similar *E. coli* presence on both poly(V3D3) and pp(V3D3). The FITC filter reveals the presence of both live and dead bacterial cells stained by SYTO™9 and the TXRED filter shows the presence of dead cells stained by PI. By comparing both images, it can be seen that on the image obtained through the FITC filter, the live cells appear in very bright green, whereas the dead cells appear with a less bright colour. The latter can also be seen in the images obtained with the TXRED filter, confirming that they are dead cells. Some of these dead cells are highlighted by red arrows in Figure 1, whereas some live bacteria are shown with green arrows.

Furthermore, these images show that after 3 h incubation, the *E. coli* cells can be found on poly(V3D3) and pp(V3D3) as individual cells that do not seem to agglomerate. From these images it seems that there is a majority of dead cells, however counting the cells over all images will give a better understanding of the global adhesive and bactericidal properties of these surfaces.

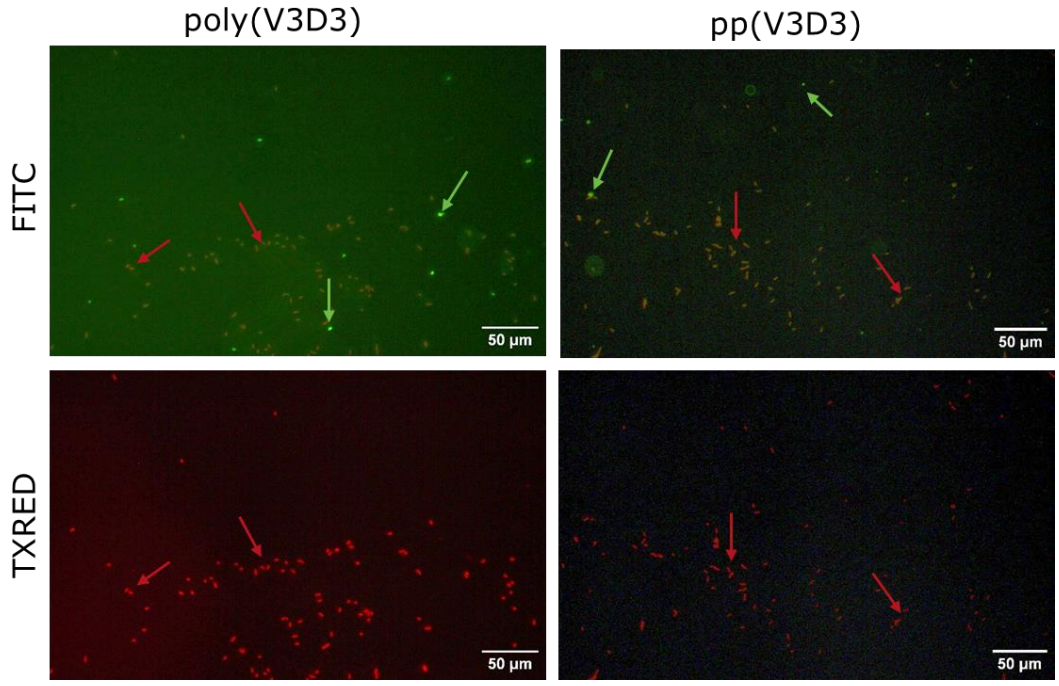

Figure 2: Fluorescence microscopy images of E. coli *on poly(V3D3) and pp(V3D3) after 3 h incubation. The SYTO™9 stains both live and dead cells and can be seen with the FITC filter, the PI stains dead cells which can be seen with the TXRED filter. The green arrows highlight some live cells which appear bright green, the red arrows highlight some dead cells which appear in both green and red.*

The ratio of the average number of cells on poly(V3D3) and pp(V3D3) on the average number of cells on SiO_2 from the same experiment (Figure 3) shows that the average number of cells on

poly(V3D3) is very similar to the average on SiO_2 as the ratio is close to 1. The number of *E. coli* cells on pp(V3D3) is very slightly higher but this difference is not significant considering the error bars. Furthermore, pp(V3D3) seems to be slightly less bactericidal than poly(V3D3).

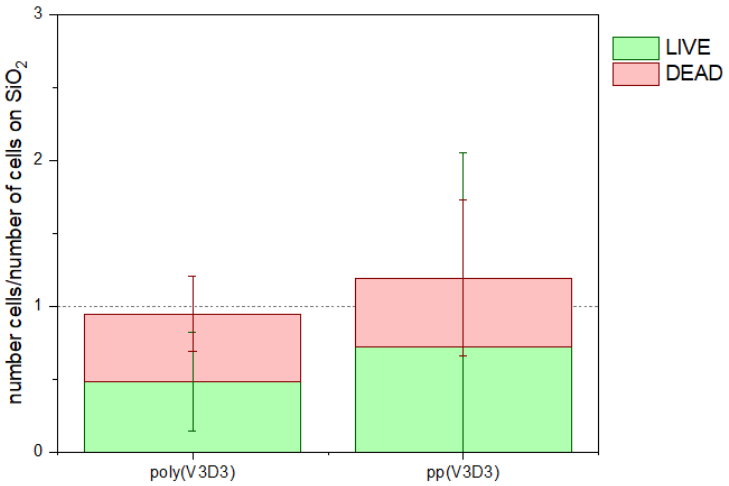

Figure 3: Ratio of the average number of live and dead E. coli *cells per mm² on poly(V3D3) and pp(V3D3) on the average number of live and dead cells per mm² on thermal SiO_2 after 3 h incubation. The grey dashed line highlights a ratio equal to 1.*

The similar behaviour of *E. coli* on these surfaces can result from the similar surface properties (Table 1). Indeed, all surfaces show a very low Rq roughness (< 0.4 nm) which should therefore not induce any mechanical deformation of the bacterial membranes. The WCA on poly(V3D3) is slightly higher than on pp(V3D3) (95° and 81° respectively), however, these WCA at the interface between hydrophilicity and hydrophobicity do not seem to be extreme enough for repelling bacteria. Furthermore, although the organisation and structure of the two polymers is different, the chemical composition remains similar, with a higher carbon content for poly(V3D3).

Table 1: Chemical composition, WCA and Rq roughness for SiO_2, poly(V3D3) and pp(V3D3).

Sample	Chemical composition	WCA (°)	Rq (nm)
SiO_2	Si fully substituted by O	51 ± 8	< 0.5
poly(V3D3)	Si-O-Si rings linked by PE-like chains with di-substituted Si by O	95 ± 0.1	0.4
pp(V3D3)	tri-substituted Si by O with lower percentage of C	81 ± 0.8	0.3

In comparison to the literature, organosilicon polymers have previously shown antiadhesive activity towards microorganisms. However, this was in very different conditions. Saulou *et al.* deposited HMDSO by PECVD and tested the resulting coatings against *S. cerevisiae* yeast cells adhesion in hydrodynamic conditions[14]. In these conditions the organosilicon thin films showed good detachment of the yeast in comparison to stainless steel. This study also showed that embedding antimicrobial silver nanoparticles into the organosilicon matrix, reduced the antiadhesive effect[14].

Furthermore, it has been shown that HMDSO coatings with a higher carbon content, are more antibiofouling than coatings with a higher oxygen content. This chemical composition can be tuned by

adjusting the HMDSO/O_2 ratio during deposition.[15]. This is coherent with the slightly higher number of cells on pp(V3D3) than on poly(V3D3).

3.1.1.2. *E. coli* adhesion on poly(V3D3) over time

Surfaces functionalised with conventional poly(V3D3) were also incubated for longer times to see how biofilm development was influenced by the coating. Here, as bacteria start to agglomerate after 6 h incubation, it was difficult to count the number of individual cells (Figure 4). Therefore, the area covered by *E. coli* cells was quantified and given as a percentage of the total area.

The fluorescent microscopy images show an increase in bacteria on both SiO_2 and poly(V3D3) surfaces as the incubation time increases. Moreover, as many cells appear in bright green through the FITC filter, it seems that there is a high percentage of live bacteria in these conditions.

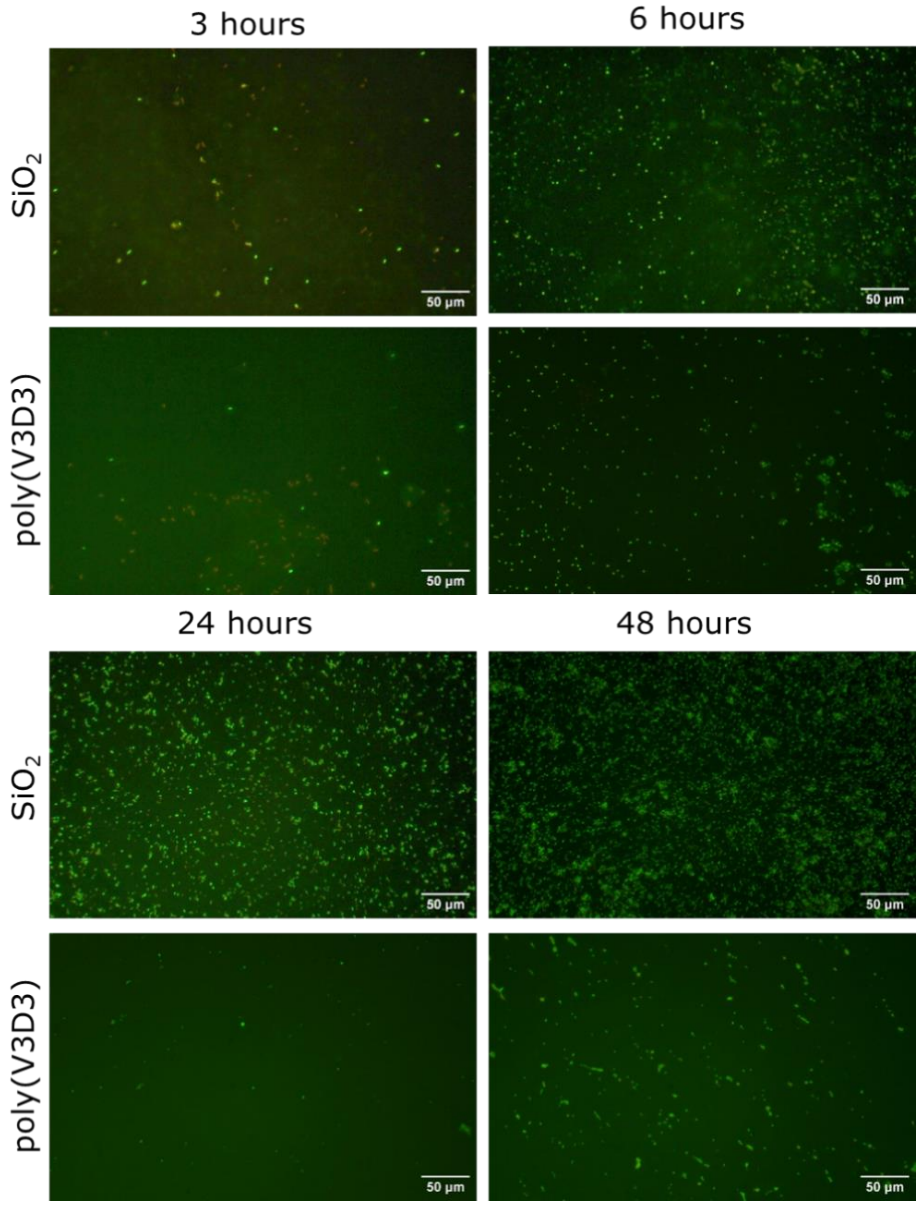

Figure 4: Fluorescence microscopy images of E. coli *on thermal SiO_2 or poly(V3D3) after various incubation times (3, 6, 24 and 48 h). These images were obtained with a FITC filter and show the total number of bacteria.*

Figure 5a shows the average percentage calculated from all microscopy images of the surface covered by both live and dead bacteria. This figure shows that even after 48 h incubation, on average under 15 % of both SiO_2 and poly(V3D3) surfaces have been colonised. Furthermore, there are more live cells than dead ones on all surfaces.

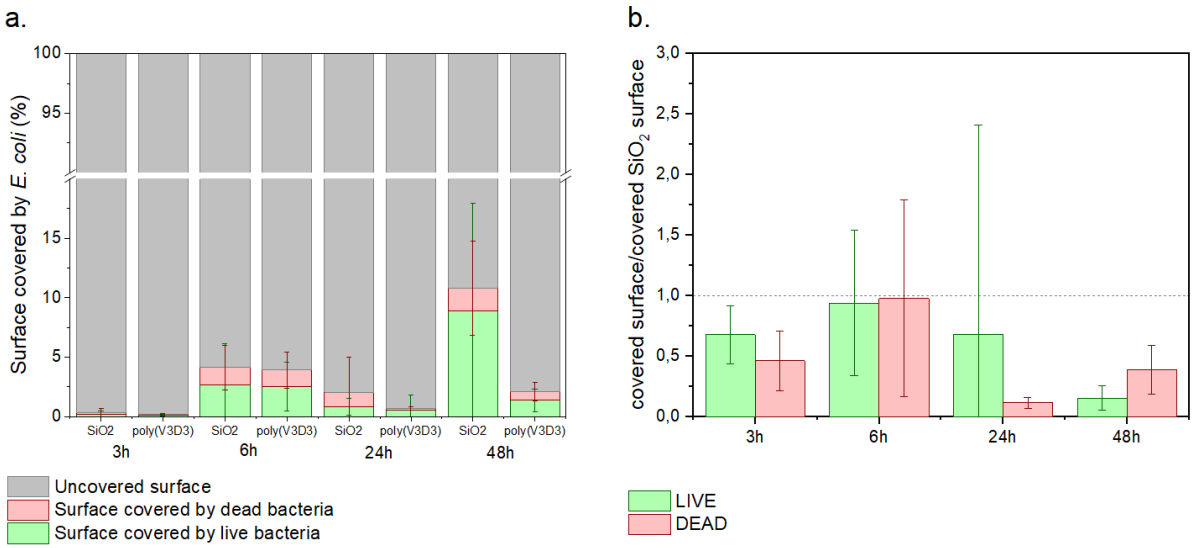

Figure 5: a. Percentage of thermal SiO_2 and poly(V3D3) surfaces covered by live (green) or dead (red) E. coli *after various incubation times (3, 6, 24 and 48 h). b. Ratio of the percentage of poly(V3D3) covered by live and dead* E. coli *on the percentage of thermal SiO_2 covered in live and dead* E. coli*. The grey dashed line highlights a ratio equal to 1. For the 48 h experiment, the saturated bacterial suspension was removed after 24 h and fresh culture media was added to the wells.*

As seen more precisely in Figure 3, and as it can be seen again here, after 3 and 6 h, there are no significant differences between the bacterial adhesion on SiO_2 or poly(V3D3). After 24 h, the number of bacteria on the two substrates decreases. We assume this comes from reaching the death phase in the growth cycle of *E. coli*. Indeed, in a nutrient rich media, such as the one used here, bacteria exhibit a growth cycle in four phases: the lag phase, the log phase, the stationary phase and the death phase[16]. During the log phase, only the cell size increases, cell division then occurs in the log phase, exponentially increasing the number of bacteria in the media until no more nutrients are available or toxins accumulate. Bacteria then begin to die leading to the stationary phase, where there are as many dead bacteria as there are live. As the proportion of dead cells increases, the death phase is reached[16]. Here, after 6 h incubation, there are still more live cells than dead ones on both surfaces. Therefore, the stationary phase has not yet been reached. However, after 24 h, the decrease in number of bacteria shows that the growth cycle has reached the death phase. When adding fresh culture media after 24 h, the bacteria enter the log phase again and their number increases as it can be seen after 48 h.

On both surfaces, the evolution of the number of bacteria over time is similar, however, there seem to be less adhered bacteria on the poly(V3D3) surfaces than on SiO_2 after a certain time. This can be seen in Figure 5b where the ratio between covered poly(V3D3) surface and covered SiO_2 surface is equal to 1 after 6h, but decreases after 24 and 48 h. This is coherent with the observations mentioned in the literature, stating that a silicon oxide type film with a higher carbon content has better antibiofouling properties[15].

3.1.1.3. *S. epidermidis* adhesion on poly(V3D3) over time

The same experiments were conducted using *S. epidermidis* to evaluate how a different bacterial specie behaves on the same surfaces. For the same reasons as previously, the areas covered by bacteria were quantified rather than individual cells counted. Furthermore, spherical *S. epidermidis* naturally tend to agglomerate into grape bunch like groups[17]. This can be seen in the microscopy images even after 3 h incubation (Figure 6). This phenomenon also makes counting each individual bacterium impossible.

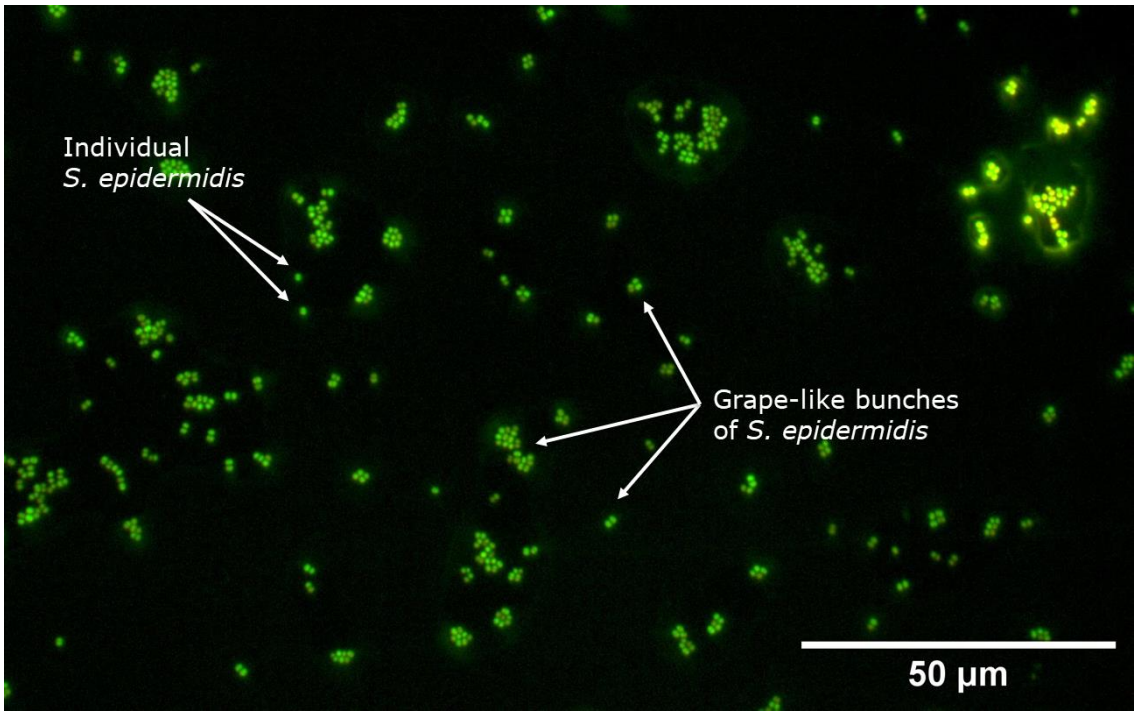

Figure 6: Fluorescent microscopy images obtained with an FITC filter showing S. epidermidis *cells stained with SYTO™9 after 3 h incubation.*

The fluorescent microscopy images shown in Figure 7 show that *S. epidermidis* adheres to both SiO_2 and poly(V3D3). In comparison with the images acquired with *E. coli*, the coverage seems to be higher with *S. epidermidis*. Moreover, close observation of the images after 48 h reveals different levels of *S. epidermidis* upon the surface. Indeed, some bacteria appear in very bright green but underneath, there seem to be more cells which appear in a less bright colour, presumably as they are older. This highlights the importance of impeding bacterial adhesion at the start, as the first few cells that adsorb onto a given surface can then act as a conditioning film for any surrounding bacteria as well as favour the multiplication of the cells.

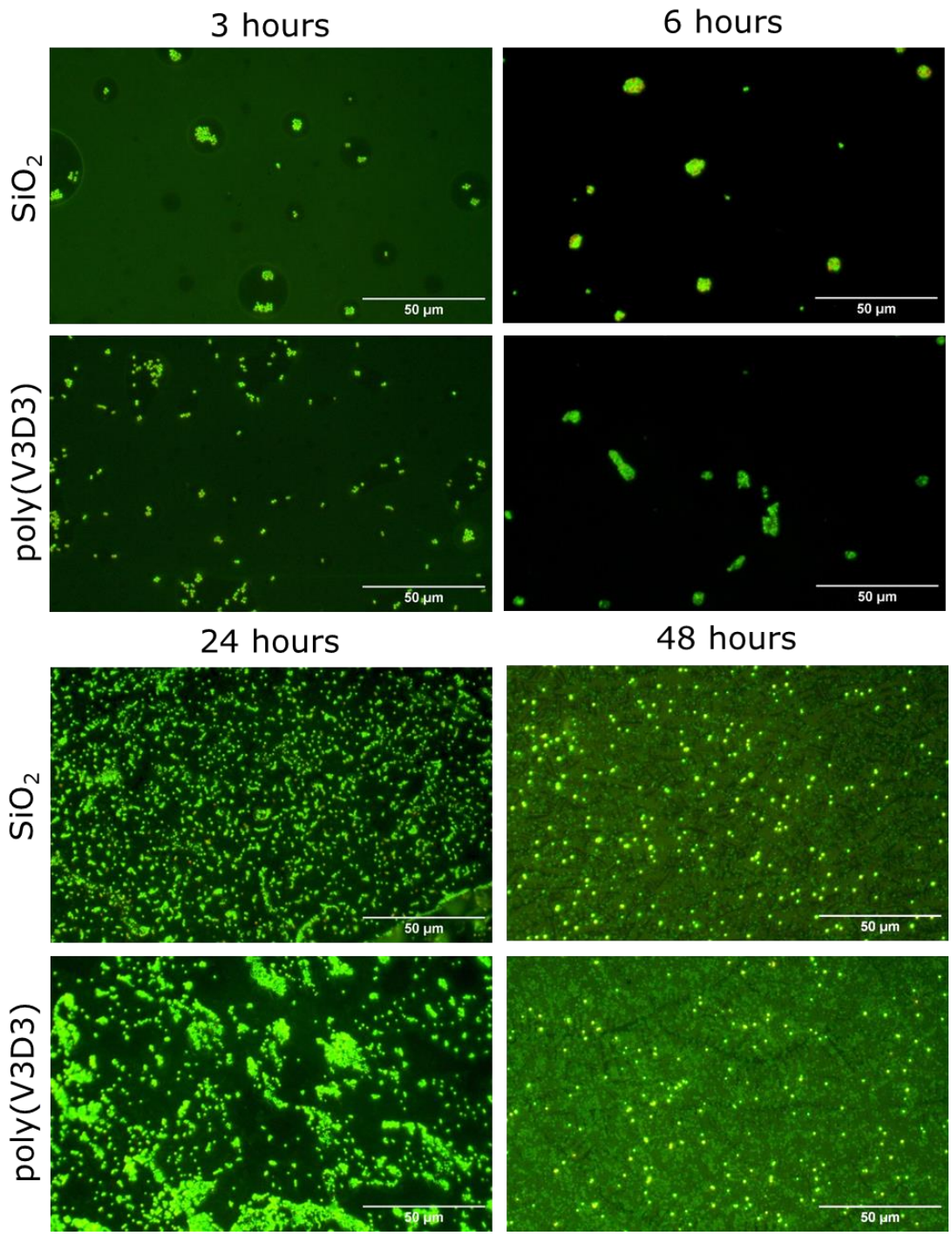

Figure 7: Fluorescence microscopy images of S.epidermidis *on thermal SiO_2 or poly(V3D3) after various incubation times (3, 6, 24 and 48 h). These images were obtained with a FITC filter and show the total number of bacteria.*

Figure 8a shows the average percentage calculated from all microscopy images of the surface covered by both live and dead bacteria. Furthermore, this figure shows that even after 48 h incubation, on average up to 20 % of SiO_2 and around 30 % of poly(V3D3) surfaces have been colonised, which is more than twice the area colonised by *E. coli*.

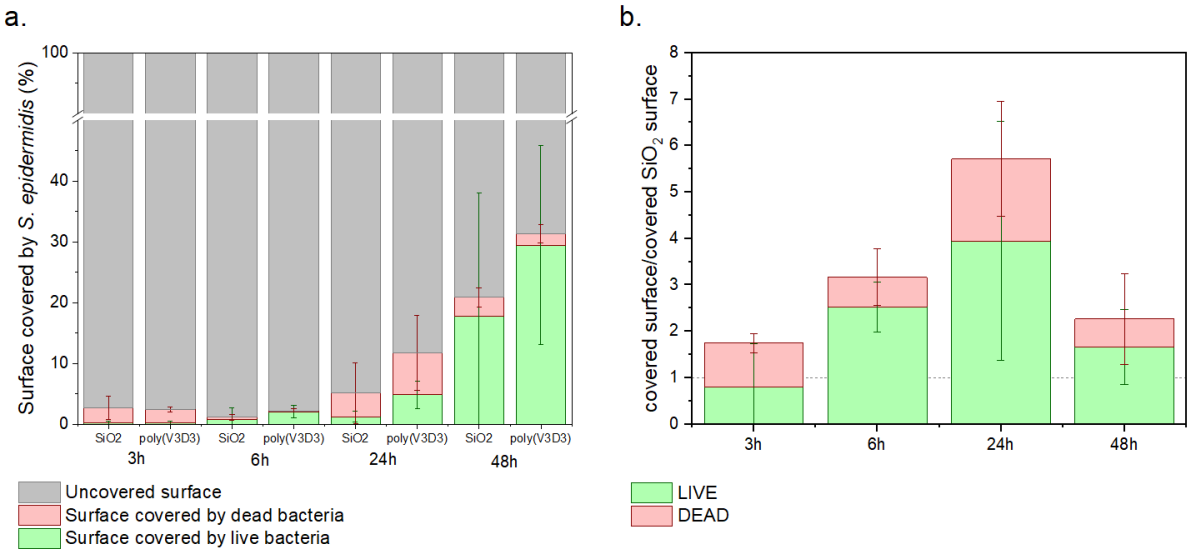

Figure 8: a. Percentage of thermal SiO_2 and poly(V3D3) surfaces covered by live (green) or dead (red) S. epidermidis *after various incubation times (3, 6, 24 and 48 h). b. Ratio of the percentage of poly(V3D3) covered by live and dead* S. epidermidis *on the percentage of thermal SiO_2 covered in live and dead* S. epidermidis*. The grey dashed line highlights a ratio equal to 1. For the 48 h experiment, the saturated bacterial suspension was removed after 24 h and fresh culture media was added to the wells.*

These results also show that *S. epidermidis* have a different growth cycle to *E. coli*. Indeed, after 3 h incubation, the majority of the *S. epidermidis* cells are dead. Their number decreases after 6 h incubation, possibly due to cell detachment, but most cells that can be seen are alive. After 24 h incubation, the number of cells has increased again, covering around 5 % of the SiO_2 surfaces and around 12 % of the poly(V3D3) surfaces. However, more than half the cells are dead, suggesting the beginning of the death phase[16]. After 24 h, fresh culture media is added, allowing the remaining live bacteria to continue their growth and replication. This leads to the percentage of area covered in bacteria more than doubling in 24 h. The vast majority of *S. epidermidis* cells observed at this stage on the surfaces are alive.

Furthermore, it seems that, contrarily to *E. coli*, the hydrophobic poly(V3D3) enhances the bacterial adhesion of *S. epidermidis* in comparison to SiO_2. This can be seen in Figure 8b where the ratio between poly(V3D3) covered surface and SiO_2 covered surface is higher than 1 for all incubation times. It has previously been shown that water repellent surfaces can attract *S. epidermidis*[18]. Differences between the adhesion and viability of different species of bacteria have previously been noted in the literature. Generally explained by the membrane differences between Gram-negative and Gram-positive bacteria[19], lower adhesion of *E. coli* may be due to its motility allowing it to detach from the surface. *S. epidermidis* on the other hand shows no motility and therefore would not have this capacity[8]. Furthermore, the difference in shape and size, can be advantageous for spherical *S. epidermidis* as it requires only a small surface of the substrate to adhere to it[20].

3.1.2. E. coli *adhesion on hydrophilic polymers poly(VP-co-EGDA)*

E. coli adhesion and viability was also evaluated on hydrophilic copolymers poly(VP-co-V3D3) which were studied in chapter 4. Three different coatings obtained by varying the injected fraction of

VP were studied to see whether this impacted the bacteria's behaviour. These three coatings all have a similar roughness but their WCA varies between 50° and 84° (Table 2).

Table 2: WCA and Rq roughness of copolymers poly(VP-co-V3D3) with different injection fractions of hydrophilic monomer VP.

Injection fractions of VP (%)	WCA (°)	Rq (nm)
62.6	84 ± 0.2	0.5
80.6	73 ± 0.7	0.5
87.2	50 ± 2	0.7

Figure 9 shows that as the injected mass percentage of VP increases, there are fewer adhered bacteria on the surface. This could be due to the increased hydrophilicity of the copolymer. Indeed, with 62 % of VP, the WCA is around 84°. This value decreases to 50° with a mass percentage of 87 % for the hydrophilic precursor. In comparison to the results on poly(V3D3), for which the ratio of cells on cells counted on SiO_2 was close to 1, it seems that the copolymer containing the least amount of VP leads to higher *E. coli* adhesion. On the other hand, when the injected fraction of VP reaches 87 %, the bacterial adhesion appears to be lower than on poly(V3D3) or pp(V3D3).

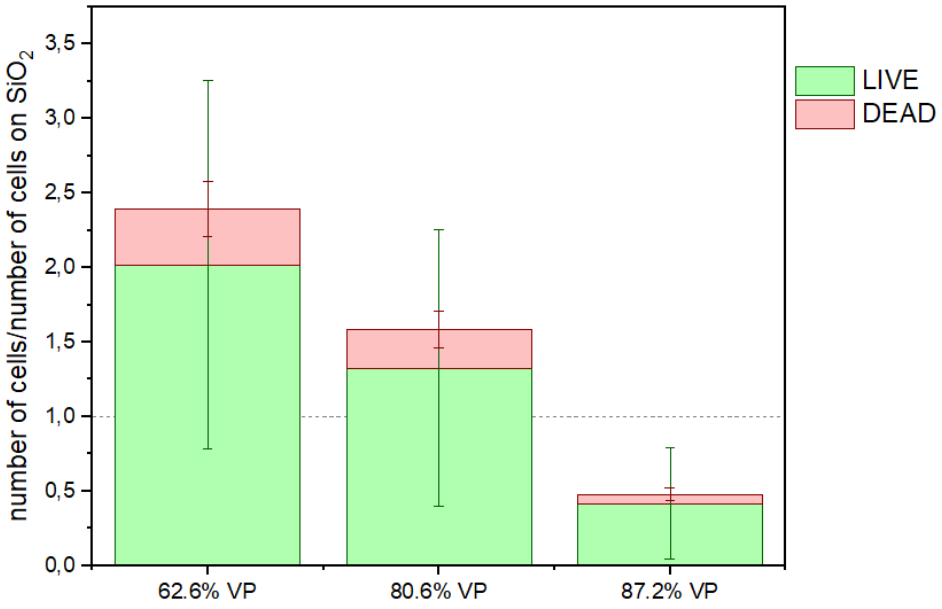

Figure 9: Ratio of the average number of live and dead E. coli *cells per mm² on poly(VP-co-V3D3) with different injected fractions of VP on the average number of live and dead* E. coli *cells per mm² on native SiO_2 after 3 h incubation. The grey dashed line highlights a ratio equal to 1.*

While Figure 9 shows that the majority of *E. coli* cells are alive, this is only in comparison to the native SiO_2 as the average values of live and dead bacteria on poly(VP-co-V3D3) were divided by the average values of live and dead bacteria on the silicon substrate. However, the microscopy images (Figure 10) show that these surfaces are antibacterial as the bacteria stained by SYTO™9 are also stained by PI and can be seen through both filters. Furthermore, as marked by the white arrows, the images obtained in dark field, highlight some bacteria which seem to have a deformed shape and not

with a nice rod shape as *E. coli* normally have. It is unclear whether this represents deformation of the bacterial membrane or agglomeration of cells.

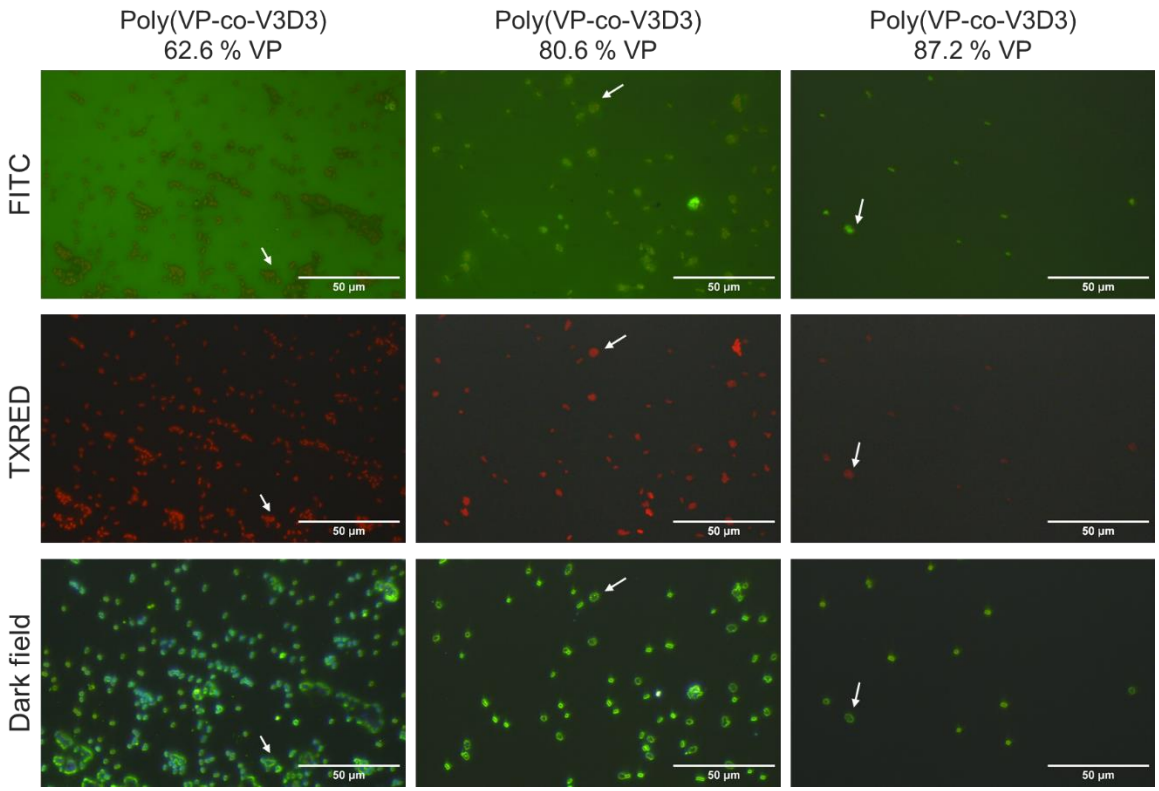

Figure 10: Fluorescence microscopy images of E. coli *on poly(VP-co-V3D3) samples after 3 h incubation. The white arrows highlight the presence of deformed bacteria which could be due to membrane deformation of agglomeration of various cells.*

These results show that *E. coli* adhesion on copolymer poly(VP-co-V3D3) depends on the injected fraction of VP, and consequently the fraction of VP contained in the copolymer film. This could be due to the increased wettability. However, as all films exhibit bactericidal activity, the lower adhesion could also be a consequence of a bactericidal effect.

Similar observations have been made in the literature. Indeed, Guo *et al.* developed a PVP-PDMS-PVP triblock copolymer containing varying amounts of PVP. They showed that the higher the amount of PVP in their copolymer, the lower the adhesion of diatoms. They suggested that this was due to the increasing hydrophilicity of the surfaces, although the lowest WCA obtained in their study was 97°[21].

3.2.Antiadhesive effect of structured surfaces

3.2.1. E. coli *adhesion on plasma-etched surfaces with high roughness*

To study the influence of the surface roughness on the bacterial adhesion, the plasma-etched SiOCH-like polymer resist substrates studied in chapter 5 were submitted to incubation in bacterial suspensions of *E. coli* and fluorescence microscopy was carried out (Figure 11). These microscopy images show that after 3 h incubation, *E. coli* cells adhere individually to the plasma etched polymer

resist. Furthermore, while some cells appear bright green through the FITC filter, most bacteria seem to be dead as they have been stained by PI. Crystallised shapes can be seen in the FITC image of SF_6 (6 sccm) plasma etched polymer resist. It is assumed these are salt crystals from PBS and that they appear here rather than on other surfaces due to poor drying as the PBS can infiltrate the nanostructures and pores of the substrate.

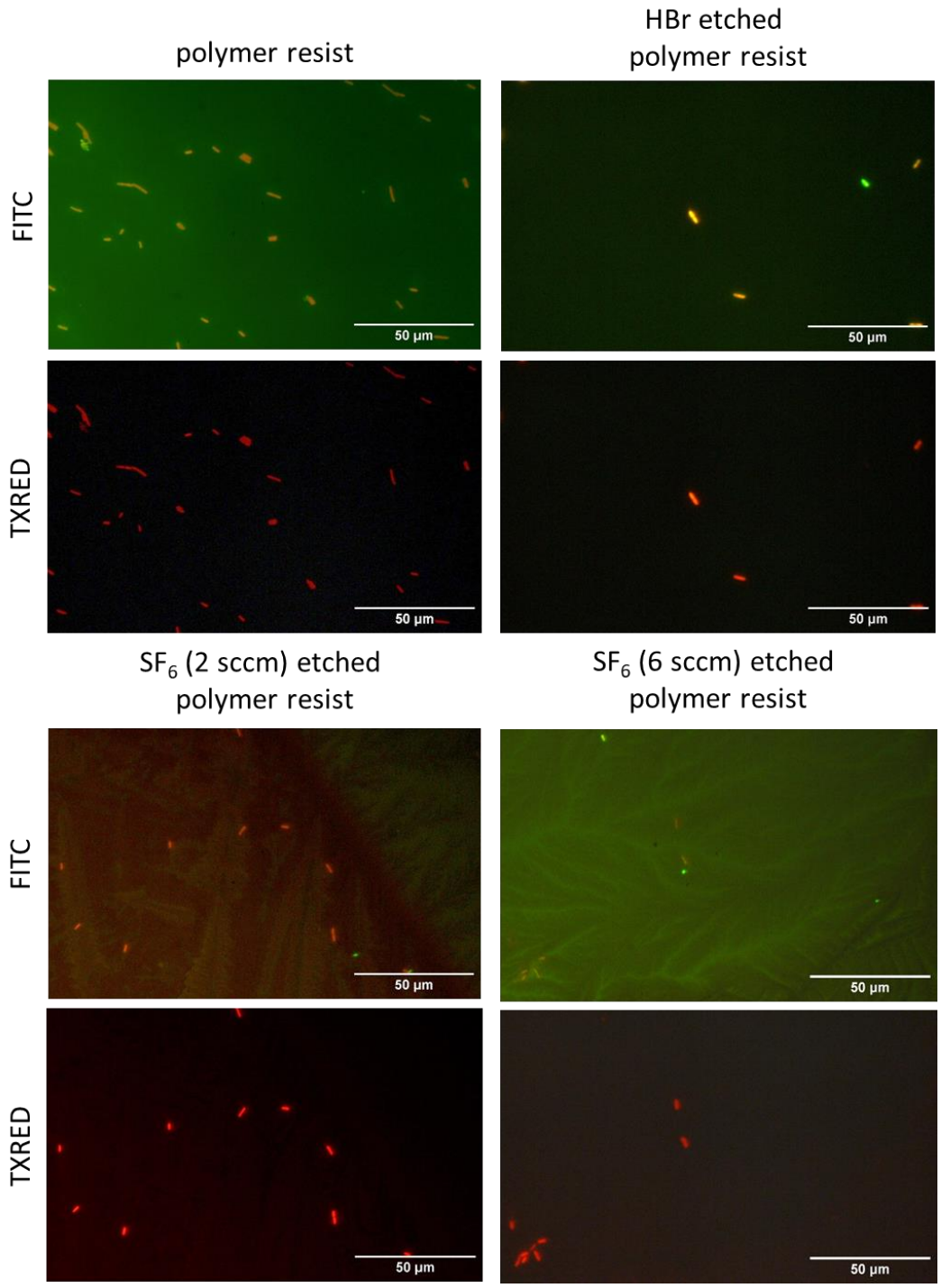

Figure 11: Fluorescence microscopy images of E. coli *on polymer resist with and without plasma etching after 3 h incubation. The green stained cells represent both live and dead bacteria. The red stained cells are dead.*

The average number of cells counted on all microscopy images was divided by the average number of cells on the witness thermal SiO_2 sample which was incubated in the same bacterial suspension. This number is separated into live and dead cells and is represented in Figure 12.

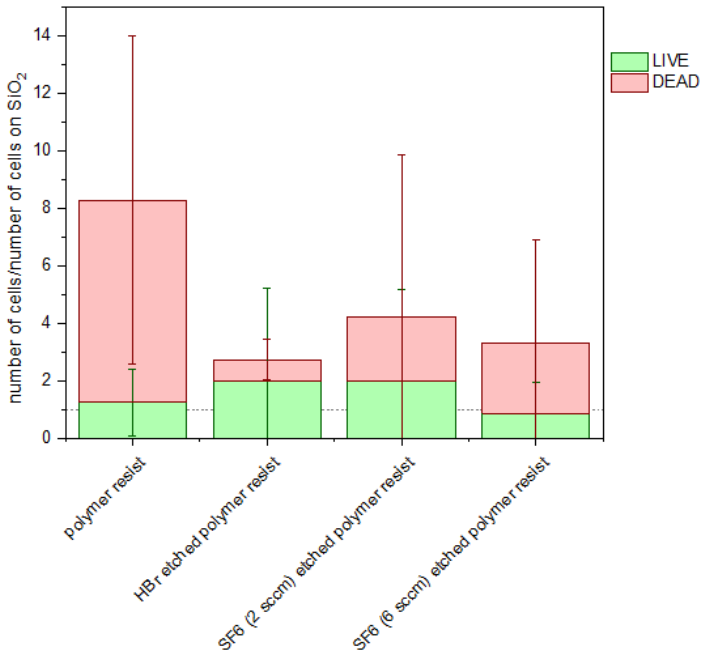

Figure 12: Average number of live and dead E. coli *cells after 3 h incubation on polymer resist with and without HBr, SF_6 (2 sccm) or SF_6 (6 sccm) plasma etching, divided by the average number of live and dead* E. coli *cells on thermal SiO_2 from the same experiment. The grey dashed line highlights a ratio equal to 1.*

It can be seen that the number of cells on the polymer resist substrates, with and without plasma etching, is higher than on SiO_2. The higher adhesion on the plasma-etched surfaces could be explained by the higher Rq roughness (Table 3), as the nanoroughness leads to higher available surface area for the bacteria to attach to[22,23]. However, it has been shown that the adhesion of bacteria on nanostructures highly depends on the specie and its properties (size, shape, motility, membrane…)[24]. Furthermore, this does not explain the highest adhesion which can be seen on the polymer resist before plasma etching which may be due to the different surface chemistry.

Table 3: Chemical composition, WCA and Rq roughness of plasma treated polymer resist.

Sample	Chemical composition	WCA (°)	Rq (nm)
SiO_2 control substrate	SiO_2	51 ± 8	< 0.5
Polymer resist	Organic polymer containing Si/SiO_2	85 ± 0.2	0.6
HBr etched polymer resist	Organic polymer containing less C	33 ± 4	1.3
SF_6 (2 sccm) etched polymer resist	~ SiO_2	44 ± 0.4	2
SF_6 (6 sccm) etched polymer resist	~ SiO_2	34 ± 0.1	6.1

All of these surfaces appear to be antimicrobial as the majority of bacteria observed by fluorescence microscopy is stained with both SYTO™9 and PI (Figure 11). However, there does not seem to be an increase of bactericidal effect as the roughness increases, which could have been the sign of mechanical deformation of the bacterial membranes.

3.2.2. E. coli adhesion on poly(V3D3) and pp(V3D3) functionalised plasma etched surfaces

In this paragraph the effects of combining hydrophobic coatings of poly(V3D3) or pp(V3D3) with SF_6 (6 sccm) plasma etched polymer resist was studied. Indeed, adding one of these thin films led to surfaces with similar roughness but a large range of wettabilities (WCA between 34° and 113°) (Table 4).

Table 4: WCA and Rq roughness of SF_6 (6 sccm) plasma etched polymer resist with and without a coating of poly(V3D3) or pp(V3D3).

Sample	WCA (°)	Rq roughness (nm)
SiO_2	51 ± 8	< 0.5
SF_6 (6 sccm) etched polymer resist	34 ± 0.1	6.1
6 nm of poly(V3D3) on SF_6 (6 sccm) etched polymer resist	113 ± 0.1	7.3
8 nm of pp(V3D3) on SF_6 (6 sccm) etched polymer resist	56 ± 2	4.9

The fluorescence microscopy images (Figure 13) show that while there are some bright green *E. coli* cells on the FITC images, they mostly appear to be dead cells for all three surfaces.

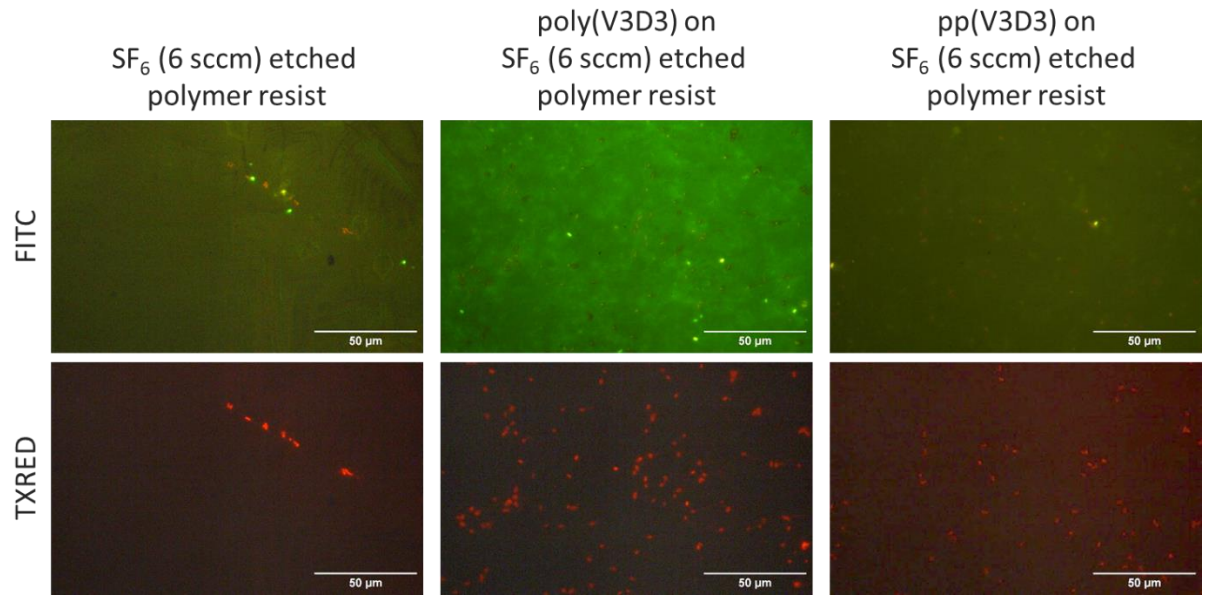

Figure 13: Fluorescence microscopy images of E. coli *on SF_6 (6 sccm) plasma etched polymer resist with and without a coating of poly(V3D3) or pp(V3D3) after 3h incubation.*

The ratio between the average number of live and dead cells on these functionalised nanostructured surfaces and the average number of live and dead cells on SiO_2 shows a higher adhesion of *E. coli* to the surfaces coated with poly(V3D3) or pp(V3D3), with roughly half of the cells being alive and half of them being dead (Figure 14).

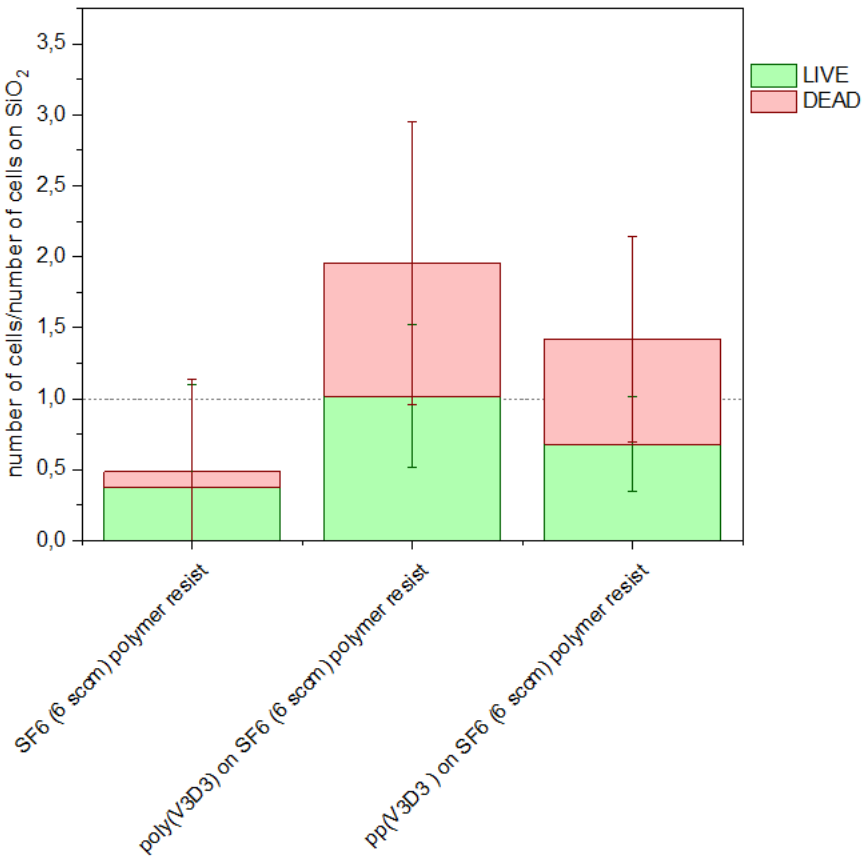

Figure 14: Average number of live and dead E. coli *cells after 3 h incubation on SF_6 (6 sccm) plasma etched polymer resist with and without a coating of poly(V3D3) or pp(V3D3), divided by the average number of live and dead* E. coli *cells on thermal SiO_2 from the same experiment. The grey dashed line highlights a ratio equal to 1. The bacterial suspension was carried out with the preculture step.*

It has previously been shown that when combining nanostructures with a functional coating leading to structured surfaces with variable wettabilities, the bacterial adhesion increases with the WCA until the latter reaches 130° where the Cassie-Baxter effect can be reached[25]. This is coherent with what is being observed here and it would be interesting to develop a similar surface with a WCA > 130° to further confront this observation.

However, the ratio of cells on SF_6 (6 sccm) plasma etched polymer resist on the average number of cells on SiO_2 is lower here than in the previous section which makes any conclusions difficult to affirm. This difference could be due to the preculture step which was carried out here and not previously.

3.2.3. E. coli *adhesion on poly(VP-co-V3D3) functionalised plasma etched surfaces*

SF_6 (6 sccm) plasma etched polymer resist substrates coated with hydrophilic poly(VP-co-V3D3) were also immerged in *E. coli* suspensions to see whether they had an impact on the bacterial adhesion. In this experiment, three samples of SF_6 (6 sccm) plasma etched polymer resist, poly(VP-co-V3D3) on silicon with native SiO_2 and poly(VP-co-V3D3) on SF_6 (6 sccm) plasma etched polymer resist were studied. The copolymer with a VP mass percentage of 87 % was used as it was the most hydrophilic and showed the least bacterial adhesion on planar substrates. However, as it was seen in

chapter 5 and as summarized in Table 5, when combining the copolymer with the plasma etched surface, although both surfaces initially are quite hydrophilic, the WCA increases to 69°.

Table 5: WCA and Rq roughness of SF_6 (6 sccm) plasma etched polymer resist with and without a coating of poly(VP-co-V3D3).

Sample	WCA (°)	Rq roughness (nm)
SiO_2	51 ± 8	< 0.5
SF_6 (6 sccm) etched polymer resist	34 ± 0.1	6.1
poly(VP-co-V3D3)	50 ± 2	0.7
poly(VP-co-V3D3) on SF_6 (6 sccm) etched polymer resist	69 ± 0.8	not measured

The microscopy images (Figure 15) show that the *E. coli* cells adhere to all surfaces individually after 3 h incubation. These bacteria also appear to be predominantly dead as they again appear in both FITC and TXRED images.

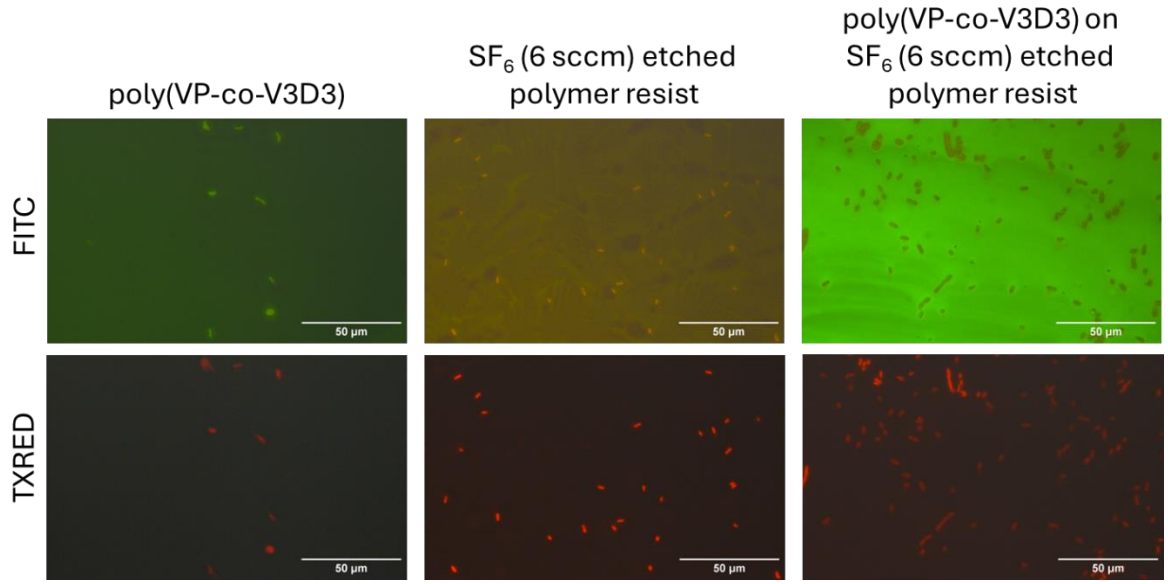

Figure 15: Fluorescence microscopy images of E. coli *on SF_6 (6 sccm) plasma etched polymer resist with and without a coating of poly(VP-co-V3D3) after 3 h incubation.*

In Figure 16, the ratio between average number of cells on these surfaces and the average number of cells on SiO_2, shows that the surface on which *E. coli* appear to adhere to the least is planar poly(VP-co-V3D3) which has a WCA around 50°. The plasma etched surface which is more hydrophilic (WCA = 34°) seems to be less effective at limiting the adhesion of *E. coli*. This could be due to the higher roughness of the plasma etched surface giving more attachment points to the bacteria as mentioned previously[22]. Furthermore, the highest E. coli adhesion appears to occur on the poly(VP-co-V3D3) functionalised SF_6 (6 sccm) plasma etched polymer resist. This could be a result of the decreased wettability observed for these substrates.

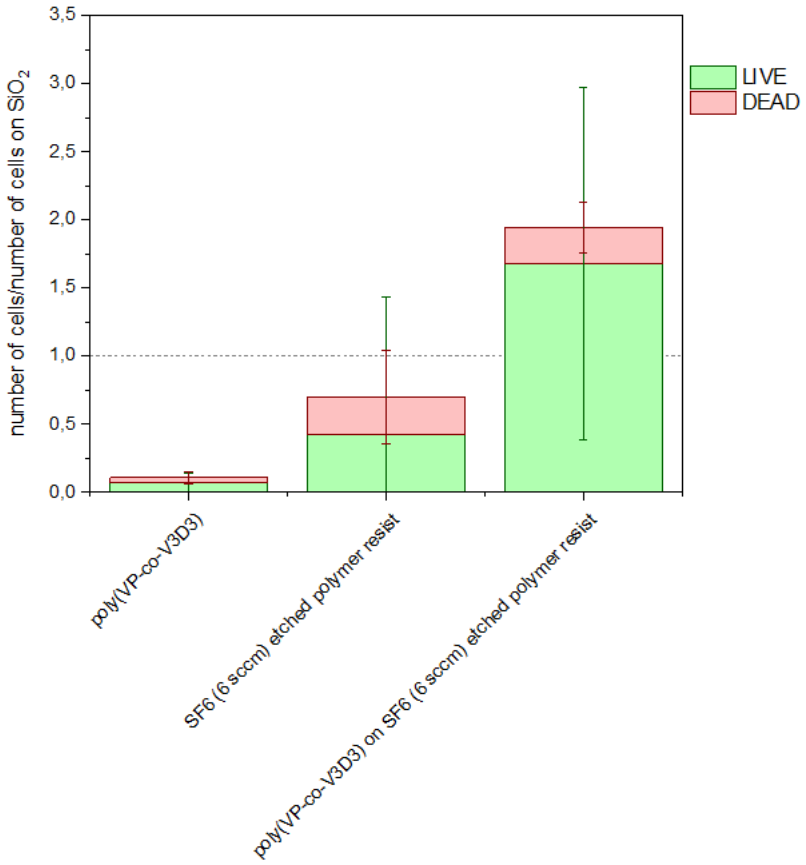

Figure 16: Average number of live and dead E. coli *cells after 3 h incubation on SF_6 (6 sccm) plasma etched polymer resist with and without a coating of poly(VP-co-V3D3), divided by the average number of live and dead* E. coli *cells on native SiO_2 from the same experiment. The grey dashed line highlights a ratio equal to 1. The bacterial suspension was carried out with the preculture step.*

3.2.4. E. coli *adhesion on surfaces with hierarchical structures created by Nano Imprint Lithography and plasma etching*

3.2.4.1. Effect of the size of the microlines

In order to evaluate whether microstructures could influence *E. coli* adhesion, substrates modified by both NIL and SF_6 (6 sccm) plasma etching were studied. This combination was chosen as it led to superhydrophilic surfaces whereas when combining NIL with the other plasma gases, the wettability was not as strong.

On each sample, various zones were observed, with each different zone corresponding to different sized microstructures. First, the microlines will be studied. Both the width of the lines and the space between them varied. However, the density (space/width) is around 2.7 for all areas. As much as possible, the same zones were observed over three different samples from the experiment.

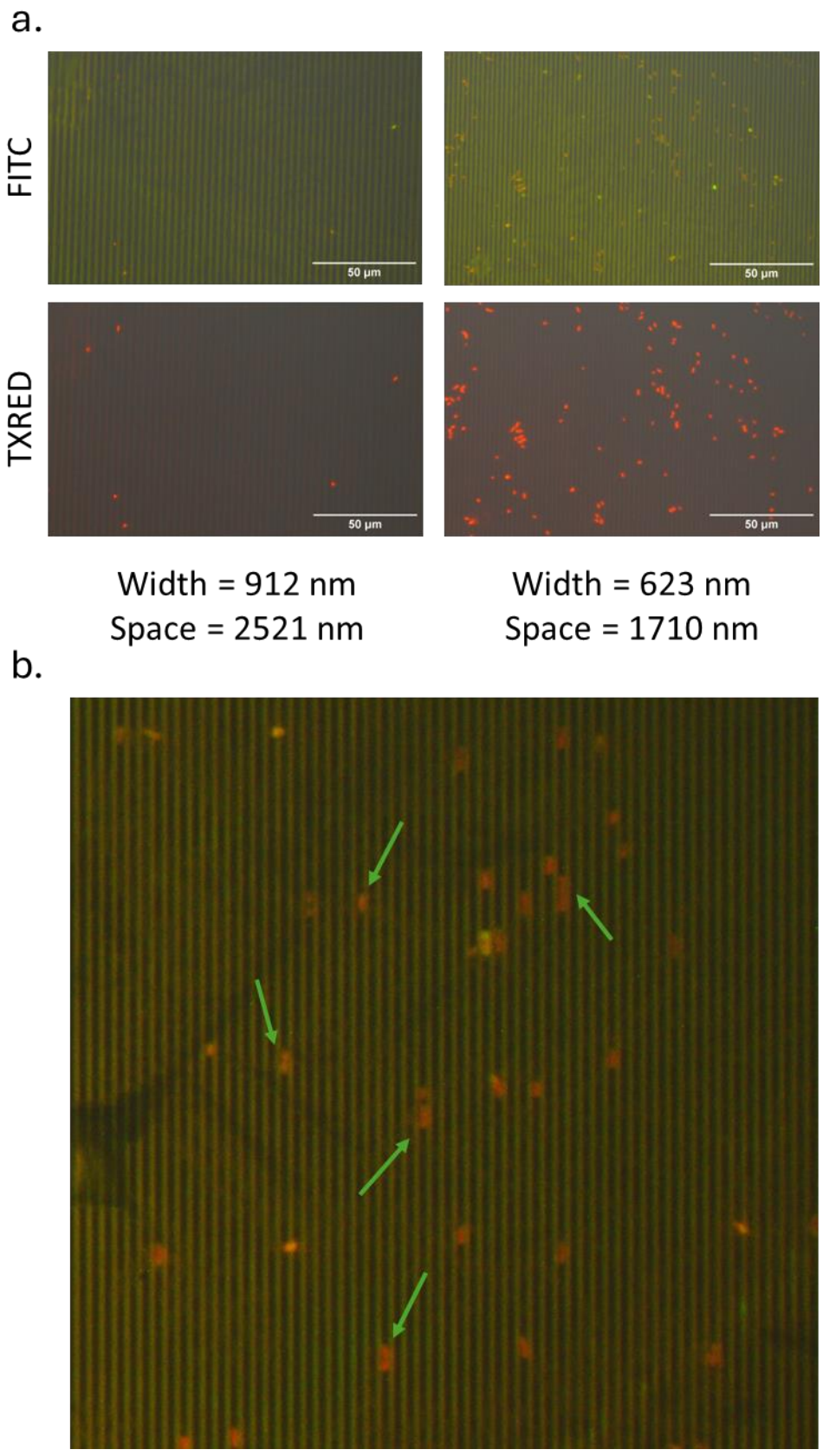

Figure 17: Fluorescence microscopy images of E. coli *after 3 h incubation on polymer resist substrates modified by NIL and SF_6 (6 sccm) plasma etching. a.* E. coli *adhesion and viability on microlines with different sizes, b. Alignment of some* E. coli *cells in between the lines (width = 366 nm; space = 912 nm).*

The fluorescence microscopy images seem to show a difference in *E. coli* adhesion depending on the size of the microlines (Figure 17a). This may be due to the capacity of some lines of specific sizes to trap the rod-shaped bacteria between two lines. This phenomenon can be seen in Figure 17b, highlighted by the green arrows. Indeed, many cells seem to align with the microlines, and more precisely between two lines, presumably then getting trapped in this space.

To see whether the size of these lines and the space between them did have an effect on microbial adhesion, Figure 18 represents the total number of *E. coli* cells/mm² depending on the line width and the space between these lines. Both a and b represent the same data points but with different perspectives. The data points appear diagonally because while the dimensions of the lines and spaces vary, the density (density = width/(width + space)) is always the same. The NIL modified substrates studied in this thesis also present microlines with different densities which could be studied in the future to complete this work.

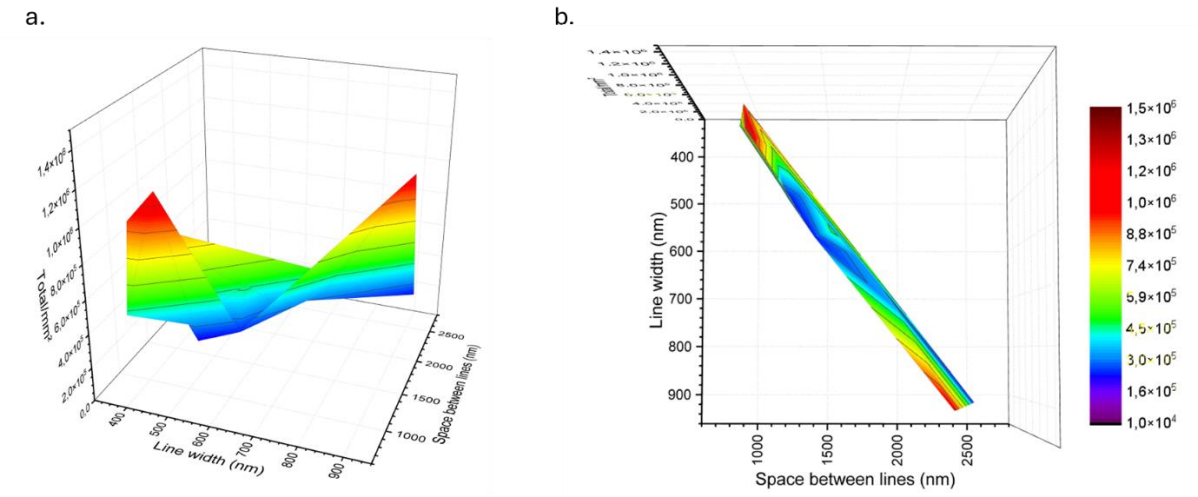

Figure 18: Number of E. coli *cells on polymer resist modified by NIL and SF_6 (6 sccm) plasma etching. The microstructures created by NIL were lines which had various widths and spacing between one another but with the same density. a. represents an angle view and b. represents a view from the top of the same results.*

This data reveals a minimum number of *E. coli* cells in zones with lines between 450 and 700 nm, and a spacing between 1 200 and 1 800 nm. For lines under 450 nm wide and a spacing under 1 200 nm, the dimensions may be too small in comparison to the size of the *E. coli* cells (which is around 5 x 0.8 µm) to be effective. As the spacing between two lines increases, more bacteria may be able to get trapped in between like in Figure 17b. Indeed, Lou *et al.* showed that when the dimensions of microstructures were higher than the foulant's, antibiofouling was decreased[26].

3.2.4.2. Microlines functionalised with hydrophobic thin films

When functionalising these SF_6 (6 sccm) plasma etched microstructured surfaces with poly(V3D3) or pp(V3D3), while the bacteria can be seen by eye in the green fluorescent microscopy images (Figure 19), the contrast between the bacteria and the microstructures themselves is not high enough for the software to be able to identify and count the bacteria. Therefore, the number of dead bacteria on these surfaces will be presented Figure 20 in order to give an idea of the bacterial adhesion on these surfaces.

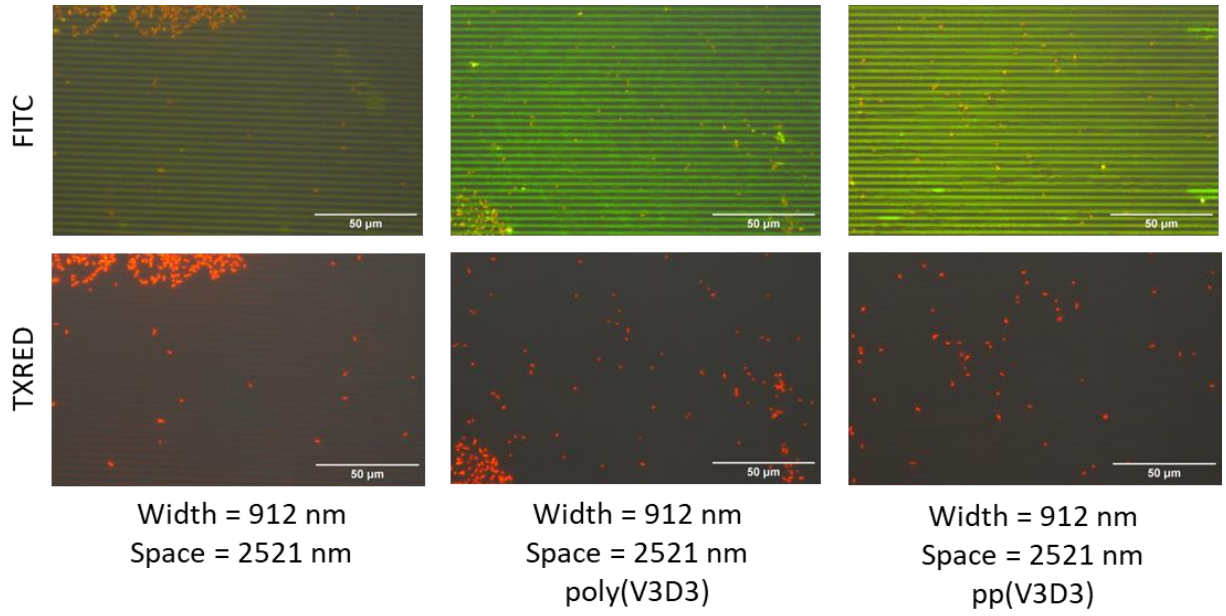

Figure 19: Fluorescence microscopy images of E. coli *after 3 h incubation on polymer resist substrate modified by NIL and SF_6 (6 sccm) plasma etching with and without a coating of poly(V3D3) or pp(V3D3).*

The fluorescence microscopy images show that while most *E. coli* cells adhere individually to all three surfaces, in some cases, they can agglomerate as seen at the top left corner of the images of the surface without functionalisation. This phenomenon can also be seen on the bottom left corner of the images of the surface coated with poly(V3D3). While no such behaviour can be seen on the pp(V3D3) coated surfaces, it is likely that this is only due to the random imaging of a small zone of the surface, and not a consequence of the different surface chemistry.

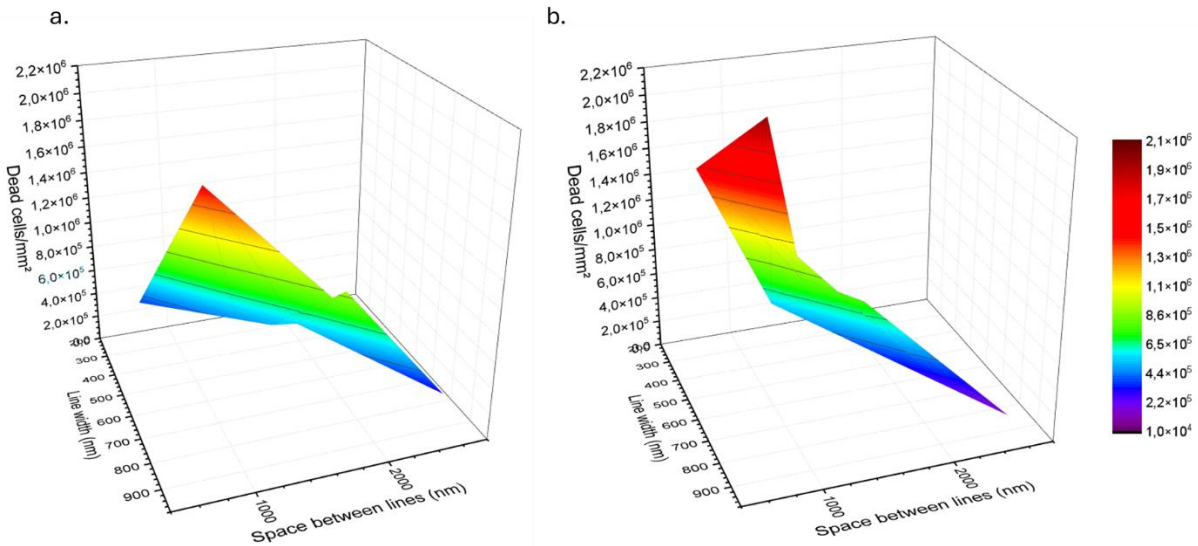

Figure 20: Number of dead E. coli *cells on polymer resist modified by NIL and SF_6 (6 sccm) plasma etching with a coating of a. poly(V3D3) or b. pp(V3D3), after 3 h incubation. The microstructures created by NIL were lines which had various widths and spacing between one another but with the same density.*

These results show that there are fewer bacteria adhered to the substrates functionalised with poly(V3D3) than with pp(V3D3). This could be an effect of the higher hydrophobicity of these surfaces and is also coherent with the observations drawn on planar surfaces functionalised with the same coatings (section 3.1.1.1) which was attributed to the higher carbon content of the conventional polymer[15]. Similarly to the observed behaviour on the uncoated structures, there seem to be a higher number of bacteria on lines with a width under 450 nm and a spacing under 1 200 nm.

3.2.4.3. Effect of microsized pillars on the adhesion of *E. coli*

As some of the microstructures created by NIL were pillars, with varying size, shape and configuration, fluorescence microscopy images were also taken on some of these zones to evaluate their impact on *E. coli* adhesion. As it can been seen in Figure 21a and b, while some bacteria can get lodged between the pillars, they mostly tend to be found on top of the pillars.

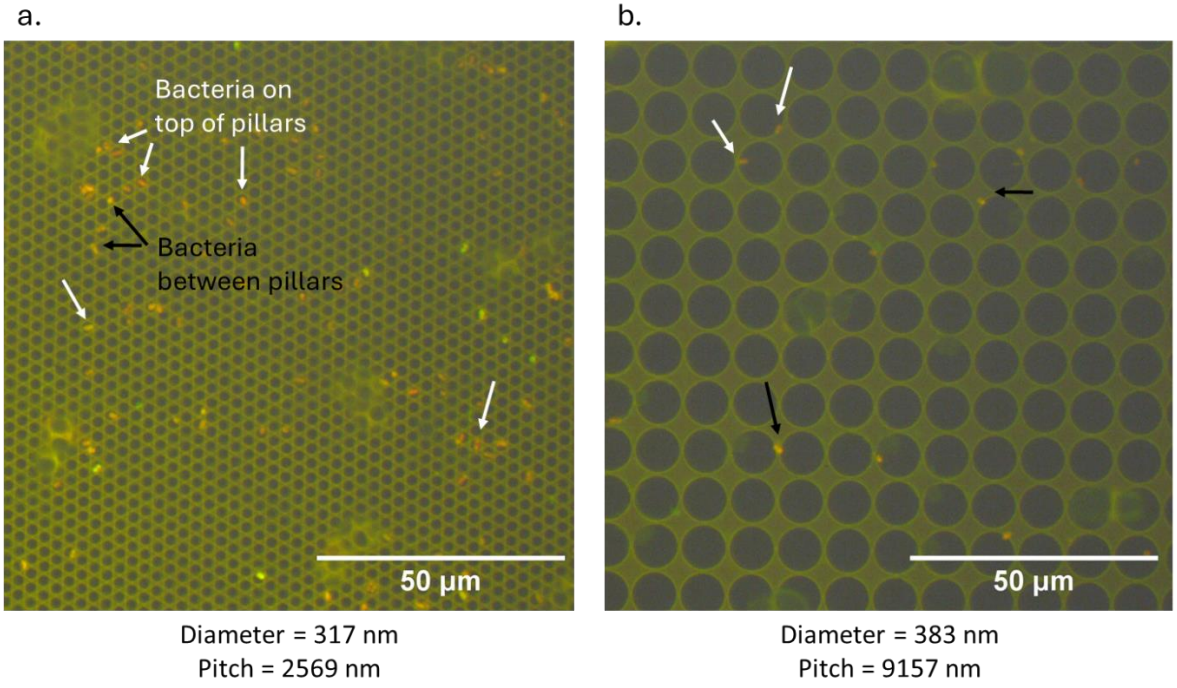

Figure 21: Fluorescence microscopy images of E. coli *after 3 h incubation on polymer resist substrates modified by NIL and SF_6 (6 sccm) plasma etching. These images were obtained with the FITC filter. The dimensions of the pillars were: a. diameter = 317 nm and pitch = 2 569 nm and b. diameter = 383 nm and pitch = 9 157 nm. The black arrows highlight bacteria lodged between pillars and the white arrows show bacteria on the top of pillars.*

Quantification of the number of cells on these surfaces seems to show a decrease in number of bacteria with the size of the pitch, especially on the surfaces without an additional polymer coating. Repeating the manipulations and increasing the statistics and the simultaneous variation in diameter and width would surely lead to more solid conclusions.

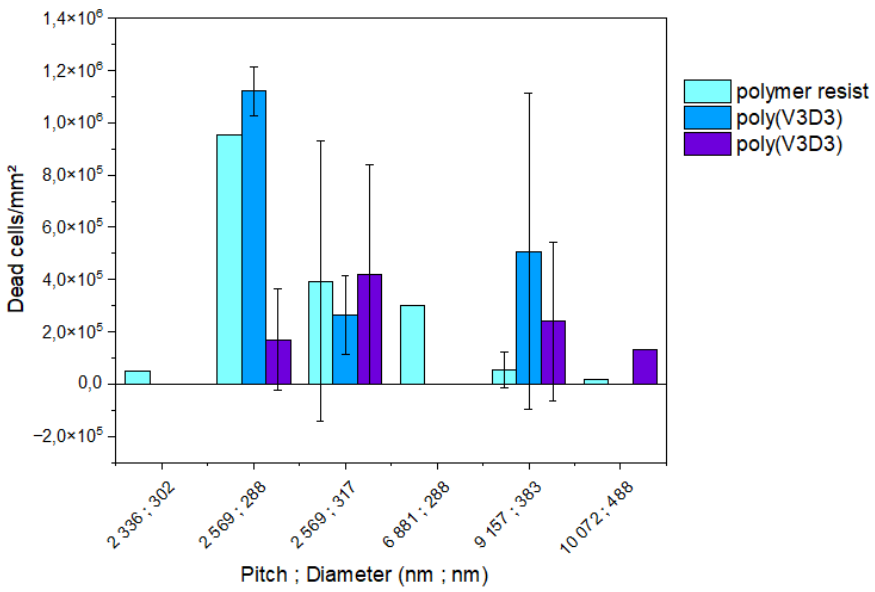

Figure 22: Number of dead E. coli *cells after 3 h incubation on polymer resist modified by NIL and SF_6 (6 sccm) plasma etching with and without a coating of poly(V3D3) or pp(V3D3) as a function of the diameter and width of the microsized pillars.*

The study of surfaces with microscale lines and pillars of different dimensions can rapidly show the promise of a certain structure to decrease bacterial adhesion. For example, here, it seems that thin lines that are close together will not lead to the most effective antibiofouling surfaces. To ameliorate statistical analysis, the mould's design could be modified allowing bigger surfaces with the same microstructure design on each sample. Indeed, here, as each 1 cm² sample only has 2 small areas with same line dimensions (and only one type of pillar per cm²), even with 3 samples per experiment, the total area covered by the same dimension structures remains very small (300 µm²).

3.3.Summarising *E. coli* adhesion on our functionalised surfaces

Throughout this work, surfaces were created through various combinations of plasma etching and thin film deposition. This gave a variety of different substrates with specific chemical composition, roughness and wettability.

The following figure is a summary of all the results discussed in this chapter, minor those on the microstructures. It represents the average number of cells adhered to the various surfaces divided by the average number of cells found on SiO_2 from the same experiment, as a function of the Rq roughness and the WCA of the surface. This shows that for a given WCA, increasing the nanoroughness of the surface generally leads to higher bacterial adhesion. This could be due to an increasing amount of attachment points the bacteria can use to anchor themselves to the surface. For the planar surfaces studied here, it seems that the bacterial adhesion decreases as the surface becomes more hydrophilic. It also seems that the chemistry of the surface has a non negligeable effect with the polymer resist being the most incline to *E. coli* adhesion in comparison to the other materials. The planar poly(VP-co-V3D3) deposited with an injection fraction of VP of 87 % is the most antiadhesive in these conditions.

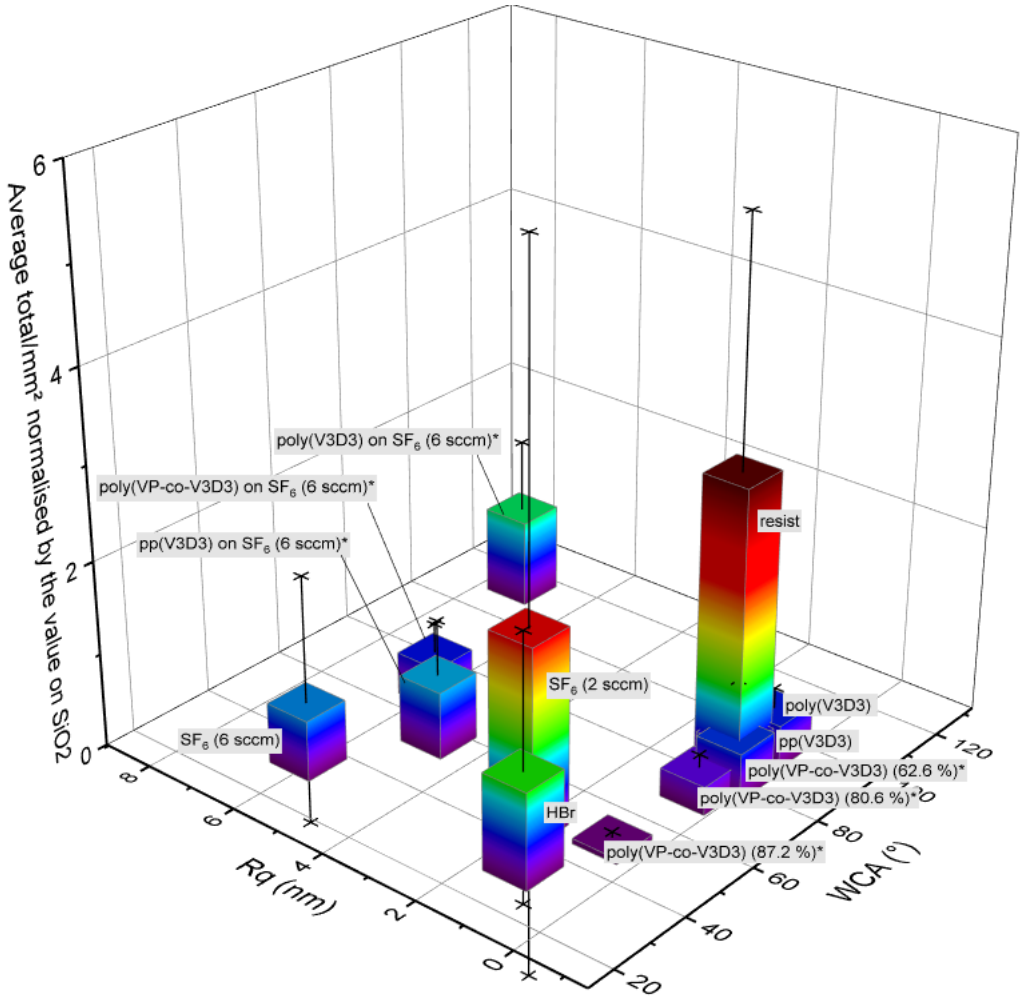

Figure 23: Graphical summary of the number of E. coli *cells depending on the surface wettability and roughness after 3 h incubation. For the substrates appearing in various experiments, the average value is given. The * correspond to the experiments where a preculture step was added.*

4. Conclusions

In this work, various surfaces were studied to evaluate their impact on bacteria, and more precisely on *E. coli* adhesion and viability. It showed the potential of our nontoxic antibiofouling surfaces which were developed without the use of fluorine or metallic nanoparticles. By functionalising planar, rough and microstructured substrates with polymer thin films, a systematic study could be carried out.

First of all, this study highlighted the importance of surface chemistry to control bacterial adhesion. Indeed, as it was seen when comparing poly(V3D3) and pp(V3D3) functionalised surfaces, lower adhesion could be seen for the conventional polymer poly(V3D3). While there is a slight WCA difference between the two coatings, it is thought that the impacting property is the amount of carbon found in each polymer. This is a result of the deposition method, as plasma polymerisation leads to a coating with a lower carbon content than iCVD as it was seen previously in this manuscript.

Concerning copolymer poly(VP-co-V3D3), by increasing the fraction of VP in the final coating, and consequently reaching lower wettability, *E. coli* adhesion was decreased. This shows the potential of iCVD for antimicrobial coatings as the technique allows fine tuning of the final thin film.

Concerning the microstructures studied in this work, it was shown that the dimensions of the structures could influence the bacterial adhesion, notably with cells getting trapped in between lines when the spacing is too wide. Only a small proportion of the NIL fabricated substrates were studied here. Their controlled design would allow the study of lines and pillars with different sizes and densities in future work although creating a mould with a larger surface of the same pattern would allow better statistical analysis.

This study also showed, with the incubation tests over various times, that two bacterial species can have a very different response to the same surface. Indeed, *S. epidermidis* adhesion was enhanced on poly(V3D3) whereas the same surface limited adhesion of *E. coli* after 48 h. Therefore, when developing an antimicrobial surface, it is very important to specify the application and environment prior to development. Furthermore, the microbiology assay carried out here only assessed the bacterial adhesion on the different surfaces. The potential contact-killing effect of the different chemistries on the surrounding bacteria could also be studied by collecting and reincubating the supernatant.

Throughout this work, the main surface properties that were studied were chemistry, wettability and roughness. However, it has also been shown in the literature that others, such as the surface charge[27] and stiffness[28] must be taken into account when developing antibiofouling surfaces. Different culture medias can also have a significant effect on bacterial adhesion[29] and could be studied in future work.

5. Bibliography

(1) Sharma, G.; Sharma, S.; Sharma, P.; Chandola, D.; Dang, S.; Gupta, S.; Gabrani, R. Escherichia Coli Biofilm: Development and Therapeutic Strategies. *Journam of Applied Microbiology.* **2016**, *121* (2), 309–319. https://doi.org/10.1111/jam.13078.

(2) Salo, J.; Sevander, J.-J.; Tapiainen, T.; Ikäheimo, I.; Pokka, T.; Koskela, M.; Uhari, M. Biofilm Formation by Escherichia Coli Isolated from Patients with Urinary Tract Infections. *Clinical Nephrology.* **2009**, *71* (5), 501–507. https://doi.org/10.5414/cnp71501.

(3) *Escherichia coli (Migula) Castellani and Chalmers - 8739 | ATCC*. https://www.atcc.org/products/8739 (accessed 2024-03-14).

(4) Sabaté Brescó, M.; Harris, L. G.; Thompson, K.; Stanic, B.; Morgenstern, M.; O'Mahony, L.; Richards, R. G.; Moriarty, T. F. Pathogenic Mechanisms and Host Interactions in Staphylococcus Epidermidis Device-Related Infection. *Frontiers in Microbiology.* **2017**, *8*. https://doi.org/10.3389/fmicb.2017.01401.

(5) *Staphylocoque*. Institut Pasteur. https://www.pasteur.fr/fr/centre-medical/fiches-maladies/staphylocoque (accessed 2024-03-20).

(6) *14990 - 14990 | ATCC*. https://www.atcc.org/products/14990 (accessed 2024-03-20).

(7) Sjollema, J.; Zaat, S. A. J.; Fontaine, V.; Ramstedt, M.; Luginbuehl, R.; Thevissen, K.; Li, J.; Van Der Mei, H. C.; Busscher, H. J. In Vitro Methods for the Evaluation of Antimicrobial Surface Designs. *Acta Biomaterialia.* **2018**, *70*, 12–24. https://doi.org/10.1016/j.actbio.2018.02.001.

(8) Stalet, M. Protections Anti-Microbiennes : Combinaison de La Fonctionnalisation et de La Nano-Structuration Pour Explorer Les Interactions Cellule/Surface, Thèse de doctorat, Université Grenoble Alpes et Université de Sherbrooke, **2024**.

(9) *Mueller Hinton Broth suitable for microbiology, NutriSelect® Plus*. http://www.sigmaaldrich.com/ (accessed 2024-03-20).

(10) Humblot, V.; Yala, J.-F.; Thebault, P.; Boukerma, K.; Héquet, A.; Berjeaud, J.-M.; Pradier, C.-M. The Antibacterial Activity of Magainin I Immobilized onto Mixed Thiols Self-Assembled Monolayers. *Biomaterials* **2009**, *30* (21), 3503–3512. https://doi.org/10.1016/j.biomaterials.2009.03.025.

(11) Bouloussa, H.; Saleh-Mghir, A.; Valotteau, C.; Cherifi, C.; Hafsia, N.; Cohen-Solal, M.; Court, C.; Crémieux, A.-C.; Humblot, V. A Graftable Quaternary Ammonium Biocidal Polymer Reduces Biofilm Formation and Ensures Biocompatibility of Medical Devices. *Advances Materials and Interfaces* **2021**, *8* (5), 2001516. https://doi.org/10.1002/admi.202001516.

(12) *1X Phosphate-Buffered Saline (PBS) Recipe Calculator*. https://www.sigmaaldrich.com/FR/fr/support/calculators-and-apps/1x-phosphate-buffered-saline (accessed 2024-03-20).

(13) *LIVE/DEAD™* Bac*Light™* *Bacterial Viability Kits*. https://www.thermofisher.com/order/catalog/product/fr/fr/L7012 (accessed 2024-03-14).

(14) Saulou, C.; Despax, B.; Raynaud, P.; Zanna, S.; Marcus, P.; Mercier-Bonin, M. Plasma Deposition of Organosilicon Polymer Thin Films with Embedded Nanosilver for Prevention of Microbial Adhesion. *Applied Surface Science.* **2009**, *256* (3), S35–S39. https://doi.org/10.1016/j.apsusc.2009.04.118.

(15) Navabpour, P.; Teer, D.; Su, X.; Liu, C.; Wang, S.; Zhao, Q.; Donik, C.; Kocijan, A.; Jenko, M. Optimisation of the Properties of Siloxane Coatings as Anti-Biofouling Coatings: Comparison of PACVD and Hybrid PACVD-PVD Coatings. *Surface and Coatings Technology.* **2010**, *204* (20), 3188–3195. https://doi.org/10.1016/j.surfcoat.2010.03.011.

(16) *Bacteria - Reproduction, Nutrition, Environment | Britannica*. https://www.britannica.com/science/bacteria/Growth-of-bacterial-populations (accessed 2024-04-16).

(17) Durand, G. Caractérisation, Épidémiologie et Pathogénie d'un Clone de Staphylococcus Aureus Résistant à La Méticilline Portant Le Gène de La Toxine Du Choc Toxique Staphylococcique (TSST-1), Thèse de doctorat, Université Claude Bernard Lyon, **2006**.

(18) Raulio, M.; Järn, M.; Ahola, J.; Peltonen, J.; Rosenholm, J. B.; Tervakangas, S.; Kolehmainen, J.; Ruokolainen, T.; Narko, P.; Salkinoja-Salonen, M. Microbe Repelling Coated Stainless Steel Analysed by Field Emission Scanning Electron Microscopy and Physicochemical Methods. *Journal of Industrial Microbiology and Biotechnology.* **2008**, *35* (7), 751–760. https://doi.org/10.1007/s10295-008-0343-8.

(19) Chen, C.; Enrico, A.; Pettersson, T.; Ek, M.; Herland, A.; Niklaus, F.; Stemme, G.; Wagberg, L. Bactericidal Surfaces Prepared by Femtosecond Laser Patterning and Layer-by-Layer Polyelectrolyte Coating | Elsevier Enhanced Reader. *Journal of Colloid and Interface Science.* **2020**, *575*, 286–297. https://doi.org/10.1016/j.jcis.2020.04.107.

(20) Oopath, S. V.; Baji, A.; Abtahi, M.; Luu, T. Q.; Vasilev, K.; Truong, V. K. Nature-Inspired Biomimetic Surfaces for Controlling Bacterial Attachment and Biofilm Development. *Advanced Materials and Interfaces* **2023**, *n/a* (n/a), 2201425. https://doi.org/10.1002/admi.202201425.

(21) Guo, H.; Liu, X.; Zhao, W.; Xie, C.; Zhu, Y.; Wen, C.; Li, Q.; Sui, X.; Yang, J.; Zhang, L. A Polyvinylpyrrolidone-Based Surface-Active Copolymer for an Effective Marine Antifouling Coating. *Progress in Organic Coatings.* **2021**, *150*, 105975. https://doi.org/10.1016/j.porgcoat.2020.105975.

(22) Vellwock, A. E.; Yao, H. Biomimetic and Bioinspired Surface Topographies as a Green Strategy for Combating Biofouling: A Review. *Bioinspiration & Biomimetics.* **2021**, *16* (4), 041003. https://doi.org/10.1088/1748-3190/ac060f.

(23) Aguilar-Sanchez, A.; Jalvo, B.; Mautner, A.; Rissanen, V.; Kontturi, K. S.; Abdelhamid, H. N.; Tammelin, T.; Mathew, A. P. Charged Ultrafiltration Membranes Based on TEMPO-Oxidized Cellulose Nanofibrils/Poly(Vinyl Alcohol) Antifouling Coating. *RSC Advances.* **2021**, *11* (12), 6859–6868. https://doi.org/10.1039/D0RA10220B.

(24) Doll, P. W.; Doll, K.; Winkel, A.; Thelen, R.; Ahrens, R.; Stiesch, M.; Guber, A. E. Influence of the Available Surface Area and Cell Elasticity on Bacterial Adhesion Forces on Highly Ordered Silicon Nanopillars. *ACS Omega* **2022**. https://doi.org/10.1021/acsomega.2c00356.

(25) Dou, X.-Q.; Zhang, D.; Feng, C.; Jiang, L. Bioinspired Hierarchical Surface Structures with Tunable Wettability for Regulating Bacteria Adhesion. *ACS Nano* **2015**, *9* (11), 10664–10672. https://doi.org/10.1021/acsnano.5b04231.

(26) Lou, T.; Bai, X.; He, X.; Yuan, C. Antifouling Performance Analysis of Peptide-Modified Glass Microstructural Surfaces. *Applied Surface Science.* **2020**, 148384. https://doi.org/10.1016/j.apsusc.2020.148384.

(27) Kulaga, E. Antimicrobial Coatings for Soft Materials, Thèse de doctorat, Université de Haute Alsace, 2014.

(28) Vigué, A.; Vautier, D.; Kaytoue, A.; Senger, B.; Arntz, Y.; Ball, V.; Ben Mlouka, A.; Gribova, V.; Hajjar-Garreau, S.; Hardouin, J.; Jouenne, T.; Lavalle, P.; Ploux, L. Escherichia Coli Biofilm Formation, Motion and Protein Patterns on Hyaluronic Acid and Polydimethylsiloxane Depend on Surface Stiffness. *Journal of Functional Biomaterials.* **2022**, *13* (4), 237. https://doi.org/10.3390/jfb13040237.

(29) Marguier, A.; Poulin, N.; Soraru, C.; Vonna, L.; Hajjar-Garreau, S.; Kunemann, P.; Airoudj, A.; Mertz, G.; Bardon, J.; Delmée, M.; Roucoules, V.; Ruch, D.; Ploux, L. Bacterial Colonization of Low-Wettable Surfaces Is Driven by Culture Conditions and Topography. *Adv. Mater. Interfaces* **2020**, *n/a* (n/a), 2000179. https://doi.org/10.1002/admi.202000179.

General conclusions and perspectives

This thesis explored, from a material science point of view, the development and characterisation of antibiofouling surfaces created by combining polymer thin film coatings and topography. A systematic study of certain surface properties such as chemistry, wettability and roughness was carried out with the aim of determining how they would influence bacterial adhesion.

More precisely, after describing in the first chapter, the state of the art on hydrophobic and hydrophilic chemical compounds associated with structures for antimicrobial surfaces, focus was set on depositing polymers using the innovative initiated Chemical Vapour Deposition (iCVD) method. Various polymers were studied: hydrophobic poly(V3D3) was compared to plasma polymer pp(V3D3) which was deposited by Dielectric Barrier Discharge Cold Atmospheric Plasma (DBD-CAP) for the first time. Superhydrophilic conventional polymer PVP was also deposited by iCVD before using V3D3 as a crosslinking agent to create copolymer poly(VP-co-V3D3). To our knowledge, this copolymer had never before been developed and deposited by iCVD or any other technique. These deposition processes were presented in the second chapter along with the characterisation methods which were used.

The third chapter focused on the deposition of organosilicon polymer poly(V3D3). The conventional polymer, deposited by iCVD, was compared to plasma polymer pp(V3D3). While both techniques led to smooth coatings, other surface properties were modified by the deposition technique. Conventional poly(V3D3) had a higher WCA which was attributed to the higher carbon content of the thin film. Indeed, as iCVD relies on free radical polymerisation, poly(V3D3) conserves its siloxane rings from the V3D3 monomer and contains a PE-like backbone with Si atoms being di-substituted by O. On the other hand, plasma polymerisation leads to the modification of the functional groups of the monomer, the Si becomes tri-substituted by O as less C is found in the final film, and crosslinking occurs without any controlled structure.

The fourth chapter of this manuscript focused on the development of superhydrophilic PVP by iCVD. It was shown that a two-regime mechanism could be observed when considering the thin film growth kinetics. While this mechanism has previously been observed[1] it is not yet widely discussed in the iCVD community. The resulting smooth thin films exhibit very good wettability. However, their solubility impedes their use as antibiofouling coatings. In order to obtain an insoluble hydrophilic polymer, V3D3 was used as a crosslinking agent. With its slower kinetics than acrylates, which are often used as crosslinkers, and its three vinyl bonds, V3D3 offers ideal properties for a crosslinking agent. By using FTIR spectroscopy, it was shown that it is possible to tune the fraction of each monomer in the copolymer by varying their injected fractions. Furthermore, application of the Fineman Ross equation allowed the evaluation of the reactivity ratios for each monomer and underlined the formation of a random copolymer. These copolymers showed increasing wettability with a higher proportion of hydrophilic VP and were insoluble in PBS, making them good candidates for antibiofouling surfaces.

Chapter 5 presented and discussed the use of hierarchical structures with microscale lines and pillars fabricated by NIL and nanoscale roughness achieved by plasma etching. It was shown that different plasma gases led to a different level of roughness and consequently various wettabilities. The plasma etched surfaces were then functionalised with the polymer thin films studied in this work and it was shown that for hydrophobic poly(V3D3), the Wenzel effect could be achieved, thus increasing the hydrophobicity, as long as the coating was thin enough to conserve the surface roughness. The hydrophobicity was further increased when poly(V3D3) was coated onto microstructures, presumably as the Cassie-Baxter effect was achieved and air bubbles were trapped between the structures, inhibiting the water droplet from spreading. However, when functionalising these structures with hydrophilic poly(VP-co-V3D3), the wettability was not increased as predicted by the Wenzel effect. This highlights the complexity of combining thin films and topography for antibiofouling applications as the surface properties of the final substrate depend on many factors such as the choice of monomer, the

method of deposition, the thickness of the thin film, the nanoscale roughness and the size and shape of microstructures.

This was further seen in chapter 6 where these surfaces were incubated with bacterial suspensions to study the influence of the surface properties on the adhesion and viability of *E. coli* and *S. epidermidis*. It was shown that poly(V3D3) was slightly more effective than pp(V3D3) at reducing *E. coli* adhesion. This could be due to the slightly higher hydrophobicity, although it is also thought to be a result of the higher carbon content in the conventional polymer. Furthermore, this same polymer showed limited adhesion of *E. coli* in comparison to SiO_2 after an incubation time over 6 h. The contrary was observed with *S. epidermidis*, highlighting the necessity to adapt antibiofouling surfaces to the environment in which they shall be found. Concerning the copolymer poly(VP-co-V3D3), the adhesion of *E. coli* cells was reduced as the VP fraction in the copolymer increased, consequently reducing the WCA. This chapter also showed the importance of microstructure size which must be adapted to inhibit bacteria getting trapped between microstructures.

The multidisciplinary aspect of this thesis and the various conclusions that have been drawn lead to different perspectives which can be considered to prolong this work.

Optimising the DBD-CAP deposition of pp(V3D3)

As it was seen in the third chapter of this manuscript, while AFM imaging shows a low roughness for DBD-CAP deposited plasma polymer pp(V3D3) on planar silicon wafers, optical microscopy revealed the appearance of the coffee ring effect, which seemed to increase with the thickness of the coating due to having to repeat the plasma torch movement to increase the thin film's thickness. By adjusting the deposition parameters, for example by increasing the speed of the torch, or reducing the amount of injected precursor, it is believed that this coffee ring effect could be decreased.

Moreover, while spectroscopic ellipsometry data could be fit correctly over all coatings, the appearance of lines following the plasma torch pattern led to believe that as the overall thickness increases, it may become inhomogeneous. These disparities may also be reduced by adjusting the deposition parameters such as the torch movement pattern, the speed of movement and the distance between the torch outlet and the substrate. However, concerning the last option, it has been shown that a higher distance can lead to increased roughness[2]. Therefore, a design of experiments would be necessary to determine the factors with the highest impact and optimise the deposition process of pp(V3D3).

Increasing the wettability of copolymer poly(VP-co-V3D3)

As it was shown in chapter 4, the iCVD deposition of copolymers was made possible by co-injecting two monomers simultaneously. In this work, V3D3 was injected alongside VP in order to crosslink the hydrophilic thin film and make it insoluble and applicable to antibiofouling surfaces. It was shown that by increasing the fraction of VP in the copolymer, the hydrophilicity could be increased. However, in the studied conditions, the lowest WCA that was obtained was around 50°.

To further increase the wettability of these copolymer thin films, it would be necessary to increase the injected fraction of VP. To do so, without reaching a saturation ratio $P_m/P_{sat} > 1$ for VP, the flow of carrier gas used for both precursors must be modified. As this fraction is modified, varying the

pressure and temperature of the chamber can allow to tune the saturation ratios P_m/P_{sat} for each monomer. Ideally, keeping the highest possible P_m/P_{sat} for VP and the lowest possible for V3D3. This would favour the adsorption of VP in comparison to V3D3 on the surface and should increase the wettability of the coating.

Furthermore, gradient copolymers could be developed with the intention of increasing their robustness while conserving superhydrophilicity. This could be achieved by depositing a layer of crosslinked poly(VP-co-V3D3) before reducing the injection of V3D3 until only VP is flowing. It would be interesting to study this path to see whether superhydrophilicity and insolubility could be reached.

Further characterisation of surface properties

In this study, the main surface properties which were studied were chemical composition, roughness and wettability. However, it has also been shown that other factors can be impacting on bacterial adhesion. For example, charged surfaces can destabilize bacterial membranes, consequently killing the cells. Furthermore, it has also been noted that surface stiffness[3] can have an impact on bacterial adhesion. To carry out a full study of the influence of a given surface on bacterial adhesion and viability, zeta potential and nanoindentation or AFM can be used to analyse the surface charge and stiffness respectively. These surface characterisations would be complementary to those which were carried out in this work.

Preliminary studies were conducted to characterise the surface stiffness of poly(V3D3) and pp(V3D3). This was carried out by AFM in Force Volume mode. These first measurements seem to show that except for the pp(V3D3) coating obtained with just one repetition of the torch movement, poly(V3D3) has a slightly higher Young's modulus (Figure 1). It is thought that the higher value for pp(V3D3) obtained with one torch repetition is due to interference from the substrate as the coating is only around 11 nm.

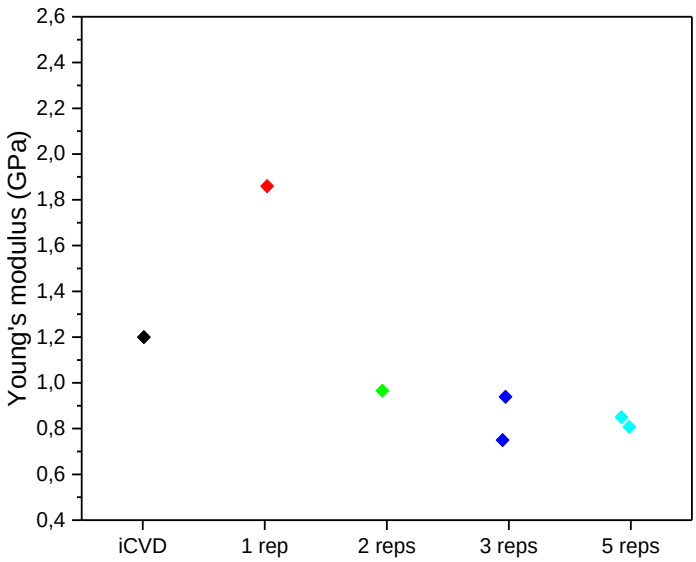

Figure 1: Young's modulus at ambient temperature for plasma polymers of V3D3 deposited by DBD-CAP with a monomer flowrate of 0.7 slm, a plasma power of 150 W and a varying number of plasma torch repetition.

Development of a standard microbiology assay for antibiofouling surfaces

The lack of standard microbiology assays for studying antibiofouling surfaces is an important issue that needs to be addressed to allow better comparisons between studies. This has also been pointed out recently in other studies[4,5] such as Catley *et al.* who underline the fact that in many studies, the variation of more than 1 surface property at a time makes it very difficult to draw conclusions on the bactericidal effect of nanostructured surfaces[4]. This was also mentioned by Linklater *et al*. who carried out in 2022 the first systematic study of the effect of polymer type and nanopillar geometry on two species of bacteria[6].

Furthermore, it has also been shown that for a given surface, the culture conditions, such as culture media, incubation time and bacterial species, used to test bacterial adhesion can have a strong impact on biofilm formation[7]. This adds to the complexity of designing standard microbiology assays which can be used to compare data from the literature. However, as antibiofouling surfaces can be designed with different applications in mind, assays should also be adapted to the environment of use.

Towards stimuli responsive antibacterial/antibiofouling surfaces

While in this study the polymers were chosen for their wettability properties, these chemical compounds can also exhibit many other interesting properties. For instance, some polymers can switch their characteristics in response to stimuli such as temperature (poly(*N*-isopropylacrylamide) (PNIPAAm)), light or pH (poly(2-((2-hydroxy-3-(methacryloyloxy)propyl)dimethylammonio)acetate (poly(CBOH))). This could be interesting for developing antibiofouling surfaces as it could allow coatings which are both antibacterial and antibiofouling and are able to self-remove foulants as their conformation changes in response to the environment[8].

By conformally depositing stimuli responsive polymers by iCVD onto micro and/or nanostructures, it could be possible to multiply the antibacterial effects and thus develop a more efficient antibiofouling surface. For instance, we could imagine a substrate covered with hierarchical structures which mechanically deform and kill bacterial cells, functionalised with a stimuli responsive polymer able to change conformation and remove the dead foulants.

Bibliography

(1) Bonnet, L.; Altemus, B.; Scarazzini, R.; Veillerot, M.; D'Agosto, F.; Faguet, J.; Jousseaume, V. Initiated-Chemical Vapor Deposition of Polymer Thin Films: Unexpected Two-Regime Growth. *Macromolecular Materials & Engineering* **2017**, *302* (12), 1700315. https://doi.org/10.1002/mame.201700315.

(2) Zabihzadeh Khajavi, M.; Nikiforov, A.; Nilkar, M.; Devlieghere, F.; Ragaert, P.; De Geyter, N. Degradable Plasma-Polymerized Poly(Ethylene Glycol)-Like Coating as a Matrix for Food-Packaging Applications. *Nanomaterials* **2023**, *13* (20), 2774. https://doi.org/10.3390/nano13202774.

(3) Vigué, A.; Vautier, D.; Kaytoue, A.; Senger, B.; Arntz, Y.; Ball, V.; Ben Mlouka, A.; Gribova, V.; Hajjar-Garreau, S.; Hardouin, J.; Jouenne, T.; Lavalle, P.; Ploux, L. Escherichia Coli Biofilm Formation, Motion and Protein Patterns on Hyaluronic Acid and Polydimethylsiloxane Depend on Surface Stiffness. *Journal of Functional Biomaterials* **2022**, *13* (4), 237. https://doi.org/10.3390/jfb13040237.

(4) Catley, T. E.; Corrigan, R. M.; Parnell, A. J. Designing Effective Antimicrobial Nanostructured Surfaces: Highlighting the Lack of Consensus in the Literature. *ACS Omega* **2023**, *8* (17), 14873–14883.

(5) Stalet, M. Protections Anti-Microbiennes : Combinaison de La Fonctionnalisation et de La Nano-Structuration Pour Explorer Les Interactions Cellule/Surface, Université Grenoble Alpes et Université de Sherbrooke, 2024.

(6) Linklater, D. P.; Saita, S.; Murata, T.; Yanagishita, T.; Dekiwadia, C.; Crawford, R. J.; Masuda, H.; Kusaka, H.; Ivanova, E. P. Nanopillar Polymer Films as Antibacterial Packaging Materials. *ACS Applied Nano Materials.* **2022**, *5* (2), 2578–2591. https://doi.org/10.1021/acsanm.1c04251.

(7) Marguier, A.; Poulin, N.; Soraru, C.; Vonna, L.; Hajjar-Garreau, S.; Kunemann, P.; Airoudj, A.; Mertz, G.; Bardon, J.; Delmée, M.; Roucoules, V.; Ruch, D.; Ploux, L. Bacterial Colonization of Low-Wettable Surfaces Is Driven by Culture Conditions and Topography. *Advanced Materials & Interfaces* **2020**, *n/a* (n/a), 2000179. https://doi.org/10.1002/admi.202000179.

(8) Maan, A. M. C.; Hofman, A. H.; Vos, W. M. de; Kamperman, M. Recent Developments and Practical Feasibility of Polymer-Based Antifouling Coatings. *Advanced Functional Materials* **2020**, *30* (32), 2000936. https://doi.org/10.1002/adfm.202000936.

Appendix

Appendix A: Literature data parameters for PVP deposition by iCVD

Title	Author	Year	Flowrate (sccm)			Vaporisation Temperature (°C)			Temperature (°C)		Pressure (mTorr)
			VP	EGDA	TBPO	VP	EGDA	TBPO	filament	substrate	
Initiated chemical vapor deposition of polyvinylpyrrolidone-based thin films	Chan	2006	7		1	80	65	25	280	35	500
			6,5								
			6								
			5,5								
			5								
			10	0	1	80	65	25	280	35	420
			9,5	0,5							
			9	1							
			8,5	1,5							
			8	2							
Vapor-based grafting of crosslinked poly(N-vinylpyrrolidone) coatings with tuned hydrophilicity and anti-biofouling properties	Sun	2016	5	0	0,6	80	65	30	280	35	500
			5	0,15							
			4	0,15							
			3	0,6							
			1,5	0,6							
			1	0,6							
			0	0,6							
Solvent-free graft-from polymerisation of polyvinyl pyrrolidone imparting ultra-low bacterial fouling and improved biocompatibility	Sun	2019	5	0,15	0,6	80	58	25	260	35	500
Experimental and theoretical investigation of dye sensitized solar cells integrated with crosslinked	Smolin	2017	1	0,05	0,1	90	70	room temp	270	51	150
				0,1						50	
				0,2						45	
				0,3						40	

poly(vinylpyrrolidone) polymer electrolyte using icvd										
Kinetic analysis of the icvd of poly(vinylpyrrolidone) and poly(4-vinylpyridine)	Janakiraman	2015	1		0,2	80		room temp	270	33	100
											150
											200
											250
			1		0,2	80		room temp	270	30	150
										34	
										38	
										43	
Sub-20 nm Bilayer Hydrophilic Poly(Vinyl Pyrrolidone) Coatings for Antifouling Nanofiltration Membranes	Liu	2021	1	0,2	0,6	70	80	25	260	35	500
			1,5	0,2	0,6						
			2	0,1	0,6						
			3	0,1	0,6						
Kinetically Limited Bulk Polymerisation of Polymer Thin Films by Initiated Chamical Vapor Deposition	Prasath	2023	0,75		0,25	90		room temp	280	10	25
											49
										15	33
											65
										20	49
											97
										25	80
											160

Appendix B: XPS fit data

Poly(V3D3)

C 1s				
Thickness (nm)	**Bond**	**Binding energy (eV) (± 0.1 eV)**	**fwhm**	**Area (%)**
15	C-C/C-Si	284.8	1.6	92
	C-O	286.1	1.6	8
48	C-C/C-Si	284.8	1.6	93
	C-O	286.1	1.6	7

Si 2p				
Thickness (nm)	**Bond**	**Binding energy (eV) (± 0.1 eV)**	**fwhm**	**Area (%)**
15	O-Si-C	102.3	1.7	92
	SiO_X	103.7	1.4	8
48	O-Si-C	102.4	1.7	92
	SiO_X	103.7	1.4	8

O 1s				
Thickness (nm)	**Bond**	**Binding energy (eV) (± 0.1 eV)**	**fwhm**	**Area (%)**
15	O-Si	532.5	1.6	93
	C-O	533.6	1.7	7
48	O-Si	532.5	1.6	92
	C-O	533.6	1.7	8

Pp(V3D3)

C 1s				
Thickness (nm)	**Bond**	**Binding energy (eV) (± 0.1 eV)**	**fwhm**	**Area (%)**
11	C-C/C-Si	284.8	1.6	78
	C-O	286.3	1.8	19
	O=C	288.9	1.8	4
32	C-C/C-Si	284.8	1.6	79
	C-O	286.3	1.8	18
	O=C	288.9	1.8	4
49	C-C/C-Si	284.8	1.6	78
	C-O	286.3	1.8	18
	O=C	288.9	1.8	4
65	C-C/C-Si	284.8	1.6	78
	C-O	286.3	1.8	18
	O=C	288.9	1.8	4
80	C-C/C-Si	284.8	1.6	78
	C-O	286.3	1.8	18
	O=C	288.9	1.8	4

Si 2p				
Thickness (nm)	**Bond**	**Binding energy (eV) (± 0.1 eV)**	**fwhm**	**Area (%)**
11	Si-C	101.3	1.4	14
	O-Si-C	102.7	1.4	58
	SiO_X	103.6	1.6	28
32	O-Si-C	102.7	1.6	71
	SiO_X	103.5	1.6	29
49	O-Si-C	102.7	1.6	72
	SiO_X	103.5	1.6	28
65	O-Si-C	102.7	1.6	71
	SiO_X	103.5	1.6	29
80	O-Si-C	102.7	1.6	74
	SiO_X	103.6	1.6	26

O 1s				
Thickness (nm)	**Bond**	**Binding energy (eV) (± 0.1 eV)**	**fwhm**	**Area (%)**
11	O-Si	532.6	1.6	87
	C-O	533.8	1.6	13
32	O-Si	532.6	1.6	88
	C-O	533.6	1.6	12
49	O-Si	532.5	1.6	87
	C-O	533.6	1.6	13
65	O-Si	532.6	1.6	89
	C-O	533.7	1.6	11
80	O-Si	532.6	1.6	87
	C-O	533.6	1.6	13

PVP

C 1s				
Thickness (nm)	**Bond**	**Binding energy (eV) (± 0.1 eV)**	**fwhm**	**Area (%)**
10	C-C	284.8	1.5	47
	C-N	285.7	1.5	33
	C-O	286.2	1.5	6
	O=C	287.6	1.5	14
67	C-C	284.8	1.5	45
	C-N	285.7	1.5	38
	C-O	286.2	1.5	1
	O=C	287.5	1.5	16
297	C-C	284.8	1.5	45
	C-N	285.7	1.5	38
	C-O	286.2	1.5	1
	O=C	287.5	1.5	15

N 1s				
Thickness (nm)	**Bond**	**Binding energy (eV) (± 0.1 eV)**	**fwhm**	**Area (%)**
10	N-C	399.6	1.7	100
67	N-C	399.6	1.7	100
297	N-C	399.6	1.6	100

O 1s				
Thickness (nm)	**Bond**	**Binding energy (eV) (± 0.1 eV)**	**fwhm**	**Area (%)**
10	O=C	531.1	1.6	71
	O-Si	532.4	1.6	27
	O-C	533.7	1.4	3
67	O=C	531.0	1.6	83
	O-Si	532.4	1.5	16
	O-C	533.6	1.4	1
297	O=C	531.0	1.6	85
	O-Si	532.4	1.5	14
	O-C	533.6	1.4	1

Poly(VP-co-V3D3)

C 1s				
Injected fraction of VP (%)	**Bond**	**Binding energy (eV) (± 0.1 eV)**	**fwhm**	**Area (%)**
62.6	C-C/C-Si	284.8	1.5	59
	C-N	285.8	1.5	24
	C-O	286.2	1.5	9
	O=C	287.7	1.5	8
80.6	C-C/C-Si	284.8	1.5	51
	C-N	285.9	1.5	35
	C-O	286.2	1.5	3
	O=C	287.7	1.5	11
87.2	C-C/C-Si	284.8	1.5	47
	C-N	285.8	1.5	36
	C-O	286.2	1.5	3
	O=C	287.7	1.5	13

N 1s				
Injected fraction of VP (%)	**Bond**	**Binding energy (eV) (± 0.1 eV)**	**fwhm**	**Area (%)**
62.6	N-C	400	1.7	100
80.6	N-C	399.9	1.7	100
87.2	N-C	399.8	1.6	100

O 1s				
Injected fraction of VP (%)	**Bond**	**Binding energy (eV) (± 0.1 eV)**	**fwhm**	**Area (%)**
62.6	O=C	531.2	1.4	12
	O-Si	532.3	1.6	80
	C-O	533.5	1.4	7
80.6	O=C	531.2	1.4	26
	O-Si	532.3	1.6	70
	C-O	533.7	1.5	4
87.2	O=C	531.2	1.5	48
	O-Si	532.3	1.6	50
	C-O	533.7	1.5	2

Si 2p				
Injected fraction of VP (%)	**Bond**	**Binding energy (eV) (± 0.1 eV)**	**fwhm**	**Area (%)**
62.6	O-Si-C	102.2	1.7	91
	SiO_X	103.6	1.5	9
80.6	O-Si-C	102.2	1.7	94
	SiO_X	103.7	1.4	6
87.2	O-Si-C	102.2	1.7	95
	SiO_X	103.8	1.4	5

Polymer resist with and without plasma etching

C 1s				
Substrate	**Bond**	**Binding energy (eV) (± 0.1 eV)**	**fwhm**	**Area (%)**
Polymer resist	C-C/C-Si	284.8	1.5	67
	C-O	286.3	1.5	19
	O=C	288.8	1.3	14
HBr etched polymer resist	C-C/C-Si	284.8	1.5	62
	C-O	286.3	1.8	29
	O=C	288.7	1.8	9
SF6 (2 sccm) etched polymer resist	C-C/C-Si	284.8	1.6	67
	C-O	286.3	1.8	27
	O=C	288.9	1.8	6
SF6 (6 sccm) etched polymer resist	C-C/C-Si	284.8	1.6	62
	C-O	286.3	1.8	29
	O=C	288.7	1.8	9

Si 2p				
Substrate	**Bond**	**Binding energy (eV) (± 0.1 eV)**	**fwhm**	**Area (%)**
Polymer resist	O-Si-C	102.4	1.5	100
HBr etched polymer resist	SiO_X	103.4	1.7	100
SF6 (2 sccm) etched polymer resist	SiO_X	103.4	1.7	100
SF6 (6 sccm) etched polymer resist	SiO_X	103.4	1.7	100

O 1s				
Substrate	**Bond**	**Binding energy (eV) (± 0.1 eV)**	**fwhm**	**Area (%)**
Polymer resist	O-Si	532.0	1.4	67
	O-C	533.3	1.6	33
HBr etched polymer resist	O-Si	532.8	1.7	100
SF6 (2 sccm) etched polymer resist	O-Si	532.7	1.7	100
SF6 (6 sccm) etched polymer resist	O-Si	532.7	1.7	100

Poly(V3D3) on SF_6 (6 sccm) plasma etched polymer resist

C 1s					
Substrate	**Poly(V3D3) thickness (nm)**	**Bond**	**Binding energy (eV) (± 0.1 eV)**	**fwhm**	**Area (%)**
SF6 (6 sccm) plasma etched polymer resist	6	C-C/C-Si	284.8	1.6	90
		C-O	286.1	1.6	10
		O=C	289.0	1.6	0.5
	13	C-C/C-Si	284.8	1.6	94
		C-O	286.1	1.5	6
	38	C-C/C-Si	284.8	1.6	96
		C-O	286.1	1.5	4

Si 2p					
Substrate	**Poly(V3D3) thickness (nm)**	**Bond**	**Binding energy (eV) (± 0.1 eV)**	**fwhm**	**Area (%)**
SF6 (6 sccm) plasma etched polymer resist	6	O-Si-C	102.2	1.7	42
		SiO_X	103.6	1.7	58
	13	O-Si-C	102.2	1.6	73
		SiO_X	103.6	1.7	27
	38	O-Si-C	102.2	1.6	91
		SiO_X	103.4	1.4	9

O 1s					
Substrate	**Poly(V3D3) thickness (nm)**	**Bond**	**Binding energy (eV) (± 0.1 eV)**	**fwhm**	**Area (%)**
SF6 (6 sccm) plasma etched polymer resist	6	O-Si	532.5	1.5	75
		O-C	533.6	1.6	25
	13	O-Si	532.4	1.5	83
		O-C	533.6	1.6	17
	38	O-Si	532.3	1.5	94
		O-C	533.6	1.7	6

Pp(V3D3) on SF_6 (6 sccm) plasma etched polymer resist

C 1s				
Substrate	**Bond**	**Binding energy (eV) (± 0.1 eV)**	**fwhm**	**Area (%)**
SF6 (6 sccm) plasma etched polymer resist	C-C/C-Si	284.8	1.6	67
	C-O	286.1	1.8	28
	O=C	289.0	1.8	5

Si 2p				
Substrate	**Bond**	**Binding energy (eV) (± 0.1 eV)**	**fwhm**	**Area (%)**
SF6 (6 sccm) plasma etched polymer resist	O-Si-C	102.5	1.6	12
	SiO_X	103.6	1.8	88

O 1s				
Substrate	**Bond**	**Binding energy (eV) (± 0.1 eV)**	**fwhm**	**Area (%)**
SF6 (6 sccm) plasma etched polymer resist	SiO_X	532.7	1.6	74
	O-C	533.6	1.6	26

Appendix C: Reflectivity profiles for pp(V3D3)

a. Pp(V3D3) with a thickness of 11 nm, obtained with 1 repetition of the plasma torch's movement

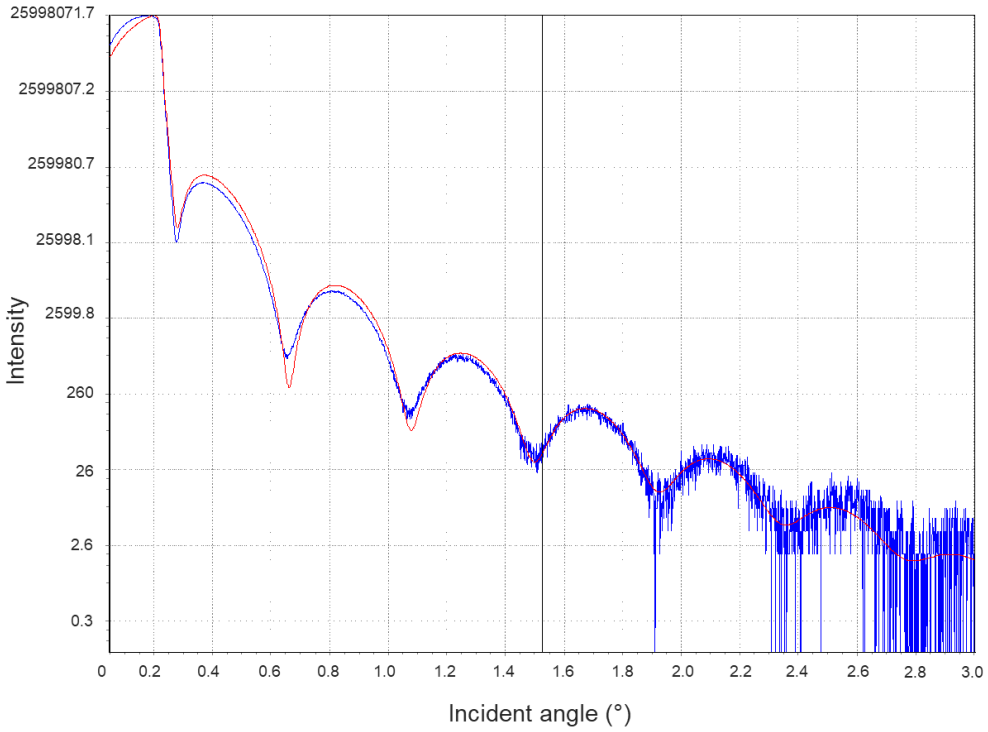

b. Pp(V3D3) with a thickness of 49 nm, obtained with 3 repetitions of the plasma torch's movement

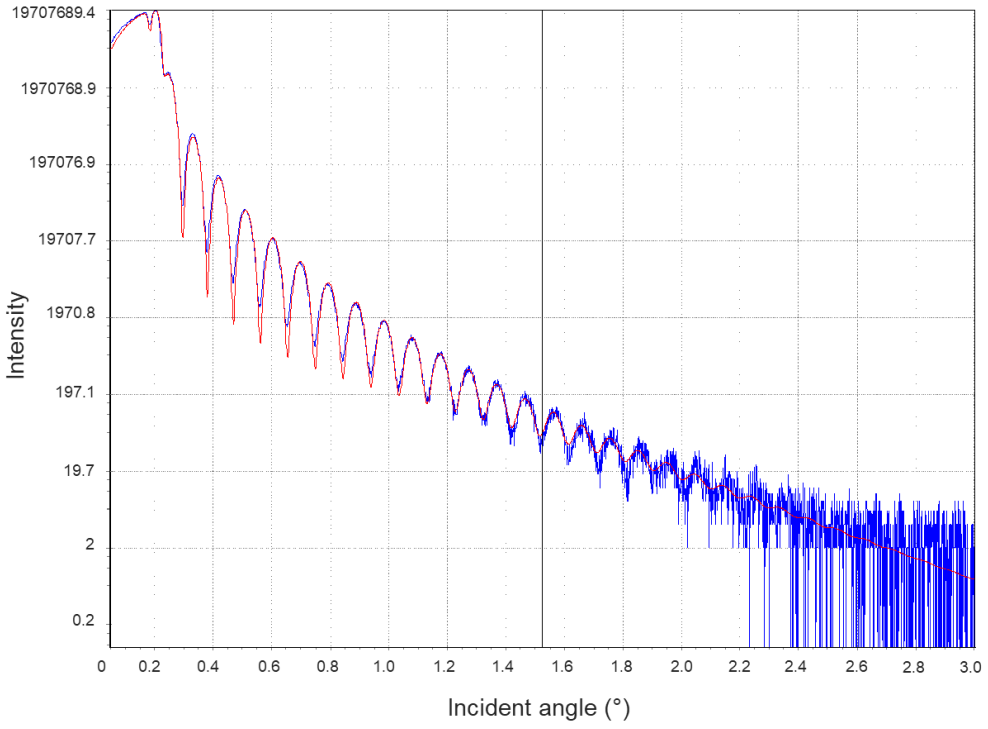

c. Pp(V3D3) with a thickness of 80 nm, obtained with 5 repetitions of the plasma torch's movement

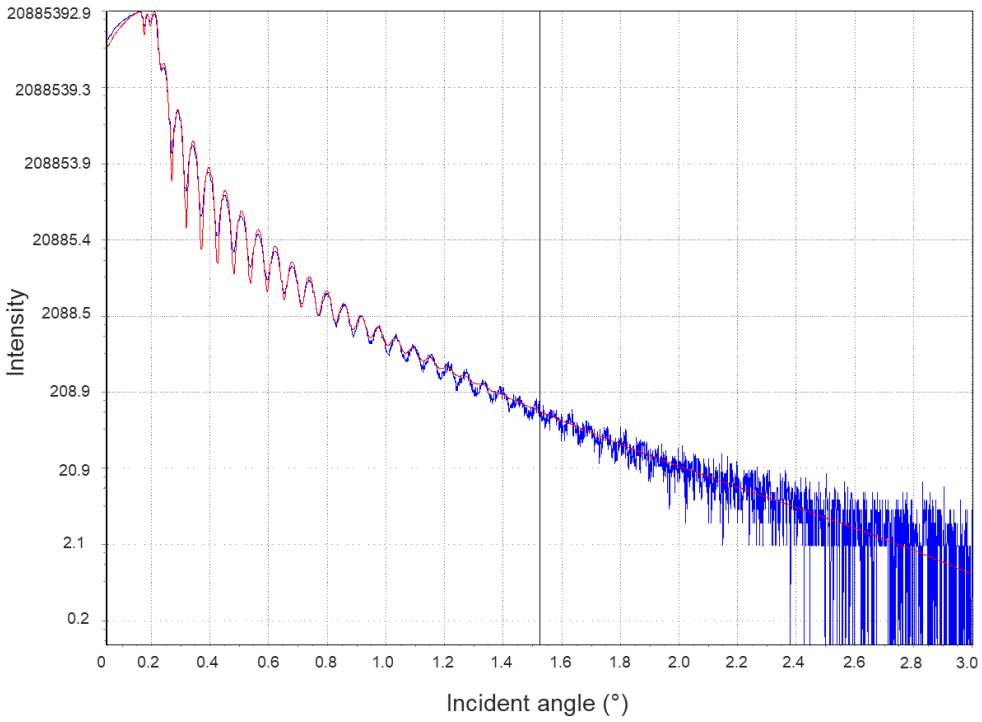

d. Poly(V3D3) with a thickness of 48 nm

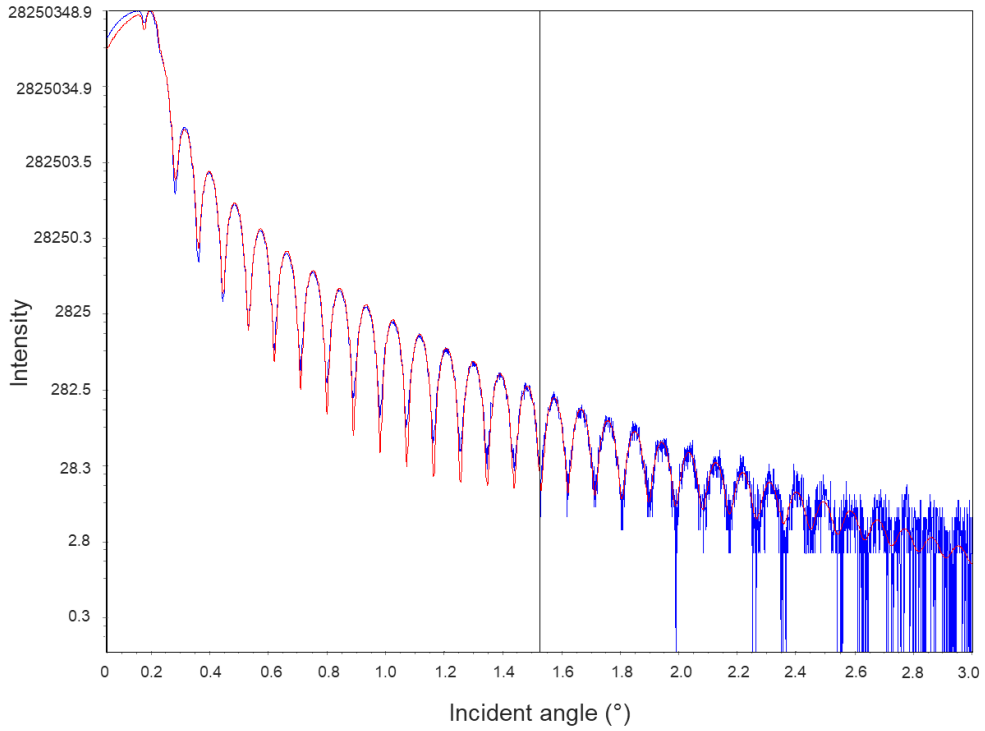

Appendix D: Spectroscopic Ellipsometry mapping

Note: For all coatings, the silicon wafer was placed into the iCVD equipment with the same orientation and the mappings were also all carried out with the same orientation of the silicon wafer.

a. PVP coatings deposited by iCVD onto a 200 mm silicon wafer with a reacter pressure of 1.5 Torr and a substrate temperature of 37°C.

time of deposition = 100 s

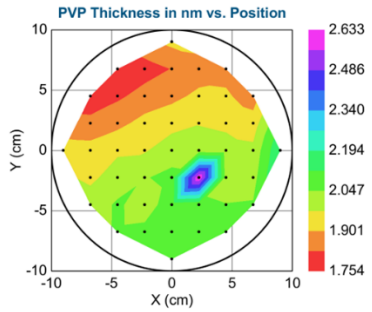

time of deposition = 200 s

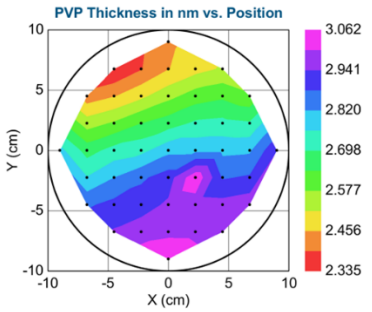

time of deposition = 800 s

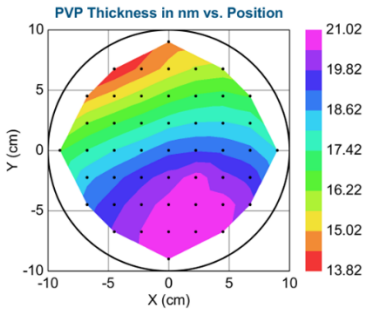

time of deposition = 1600 s

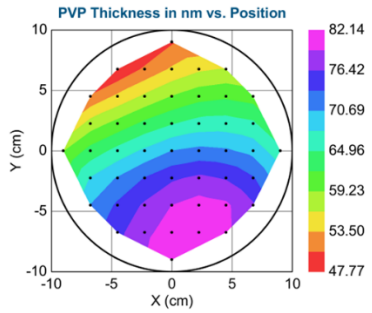

time of deposition = 3200 s

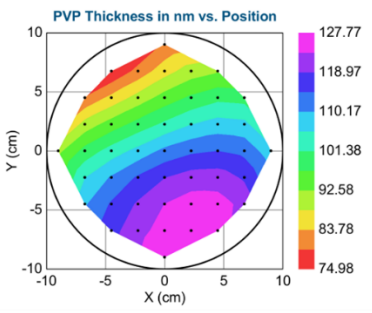

time of deposition = 6400 s

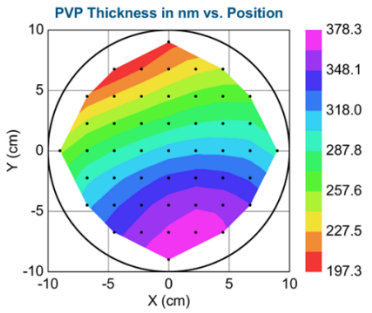

b. Poly(VP-co-V3D3) coatings deposited by iCVD onto a 200 mm silicon wafer with a reactor pressure of 1.5 Torr and a substrate temperature of 40°C.

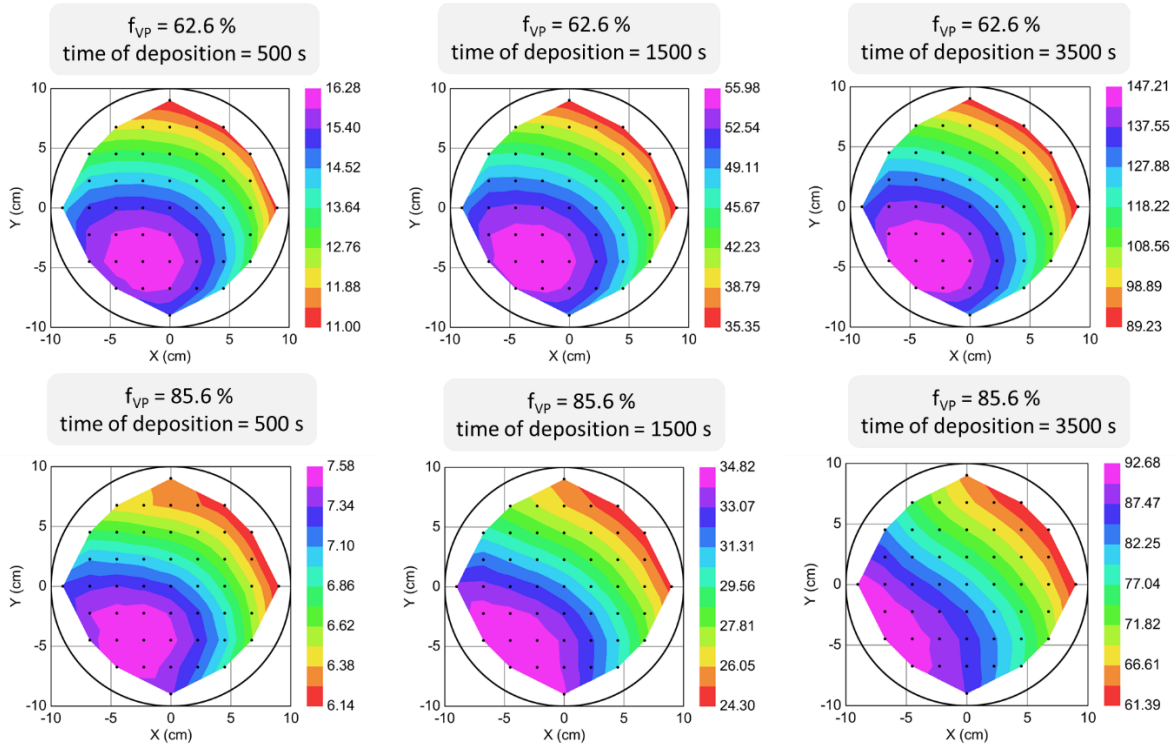

Appendix E: Schematic representation of the pattern of structures on a 200 mm silicon wafer

For each 1 cm² zone, the yellow zones represent horizontal lines, the green zones represent vertical lines and the white zones correspond to pillars. The top number corresponds to the width of the lines (or diameter of the pillars) and the bottom number corresponds to the space between the lines (or the pitch which is the distance between the center of two adjacent pillars).

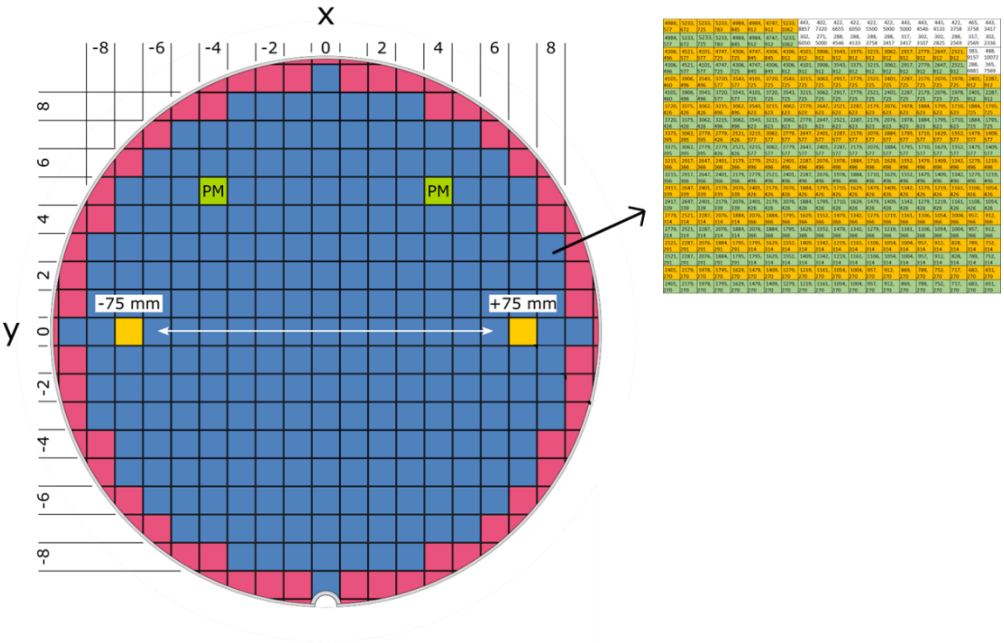

4984, 577	5233, 672	5233, 725	5233, 783	4984, 845	4984, 912	4747, 912	5233, 1062	443, 8857	402, 7320	422, 6655	422, 6050	422, 5500	422, 5000	443, 5000	443, 4546	443, 4133	422, 3758	465, 3758	443, 3417
4984, 577	5233, 672	5233, 725	5233, 783	4984, 845	4984, 912	4747, 912	5233, 1062	302, 6050	275, 5000	288, 4546	288, 4133	288, 3758	288, 3417	317, 3417	302, 3107	302, 2825	288, 2569	317, 2569	302, 2336
4306, 496	4521, 577	4101, 577	4747, 725	4306, 725	4747, 845	4306, 845	4306, 912	4101, 912	3906, 912	3543, 912	3375, 912	3215, 912	3062, 912	2917, 912	2779, 912	2647, 912	2521, 912	383, 9157	488, 10072
4306, 496	4521, 577	4101, 577	4747, 725	4306, 725	4747, 845	4306, 845	4306, 912	4101, 912	3906, 912	3543, 912	3375, 912	3215, 912	3062, 912	2917, 912	2779, 912	2647, 912	2521, 912	288, 6881	365, 7569
4101, 460	3906, 496	3543, 496	3720, 577	3543, 577	4101, 725	3720, 725	3543, 725	3215, 725	3062, 725	2917, 725	2779, 725	2521, 725	2401, 725	2287, 725	2179, 725	2076, 725	1978, 725	2401, 912	2287, 912
4101, 460	3906, 496	3543, 496	3720, 577	3543, 577	4101, 725	3720, 725	3543, 725	3215, 725	3062, 725	2917, 725	2779, 725	2521, 725	2401, 725	2287, 725	2179, 725	2076, 725	1978, 725	2401, 912	2287, 912
3720, 426	3375, 426	3062, 426	3215, 496	3062, 496	3543, 623	3215, 623	3062, 623	2779, 623	2647, 623	2521, 623	2287, 623	2179, 623	2076, 623	1978, 623	1884, 623	1795, 623	1710, 623	1884, 725	1795, 725
3720, 426	3375, 426	3062, 426	3215, 496	3062, 496	3543, 623	3215, 623	3062, 623	2779, 623	2647, 623	2521, 623	2287, 623	2179, 623	2076, 623	1978, 623	1884, 623	1795, 623	1710, 623	1884, 725	1795, 725
3375, 395	3062, 395	2779, 395	2779, 426	2521, 426	3215, 577	3062, 577	2779, 577	2647, 577	2401, 577	2287, 577	2179, 577	2076, 577	1884, 577	1795, 577	1710, 577	1629, 577	1552, 577	1479, 577	1409, 577
3375, 395	3062, 395	2779, 395	2779, 426	2521, 426	3215, 577	3062, 577	2779, 577	2647, 577	2401, 577	2287, 577	2179, 577	2076, 577	1884, 577	1795, 577	1710, 577	1629, 577	1552, 577	1479, 577	1409, 577
3215, 366	2917, 366	2647, 366	2401, 366	2179, 366	2779, 496	2521, 496	2401, 496	2287, 496	2076, 496	1978, 496	1884, 496	1710, 496	1629, 496	1552, 496	1479, 496	1409, 496	1342, 496	1279, 496	1219, 496
3215, 366	2917, 366	2647, 366	2401, 366	2179, 366	2779, 496	2521, 496	2401, 496	2287, 496	2076, 496	1978, 496	1884, 496	1710, 496	1629, 496	1552, 496	1479, 496	1409, 496	1342, 496	1279, 496	1219, 496
2917, 339	2647, 339	2401, 339	2179, 339	2076, 339	2401, 426	2179, 426	2076, 426	1884, 426	1795, 426	1710, 426	1629, 426	1479, 426	1409, 426	1342, 426	1279, 426	1219, 426	1161, 426	1106, 426	1054, 426
2917, 339	2647, 339	2401, 339	2179, 339	2076, 339	2401, 426	2179, 426	2076, 426	1884, 426	1795, 426	1710, 426	1629, 426	1479, 426	1409, 426	1342, 426	1279, 426	1219, 426	1161, 426	1106, 426	1054, 426
2779, 314	2521, 314	2287, 314	2076, 314	1884, 314	2076, 366	1884, 366	1795, 366	1629, 366	1552, 366	1479, 366	1342, 366	1279, 366	1219, 366	1161, 366	1106, 366	1054, 366	1004, 366	957, 366	912, 366
2779, 314	2521, 314	2287, 314	2076, 314	1884, 314	2076, 366	1884, 366	1795, 366	1629, 366	1552, 366	1479, 366	1342, 366	1279, 366	1219, 366	1161, 366	1106, 366	1054, 366	1004, 366	957, 366	912, 366
2521, 291	2287, 291	2076, 291	1884, 291	1795, 291	1795, 314	1629, 314	1552, 314	1409, 314	1342, 314	1219, 314	1161, 314	1106, 314	1054, 314	1004, 314	957, 314	912, 314	828, 314	789, 314	752, 314
2521, 291	2287, 291	2076, 291	1884, 291	1795, 291	1795, 314	1629, 314	1552, 314	1409, 314	1342, 314	1219, 314	1161, 314	1106, 314	1054, 314	1004, 314	957, 314	912, 314	828, 314	789, 314	752, 314
2401, 270	2179, 270	1978, 270	1795, 270	1629, 270	1479, 270	1409, 270	1279, 270	1219, 270	1161, 270	1054, 270	1004, 270	957, 270	912, 270	869, 270	789, 270	752, 270	717, 270	683, 270	651, 270
2401, 270	2179, 270	1978, 270	1795, 270	1629, 270	1479, 270	1409, 270	1279, 270	1219, 270	1161, 270	1054, 270	1004, 270	957, 270	912, 270	869, 270	789, 270	752, 270	717, 270	683, 270	651, 270

Appendix F: Water Contact Angle of polymer resist treated with SF_6 (2 sccm) plasma

a. With an additional coating of poly(V3D3) or pp(V3D3)

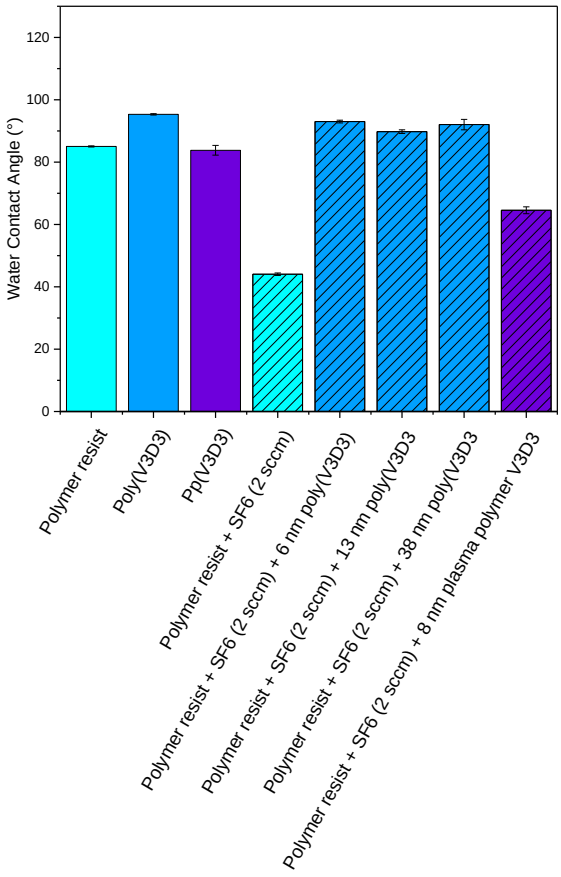

b. With an additional coating of poly(VP-co-V3D3)

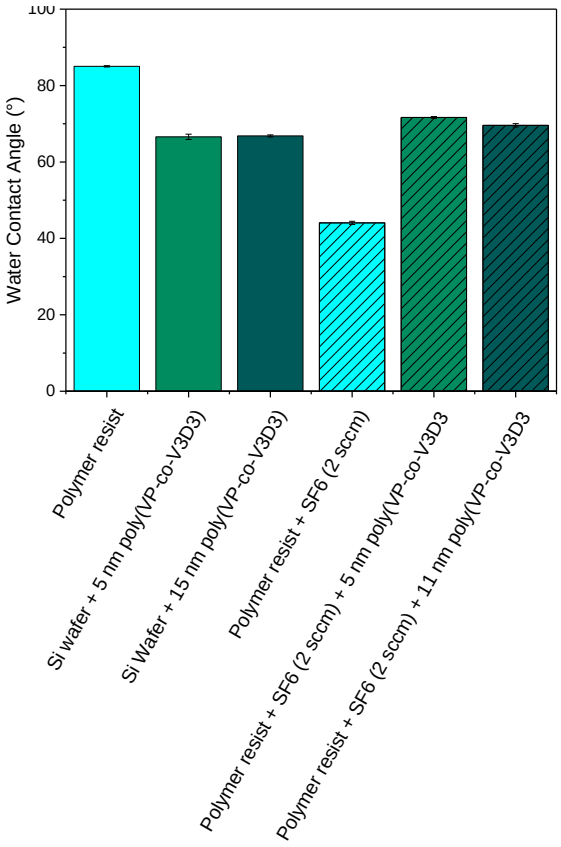

Appendix G: Composition of media used in the microbiology assays

a. Mueller Hinton culture media

Ingredients	Quantity (g/L)
Beef infusion solids	2.0
Starch	1.5
Casein hydrosylate	17.5
Final pH 7.4 +/- 0.2 at 25°C	

b. Phosphate Buffer Saline (PBS) 1X

Ingredients	Concentration (mM)
NaCl	137
KCl	2.7
Na_2HPO_4	10
KH_2PO_4	1.8

Résumé en français

Ingénierie de surfaces antimicrobiennes : combinaison de topographie et de fonctionnalisation par dépôt chimique en phase vapeur par polymérisation amorcée in situ et plasma atmosphérique froid

La formation de biofilm est une problématique qui touche de très nombreux domaines allant de l'industrie marine aux dispositifs médicaux en passant par le traitement de l'eau. Les bactéries créent cette matrice protectrice afin d'assurer leur survie puisqu'elles sont moins vulnérables aux biocides et aux antibiotiques sous forme de biofilm plutôt que sous forme planctonique. Dans le milieu médical, la formation de biofilm peut entrainer des infections qui peuvent être mortelles, en plus d'une défaillance de matériel[1]. Le tout s'accompagne de coûts surélevés.

Traditionnellement, le biofilm est éliminé par des moyens curatifs. Cependant, puisque sa formation commence par l'adhésion de bactéries en surface, de nouvelles approches préventives bioinspirées sont en cours d'exploration. En effet, dans la nature, de nombreuses espèces ont développé des surfaces autonettoyantes ou antibiofouling afin de se protéger de la colonisation par d'autres espèces. Ceci est le cas par exemple de la feuille de lotus qui détient ses propriétés superhydrophobes d'une combinaison de chimie à base de nonacosanols et nonacosandiols et de microstructures en surface[2,3] (Figure 1a). Cette alliance de chimie et de topographie permet l'obtention de l'effet Cassie-Baxter qui explique la superhydrophobie par la présence de microgouttelettes d'air piégées entre les microtubules de la feuille de lotus[4] (Figure 1c).

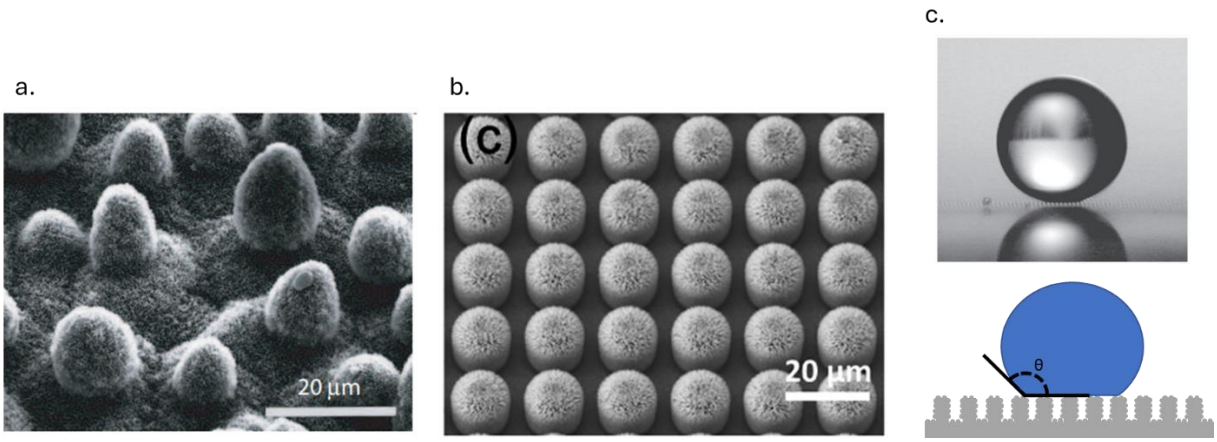

Figure 1 : a. Microstructures à la surface d'une feuille de lotus[3]. b. Reproduction de la topographie de la feuille de lotus[5]. c. Effet Cassie-Baxter[3].

De nombreuses études cherchent maintenant à combiner une chimie spécifique avec des micro et/ou nanostructures afin de développer des surfaces superhydrophobes mais aussi superhydrophiles dans le but d'empêcher l'adhésion réversible de bactéries en surface, étape initiale à la formation de biofilm[6].

Le chapitre 1 constitue une revue de la littérature sur ce type de surfaces antibiofouling et antibactériennes, ainsi que sur les techniques de fonctionnalisation chimique.

En ce qui concerne les études sur les surfaces antibiofouling par combinaison de chimie et de topographie, malgré la multitude de composés chimiques et de structures étudiés, des limites à ces surfaces innovantes peuvent être soulevées. En effet, pour concevoir des surfaces superhydrophobes, l'utilisation de composés fluorés est toujours prévalente. Cependant, des restrictions à l'usage de certains de ces composés tels que les per- et polyfluoroalkylées (PFAS), limitent leur utilisation hors du laboratoire[7]. Concernant les surfaces hydrophiles, il y a de nombreux composés chimiques qui sont étudiés. Dans certains cas, l'objectif est de créer une forte couche d'hydratation. Dans d'autres, le composé hydrophile est utilisé car il est aussi bactéricide. De plus, à cause de l'émergence récente de

ce champ d'étude, il manque de synergie entre les différents travaux et d'études systématiques afin de mieux déterminer quel type de structuration serait la plus efficace contre l'adhésion bactérienne[8].

La plupart de ces études fonctionnalisent des surfaces préalablement structurées avec la chimie hydrophile ou hydrophobe désirée. L'utilisation de polymères permet de travailler avec des composés variés, robustes, à bas-coût, non-toxiques et souvent biocompatibles[9]. De plus, les polymères peuvent être déposés en couches minces sur des surfaces diverses, planes ou structurées. Cette fonctionnalisation peut se faire par voie liquide ou en phase vapeur. Ces techniques de dépôt sont aussi présentées dans le premier chapitre de ce manuscrit, en donnant les avantages et inconvénients de chacune d'entre-elles, permettant d'orienter le choix vers celles utilisées au cours de ces travaux.

Cette analyse de la littérature et des techniques de dépôts de polymères en couches minces permet de définir la stratégie et les objectifs de cette thèse. L'idée est de contribuer à la recherche d'une surface empêchant l'adhésion initiale de bactéries en fonctionnalisant des surfaces structurées avec des nano et/ou des microstructures par dépôt chimique phase vapeur de polymères ou par dépôt par plasma froid atmosphérique. La stratégie employée repose sur l'utilisation d'une chimie hydrophobe ou hydrophile. L'étude de propriétés de surfaces telles que la chimie, la rugosité, la densité et la mouillabilité permettra une compréhension des matériaux et l'impact de la méthode de dépôt sur ces derniers. Une étude systématique d'adhésion de bactéries sur les différentes surfaces développées au cours de ce travail mettra en lumière l'impact des différentes propriétés.

Deux techniques de dépôt de polymères seront utilisées : le dépôt chimique phase vapeur par polymérisation amorcée in situ (initiated Chemical Vapour Deposition ou iCVD) et le dépôt par plasma atmosphérique froid par décharge à barrière diélectrique (Dielectric Barrier Discharge Cold Atmospheric Plasma ou DBD-CAP). L'iCVD est basée sur la polymérisation radicalaire, ce qui permet de conserver les fonctions chimiques du monomère[10]. De plus, il a été montré que l'iCVD permet d'obtenir des couches minces très conformes[11,12]. Le DBD-CAP est une méthode versatile et facile à mettre en place, permettant alors de comparer l'effet de la méthode de dépôt sur le matériau obtenu.

Les monomères choisis sont le 1,3,5-trivinyl-1,3,5-trimethylcyclotrisiloxane (V3D3) (Figure 2a) qui permet d'obtenir le poly(V3D3), matériau hydrophobe et biocompatible[13,14] et le vinylpyrrolidone (VP) (Figure 2b) qui donne le poly(vinylpyrrolidone) (PVP), superhydrophile et aussi biocompatible[15,16].

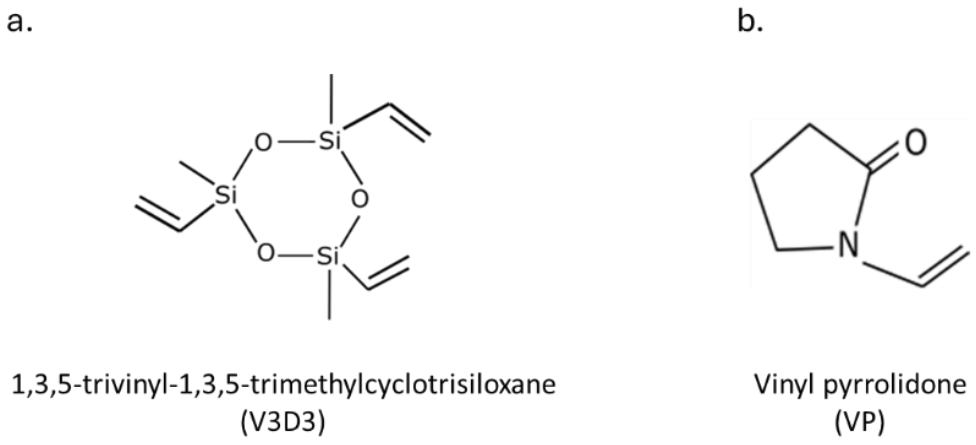

Figure 2 : a. 1,3,5-trivinyl-1,3,5-trimethylcyclotrisiloxane (V3D3). B. Vinylpyrrolidone (VP).

Le chapitre 2 décrit les deux techniques de dépôts utilisées au cours de ce travail.

Tout d'abord, l'iCVD (Figure 3a) fonctionne en injectant le monomère d'intérêt sous forme de vapeur dans une chambre sous vide dans laquelle se trouve le substrat qui est refroidi par un système fermé de circulation d'huile. Le monomère, intact, se condense en surface du substrat, avant l'injection d'un amorceur de radicaux : le tert-butyle de peroxide (TBPO). Ce dernier est pyrolisé par un filament chauffé à environ 250°C, formant ainsi des radicaux qui rencontrent les monomères en surface du substrat, amorçant la polymérisation radicalaire. Le temps de dépôt permet de contrôler l'épaisseur de la couche mince finale.

Le DBD-CAP utilisé ici, le Plasmaspot®, est composé de deux électrodes circulaires, placées l'une dans l'autre (Figure 3b). Le monomère est injecté sous forme de microgouttelettes à travers l'électrode centrale, poussé par de l'azote. Un plasma d'azote se forme entre les deux électrodes et active le monomère en sortie de la torche, à la surface du substrat. Cette activation du monomère entraîne la formation de nombreuses espèces réactives telles que des radicaux, électrons et ions qui réagissent les unes avec les autres, formant ainsi une couche mince réticulée, communément appelée polymère plasma. La particularité de l'équipement utilisé ici est que la torche plasma peut se déplacer, permettant de fonctionnaliser des surfaces plus ou moins grandes. Il est aussi possible de superposer les passages de la torche sur une même zone.

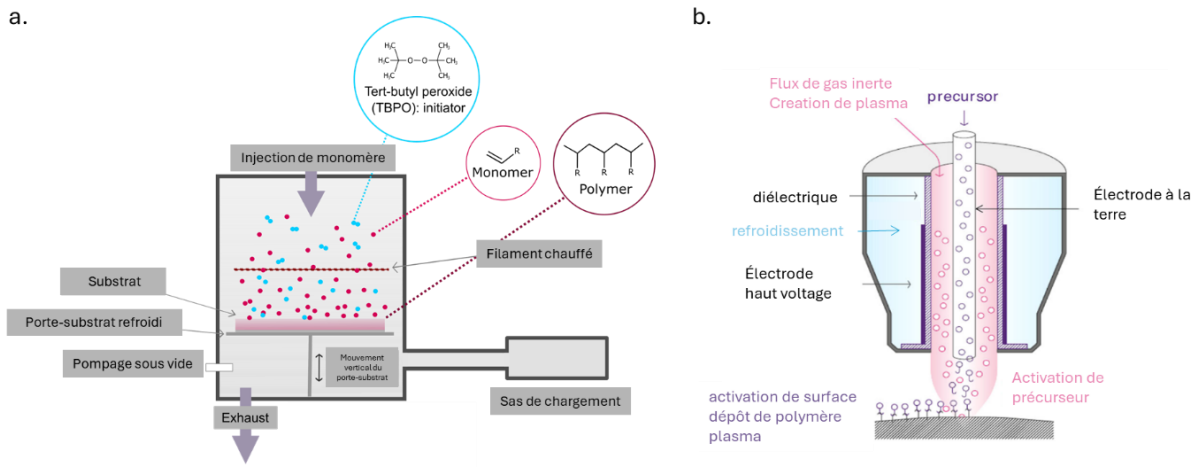

Figure 3 : Représentation schématique de a. l'iCVD, b. le DBD-CAP utilisés au cours de ces travaux[17].

De nombreuses techniques de caractérisation sont aussi utilisées dans ce travail afin d'analyser et comprendre les différentes propriétés des matériaux développés. Elles sont décrites dans le chapitre 2. L'ellipsométrie spectroscopique permet de mesurer l'épaisseur des couches minces déposées et de déterminer l'indice optique des polymères. La réflectivité des rayons X (XRR) est utilisée pour évaluer la densité des matériaux. La spectroscopie infrarouge par transformée de Fourier (FTIR) permet d'analyser les liaisons chimiques. La spectroscopie photoélectronique X (XPS) permet d'identifier les liaisons chimiques présentes à la surface de la couche mince polymérique. La microscopie à force atomique (AFM) permet quant à elle d'analyser la topographie et d'évaluer la rugosité de surface. Finalement, afin de caractériser l'état de mouillabilité des différentes surfaces, les angles de gouttes (WCA) sont mesurés.

Dans le chapitre 3 de ce manuscrit sont décrits, analysés et comparés les dépôts de poly(V3D3) par iCVD et pp(V3D3) par DBD-CAP.

Tout d'abord, confirmant des études de la littérature, les dépôts par iCVD de poly(V3D3), dont la recette avait été préalablement optimisée par notre équipe, montrent une linéarité entre l'épaisseur de la couche mince et le temps de dépôt[18]. Les analyses chimiques par FTIR et XPS permettent ensuite de vérifier la polymérisation radicalaire, conservant les groupements fonctionnels du monomère V3D3 (un cycle de siloxanes) qui deviennent reliés les uns aux autres par une chaine de type polyéthylène (Figure 4a). L'acquisition d'images par AFM permet de constater que les couches de poly(V3D3) obtenues ont une très faible rugosité (< 0.4 nm), confirmant encore une fois certaines études similaires[14]. La mesure d'angles de gouttes permet de montrer que le poly(V3D3) est un polymère hydrophobe avec des WCA = 95°. Cette hydrophobie est prometteuse pour des surfaces antiadhésives sans composé fluoré. De plus, des études de stabilité dans du PBS (tampon phosphate salin) pendant 24 h montrent que le poly(V3D3) est insoluble dans ce milieu. Ceci permet alors d'utiliser des surfaces fonctionnalisées par le poly(V3D3) pour des expériences de microbiologie qui requièrent l'incubation d'échantillons dans des milieux liquides tels que le PBS.

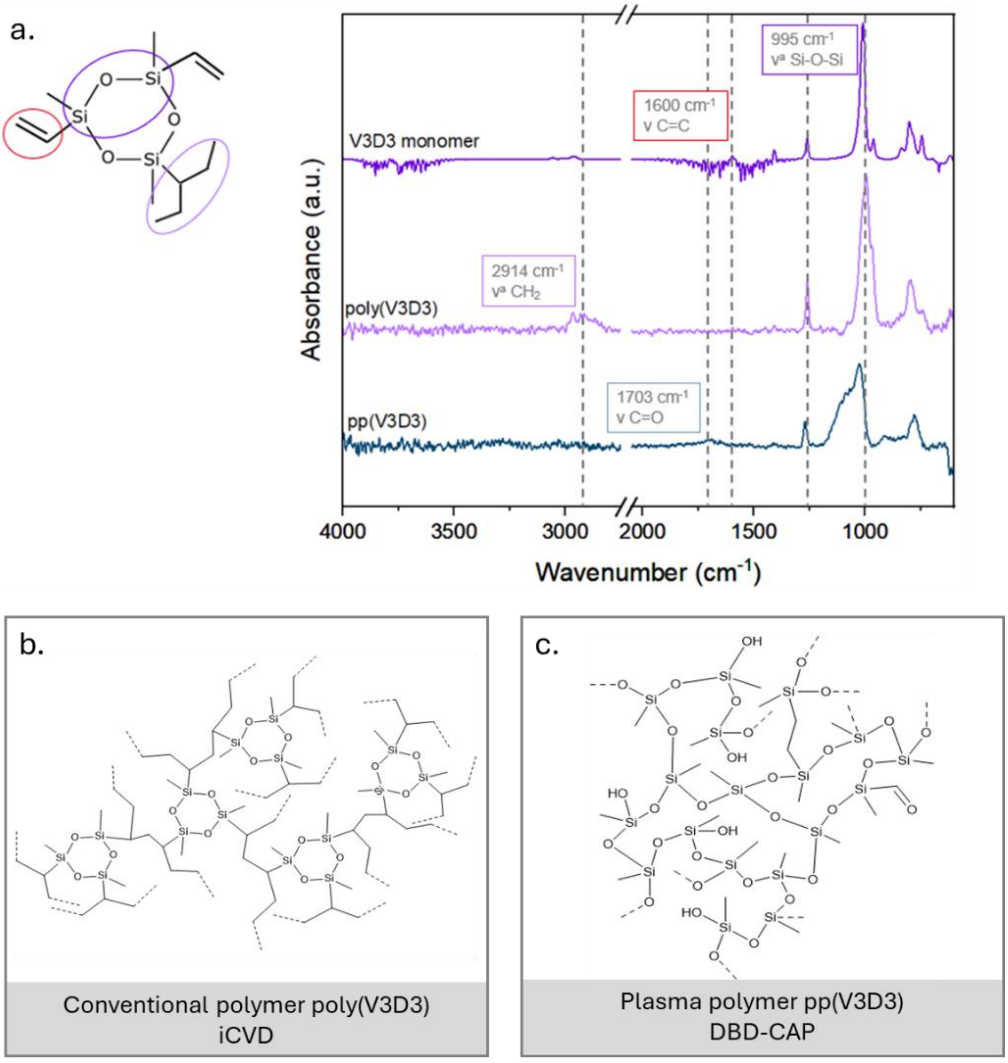

Figure 4 : a. Spectre FTIR du monomère V3D3, du poly(V3D3) déposé par iCVD et du pp(V3D3) déposé par DBD-CAP. Les deux dépôts analysés ont une épaisseur de 65 nm. b. Représentation schématique de poly(V3D3) déposé par iCVD. c. Représentation schématique de pp(V3D3) déposé par DBD-CAP.

La technique DBD-CAP a été utilisée, pour la première fois à notre connaissance, pour déposer des polymères plasmas pp(V3D3). Les mesures par ellipsométrie spectroscopie permettent de voir qu'ici, l'épaisseur des couches minces de polymères plasma augmente avec la puissance du plasma et le flux d'injection du monomère. Cependant, la variation de ces paramètres ne permet pas d'obtenir des épaisseurs au-delà de 25 nm tout en respectant les recommandations du constructeur. Répéter le mouvement de la torche plasma afin de superposer les couches de polymère, en revanche, permet d'augmenter l'épaisseur du dépôt. En effet, après 5 répétitions, il est possible d'atteindre des épaisseurs autour de 80 nm. L'AFM montre des faibles rugosités de surface même si des inhomogénéités ont pu être observées par microscopie optique. Les analyses chimiques permettent de montrer quelques différences par rapport au poly(V3D3) iCVD. En effet, le FTIR montre des modifications du pic correspondant aux siloxanes, résultant d'une modification de conformation et possiblement d'une ouverture de cycle (Figure 4a). De plus, le spectre montre aussi que le Si ne se trouve plus dans une configuration où il est di-substitué par l'oxygène, mais est ici tri-substitué par O. On peut aussi apercevoir l'incorporation de groupes hydroxyles et carbonyles qui peuvent venir de l'incorporation de molécules atmosphériques (Figure 4a). Ceci impacte légèrement l'hydrophobie du dépôt puisque les angles de goutte mesurés sont ici autour de 80°.

Cette étude montre que le choix de la technique de dépôt peut exercer une influence sur le matériau final avec ici la création du poly(V3D3) obtenu par polymérisation radicalaire lors du dépôt iCVD et du polymère plasma pp(V3D3) obtenu par DBD-CAP. Malgré les différences de structure chimique observées (Figure 4b et c), les deux techniques donnent des couches minces avec une faible rugosité, une densité similaire et une grande stabilité dans le toluène et le PBS. Le poly(V3D3) est légèrement plus hydrophobe que le pp(V3D3). Cependant, les deux couches minces semblent être de bons candidats pour des couches antibiofouling hydrophobes.

Dans le chapitre 4, le dépôt de PVP par iCVD est réalisé avant de se concentrer sur les copolymères poly(VP-co-V3D3).

Pour commencer, le polymère superhydrophile PVP est étudié. Conformément à des précédentes études portant sur le dépôt par iCVD de ce même matériau, l'analyse FTIR des couches minces obtenues montre la polymérisation radicalaire et la conservation des groupements fonctionnels[19]. L'XPS confirme la conservation des groupements fonctionnels en surface. Contrairement au dépôt de poly(V3D3), la cinétique de croissance de la couche mince de PVP semble être une cinétique en deux étapes. Ceci a déjà été observé dans l'équipe pour le dépôt iCVD de polyacrylates et un mécanisme de croissance a été suggéré[20]. L'AFM montre que l'on obtient des dépôts ayant une faible rugosité. Cependant, la microscopie optique met en évidence la présence de cristaux lorsque l'épaisseur du polymère déposé augmente. Il semblerait que ceci puisse être le résultat de la présence d'oligomères dans le réacteur iCVD qui pourraient être éliminés en ajustant la température du substrat[21]. La mesure d'angles de goutte confirme la superhydrophilie du PVP mais met en lumière la solubilité de celui-ci dans l'eau.

Afin de contrer la solubilité du polymère, le V3D3 est utilisé comme agent réticulant. Les deux monomères, le VP et le V3D3, sont injectés simultanément dans le réacteur iCVD et la polymérisation radicalaire permet la formation de couches minces de copolymères en surface du substrat. La spectroscopie FTIR permet de montrer qu'en faisant varier les fractions injectées de chaque monomère, les fractions de VP et de V3D3 contenu dans le copolymère final varient aussi. En appliquant l'équation de Fineman-Ross, les ratios de réactivité peuvent être déterminés[22]. Cela permet de définir le type de copolymère obtenu. Il semblerait que dans le cas du poly(VP-co-V3D3) déposé par iCVD, ce soit un copolymère aléatoire comme illustré dans la Figure 5b. De plus, l'AFM montre la

disparition des inhomogénéités cristallines observées dans le PVP. La mesure d'angle de goutte montre qu'avec une fraction injectée de VP de 87 %, il est possible d'obtenir des couches minces hydrophiles avec des WCA autour de 50°. Enfin, la réticulation du VP avec le V3D3 comme agent réticulant permet de rendre le polymère insoluble dans le PBS comme souhaité, et donc compatible avec des expériences de microbiologie en milieu aqueux.

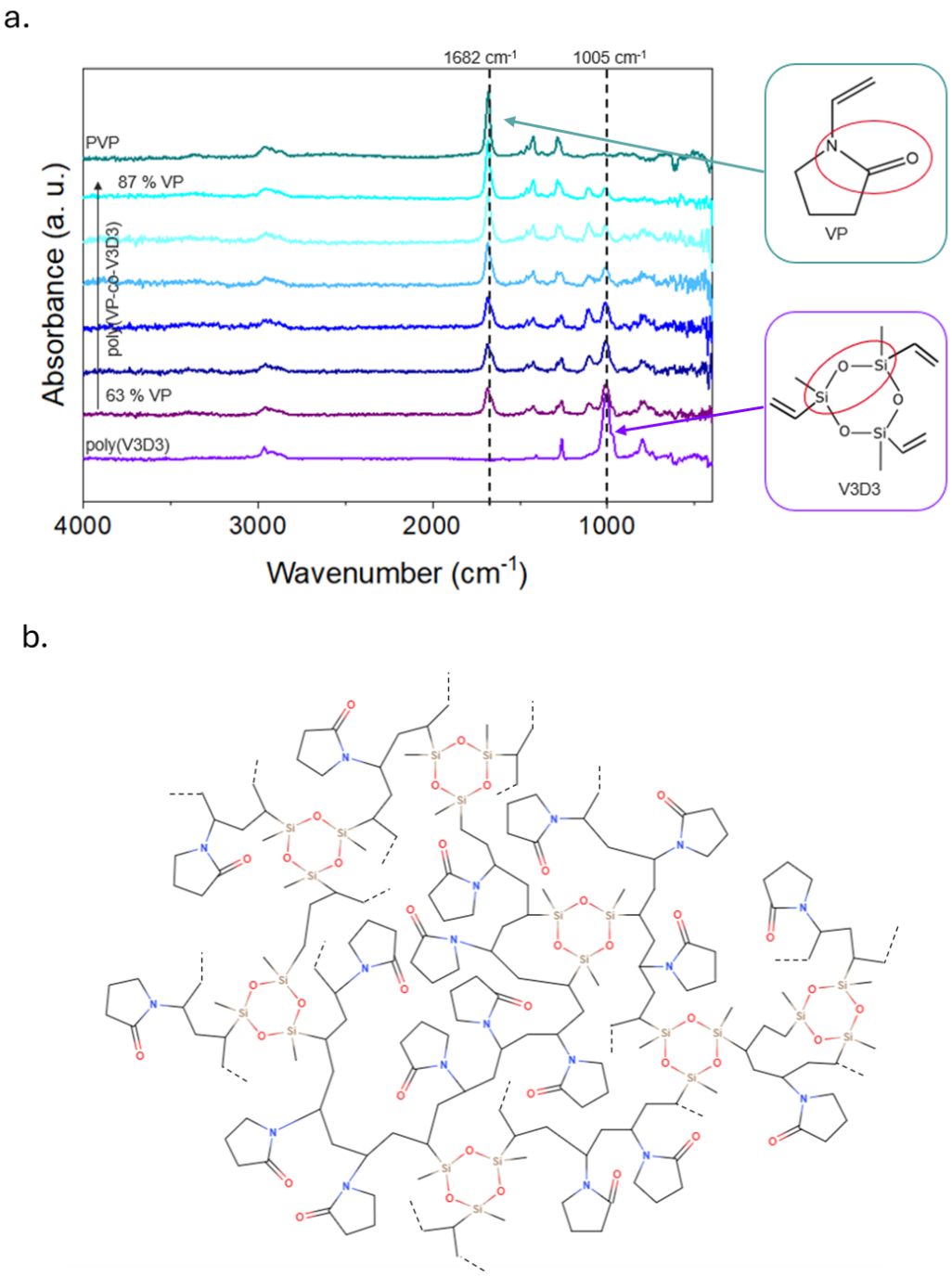

Figure 5 : a. Spectre FTIR du poly(VP-co-V3D3) avec des pourcentages injectés de VP variables. Le pic à 1682 cm^{-1} est spécifique du VP. Celui à 1005 cm^{-1} est spécifique du V3D3. b. Représentation schématique d'un poly(VP-co-V3D3).

Dans le chapitre 5, l'étude de la combinaison de topographie et des polymères développés est présentée, analysée et discutée.

Premièrement, les protocoles de création de surfaces micro et nanostructurées sont présentés. Ces derniers, basés sur un brevet déposé par le CEA Leti[23], reposent sur la lithographie à nanoimpression (NIL) d'une résine de type SiOCH pour la création de lignes et piliers micrométriques. Une étape de gravure plasma est ensuite mise en place afin d'apporter une rugosité nanométrique tout en conservant les microstructures (Figure 6). Plusieurs types de plasmas sont utilisés : un plasma HBr qui apporte une faible rugosité, et un plasma SF_6. Ce dernier est créé avec 2 flux différents de SF_6 : soit 2 sccm (standard cubic centimetre per minute), soit 6 sccm. L'AFM montre que la rugosité de surface obtenue avec 6 sccm de SF_6 est la plus importante.

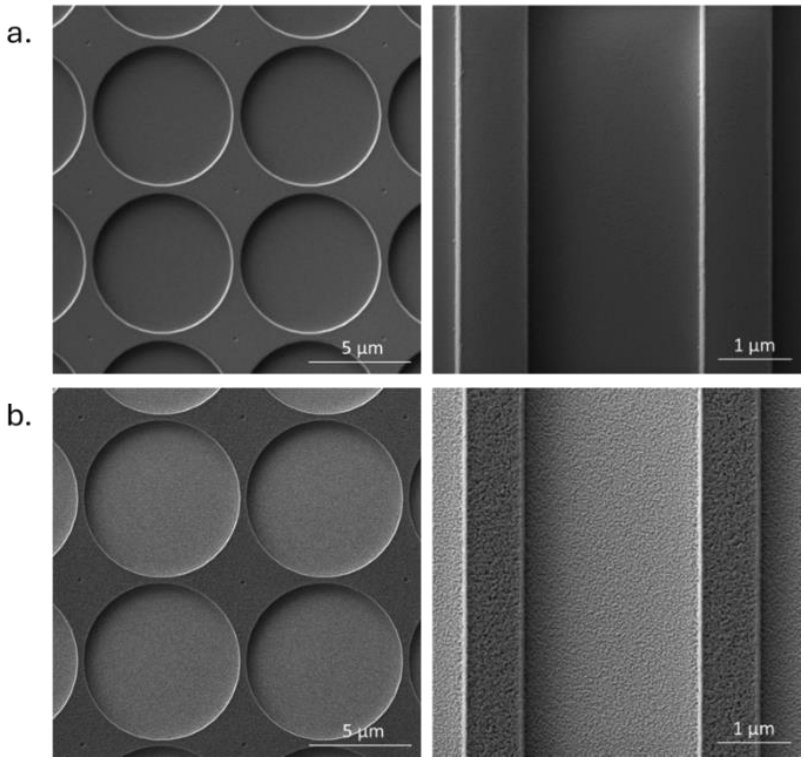

Figure 6 : Images par microscopie électronique à balayage des microstructures a. avant et b. après gravure plasma avec 6 sccm de SF_6.

La mesure d'angle de goutte permet de visualiser l'effet de la topographie de surface sur la mouillabilité. En effet, avant toute modification de structure, la résine utilisée a un WCA autour de 85°. Après un traitement plasma HBr ou SF_6, la surface devient beaucoup plus hydrophile avec des WCA entre 30 et 45°. Ceci peut être du à la modification topographique, mais aussi à l'apparition de groupements hydrophiles tels que des silanols à l'issu de la gravure plasma[24]. Lorsque la résine est modifiée par NIL afin d'apporter des microstructures, la surface devient plus hydrophobe avec des angles de goutte autour de 120°. La surface modifiée par NIL et plasma SF_6 (6 sccm) devient quant-à-elle, superhydrophile.

La mouillabilité des résines structurées peut aussi être modifiée par fonctionnalisation de surface avec les couches minces polymériques étudiées dans les chapitres précédents. En effet, en déposant une couche de poly(V3D3) de quelques nms sur la résine gravée par plasma, ce qui permet de conserver la rugosité nanométrique, l'angle de goutte devient plus hydrophobe que sur poly(V3D3)

plan. Ceci est dû à l'effet Wenzel qui amplifie le caractère hydrophobe ou hydrophile d'un matériau en lui apportant une rugosité[4]. En déposant du poly(V3D3) sur des surfaces ayant des microstructures ainsi qu'une rugosité nanométrique, la mesure d'angle de goutte n'est plus possible car la gouttelette d'eau n'adhère pas à la surface à cause de sa grande hydrophobie. Ceci est le résultat de l'effet Cassie-Baxter, ou l'effet lotus, qui décrit le piégeage de microbulles d'air dans les structures en surface. Dans les conditions étudiées dans ces travaux, le dépôt de pp(V3D3) ou de poly(VP-co-V3D3) sur des substrats structurées n'a pas entrainé de modifications significatives de l'angle de goutte, montrant ainsi la complexité des phénomènes entrant en jeu pour atteindre l'effet Wenzel ou Cassie-Baxter.

Dans le chapitre 6 de ce manuscrit de thèse, les expériences de microbiologie réalisées permettant d'évaluer l'adhésion de bactéries sur les différentes surfaces développées sont décrites et discutées.

Tout d'abord, les protocoles expérimentaux mis en place sont décrits. Il s'agit de préparer une suspension bactérienne de *Escherichia coli* (ou *Staphylococcus epidermidis*) dans laquelle des échantillons des surfaces développées dans les chapitres précédents sont incubées à 37°C pendant 3 h ou plus. Après ce temps d'incubation et des étapes de rinçage afin d'éliminer toute bactérie non adhérée, les échantillons sont incubés dans une solution de coloration LIVE/DEAD pendant 15 min avant d'être rincés de nouveau puis séchés à l'air libre. La microscopie par fluorescence est ensuite utilisée afin de visualiser l'adhésion mais aussi la viabilité des bactéries en surface des différents substrats. Le SiO_2 est utilisée comme témoin.

Avec le poly(V3D3) et le pp(V3D3), qui ont une rugosité et une hydrophobie similaire, mais une structure chimique différente, les résultats montrent une adhésion de *E. coli* similaire à celle sur SiO_2 après 3h d'incubation. Après un temps d'incubation plus long en revanche, l'adhésion de *E. coli* est significativement réduite sur poly(V3D3) par rapport à SiO_2. Ceci peut être du à la plus grande teneur en carbone dans le poly(V3D3)[25]. Cependant, les mêmes expériences avec *S. epidermidis* montrent une plus grande adhésion sur poly(V3D3) que sur SiO_2, montrant la difficulté à développer des surfaces antibactériennes et antifouling universelles.

L'incubation des surfaces de poly(VP-co-V3D3) a été réalisé avec des copolymères développés en injectant différentes proportions de monomères. Les fractions injectées de VP sont de 63 %, 81 % et 87 %, entrainant des angles de goutte de 84°, 73° et 50°, respectivement. Ceci a un fort impact sur l'adhésion de *E. coli* sur la surface qui décroit fortement avec la présence de VP dans le copolymère (Figure 7). Notamment avec 87 % de VP, l'adhésion bactérienne est plus faible que sur SiO_2, poly(V3D3) ou pp(V3D3).

Les expériences microbiologiques réalisées avec les surfaces micro et/ou nanostructurées fonctionnalisées ou non avec les couches minces de polymères montrent les difficultés à trouver les paramètres idéaux pour limiter la formation de biofilm. La taille de microstructures peut notamment entrainer un piégeage des bactéries si elle n'est pas adaptée.

Ces études d'adhésion bactérienne montrent l'importance de la chimie de surface, de sa rugosité et sa topographie ainsi que de sa mouillabilité ou son hydrophobie pour limiter l'adhésion de bactéries. Cependant, d'autres paramètres comme la charge de la surface[26] et sa dureté[27] peuvent aussi avoir un effet non-négligeable. De plus, comme il a été montré ici avec *E. coli* et *S. epidermidis*, il est difficile de générer des surfaces qui sont antiadhésives envers plusieurs espèces de bactéries.

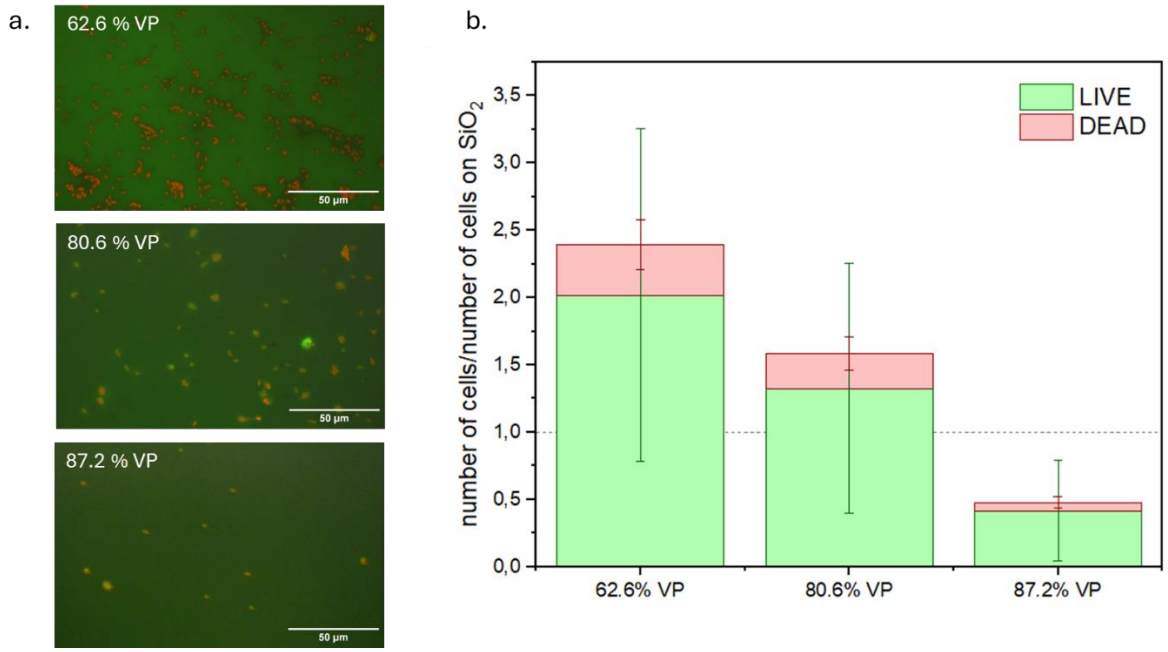

Figure 7 : a. Images obtenues par microscopie par fluorescence de l'adhésion de E.coli *sur des poly(VP-co-V3D3) avec différentes fractions injectées de VP. b. Nombre de cellules bactériennes vivantes et mortes sur ces mêmes surfaces.*

Pour conclure, au cours de ce projet de thèse multidisciplinaire, plusieurs surfaces ont été développées par fonctionnalisation de surfaces planes ou structurées à échelle nano et/ou micrométrique. L'iCVD a été utilisé pour déposer du poly(V3D3) et la conservation des groupements fonctionnels et de la structure du monomère V3D3 permet une meilleure hydrophobie que lorsque le même monomère est déposé par DBD-CAP pour obtenir le pp(V3D3). Le polymère superhydrophile PVP a aussi été déposé par iCVD puis réticulé avec le V3D3 afin de le rendre insoluble et utilisable dans les conditions expérimentales nécessaires en microbiologie. Cette codéposition, qui permet d'obtenir le poly(VP-co-V3D3), une première dans la littérature, montre la possibilité d'utiliser l'iCVD pour créer des couches minces de copolymères par polymérisation radicalaire. En modifiant les flux de chaque précurseur, certaines propriétés telles que l'hydrophilie peuvent être ajustées. Finalement, les études de microbiologie montrent l'importance de contrôler chaque propriété de surface afin de limiter l'adhésion bactérienne et par conséquent, la formation de biofilm.

De nombreuses perspectives peuvent être envisagées pour poursuivre ce travail. Par exemple, modifier les paramètres de dépôts du poly(VP-co-V3D3) par iCVD pourrait permettre d'obtenir un copolymère superhydrophile tout en étant insoluble. D'autres propriétés de surfaces telles que la charge et la dureté pourraient aussi être étudiées afin de voir leur influence sur l'adhésion bactérienne. La fonctionnalisation de micro ou nanostructures avec des polymères réversibles pourraient permettre le développement de surfaces ayant une double action antibactérienne et antibiofouling.

Bibliographie

(1) Bixler, G. D.; Bhushan, B. Biofouling: Lessons from Nature. *Philosophical Transactions of the Royal Society A: Mathematical, Physical and Engineering Science* **2012**, *370* (1967), 2381–2417. https://doi.org/10.1098/rsta.2011.0502.

(2) Ensikat, H. J.; Ditsche-Kuru, P.; Neinhuis, C.; Barthlott, W. Superhydrophobicity in Perfection: The Outstanding Properties of the Lotus Leaf. *Beilstein Journal of Nanotechnology.* **2011**, *2*, 152–161. https://doi.org/10.3762/bjnano.2.19.

(3) Reyssat, M. C. Splendeur et misère de l'effet lotus. phdthesis, Université Pierre et Marie Curie - Paris VI, 2007. https://pastel.archives-ouvertes.fr/tel-00154505 (accessed 2022-09-13).

(4) Belaud, V.; Valette, S.; Stremsdoerfer, G.; Bigerelle, M.; Benayoun, S. Wettability versus Roughness: Multi-Scales Approach. *Tribology International* **2015**, *82*, 343–349. https://doi.org/10.1016/j.triboint.2014.07.002.

(5) Jiang, R.; Hao, L.; Song, L.; Tian, L.; Fan, Y.; Zhao, J.; Liu, C.; Ming, W.; Ren, L. Lotus-Leaf-Inspired Hierarchical Structured Surface with Non-Fouling and Mechanical Bactericidal Performances | Elsevier Enhanced Reader. *Chemical Engineering Journal* **2020**, *398*, 125609. https://doi.org/10.1016/j.cej.2020.125609.

(6) Durand, H.; Whiteley, A.; Mailley, P.; Nonglaton, G. Combining Topography and Chemistry to Produce Antibiofouling Surfaces: A Review. *ACS Applied Bio Materials* **2022**, acsabm.2c00586. https://doi.org/10.1021/acsabm.2c00586.

(7) Zaggia, A.; Ameduri, B. Recent Advances on Synthesis of Potentially Non-Bioaccumulable Fluorinated Surfactants. *Current Opinion in Colloid & Interface Science* **2012**, *17* (4), 188–195. https://doi.org/10.1016/j.cocis.2012.04.001.

(8) Stalet, M. Protections Anti-Microbiennes : Combinaison de La Fonctionnalisation et de La Nano-Structuration Pour Explorer Les Interactions Cellule/Surface, Université Grenoble Alpes et Université de Sherbrooke, 2024.

(9) Maan, A. M. C.; Hofman, A. H.; Vos, W. M. de; Kamperman, M. Recent Developments and Practical Feasibility of Polymer-Based Antifouling Coatings. *Advanced Functional Materials.* **2020**, *30* (32), 2000936. https://doi.org/10.1002/adfm.202000936.

(10) Coclite, A. M.; Howden, R. M.; Borrelli, D. C.; Petruczok, C. D.; Yang, R.; Yagüe, J. L.; Ugur, A.; Chen, N.; Lee, S.; Jo, W. J.; Liu, A.; Wang, X.; Gleason, K. K. 25th Anniversary Article: CVD Polymers: A New Paradigm for Surface Modifi Cation and Device Fabrication. *Advanced Materials.* **2013**, *25* (38), 5392–5423. https://doi.org/10.1002/adma.201301878.

(11) Moni, P.; Al-Obeidi, A.; Gleason, K. K. Vapor Deposition Routes to Conformal Polymer Thin Films. *Beilstein Journal of Nanotechnology* **2017**, *8*, 723–735. https://doi.org/10.3762/bjnano.8.76.

(12) Zavvou, Z. Dépôt iCVD de Couches Minces de Polymères Pour Des Applications En Électronique de Puissance. These de doctorat, Université Grenoble Alpes, 2023. https://www.theses.fr/s228349 (accessed 2023-12-07).

(13) Pryce Lewis, H. G.; Edell, D. J.; Gleason, K. K. Pulsed-PECVD Films from Hexamethylcyclotrisiloxane for Use as Insulating Biomaterials. *Chemistry of Materials* **2000**, *12* (11), 3488–3494. https://doi.org/10.1021/cm0003370.

(14) O'Shaughnessy, W. S.; Murthy, S. K.; Edell, D. J.; Gleason, K. K. Stable Biopassive Insulation Synthesized by Initiated Chemical Vapor Deposition of Poly(1,3,5-Trivinyltrimethylcyclotrisiloxane). *Biomacromolecules* **2007**, *8* (8), 2564–2570. https://doi.org/10.1021/bm070242s.

(15) Teodorescu, M.; Bercea, M. Poly(Vinylpyrrolidone) - A Versatile Polymer for Biomedical and Beyond Medical Applications. *Polymer-Plastics Technology and Engineering* **2015**, *54* (9), 923–943. https://doi.org/10.1080/03602559.2014.979506.

(16) Chan, K.; Kostun, L. E.; Tenhaeff, W. E.; Gleason, K. K. Initiated Chemical Vapor Deposition of Polyvinylpyrrolidone-Based Thin Films. *Polymer* **2006**, No. 47, 6941–6947. https://doi.org/10.1016/j.polymer.2006.07.068.

(17) Borek-Donten, J.; Nisol, B.; Filimon, M.; Lopes, M.; Collard, D.; Chassaing, M.; Cauchie, H.-M.; Heyberger, R. The Industrial Process for Virucidal Plasma Coatings on Textiles: From Idea to Upscaling. *Plasma Processes & Polymers* **2022**, *19* (10), 2100249. https://doi.org/10.1002/ppap.202100249.
(18) Zavvou, C.; Cluzel, J.; Mariolle, D.; Lefevre, A.; Jousseaume, V. Poly(V3D3), an iCVD Polymer with Promising Dielectric Properties for High Voltage Capacitors. *Solid-State Electronics* **2021**, *184*, 108057. https://doi.org/10.1016/j.sse.2021.108057.
(19) Janakiraman, S.; Farrell, S. L.; Hsieh, C.-Y.; Smolin, Y. Y.; Soroush, M.; Lau. Kinetic Analysis of the Initiated Chemical Vapor Deposition of Poly(Vinylpyrrolidone) and Poly(4-Vinylpyridine). *Thin Solid Films* **2015**, *595*, 244–250. https://doi.org/10.1016/j.tsf.2015.04.083.
(20) Bonnet, L.; Altemus, B.; Scarazzini, R.; Veillerot, M.; D'Agosto, F.; Faguet, J.; Jousseaume, V. Initiated-Chemical Vapor Deposition of Polymer Thin Films: Unexpected Two-Regime Growth. *Macromolecular Materials and Engineering* **2017**, *302* (12), 1700315. https://doi.org/10.1002/mame.201700315.
(21) Shindler, S.; Franklin, T.; Yang, R. Prevention and Characterization of Thin Film Defects Induced by Contaminant Aggregates in Initiated Chemical Vapor Deposition. *The Journal of Chemical Physics* **2024**, *160* (14), 144904. https://doi.org/10.1063/5.0195014.
(22) Smolin, Y. Y.; Janakiraman, S.; Soroush, M.; Lau, K. K. S. Experimental and Theoretical Investigation of Dye Sensitized Solar Cells Integrated with Crosslinked Poly(Vinylpyrrolidone) Polymer Electrolyte Using Initiated Chemical Vapor Deposition. *Thin Solid Films* **2017**, *635*, 9–16. https://doi.org/10.1016/j.tsf.2016.12.034.
(23) Teyssedre, H.; Posseme, N.; Mehrez, Z.; May, M. Procédé de structuration de surface hybride par gravure plasma. EP 4 083 706 A1, November 2, 2022.
(24) Vinogradova, E.; Osei-Yiadom, E.; Smith, C. E.; Mueller, D. W.; Reidy, R. F. Effects of Plasmas on Porous Low Dielectric Constant CVD SiOCH Films. *Microelectronic Engineering* **2009**, *86* (2), 176–180. https://doi.org/10.1016/j.mee.2008.10.018.
(25) Navabpour, P.; Teer, D.; Su, X.; Liu, C.; Wang, S.; Zhao, Q.; Donik, C.; Kocijan, A.; Jenko, M. Optimisation of the Properties of Siloxane Coatings as Anti-Biofouling Coatings: Comparison of PACVD and Hybrid PACVD-PVD Coatings. *Surface & Coatings Technology* **2010**, *204* (20), 3188–3195. https://doi.org/10.1016/j.surfcoat.2010.03.011.
(26) Kulaga, E. Antimicrobial Coatings for Soft Materials, Université de Haute Alsace, 2014.
(27) Vigué, A.; Vautier, D.; Kaytoue, A.; Senger, B.; Arntz, Y.; Ball, V.; Ben Mlouka, A.; Gribova, V.; Hajjar-Garreau, S.; Hardouin, J.; Jouenne, T.; Lavalle, P.; Ploux, L. Escherichia Coli Biofilm Formation, Motion and Protein Patterns on Hyaluronic Acid and Polydimethylsiloxane Depend on Surface Stiffness. *Journal of Functional Biomaterials* **2022**, *13* (4), 237. https://doi.org/10.3390/jfb13040237.

Abstract

As biofilms continue to cause damage in many different industries, leading to health issues, device failure and numerous costs, the traditional strategies used to fight against biofouling are being questioned. Indeed, the rise of antibioresistance and concerns over the toxicity of other biocides bring to light the limits of such approaches. Rather than focusing on eliminating biofilm, bioinspired strategies suggest limiting the initial bacterial adsorption by developing hydrophobic or hydrophilic surfaces. In this thesis, hydrophobic fluorine-free organosilicate thin films were deposited using two innovative deposition methods: Dielectric Barrier Discharge Cold Atmospheric Plasma (DBD-CAP) and initiated Chemical Vapour Deposition (iCVD), respectively leading to plasma polymers and conventional polymers. iCVD was also used to functionalise surfaces with superhydrophilic poly(vinylpyrrolidone). While the latter had interesting wettability properties, it's solubility made it an impossible coating for devices to be found in bacterial suspensions or other liquid media. To overcome this, the organosilicate precursor was used as a crosslinking agent and both monomers were simultaneously injected into the iCVD reactor, creating hydrophilic and insoluble copolymers. As well as depositing these polymers on planar surfaces, they were used to coat substrates with microscale topography brought by nanoimprint lithography, and roughness achieved by plasma etching. Indeed, it has previously been shown in the literature that there are many advantages in combining chemistry and topography for antibiofouling surfaces. Finally, the developed surfaces were incubated with bacterial suspensions to assess their influence of bacterial adhesion.

Keywords: antibiofouling, polymer thin films, iCVD, DBD-CAP, hydrophobic, hydrophilic, topography

Résumé

Alors que les biofilms continuent de causer de nombreux dégâts dans diverses industries, entrainant des problèmes de santé, des défaillances de matériel et des couts non négligeables, les stratégies traditionnelles de lutte contre le biofilm sont remises en question. En effet, la croissance de l'antibiorésistance ainsi que la constatation de la toxicité de certains biocides, mettent en lumière les limites de telles approches. Ainsi, plutôt que de s'attaquer à l'élimination de biofilm, de nouvelles stratégies, qui consistent à éviter l'adsorption bactérienne, sont en train d'être étudiées, notamment avec des surfaces hydrophobes ou hydrophiles. Dans cette thèse, un polymère organosilicié hydrophobe mais sans fluor, a été déposé sous forme de couche mince à l'aide de deux techniques innovantes : le plasma atmosphérique froid à décharge par barrière diélectrique (DBD-CAP) et le dépôt chimique en phase vapeur par une polymérisation amorcée in-situ (iCVD), créant respectivement des polymères plasma et conventionnels. L'iCVD a aussi été utilisé pour fonctionnaliser des surfaces avec le poly(vinyl pyrrolidone) superhydrophile. Ce dernier, malgré des propriétés de mouillabilité intéressantes, ne permet pas une utilisation dans des milieux liquides tels que des suspensions bactériennes, à cause de sa solubilité. Pour palier à cela, le précurseur organosilicié a été utilisé comme agent de réticulation, et les deux monomères ont été co-injectés par iCVD, formant un copolymère hydrophile et insoluble. Ces polymères ont été déposés sur des surfaces planes, mais aussi structurées : avec des microstructures apportées par lithographie par nanoimpression, et une rugosité apportée par gravure plasma. En effet, il a été montré dans la littérature que combiner chimie et topographie peut avoir de nombreux avantages pour lutter contre le biofilm. Pour finir, ces surfaces ont été incubées dans des suspensions bactériennes, afin de regarder leur influence sur l'adhésion des bactéries.

Mots clés: antibiofouling, couche mince, polymères, iCVD, DBD-CAP, hydrophobe, hydrophile, topographie